Coupling magnetism and mechanics at a molecular level

Marc Ganzhorn

UNIVERSITÉ DE GRENOBLE

THÈSE

Pour obtenir le grade de

DOCTEUR DE L'UNIVERSITÉ DE GRENOBLE

Spécialité : **Physique**

Arrêté ministériel : 7 Aout 2006

Présentée par

Marc GANZHORN

Thèse dirigée par **Wolfgang WERNSDORFER**

préparée au sein **Institut Neel, CNRS/UJF**
et de **Ecole Doctorale de Physique, Grenoble**

Coupling Magnetism and Mechanics at a molecular scale

Thèse soutenue publiquement le **13 Mars 2013**,
devant le jury composé de :

Prof. Mairbek Chshiev
Professeur, Spintec-UDG Grenoble, Président
Dr. Takis Kontos
Charge de recherche, LPA-ENS Paris, Rapporteur
Dr. Gary Steele
Professeur assistant, TU Delft, Rapporteur
Dr. Benjamin Lassagne
Maitre de conference, LPCNO-CNRS-INSA Toulouse, Examinateur
Dr, Wolfgang Wernsdorfer
Directeur de recherche, Institut Neel-CNRS Grenoble, Directeur de thèse

"Truth suffers from too much analysis"'
Fremen saying on Arrakis, *Dune*, Frank Herbert

Acknowledgements

I performed my PhD research at the Nanoscience department of the Neel Institute in Grenoble. I thank the heads of the Institute, Alain Fontaine and Alain Schuhl, and department heads, Joel Cibert and Herve Courtois, for the warm welcome at the Institute.

I thank Prof. Mairbek Chshiev for presiding my thesis comittee, Takis Kontos and Gary Steele as referees for my manuscript and Benjamin Lassagne for participating to my jury.

Ma these a ete financier par la Fondation Nanoscience a Grenoble. Je remercie les directeurs, Roland Herino et son successeur Alain Fontaine pour avoir financer cette these et le support en continu durant ces trois dernieres annees. Merci a Maud Dayez, Feriel Kouiten, Marie-Anne Carre et Karine Argento pour m'avoir guider a travers la jungle de l'administration francaise. Enfin, merci a toi Steph pour tous les pots et fetes organise, les news de la Fondation, les fous rires au bureau, les histoires "Kinder surprise", tes conseils et ton soutien moral.

I thank in particular Wolfgang Wernsdorfer for supervising my work over the last three years. For one, I would like to thank you for all the fruitfull scientific (and non-scientific) discussions and all the valuable advice, given literally at any time, anywhere... Thank you for allowing me to use *your sionludi*, for all the countless overnight cooldowns and exchange of helium bottles and for reparing all the things I broke. Finally, I thank you for your patience (for instance reading my papers and manuscript), your confidence and your faith in me and my work. It was a real pleasure!

I'd also like to thank all the former, present and new members of the Nanospin group: The "graphene man" Andrea Candini, Edgar Bonet and Christophe Thirion, our programming masters, "Ramanpes" Manuel Lopes, Romain "roro" Maurand and Oksana Gaier; I'd also like to thank the former group members, now part of the newly formed *Hybrid group* Adrien Allain, Zheng "Vitto" Han, Laetitia Marty, Nedjma Bendiab, Vincent Bouchiat. My former officemates Subhadeep Datta, for spreading your good mood from my first day on, and Jarno Jarvinen, for numerous late night sessions of fun in the lab and the office and for showing me the way to the "D'Enfer pub"! Thanks to you Jean-Pierre Cleuziou and Viet Ngoc-Nguyen for your big help with this mysterious CVD setup of yours and for giving me a headstart on how to make ther perfect sample.

Merci aussi a toi Anastasia Varlet, pour les fous rire au bureau et la multitude de midis et soirees "Nanos"; Raoul Piquerel, pour debugger mon NanoQt et pour les belles tranches de rigolades; Antoine Reserbat, pour ton introduction au Raman et les sessions de badminton; "Sergeant" Romain Vincent et Matias Urdampilleta pour les weekends et nuits de manips collective, pour m'avoir expliquer le magnetisme moleculaire et la

cryogenie et avoir remplis mon piege a azote. Danke an Dich Stefan fuer die wertvolle wissenschaftliche und moralische Unterstuetzung, die vielen Ueberraschungen, Ideen und so vieles mehr....

Finalement un grand merci a toi Franck Balestro, d'avoir relu et corriger tout article et manuscript de these que je t'ai fais lire, d'avoir assister et insister sur les repet de soutenance/presentation, pour me donner un deuxieme point de vue et pour toujours avoir une oreille ouverte a tout probleme, scientifique ou non!

Un grand merci a la "Dreamteam" Nanofab, qui a du me supporter ma presence tout les jours en salle blanche ou a H2! Le "Grand Fournier" Thierry pour ton aide en salle blanche et litho eletronique; Evidement merci a toi Thierry Crozes pour m'avoir montrer comment faire une belle litho de facon professionelle, les soirees tennis et tes observations et reflexions "pertinentes" a certains propos..... Merci a Bruno pour m'avoir montrer le fonctionnement d'une salle blanche et d'avoir reparer tout equipement que j'ai maltraiter (surtout le Plassys). Merci a toi Gwenaelle pour avoir subi la presence d'un autre gamin dans ton entourage et merci a toi Jeff "FIB" Motte. Finalement a toi Sebastien, aka "Petit Fournier", merci pour tout les bons moments en salle, a la PTA, a midi et au cafe!!! Sans oublier les "Y faut y....." bien entendu.

Merci aussi a Ioan et Eva, pour les gros fous rires et tout les lapins qui ont envahit notre bureau. Un grand merci aussi a Eric Eyraud, pour avoir reparer tout les pieces de dilution que j'ai casse, ta bonne humeur et une fameuse bataille de polochon (les autres participants s'en souviendront...). Merci aussi a Laurent Cagnon pour un coup de main a l'ALD. Merci a toi Richard Haettel, Didier Dufeu, David Barral, Daniel Lepoittevin, Christophe Hoarau, Valerie Reita, Philippe David et tout les membres du pole magnetometrie, pole optique, du pole couches minces, du pole cryogenie, pole informatique (merci a Patrick Belmain pour avoir sauver mes donnees apres une greve totale de mon ordi) et du liquefacteur..... Merci aussi a l'administration, notament Veronique Fauvel et Sabine Gadal pour avoir resolu tous petit probleme concernant la paperasse et d'une salle de soutenance de these etant inacessible.

Finalement merci a tout les collegues de l'Institut Neel, Spintec ou autres que j'ai rencontrer ces dernieres annees et ayant contribuer a une ambiance de travail tres chaleureuse et agreable: Romain Thalineau, Christophe Blanc, Tobias, Johanna, Laetitia Pascal, Sylvain Martin, Olivier Bougeois, Olivier Buisson, Emilie, Mihai, Josephine, Christophe, Selma, Nora, etc.....

Thanks a lot to a bunch of awesome guys: Angela *the Tiramisu queen*, Liza alias *the little devil*, Stefan, Martin, Ovidiu, Iulia, Claudio, Elena, Christoph, Carina, Valentina, Francesca, Tommaso, Simone.... Thank you so much for all those awesome moments in Grenoble at Bayard, d'Enfer, Bobine or Scarpe mobile concerts ..... Or all the trips to Paris, Parma, Firenze, Stuttgart and all the place we have been together and the places we still have to go to! Thank you for your support in good and bad times (very bad times

after a certain Germany-Italy game...)!

Special thanks to Teo and Geta for some special moments (yeeees that kind of special) around Grenoble, Spain, France, Italy or Romania.

Merci a la famille Dufresnes: Seb, Elo et la petite Charlie pour des moments et weekends inoubliables a Izeaux et autour de Grenoble!

Merci aussi aux Strasbourgeois Mario et Julie, Caro, Julie, Maud, Colette, Eric pour votre support a distance ou de pres, a tout moment ou que vous soyez. Merci Service comme dirais *Kansas*!!!

Finally, I owe you, Anca, some very special thanks for your support and your help anytime, anywhere. Thank you for being there for me!!

Last, I would like to thank my family for all the unconditional support from far away. It wouldn't have been possible without you.

Contents

Chapter 1

General introduction

Mechanics at a molecular scale

Mechanical systems exist in various forms, compositions and dimensions, ranging from astronomic objects like galaxies (10^{20} m, 10^{42} kg) to molecule-size vibrating strings (10^{-9} m, 10^{-21} kg) as depicted in Fig. 1.1.

Astronomical phenomena such as the motion of a planet around its star or the trapping of light by a black hole can be described with amazing accuracy by the laws of special and general relativity established by Einstein for large and massive objects. On a more human scale (1 m, 1 kg) the dynamics of mechanical systems are governed by the classical laws of motion, such as the oscillation of a pendulum or the vibration of a guitar string.

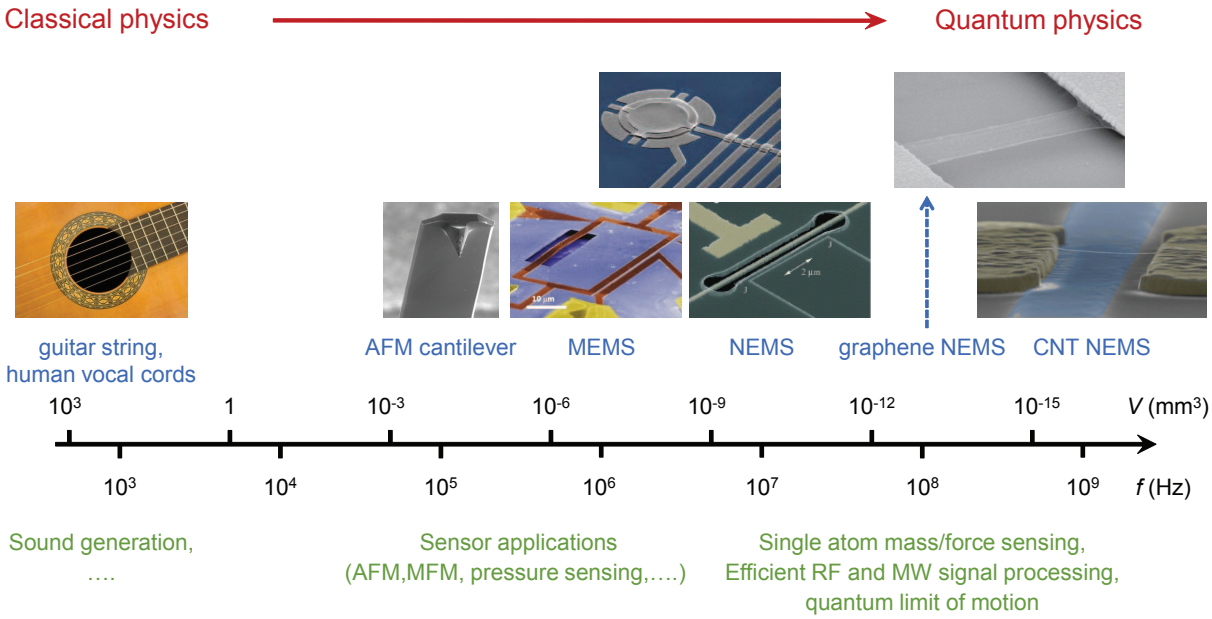

Figure 1.1: From macroscopic to quantum harmonic oscillators

Using integrated circuit technology, one can reduce the dimensions of mechanical systems even further down to the micrometer scale. Enabled by the smaller mass and higher resonance frequencies of a few hundred kilohertz, such micro-electromechanical systems

(MEMS) are widely used for sensing applications, most notably for *atomic* or *magnetic* force microscopy [1].

Upon scaling mechanical systems down to the nanometer scale, the resonance frequency further increases while the mass of the system becomes smaller. Such nanoelectromechanical systems (NEMS) are therefore ideal candidates for mass or force sensing at the atomic scale [1]. If cooled to very low temperatures, such a NEMS can reach a state where its dynamics are governed by the laws of quantum mechanics. In this case, one can observe a NEMS' zero point motion and quantum mechanical ground state [2, 3]. In such quantum oscillators one could achieve and probe the superposition of two quantum states [1].

In this context, carbon nanotubes turned out to be ideal building blocks for NEMS due to their extremely low mass ($m = 10^{-21}$ kg) and high Young's modulus ($E = 1$ TPa). In such a supramolecular NEMS, one easily reaches resonance frequencies above 1 GHz with quality factors as high as $Q = 10^5$ [1]. Indeed, carbon nanotube NEMS can detect masses as small as 10^{-24} g [4, 5] or forces down to 10^{-18} N [6], thus reaching single atom sensitivity. Due to the high resonance frequencies above 1 GHz, carbon nanotube resonators can furthermore be cooled to their quantum mechanical ground state in dilution refrigerators with a base temperature below 50 mK. Under those conditions, a carbon nanotube NEMS can be seen as the experimental implementation of a quantum (harmonic or anharmonic) oscillator.

Magnetism at a molecular scale

In analogy to mechanical systems, one can observe a large variety of magnetic systems ranging from permanent magnets (1 mm, $10^{20}\mu_B$) down to a single nuclear spin (10^{-15} m, $10^{-3}\mu_B$) as depicted in Fig. 1.2.

On a macroscopic scale, the magnetism results from the collective behaviour of a large number of magnetic moments or spins. Below the so called Curie temperature, this collective behaviour results in the formation of many areas with uniform magnetization inside the macroscopic magnet, so called magnetic domains [8]. Under the influence of a magnetic field, one can observe the creation, propagation and annihilation of these domains until the magnet reaches its full magnetization. The magnetization dynamics in such a macroscopic ferromagnet translates in a characterisic hysteresis loop depicted in Fig. 1.2.

If the size the magnet becomes smaller than the size of a magnetic domain, for example in magnetic nanoparticles or molecular clusters, one can observe a uniform reversal of the magnetization, typically on the order of $10^5\mu_B$, when the magnetic field compensates for

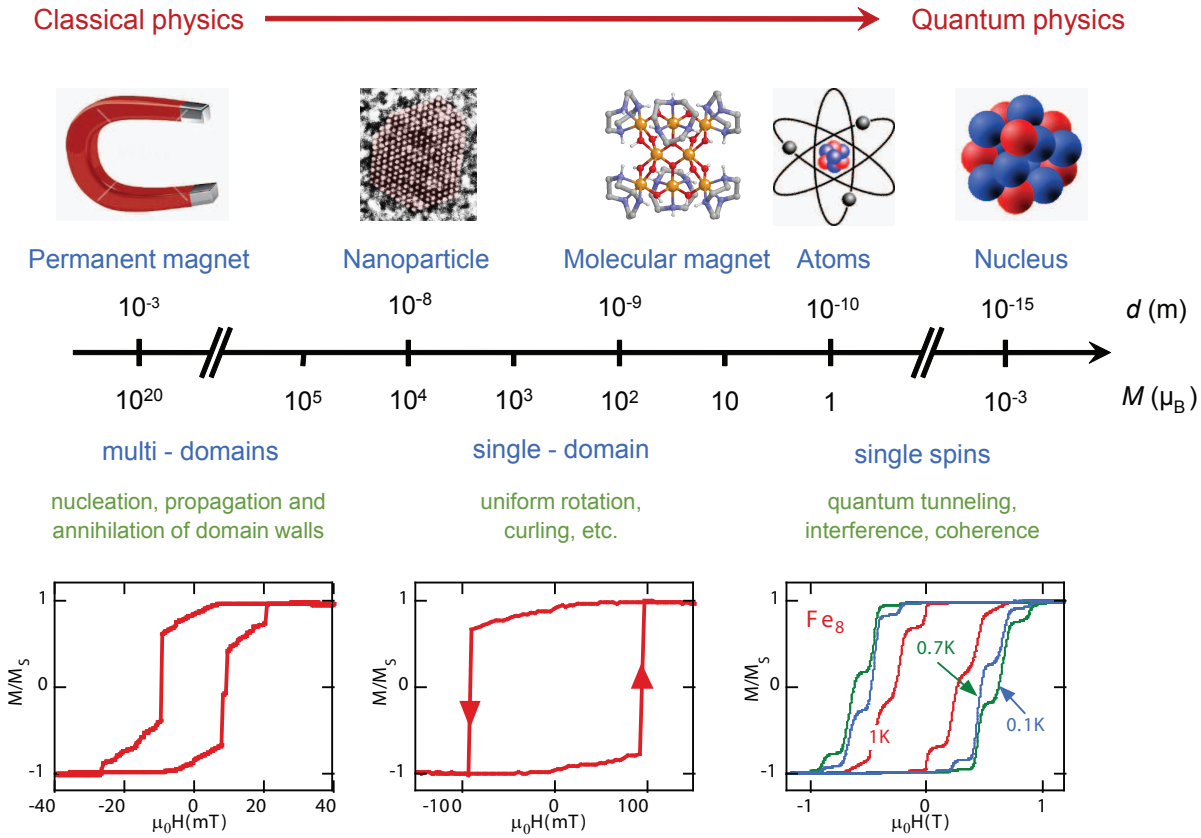

Figure 1.2: From macroscopic to quantum magnetism. Adapted from [7].

the magnet's anisotropy energy [9]. The magnetization dynamics in such a single-domain magnet is usually described in its simplest form by the Stoner-Wolfahrt model [10].

Upon scaling the magnet down to the size of a single molecule, the magnetization reduces to only a few μ_B and the magnet will be prone to a number of quantum mechanical effects. In particular, quantum tunneling of magnetization occurs in such a single molecule magnet, resulting in characteristic steps in the hysteresis curve of the magnet at cryogenic temperatures (see Fig. 1.2 for a Fe_8 molecule). Owing to the molecular nature, single molecule magnets additionaly exhibit extremely long relaxation times up to a few years and coherence times up to a few microseconds at cryogenic temperatures below 1 K, allowing for coherent manipulation of such a molecular spin. Single molecule magnets are therefore ideal building blocks for (molecular) spintronic devices and would make an excellent spin qubit [11].

Coupling Magnetism and Mechanics on a molecular scale

One can now probe the properties of micro- or nanoscopic magnetic objects using micro- or nano-electromechanical systems.

For instance, micromechanical (magnetic) cantilever are commonly used in *magnetic force* microscopy (MFM) to probe the magnetization dynamics (domain wall motion and formation, hysteresis, collective behaviour, etc...) in micro- and nano-scale structures such as magnetic thin films [12], nanoparticles [13], nanowires [14]. The spatial resolution is typically on the order of 20-100 nm, which enables the detection of a magnetic moment down to $10^7\mu_B$ and forces on the order of 10^{-12} N [15]. By pushing force microscopy to its limits, Rugar *et al.* recently demonstrated the detection of a force of 10^{-18} N from a single electron spin using an improved magnetic *resonance* force microscopy technique at cryogenic temperatures [15].

In an alternative approach, micro-cantilevers are used as *magnetic torque* detectors [16, 17]. A magnetic thin film deposited on the cantilever will induce a torsion of the latter, if exposed to an oscillating magnetic field. By those means, one can probe a magnetic moment on the order of $10^{11}\mu_B$ at room temperature.

Following the actual trend of building even smaller and more efficient detectors, we propose in this manuscript a design for a *supramolecular* torque magnetometer based on a carbon nanotube NEMS, that could probe and manipulate the magnetic moment ($\sim 1\mu_B$) or the force ($\sim 10^{-18}$ N) of a single molecule magnet at cryogenic temperatures. Such a supramolecular spintronic device (Fig. 1.3) would enable the detection of a single electronic spin and ultimately of an assembly of nuclear spin or even a single nuclear spin [18].

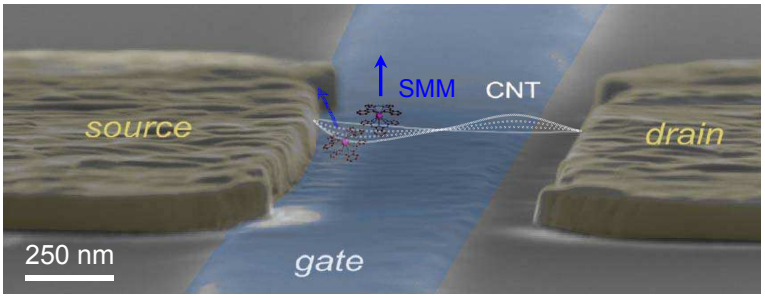

Figure 1.3: Supramolecular hybrid quantum system based on a carbon nanotube NEMS (CNT NEMS) and a single molecular magnet (SMM).

Both carbon nanotube NEMS and single molecule magnets are also potential quantum oscillators and spin qubits, respectively. Coupling both quantum systems would therefore enable the detection and coherent manipulation of a single electron or nuclear spin using a quantum oscillation. A spintronic device of such a molecular nature would consequently enable quantum information processing on a single spin or phonon level and

allow for example the entanglement of two individual molecular spins or phonons.

In this manuscript, we will first present the ultimate molecular building block for spintronic devices, so called single-molecule magnets (Chapter 2). In particular we will focus on a $TbPc_2$ complex and various approaches of probing its magnetization using carbon nanotube detectors and different coupling mechanisms (magnetic flux, electronic and mechanical coupling).

With the aim of building a supramolecular torque magnetometer capable of probing the magnetic moment of a molecular magnet, we will describe in Chapter 3 a promising candidate, a carbon nanotube nanoelectromechanical system (NEMS). We will first describe the advantages of carbon based NEMS over classical Si based resonators. Subsequently we will present the state of art of carbon nanotube NEMS and focus in particular on two different nanomechanical motions, a transverse bending mode and a longitudinal stretching mode.

In Chapter 4, we present the experimental implementation of a supramolecular torque magnetometer based on carbon nanotube NEMS and single molecule magnets. We first describe the ultraclean bottom-up fabrication process and the extensive characterisation steps of carbon nanotube NEMS at room and cryogenic temperatures. We will finally demonstrate a method of grafting a $TbPc_2$ single molecules magnet on such a carbon nanotube NEMS, that conserves both the magnetic properties of the molecule and the mechanical properties of the resonator.

In Chapter 5, we will then perform a systematic study of the transverse bending mode vibration in a carbon nanotube NEMS. We demonstrate for instance, that the dissipation of a carbon nanotube's bending mode vibration to single electron tunneling through the carbon nanotube NEMS-quantum dot critically depends on the dot's electronic environment, i.e. the capacitance, the tunnel coupling to the metal leads, the current and temperature. The findings suggest that one could achieve quality factors of 10^6 or higher by choosing appropriate gate dielectrics and/or by improving the tunnel coupling to the leads, which would notably increase the sensitivity of the carbon nanotube NEMS with respect to a magnetic torque generate by a rotating molecular magnet [19].

In Chapter 6, we demonstrate the presence of a quantized longitudinal stretching mode vibration in a carbon nanotube NEMS functionnalized with $TbPc_2$ single molecule quantum magnets. We will in particular demonstrate that the quantum mechanical nature of both systems, results in a strong coupling between the longitudinal stretching mode and the magnetization of an individual $TbPc_2$ single molecule magnet grafted to the carbon nanotube's sidewall. The strong coupling in fact enables the detection of the nuclear spin states in the $TbPc_2$ molecule [20].

Finally, we present in the conclusion of this manuscript some future prospects for the detection and (coherent) manipulation of a single (nuclear) spin using a mechanical quantum system.

Chapter 2

Introduction to Molecular Spintronics

With the discovery of the giant magnetoresistivity effect (GMR) in 1988 [21, 22], a new generation of electronics has emerged using the spin degree of freedom of the electron, so called spin transport eletronics or *spintronics*. Spintronics takes advantage of the existence of both spin-up and spin-down carriers in the electric current of micro- or nanoeletronic devices. Using various spin dependent effects arising from the interaction between the electron spin and the magnetic material, one can encode information in the spin state of the electron. Information stored in spin-dependent transport structures, like spin valves or magnetic tunnel junctions, is potentially nonvolatile and can be processed much faster and with lower power consumption than in conventional semiconductor devices [23].

New approaches involving the use of semiconductors [24] or organic materials [25] in spintronic devices were explored in order to enhance and exploit quantum coherence. Following the same trend, the dimensions of electronic devices were driven beyond the nanoscale to a molecular level [26, 11], where one could take advantage of the quantum mechanical nature of such a system.

In an effort of combining spintronics with such molecular scale electronics, a new field of *molecular spintronics* has thus emerged during the last decade. The main idea consists in integrating single magnetic molecules into nanoelectronic devices [11]. In this context, so called single-molecule magnets (SMM) seem to be an ideal candidate for such molecular spintronic devices [11]. Owing to the large variety of magnetic properties, for instance a large magnetic moment and a strong magnetic anisotropy, one can expect extremely long relaxation and coherence times for SMM based spintronic devices, making them potentially attractive for quantum information processing or quantum computing [11].

In the following chapter, we will first point out the advantages of single molecule magnets as building block for molecular spintronics (Section 2.1) and we will present a Terbium Double Decker SMM (Section 2.2), which is the main object studied throughout this manuscript. Finally, we propose different approaches of integrating an SMM into carbon based devices, thus designing a supramolecular spintronic device and a single spin detector (Section 2.3).

2.1 Towards Molecular spintronics

2.1.1 Giant magnetoresistance and metallic spintronic devices

The GMR effect was first discovered in ferromagnetic-nonmagnetic multilayer structures [21, 22]. The electric current or the resistance herein strongly depends on the relative orientation of the magnetization in the ferromagnetic layers and can be controlled by a magnetic field (Fig. 2.1c). The device resistance yields a minimum if the magnetic moments in the ferromagnetic layers are aligned parallel to each other (Fig. 2.1a) and a maximum if aligned antiparallel (Fig. 2.1b).

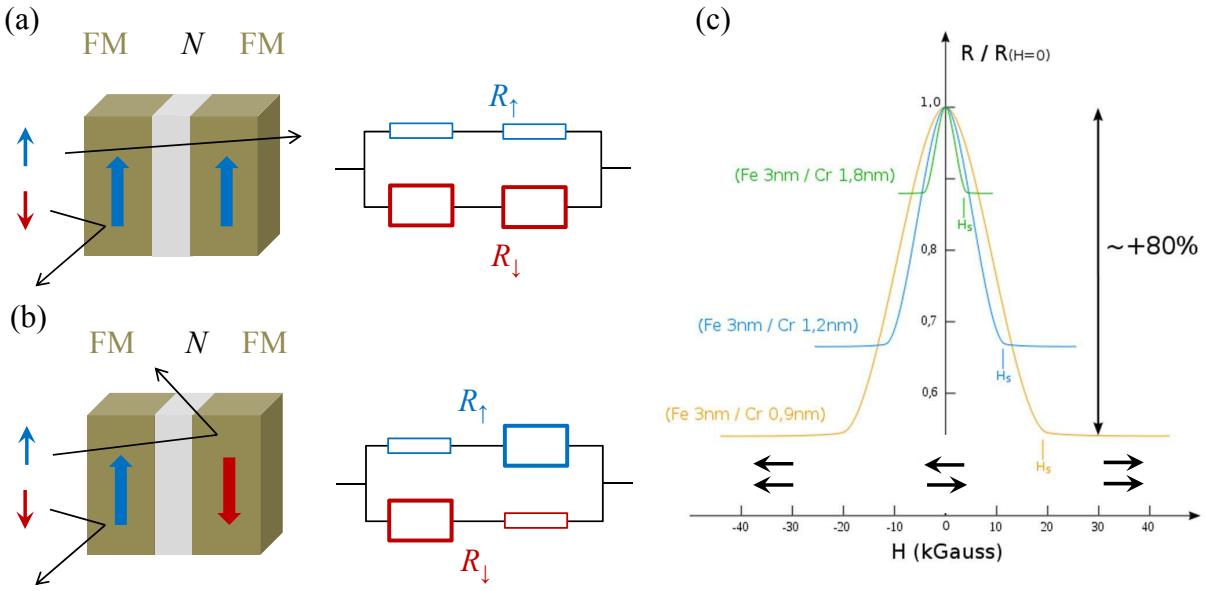

Figure 2.1: Giant magnetoresistance effect in ferromagnetic (FM)/nonmagnetic (N) multilayers. The device resistance $\Delta R/R$ depends on the relative orientation of the magnetization in the FM layers. (a) For a parallel orientation the device is in a low resistance state and (b) for an antiparallel orientation the device is in a high resistance state. The GMR can be model by two resistor circuits. In (a) the multilayer is "transparent" to one type of spin carrier, while "blocking" the spins with the opposite orientation, resulting in a low device resistance. In (b) both spin carriers are "blocked", resulting in an increased overall resistance. (c) Magnetoresistance change with the applied magnetic field for different Fe/Cr multilayers. Figure extracted and modified from [21].

GMR is the underlying mechanism to a spin valve, where a nonmagnetic *spacing* layer (typically a conductor) is sandwiched between two ferromagnetic layers (Fig. 2.2a). For a large magnetic field applied to the device, the magnetizations of both ferromagnetic layers are parallel to each other and the device is in a low resistance state. By reducing

the magnetic field, one can switch the magnetization in one of the ferromagnetic layers, resulting in an antiparallel configuration and increased resistance in the device (typical by 5 to 10 %). Further reducing the magnetic field restores a parallel orientation and a low resistance state. Spin valve devices thus exhibit a characteristic butterfly hysteresis loop as depicted in Fig. 2.2c.

Replacing the conductor by a thin insulating layer creates a magnetic tunnel junction as depicted in Fig. 2.2b. The tunnel resistance can be modulated in analogy to the magnetoresistance in a spin valve device, with magnetoresistance change between 20 to 50 %. Spin valve devices and magnetic tunnel junctions are currently used as magnetic field sensors, galvanic isolators and most notably in read heads for hard drives or as magnetoresistive random access memory (MRAM) [23].

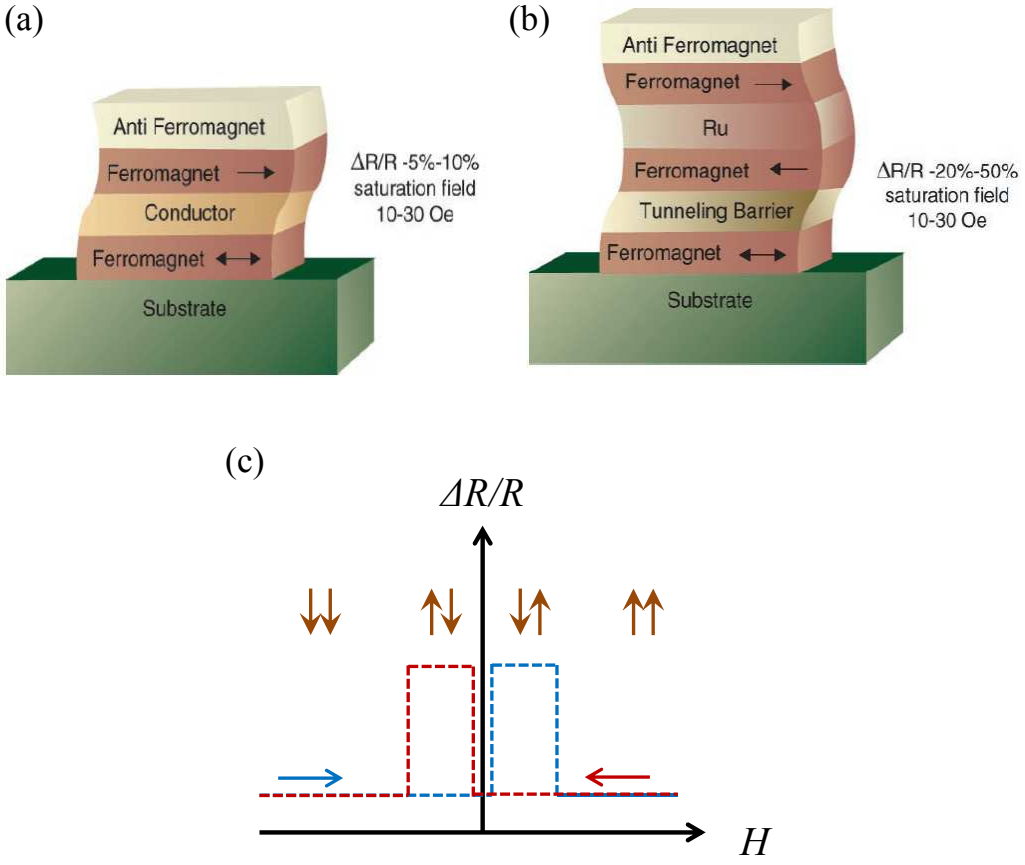

Figure 2.2: Metallic spintronic devices: (a) Metallic spin valve and (b) magnetic tunnel junction. Figures from [23] (c) Butterfly hysteresis loop of the spin valve or a magnetic tunnel junction depicting the magnetoresistance change $\Delta R/R$ as function of the applied magnetic field. The blue (red) trace corresponds to an upwards (downwards) magnetic field sweep.

2.1.2 Semiconductor and organic spintronic devices: Towards coherent spin manipulation

The new generation of spintronic devices was designed to improve quantum coherence, by using semiconductors [23, 24] or organic materials [25] as spacing layers (Fig. 2.3a).

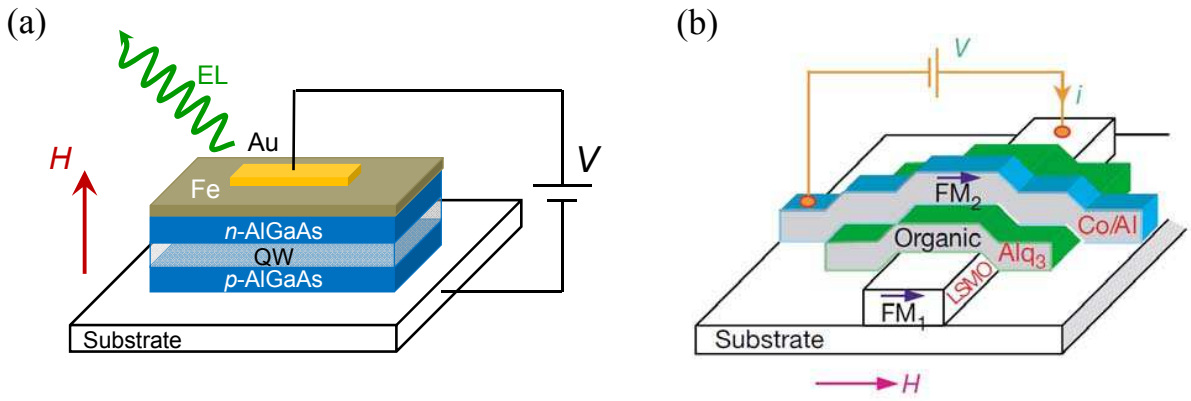

Figure 2.3: Non metallic spintronic device: (a) Ferromagnetic-semiconductor heterostructure (Fe/$Al_{0.1}Ga_{0.9}As$ spin LED). Polarized electrons are injected from the Fe layer into the seminconductor and recombine with holes in the quantum well (QW) under the emission of strongly polarized photons. Figure inspired from [24, 30] (b) Organic spin valve device. Figure extracted from [25].

Indeed, spin relaxation times in non magnetic semiconductors can reach a few hundred nanoseconds (see Fig. 2.5) and spin coherence times as high as 100 ns, three orders of magnitude longer than in ferromagnetic materials, have recently been demonstrated [24, 27]. Moreover, a highly efficient spin injection through a ferromagnet-semiconductor interface [24, 28] and the coherent spin transport in inorganic semiconductors [29] was recently demonstrated (see Fig. 2.4).

The main source of spin decoherence is a significant spin-orbit coupling in inorganic semiconductors. The same spin-orbit interaction, on the other hand, allows coherent spin manipulation by optical [29] and electrical [31] means.

Organic materials, mainly composed of light elements like carbon, have an even weaker spin-orbit coupling than semiconductors (13 meV in C-diamond vs. 340 meV in GaAs), as well as a small hyperfine interaction [25, 33]. In consequence the spin relaxation and coherence times can become extremely long [33] (blue dots Fig. 2.5). However, spin diffusion length is rather limited due to the low carrier mobility in organic materials. Nevertheless, injection, transport and detection of spin-polarized electrons through an organic spacer layer has recently been demonstrated in organic spin valves [25].

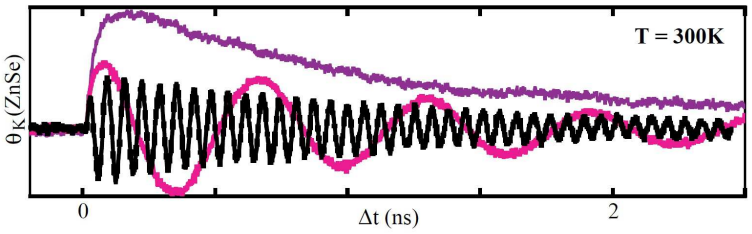

Figure 2.4: Coherent spin transport througha GaAs/ZnSe heterojunction probed by time-resolved Faraday rotation measurements. The electron spin is precessing in a magnetic field of $B = 0$ T (purple), 0.025 T (pink) and 0.25 T (black). Figure extracted from [23, 29]

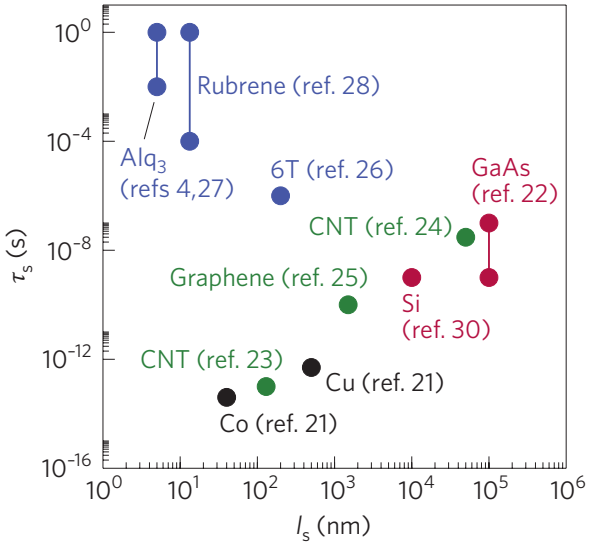

Figure 2.5: Spin relaxation time vs. spin diffusion length for different materials. Figure extracted from [32]. Cited publications in the figure correspond to references in [32]

Quantum coherence can be further improved by reducing the dimensionality of spintronics devices [11, 29]. The technological advancement in the field molecular electronics recently enabled the integration of single molecules into state-of-the-art nanoelectronic devices (Fig. 2.6). Using a single molecule with a *magnetic* center instead, one can henceforth design a *molecular-scale spintronic device* and exploit the quantum mechanical nature of such a system.

Among the large variety of magnetic molecules, the class of single molecule magnets (SMM) stands out due to unique chemical and physical properties. As we will describe in the following, they can exhibit extremely long spin relaxation times up to a few years

(a)

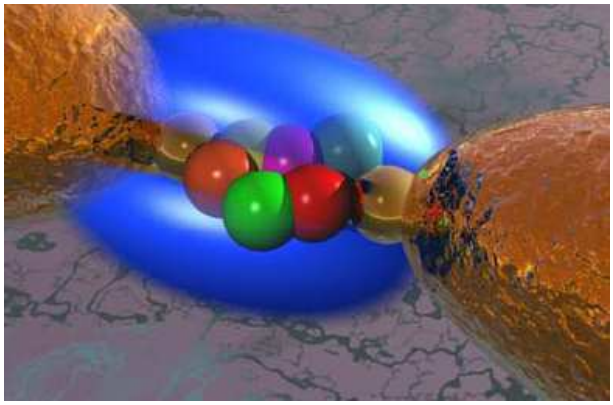

(b)

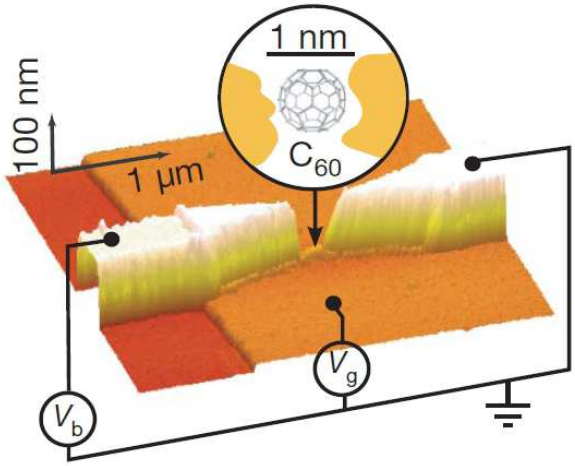

Figure 2.6: Molecular scale electronic devices: (a) Art representation of a molecular junction (M. Reed, Yale University) (b) Single Molecule Transistor with a C_{60} molecule. Image from [34]

and coherence times up to a few microseconds, making them a perfect candidate for a spin qubit and building block for molecular spintronic devices [11].

2.1.3 Molecular building block for spintronics: Single Molecule Magnets

A SMM consists of magnetic centers, typically transition metal ions, embedded in a shell of organic ligands [11, 35, 36]. The ligands are designed to ensure the bonding of the molecule to surfaces or junctions while preserving and enhancing the ions' magnetic properties. For instance, the magnetic centers will behave as a single "giant" spin due a

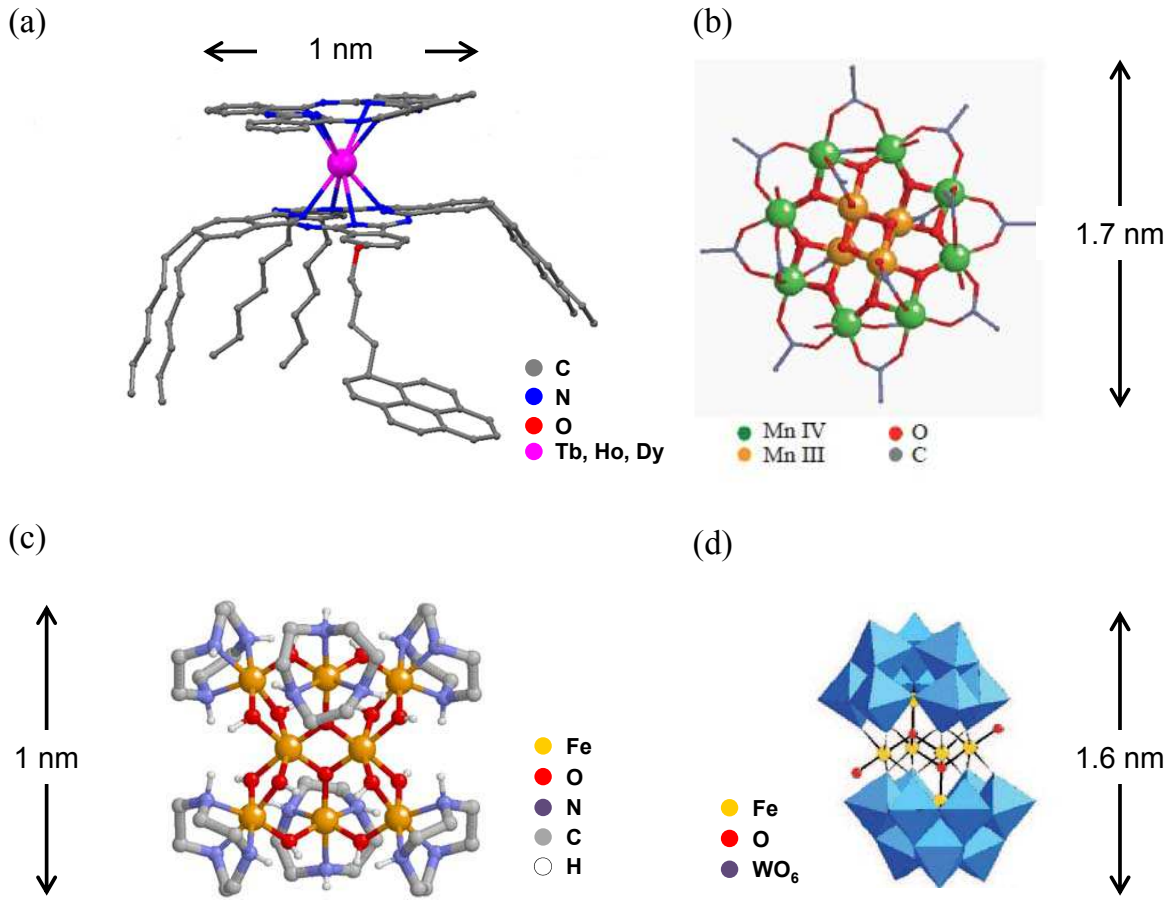

Figure 2.7: Single Molecule Magnets: (a) Mononuclear lanthanide complex $LnPc_2$. Different lanthanide ions Ln = Tb, Ho, Dy can be used as magnetic core, resulting in different magnetic properties of the complex. [39] The phthalocyanine ligand planes can be tailored with aliphatic chains and a pyrene group, which promote the grafting to sp_2 carbon [37]. (b) Mn_{12} SMM with a spin ground state of $S = 10$ (c) Fe_8 complex with a spin $S = 10$ [40] (d) Fe_6 polyoxometallate SMM with a spin $S = 5$ [41].

strong interaction promoted by the ligands [11].

One can modify the organic ligands by chemical engineering in order to change the SMM's coupling to its environment [11, 35, 36] or promote the selective grafting to a certain material, for example carbon nanotubes or graphene [37, 38]. Moreover, one can replace the magnetic centers and therefore alter the magnetic properties of the compound without affecting the ligand shell and the interaction with its environment [11, 39].

Furthermore, chemical engineering allows the synthesis of billions of perfectly identical molecules and would enable the high density integration of molecular spintronic devices. SMMs can be obtained in the form of a powder of individual molecules or a high-quality

molecular crystal, which gives an experimental access to the structural and magnetic properties of the molecules.

The magnetic properties of a single molecule magnet can be described by a single "giant" spin and a Hamiltonian of the form

$$\mathcal{H} = DS_z^2 + E\left(S_x^2 - S_y^2\right) + g\mu_B\mu_0\vec{S}\cdot\vec{H} \tag{2.1}$$

where S_x, S_y, S_z are the spin components, D the axial and E the transverse magnetic anisotropy constants (with $D \gg E$) and $g\mu_B\mu_0\vec{S}\cdot\vec{H}$ the Zeeman energy associated with an applied external magnetic field.

A SMM is characterized by a large magnetic moment and spin ground state $S \geq 1$ and a pronounced magnetic anisotropy resulting in an easy axis of magnetization along S_z. The magnetic anisotropy splits the spin ground state multiplet S into the different $m_s = -S, -S+1, \ldots, S-1, S$ states along the quantization axis z. Consequently, the potential energy for the magnetic ground state S becomes a double well potential, where states with opposite quantum number and opposite magnetization m_s and $-m_s$ are separated by an anisotropy barrier (Fig. 2.8a).

In order to reverse the magnetization, the spin has to overcome a large potential barrier $\Delta = DS_z^2$. The magnetic relaxation is therefore thermally activated (green arrows in Fig. 2.8a) and the relaxation time increases exponentially by decreasing the temperature, reaching several years below 2K for the case of a Mn_{12} SMM. The process is typically enabled by phonons in the SMM crystal and a magnetic hysteresis develops at low temperatures (Fig. 2.8b).

Alternatively, the relaxation can occur by quantum tunneling of magnetization (blue arrow in (Fig. 2.8a)). A magnetic field applied along the easy axis lifts the degenaracy between m_s and $-m_s$ and shifts the energy levels with $m_s < 0$ ($m_s > 0$) towards higher (lower) energy (Fig. 2.8c). Consequently, states with different quantum numbers can cross at distinct values of magnetic field. With the small transverse magnetic anisotropy in SMM's, describe by $E\left(S_x^2 - S_y^2\right)$ in eq. 2.1, and/or a transverse magnetic field the level crossing become in fact avoided crossings, where resonant tunneling of magnetization through the potential barrier can occur. The phenomenon translates as characteristic steps at the resonant magnetic fields in the hysteresis loop of the SMM (Fig. 2.8b).

Due to their molecular nature, SMM's also show quantum mechanical behaviour like Berry phase interference [42] and a strong quantum coherence. One can for instance observe coherence times on the order of microseconds [43, 44], making them an ideal candidate for quantum computing and coherent spin manipulation.

Their versatile designs as well as the widely tunable chemical and physical properties make SMMs the perfect building for molecular spintronic devices. In the following section we will present a rare earth based double decker SMM, which proved to be an ideal building block for molecular spintronics and a potential spin qubit [45, 46, 47, 48, 20].

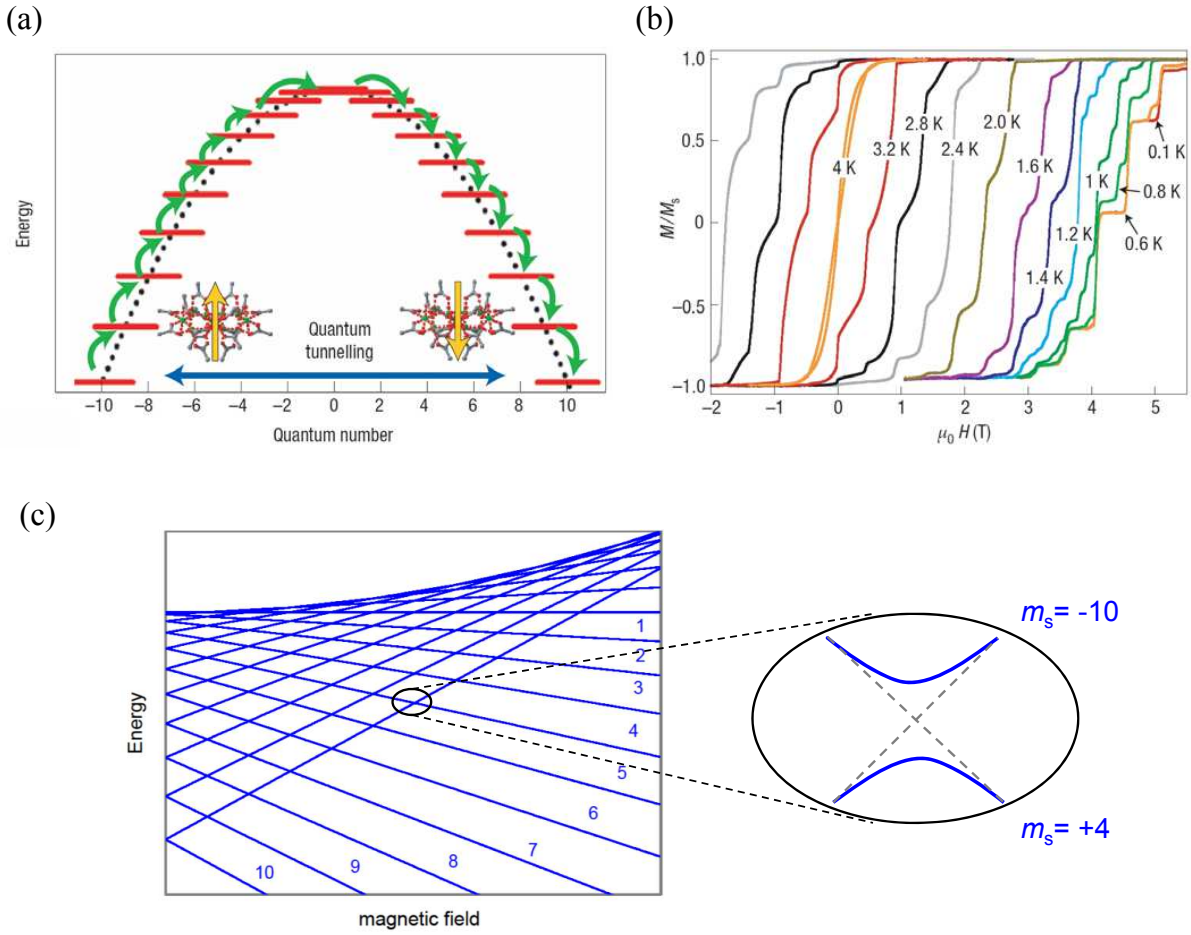

Figure 2.8: Magnetization dynamics in a SMM: (a) Double well potential of a SMM with a magnetic ground state $S = 10$. Magnetization reversal will occur via quantum tunneling of magnetization between two resonant energy levels (QTM, blue arrow) or by thermally activated, phonon assisted relaxation (green arrows). Figure from [11]. (b) Hysteresis loops of a Mn_{12} single crystal at different temperatures and for a sweep rate of 2 mT/s. Steps in the hysteresis loops are attributed to quantum tunneling of magnetization. Figure from [11]. (c) Zeeman diagram of a SMM with a magnetic ground state of $S = 10$.

2.2 Terbium Double Decker Single Molecule Magnet

In this section we describe a SMM with a single magnetic center, in this case a terbium ion Tb^{3+}, embedded between two phtalocyanines (Pc) ligand planes (Fig. 2.9). The mononuclear complex will be denoted as $TbPc_2$ in the following and was designed, synthesized and characterized by Svetlana Klyatskaya and Mario Ruben at the Karlsruhe Institute of Technology (KIT) in Germany [37].

2.2.1 Structural and magnetic properties

The magnetism of the terbium(III) or other lanthanide(III) is mainly determined by the strongly anisotropic and partially filled $4f$ orbitals in these ions. A Tb^{3+} ion exhibits an electronic structure of $[Xe]\,4f^8$ which corresponds to a spin of $S = 3$ and an orbital momentum of $L = 3$. Due to the inherentely strong spin-orbit coupling in rare earth

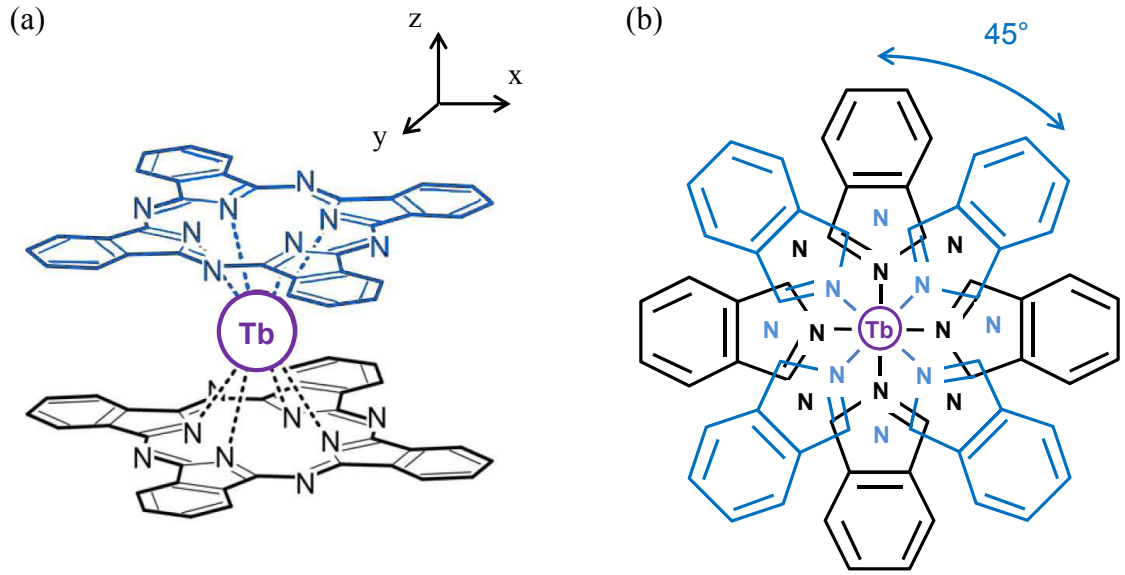

Figure 2.9: Mononuclear Terbium complex $TbPc_2$. Figure from [49] (a) Sideview and (b) topview of the molecule. The upper Pc ligang (blue) is a mirror image of the lower Pc ligand (black), rotated by 45°.

atoms, L and S are no good quantum numbers. In consequence, the magnetic moment is described by a total angular momentum $J = L - S \ldots L + S$, where $L + S$ is the ground state for more than half-shell filling (Hund's rule). The ground state of the Tb^{3+} ion thus yields $J = L + S = 6$ and is separated from the first excited state $J = 5$ by an energy of 2900 K due to the large spin-orbit coupling in the Tb^{3+} ion [50]. We can therefore restrict the discussion to the ground state multiple $J = 6$, yielding $2J + 1$ (degenerate) substates $|J, J_z\rangle$.

Ligand field

The Tb^{3+} ion is embedded between two parallel Pc ligand planes, with a quantization axis z oriented perpendicular to the Pc ligand planes. The Tb^{3+} ion is coordinated by 8 nitrogen atoms and the upper Pc ligand (blue in Fig. 2.9) is a mirror reflection of the lower Pc ligand with respect to the (x-y) plane (black in Fig. 2.9), rotated by 45° around

the z-axis. The Tb^{3+} is therefore exposed to a ligand electric field with a antiprismatic symmetry D_{4d} which is described by the following Hamiltonian [51]

$$\mathcal{H}_{\text{lf}} = \alpha A_2^0 O_2^0 + \beta \left(A_4^0 O_4^0 + A_4^4 O_4^4 \right) + \gamma \left(A_6^0 O_6^0 + A_6^4 O_6^4 \right) \tag{2.2}$$

where $\alpha = -1/99$, $\beta = 2/16335$ and $\gamma = -1/891891$ are constant parameters related to the ion [52], O_q^k the equivalent Stevens operators and A_q^k the ligand field parameters.

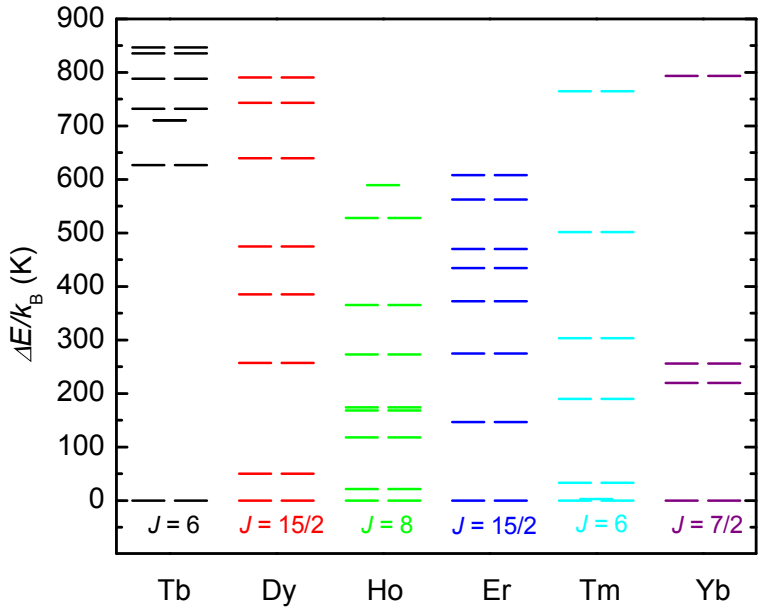

Figure 2.10: Ligand field splitting of the ground state multiplet J in different mononuclear lanthanide complexes $LnPc_2$. Modified from [51]

The Stevens operators O_q^k are defined as linear combinations of J_z, J_-, J_+ and are listed in appendix B and [50]. The ligand field parameters A_q^k can be determined experimentally by NMR or magnetic susceptibility, yielding [53]

$$\begin{aligned} A_2^0 &= 595.7K \\ A_4^0 = -328.1K \quad &, \quad A_4^4 = 47.5K \\ A_6^0 = 14.4K \quad &, \quad A_6^4 = 0 \end{aligned} \tag{2.3}$$

The diagonalization of $\mathcal{H}_{\text{cf}}$ in the $|J, m_J\rangle$ eigenbasis then reveals that the ligand field partially lifts the degeneracy of the 2J+1 substate in the ground state multiplet $J = 6$. Indeed, the degenerate ground state doublet $m_J = \pm 6$ of the Tb^{3+} ion is now separated from the first excited state doublet $m_J = \pm 5$ by approximately 600 K (see ref. [51] and Fig. 2.10). The $TbPc_2$ single molecule magnet thus behaves as an Ising spin system at cryogenic temperatures.

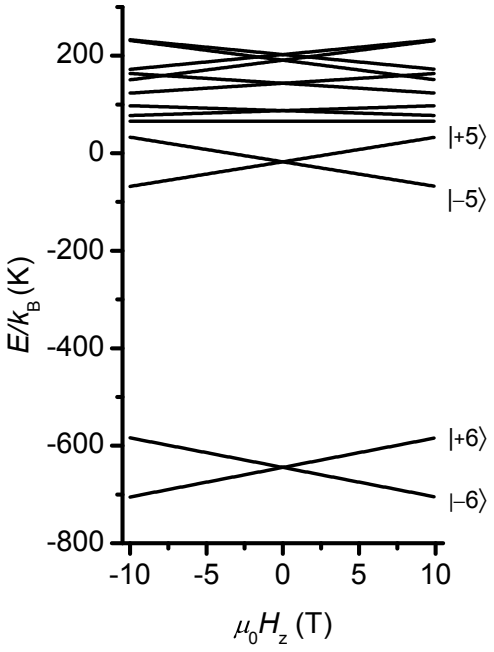

Figure 2.11: Calculated Zeeman diagram for the ground state multiplet $J = 6$ in a $TbPc_2$ SMM extracted from [49].

Furthermore, each m_J-doublet splits in an external magnetic field due to the Zeeman effect as described by the following Hamiltonian

$$\mathcal{H}_{\mathrm{TbPc_2}} = \mathcal{H}_{\mathrm{lf}} + g\mu_{\mathrm{B}}\mu_0 H_z J_z \tag{2.4}$$

where $g = 3/2$ is the g-factor of the terbium. The resulting Zeeman diagram is depicted in Fig. 2.11 [49].

In the following we will therefore restrict the discussion to the ground state doublet $m_J = \pm 6$.

Hyperfine interaction and tunnel splitting

The Tb^{3+} ion also carries a nuclear spin of $I = 3/2$ with a natural abundance of 100%, yielding (2I+1) substates $m_I = 3/2, 1/2, -1/2, -3/2$. Due to a strong hyperfine interaction between the nuclear spin $I = 3/2$ and the electronic angular momentum $J = 6$, the Hamiltonian of the $TbPc_2$ contracts two additional terms corresponding to a nuclear dipole and quadrupole interaction, respectively,

$$\mathcal{H}_{\mathrm{TbPc_2}} = \mathcal{H}_{\mathrm{lf}} + g\mu_{\mathrm{B}}\mu_0 H_z J_z \quad + \quad A_{dip}\vec{I}\cdot\vec{J} + P_{quad}\left(I_z^2 + \frac{1}{3}I(I+1)\right) \tag{2.5}$$

$$\vec{I}\cdot\vec{J} = J_z I_z \quad + \quad \frac{1}{2}\left(J_+ I_- + J_- I_+\right) \tag{2.6}$$

where $A_{dip} = 24.5$ mK is the hyperfine constant and $P_{quad} = 14.4$ mK the quadrupole constant [49].

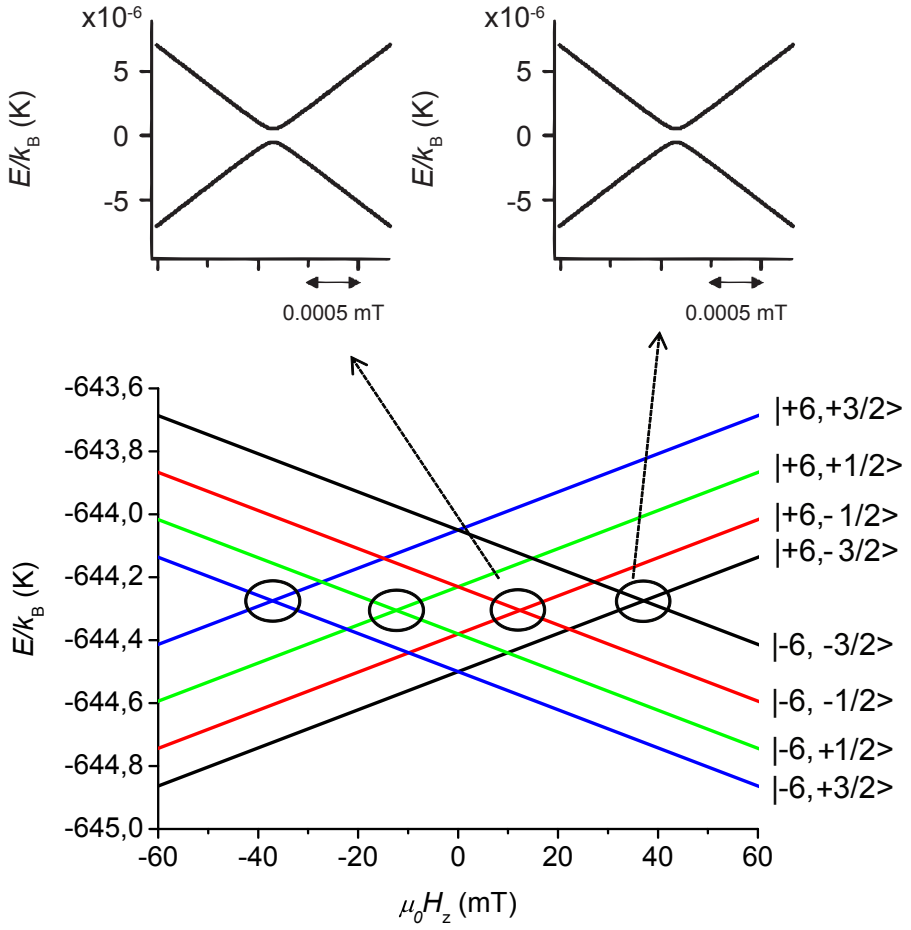

Figure 2.12: Calculated Zeeman diagram for the ground state multiplet $J = 6$ in a $TbPc_2$ SMM extracted from [49]. The black circles highlight the avoided level crossing.

The dipolar term $A_{dip}\vec{I} \cdot \vec{J}$ thus splits the electronic states from the ground state doublet $m_J = \pm 6$ into the four nuclear spin states $m_I = 3/2, 1/2, -1/2, -3/2$. The quadrupole term $P_{quad}I_z^2$ results in a non-equidistant spacing of the nuclear spin states. The *excited* nuclear spin states thus have energies of 120 mK, 270 mK and 450 mK with respect to the nuclear spin *ground* state (Fig. 2.12). [49]

Finally, it should be noted that the resulting intersections are indeed energy level crossings except the four intersections that conserve the nuclear spin (black circles Fig. 2.12). For the latter ones, an anti-crossing on the order of a few μK is observed [49]. These anti-crossings are due to the transverse anisotropy term O_4^4 in equation 2.2 which yields off diagonal terms in the ligand field Hamiltonian. In fact, the operator O_4^4 is a

linear combination of J_+^4 and J_-^4, which mixes states with m_J and states with $m_J \pm 4n$. Hence, the $m_J = +6$ state mixes with the $m_J = -6$ state, generating an avoided level crossing at the four highlighted intersections close to zero magnetic field (Fig. 2.12).

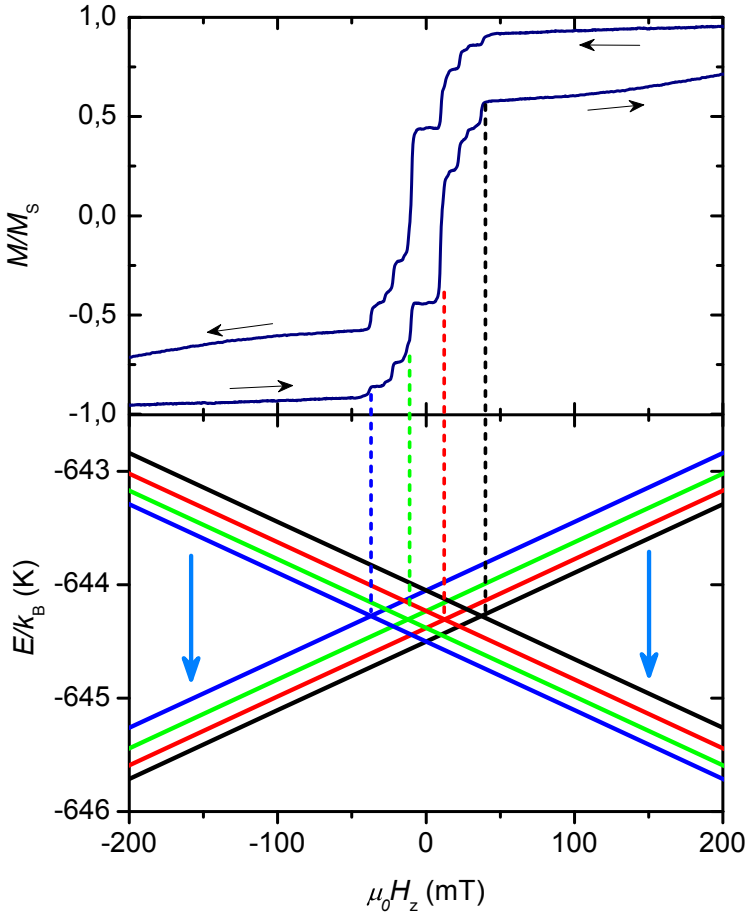

Figure 2.13: Magnetic hysteresis loop of an assembly of $TbPc_2$ SMM measured with a microSQUID in a diluted single crystal (2% $TbPc_2$ in an YPc_2 matrix) for a field sweep rate of $\nu_H = 1$ mT/s and temperature of 40 mK (top panel). Zeeman diagram of a $TbPc_2$ SMM (bottom panel). The characteristic steps in the magnetization curve around zero field correspond to QTM events in the single crystal (highlighted by the dashed lines), whereas the continuous change of the magnetization at high field is attributed to phonon-assisted relaxation (blue arrows in the Zeeman diagram).

Magnetization curves of an assembly of $TbPc_2$

By sweeping the magnetic field applied to the $TbPc_2$ SMM one can then induce a magnetization reversal from $|m_J = -6, m_I\rangle$ to $|m_J = +6, m_I'\rangle$ (and *vice versa*) either by

QTM at one of the four avoided level crossings around zero field (Section 2.2.2) or by phonon-assisted or spin-lattice relaxation at large magnetic fields (Section 2.2.3).

Fig. 2.13 shows a magnetic hysteresis loop measured by a microSQUID technique [54] of an assembly of $TbPc_2$ SMM arranged in a matrix of non-magnetic YPc_2 SMM, with a $[TbPc_2]/[YPc_2]$ ratio of 2%. Indeed upon sweeping the magnetic field from -1T up to 1T, approximately 75 % of the SMM in the crystal reverse their magnetization by QTM around zero field, resulting in sharp steps in the crystal's magnetization. The remaining SMM reverse their magnetization by phonon-assited relaxation at larger magnetic field.

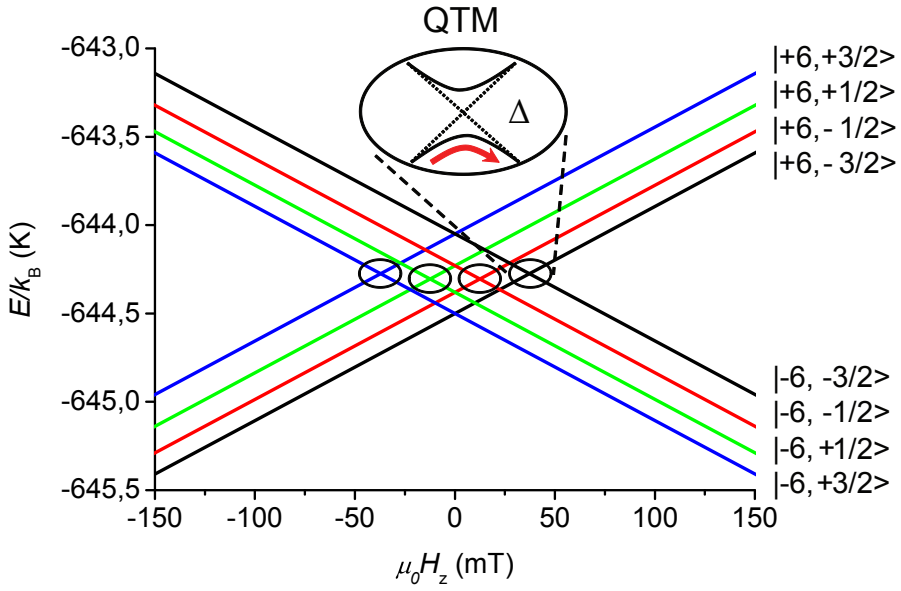

Figure 2.14: Zeeman diagram for the ground state multiplet $J = 6$ in a $TbPc_2$ SMM. Avoided level crossings are highlighted by the black circles. The enlarged region shows an avoided level crossing with tunnel splitting Δ caused by the mixing of the $m_J = -6$ and $m_J = +6$ states. The dotted lines shows the two states without mixing and the red arrows depicts the QTM process.

2.2.2 Quantum tunneling of magnetization and Landau-Zener model

At the four avoided level crossings highlighted by the black circles in Fig. 2.12 and 2.14, the nuclear spin is conserved and the small transverse anisotropy mixes the state $m_J = -6$ with the state $m_J = +6$, due to the J_+^4 and J_-^4 terms in equation 2.2. By sweeping the magnetic field through one of these avoided crossing one can therefore tunnel from the state $m_J = -6$ to the state $m_J = +6$ (and *vice versa*). Such a process is called quantum tunneling of magnetization (QTM) and has been introduced in the previous section 2.1.3.

According to Landau-Zener [55], the probability P_{QTM} for such a QTM process depends on the magnitude of the mixing, i.e. the tunnel splitting Δ, and the sweep rate of the magnetic field ν, thus yields

$$P_{\mathrm{QTM}} = 1 - exp\left(-\alpha\frac{\Delta^2}{\nu}\right) \tag{2.7}$$

For a given (nonzero) tunnel splitting, if the magnetic field is swept adiabatically slow in the vicinity of the avoided crossing, QTM from $m_J = -6$ to $m_J = +6$ (and inversely) will occur with a high probability. One observes the characteristic steps in the magnetization curves, as described in the previous section (dark blue cycle Fig. 2.15). As the magnetic field sweep rate increses the probability P_{QTM} for QTM becomes exponentially smaller. The steps associated with QTM become less pronounced and eventually vanish at large sweep rates (black cycle Fig. 2.15).

If the tunnel splitting is zero, the levels cross and no quantum tunneling of magnetization can occur independant from the sweep rate.

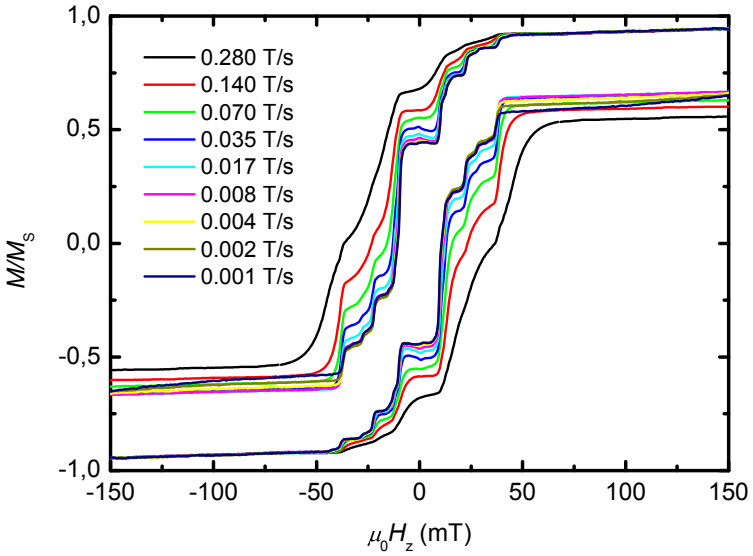

Figure 2.15: Magnetic hysteresis loop of an assembly of $TbPc_2$ SMM measured in a diluted single crystal (2% $TbPc_2$ in an YPc_2 matrix). The measurements at different field sweep rates were obtained by a microSQUID setup.

2.2.3 Spin-lattice relaxation

Alternatively, the magnetization reversal of the $TbPc_2$ SMM from $|m_J = -6, m_I\rangle$ to $|m_J = +6, m_I'\rangle$ can occur by phonon-assisted or spin-lattice relaxation as described in section 2.1.3. Spin-lattice relaxation in an SMM is due to the modulation of the molecule's

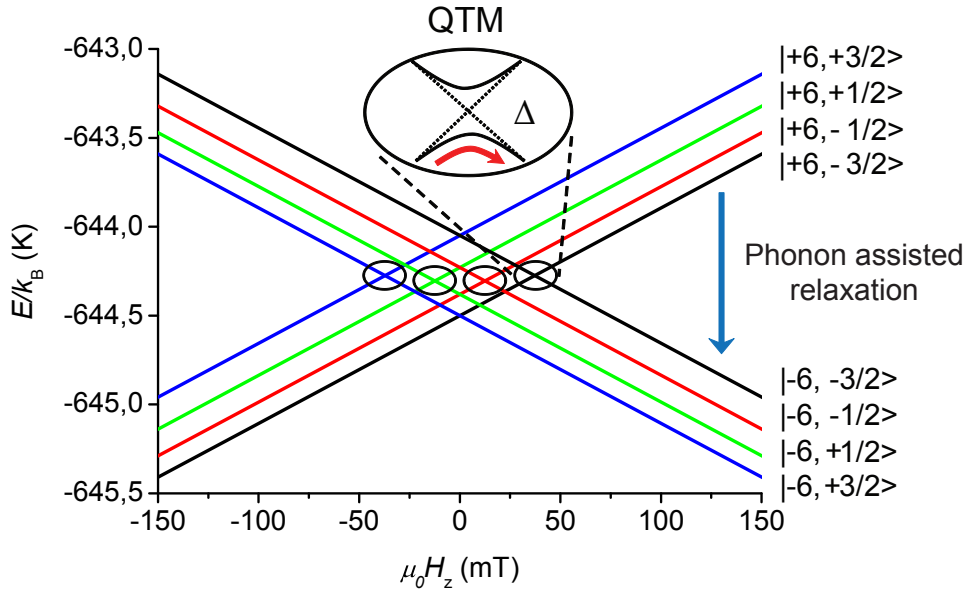

Figure 2.16: Zeeman diagram for the ground state multiplet $J = 6$ in a $TbPc_2$ SMM. Phonon assisted relaxation of the $TbPc_2$ magnetization occurs at higher magnetic field.

ligand electric field by phonons from a surrounding thermal bath, for example the lattice vibration in a diluted SMM single crystal [50]. Due to the strong spin-orbit coupling, the modulation of the ligand field will result in transitions between different spin states of the Tb^{3+} ion. The magnetization reversal can be assisted by one or multiple phonons [50] (see Fig. 2.17).

Direct relaxation process

At very low temperatures, the magnetization of the $TbPc_2$ SMM is reversed in a direct relaxation process under the emission of a phonon into the surrounding bath (Fig. 2.17a). The relaxation rate $1/\tau$ for a such a direct relaxation can therefore be expressed in terms of the absorption and emission rates of the phonon, given by Fermi's golden rule

$$\begin{aligned} \omega_{abs} &= \frac{2\pi}{\hbar}|\langle -6|\mathcal{H}'|+6\rangle|^2 \\ \omega_{em} &= \frac{2\pi}{\hbar}|\langle -6|\mathcal{H}'|+6\rangle|^2 exp\left(\frac{\hbar\omega}{k_B T}\right) \end{aligned} \tag{2.8}$$

where $\langle -6|\mathcal{H}'|+6\rangle$ is the matrix element of the pertubation Hamiltonian $\mathcal{H}'$ between the states $|m_J = -6\rangle$ and $|m_J = +6\rangle$, $\hbar\omega$ the phonon energy and T the temperature of the

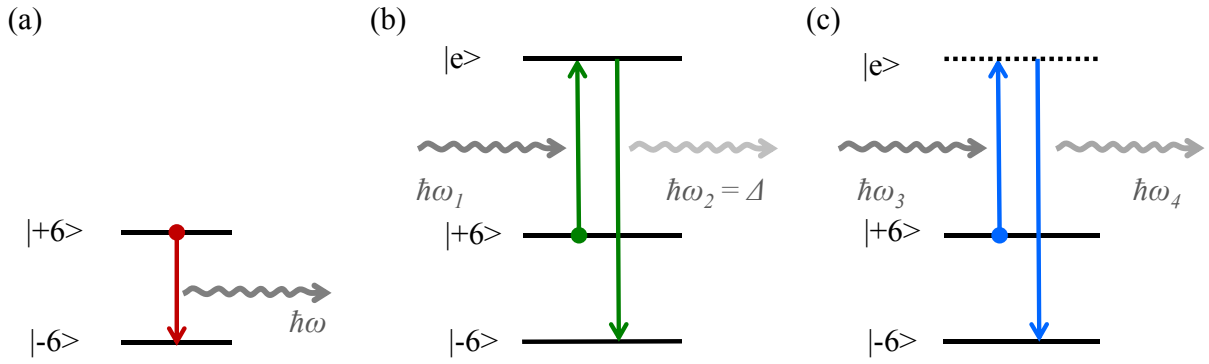

Figure 2.17: Spin-lattice relaxation processes. (a) Direct relaxation into the ground state involving the emission of a phonon with an energy $\hbar\omega$. (b) Two-phonon Orbach process. The electron is excited into a vibrational (lattice) mode by absorption of a phonon $\hbar\omega_1$, before relaxing into the ground state under the emission of a phonon $\hbar\omega_2$ with $\hbar\omega = \hbar\omega_2 - \hbar\omega_1$. (c) Two-phonon Raman process. The relaxation occurs by the absorption and emission of virtual phonons. The hyperfine splitting was omitted for simplicity.

phonon bath. The relaxation rate then holds

$$\frac{1}{\tau} = \omega_{em} + \omega_{abs} = \frac{2\pi}{\hbar}|\langle -6|\mathcal{H}'| + 6\rangle|^2 \left[1 + exp\left(\frac{\hbar\omega}{k_B T}\right)\right] \tag{2.9}$$

The relaxation from $|m_J = -6\rangle$ to $|m_J = +6\rangle$ is induced by the modulation of the ligand field by phonons, and the modified ligand field Hamiltonian yields [50]

$$\mathcal{H}_{lf} = \mathcal{H}^0_{lf} + \varepsilon\mathcal{H}^1_{lf} + \varepsilon^2\mathcal{H}^2_{lf} \tag{2.10}$$

where ε refers to the mechanical strain in the ligand.

In first order, the pertubation Hamiltonian gives $\mathcal{H}' = \varepsilon\mathcal{H}^1_{lf}$ and equation 2.9 transforms to

$$\frac{1}{\tau} = \frac{2\pi}{\hbar}\varepsilon^2|\langle -6|\mathcal{H}^1_{lf}| + 6\rangle|^2 \left[1 + exp\left(\frac{\hbar\omega}{k_B T}\right)\right] \tag{2.11}$$

The strain can be related to the phonon density of states $D(\omega)$ by $\varepsilon^2 = D(\omega)/2\rho v^2$, where v is the phonon group velocity and ρ the mass density of the phonon bath [50]. Finally one obtains

$$\frac{1}{\tau} \sim D(\omega)|\mathcal{H}^1_{lf}|^2 \left[1 + exp\left(\frac{\hbar\omega}{k_B T}\right)\right] \tag{2.12}$$

Therefore, the relaxation rate is essentially limited by the phonon density of states $D(\omega)$, the matrix element coupling the spin to phonon $|\mathcal{H}^1_{lf}|$ as well as the phonon energy $\hbar\omega$. Also, the relaxation rate intrinsically depends on the dimensionality of the phonon bath as we will describe in Section 6.

Two phonon relaxation processes

Upon increasing the temperature higher excited phonon states become accessible and a so called two-phonon Orbach process contributes to the relaxation of the SMM's magnetization. As depicted in Fig. 2.17b, the electron is excited from $|m_J = +6\rangle$ into a vibrational state $|e\rangle$ under absorption of a phonon with an energy $\hbar\omega_1$. In a second step, the electron then relaxes into the ground state $|m_J = -6\rangle$ under emission of a second phonon with an energy $\hbar\omega_2 = \hbar\omega_{\mathrm{ph}}$. The process can occur if $\omega_2 - \omega_1 = \omega$, where ω is the energy separation of the two spin states. The relaxation rate yields [50]

$$\frac{1}{\tau} \sim |\mathcal{H}_{\mathrm{lf}}^{1'}|^2 \Delta^3 \frac{1}{exp\,(\Delta/k_{\mathrm{B}}T) - 1} \tag{2.13}$$

where $|\mathcal{H}_{\mathrm{lf}}^{1'}|$ is the product of the matrix elements between the states $|m_J = -6\rangle$, $|m_J = +6\rangle$ and $|e\rangle$. The process is therefore thermally activated if $k_{\mathrm{B}}T \gtrsim \Delta$.

Finally, the relaxation can occur in a Raman like process(Fig. 2.17c). The mechanism is similar to the Orbach process, however involves a *virtual* excited state, resulting in a relaxation time of the form [50]

$$\frac{1}{\tau} \sim |\mathcal{H}_{\mathrm{lf}}^{2}|^2 \left(\frac{k_{\mathrm{B}}T}{\hbar}\right)^7 \tag{2.14}$$

where $|\mathcal{H}_{\mathrm{lf}}^{2}|$ is the second order pertubation from equation 2.10.

2.3 Carbon based supramolecular spintronics

Various designs for molecular spintronic devices using individual SMM's were proposed over the last decade [11]. One can use for instance a scanning tunneling microscopy to probe an isolated SMM on a conducting surface [56, 45, 46] (Fig. 2.18a). Alternatively, one can built a three-terminal molecular spin-transistor where an individual SMM is bridging the gap between two non-magnetic leads [47] (Fig. 2.18b). In such a configuration, the electric current is flowing directly through the molecule, leading to a strong coupling between the electrons and the magnetic core. This **direct** coupling thus enables a readout of the molecule's magnetic properties with the electronic current, but also leads to a strong back-action on the molecule's magnetic core [11].

An less invasive approach consists in coupling the SMM to a second non-magnetic molecular conductor which is subsequently used as detector. For such an **indirect** coupling, the magnetic core of the molecule is only weakly coupled to the conductor but can still affect its transport properties, thus enabling an electronic readout with only minimal back-action.

Among the different possible detectors (nanowires, carbon nanotubes, quantum dot, molecules), the carbon nanotube stands out due to its unique structural, mechanical

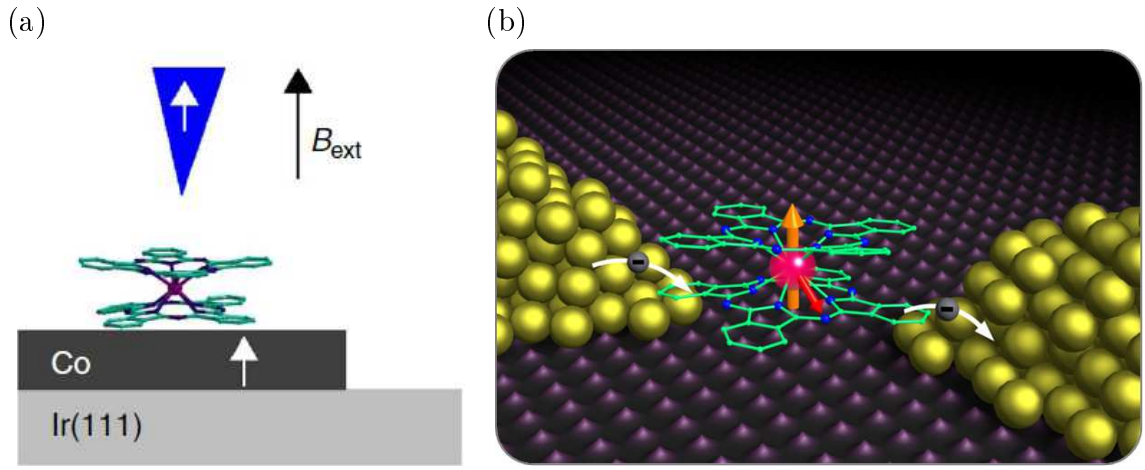

Figure 2.18: Molecular spin transistors and *direct* probing of the magnetic center. (a) Spin polarized scanning tunneling spectroscopy on an individual $TbPc_2$ grafted to a Co substrate. Wiesendanger Group [46] (b) Single molecule transistor with a $TbPc_2$ bridging the electrode gap. Wernsdorfer Group [47].

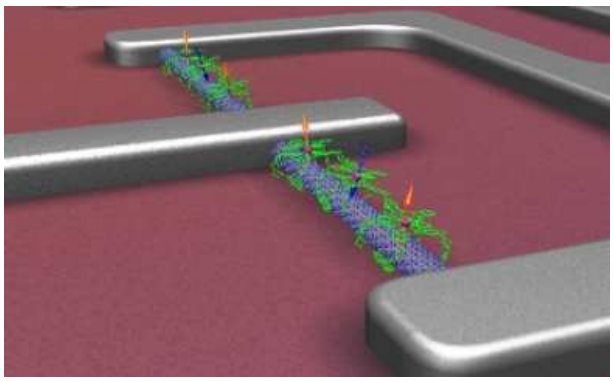

Figure 2.19: Supramolecular spintronic devices based on carbon nanotubes and single molecule magnets and *indirect* probing of the magnetic center

and electronic properties [11]. In the following we will describe different designs of a *supramolecular quantum spintronic* device (Fig. 2.19), where a carbon nanotube is used to probe an individual molecular spin *via* different coupling mechanism at cryogenic temperatures (flux coupling, electronic coupling, mechanical coupling).

2.3.1 NanoSQUID: Probing via magnetic flux

One can for instance probe the magnetic flux emanating from a single molecule magnet grafted onto a SQUID magnetometer. Indeed, the maximum magnetic flux generated by SMM's like lanthanide complexes $LnPc_2$ was estimated to be on the order of $\Phi_{SMM} \approx 10^{-5}\Phi_0$, which is well within the flux sensitivity of a SQUID, given by the quantum limit $\Phi_q \approx 10^{-8}\Phi_0$ [57, 58].

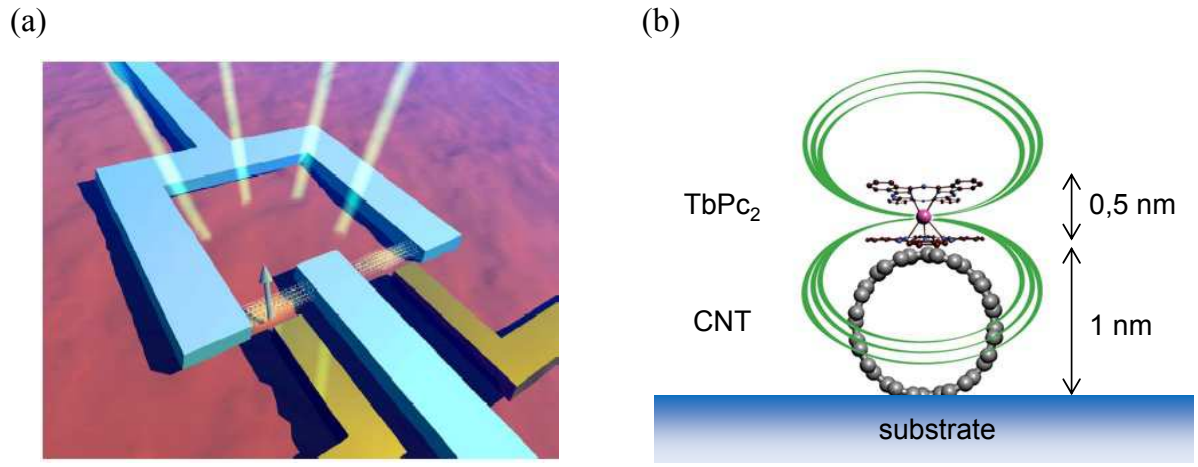

Figure 2.20: Carbon nanotube based nanoSQUID magnetometer for SMM. (a) Representation of a carbon nanotube SQUID [58]. The SQUID loop is represented in light blue and the local gates in yellow. (b) The comparable cross section of a carbon nanotube and SMM results in a strong flux coupling, as half (ideally) of the SMM flux' is penetrating the nanotube's cross section.

However, only the magnetic flux penetrating the SQUID's cross section will contribute to the measured flux quantity in the SQUID loop. The cross section of a SQUID is usually orders of magnitude larger than the size of the molecule, which typically results in a very weak flux coupling in this case.

In order probe the flux of a single molecule it is therefore essential to reduce the cross section of the SQUID, ideally to the same size than the SMM. Indeed, the cross section of a carbon nanotube is on the order of 1 nm^2 which is comparable to the size of the molecule. One obtains an almost ideal flux coupling in a carbon nanotube SQUID with a flux sensitivity of $S_\Phi \approx 10^{-4}\Phi_0/\sqrt{\text{Hz}}$ [57, 58].

Although the flux of an individual SMM is within the NanoSQUID's sensitivity at measurement frequency about a few hundreds of Hz, experimental evidence has remained elusive until now.

2.3.2 Supramolecular Spin Valve: Probing via electron transport

Alternatively, one can couple a SMM to a state-of-the-art carbon nanotube transistor and use the electric current in the nanotube to probe and manipulate the spin of the SMM. A carbon nanotube behaves as a quantum dot at very low temperatures, showing an impressive array of electronic properties ranging from Coulomb blockade [59] to Kondo effect [60]. In this regime, a carbon nanotube is sensitive to very small charge fluctuations in its environment which results in a modulation of the conductance in the carbon nanotube quantum dot. For instance, the nanotube's conductance can be altered by the magnetization reversal of a SMM grafted to the carbon nanotube's sidewall as we will describe in the following.

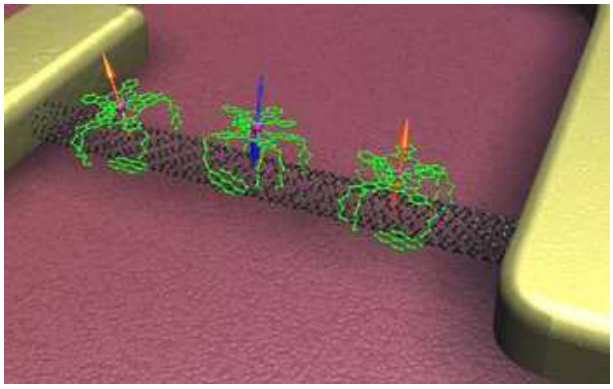

Figure 2.21: Carbon nanotube based supramolecular spin valve. Courtesy of M. Urdampilleta

Indeed, Urdampilleta et al. [48] reported a supramolecular spin valve behaviour without magnetic leads in a carbon nanotube quantum dot functionnalized with $TbPc_2$ SMMs (Fig. 2.22a).

They demonstrated that two SMM's, coupled to the carbon nanotube via π-π interaction, act as spin-polarizer and analyzer for the conduction electrons in the carbon nanotube channel. Mediated by exchange interaction, the magnetic moment of each molecule induces a localized spin polarized dot in carbon nanotube quantum dot, which can be controlled by a magnetic field (Fig. 2.22b and c).

At large negative magnetic fields, both molecular spins are oriented in parallel to each other and the quantum dot is in a high conductance state. Upon increasing the magnetic field (following the red trace in Fig. 2.22a), the molecular spin A is reversed by quantum tunneling of magnetization close to zero field (see Section 2.1.3 and 2.2), resulting in an antiparallel spin orientation and a current blockade in the quantum dot (Fig. 2.22b). By further increasing the field, the second spin B is reversed by phonon assisted relaxation (see Section 2.1.3 and 2.2), restoring a parallel spin orientation and the high conductance regime in the quantum dot (Fig. 2.22c). After reversing the sweep direction, one obtains

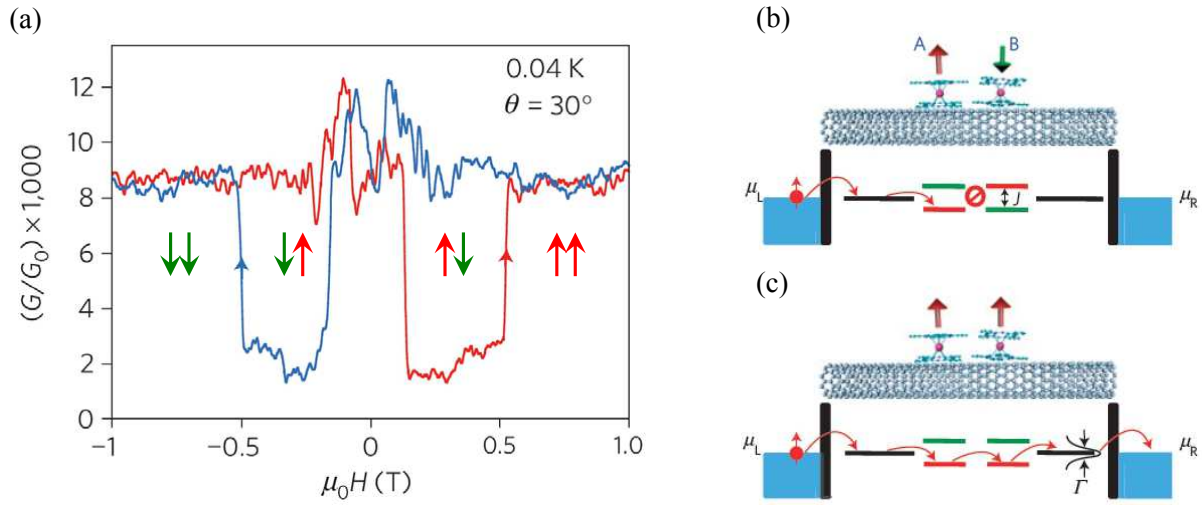

Figure 2.22: Spin valve behaviour in a supramolecular spintronic device based on a carbon nanotube quantum dot functionnalized with $TbPc_2$ SMM's. Figures from [48] (a) Butterfly hystersis loop at $T = 40$ mK. (b) Antiparallel spin configuration. The spin states are inversed in the dot A and the energy mismatch between levels with identical spin results in a current blockade. (c) Parallel spin configuration for both molecules A and B. Energy levels with same spin are aligned allowing electron transport through the carbon nanotube.

the characteristic butterfly hystersis loop of a spin valve device with a magnetoresistance ratio $(G_P - G_{AP})/G_{AP}$ up to 300 % (Fig. 2.22a). A detailed description of the mechanism can be found in [48]. Each current switching event, or switching field, can be attributed to the magnetization reversal of a SMM thus providing us with an electronic readout scheme for a molecular spin.

Indeed, the spin valve effect and the current switching exhibits the fingerprint like characteristics of the $TbPc_2$ SMM. Figure 2.23a represents the difference between the upwards (red trace in Fig 2.22a) and the downwards sweep of the magnetic field (blue trace in Fig 2.22a) during a hysteresis loop as function of the applied magnetic field angle. In the white region both molecule have the same polarization, in the red region their polarization is antiparallel. The limit between both region corresponds to the switching field associated with the phonon assisted relaxation of the second molecule B. The projection the switching field along the H_x-direction, defined as easy axis, is constant, which is consistent with Ising like uniaxial magnetic anisotropy of the $TbPc_2$.

Also, the inherently stochastic character of the SMM magnetization reversal can be revealed by repeating a hysteresis loop a certain number of times (Fig. 2.23b). Finally, the spin valve effect becomes less pronounced upon increasing the temperature and disappears above a temperature of 1K (Fig. 2.23c), which is also consistent with the thermally

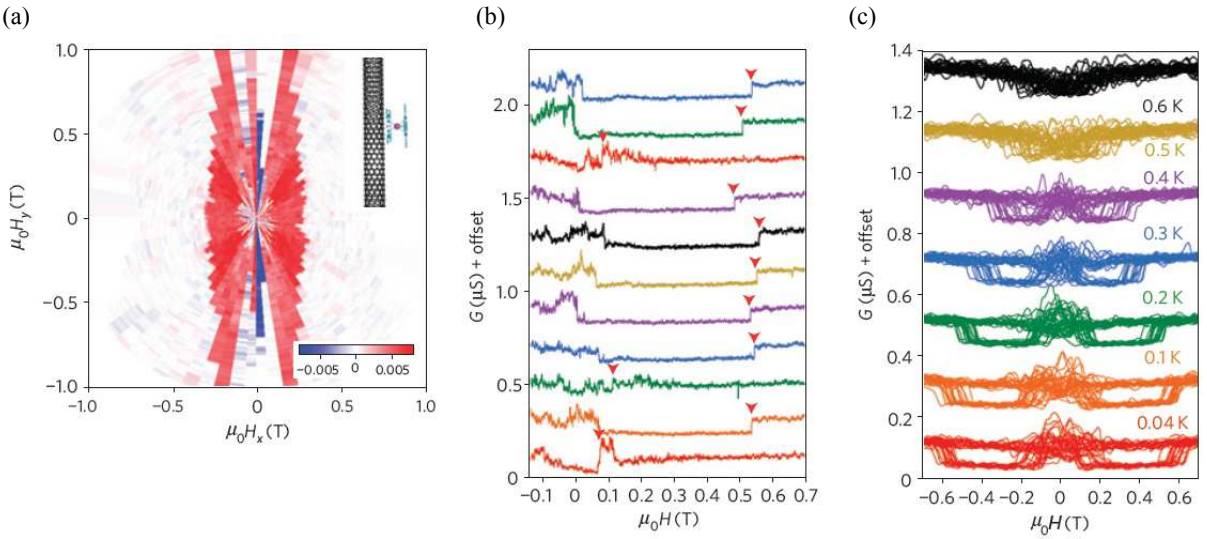

Figure 2.23: Supramolecular spin valve and molecular fingerprint. Figures from [48] (a) Angular dependance of the spin valve behaviour. The difference in conductance between the up- and downwards magnetic field sweep in a hysteresis loop is plotted as a function the magnetic field angle. For spins oriented parallel, the difference is negligeable (white color), whereas in an antiparallel configuration the difference is non zero (red color). The red-white boundary corresponds to the switching field of the second molecule B, and is consistent with the uniaxial anisotropy of the $TbPc_2$ SMM. (b) Stochastic switching of molecule B. Three times out of 11, the molecule can switch its magnetization by quantum tunneling magnetization, while 8 times out of 11 the reversal occurs by phonon assisted magnetic relaxation as predicted by the Landau Zener model (see Section 2.2). (c) 20 hysteresis loops at different temperatures.

activated magnetization reversal of a SMM (see Section 2.1.3).

For a more detailed description, the reader may refer to Urdampilleta et al. [48].

2.3.3 Magnetic torque detector: Probing via mechanical motion

Finally, one can couple a SMM to a suspended carbon nanotube NEMS and probe the molecular nanomagnet with the carbon nanotube's mechanical motion (Fig. 2.24). Such a detection scheme is based on torque magnetometry.

We consider a SMM with a magnetic moment $\vec{\mu} = \frac{g\mu_B}{\hbar}\vec{S}$ to be rigidly grafted to the suspended carbon nanotube beam. Upon applying an external magnetic field $\mu_0\vec{H_{ext}}$, the SMM magnetization will experience a torque given by

$$\vec{\Gamma}_{SMM} = \mu_0\vec{\mu} \times \vec{H}_{ext} = \frac{g\mu_0\mu_B}{\hbar}\vec{S} \times \vec{H}_{ext} \tag{2.15}$$

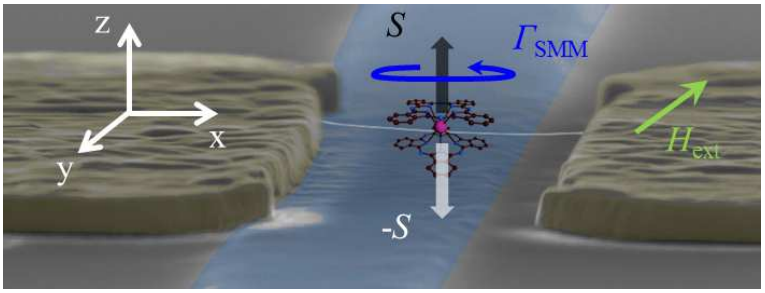

Figure 2.24: Carbon nanotube based magnetic torque detector. The magnetization reversal of a SMM from S to -S in an external magnetic field $\mu_0\vec{H}_{ext}$ induces a torque/rotation of the SMM, under conservation of the total angular momentum. The torque in the SMM then creates an additional tension in the carbon nanotube, resulting in shift of its resonance frequency.

Under conservation of the total angular momentum, the SMM starts to rotate towards the magnetic field direction, hence inducing mechanical strain in the suspended carbon nanotube beam. The additional tension in the resonator will result in a shift the mechanical resonance frequency of the carbon nanotube.

Lassagne *et al.* studied the mechanical response of a carbon nanotube NEMS to the magnetization dynamics of a nanomagnet with a uniaxial magnetic anisotropy and a magnetic moment of $100\mu_B$ [18]. They determined the magnetic hysteresis of the nanomagnet (Stoner-Wolfahrt model, Fig. 2.25a) and the magnetic field dependance of the carbon nanotube NEMS resonance frequency (Euler-Bernoulli formalism, Fig. 2.25b) for different orientation of the magnetic field with respect to the nanomagnets easy axis. The model can be readily extended to a SMM, with a magnetic moment of a few μ_B.

The calculations reveal a discontinous jump in the nanotube's resonance frequency, induced by the magnetization reversal of the nanomagnet (highlighted by the black arrows in Fig. 2.25b). Furthermore, the field dependance of the resonance frequency translates the hysteretic behaviour of the nanomagnet as well as its magnetic anistropy. For a magnetic field aligned close the nanomagnet's easy axis, a large hysteresis in the magnetization m and the frequency Δf is visible ($\theta_0 = \pi/50$, red loop in Fig. 2.25 a and b). The hysteresis gradually disappears upon rotating the magnetic field into the hard plane of the molecule ($\theta_0 = \pi/2$, black loop in Fig. 2.25 a and b). The maximum frequency shift reaches 90 kHz for a magnetic moment of $100\mu_B$.

The sensitivity for such a magnetic torque detector is limited by the frequency noise

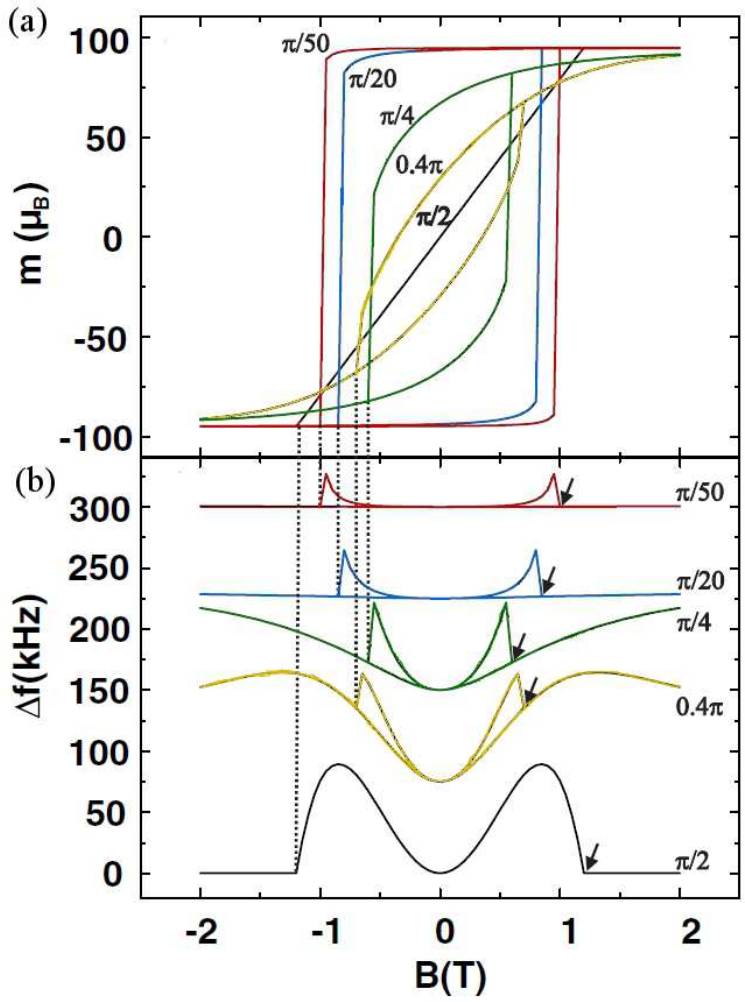

Figure 2.25: Mechanical response of carbon nanotube NEMS to the magnetization reversal of nanomagnet with uniaxial anisotropy. (a) Magnetic hysteresis loop of the nanomagnet for five different orientations of the magnetic field, with respect to its easy axis of magnetization $\theta_0 = \pi/2, 0.4\pi, \pi/4, \pi/20, \pi/50$. One can observe the uniaxial anisotropy upon rotating the magnetic field away from the easy axis. (b) Frequency shift Δf as a function of the magnetic field. The curves translate the hysteretic behavior and the magnetic anisotropy of the nanomagnet. Modified figure from [18].

induced by thermomechanical fluctuations and yields

$$\delta f_{\mathrm{th}} = \frac{1}{2\pi}\left(\frac{k_{\mathrm{B}}T}{kx_0^2}\frac{2\pi f_0 f_{BW}}{Q}\right)^{1/2} \tag{2.16}$$

For a resonance frequency $f_0 = 50$ MHz and quality factor $Q = 10^5$, a spring constant $k \approx 10^{-4}$ N/m of the carbon nanotube NEMS, one obtains a sensitivity of 150 Hz at

40 mK for a measurement bandwidth of $f_{BW} = 1$ Hz. One should therefore be able to reach a sensitivity of $1\mu_B$ at cryogenic temperatures with such a carbon based torque magnetometer, thus providing a mechanical readout scheme for a single (molecular) spin.

2.4 Outlook

In the following chapters of this manuscript, we will report on the first experimental realization of such a *supramolecular spintronic device* based on a single molecule magnet and a carbon nanotube NEMS. We will ultimately demonstrate the strong coupling between a single molecular spin and a single quantized mode of motion in a carbon nanotube NEMS and the detection of a single nuclear spin (Chapter 6). Enabled by the strong spin-motion coupling, such a supramolecular spintronic device can be the first implementation of a supramolecular torque magnetometer with a single molecule sensitivity. Coupling the magnetism and the mechanical motion of a molecular sized object could furthermore open the path quantum entanglement and quantum information processing in nanoscale solid state matter.

Chapter 3

Introduction to carbon nanotube based NEMS

Carbon nanotubes have become an essential building block for nanoelectromechanical systems (NEMS). Their very low mass and the highest known Young's modulus $E = 1$ TPa results in high resonance frequencies, high quality factors and large motion amplitudes for flexural (bending) modes in carbon nanotube NEMS compared to conventional Si based NEMS [1]. Therefore they are a perfect candidate for ultrasensitive mass sensing and force detection over a wide range of frequencies and the small carbon nanotube diameter ($d_{\mathrm{CNT}} \sim 1$ nm) should even enable single molecule detection [19].

In the previous chapter, we proposed different designs of carbon nanotube based supramolecular spintronic devices and single molecule detectors. In particular we described the design of a supramolecular torque magnetometer based on a carbon nanotube NEMS and single molecule magnets that could achieve single molecule/spin sensitivity (see Section 2.3). With the ambition of detecting and manipulating a single molecular spin, we propose in the following chapters the first implementation of a supramolecular spintronic device, based on single molecule magnets and carbon nanotube NEMS.

In this context we described the first building block, the single molecule magnets in the previous chapter 2. We will present in the following chapters 3, 4 and 5 the second building block for such a supramolecular torque detector, the carbon nanotube NEMS.

3.1 Introduction: Si based vs. carbon based NEMS

Conventional semiconductor NEMS as depicted in Fig. 3.1 are usually obtained in top-down fabrication processes by etching of a larger structure (thin film, etc...) or by depositing material (metal, semiconductor) on a resist mask which is subsequently lifted off. Upon reducing the dimensions and therefore the mass of the resonating beams, the resonance frequency for flexural modes can be increased up to a few gigahertz [1]. Top-down fabrication procedures however introduce defects into the resonator's surface, resulting in large dissipation and a low quality factor Q. Upon reducing the dimensions of the NEMS, the surface-to-volume ratio and thus the defect density increases [1]. In consequence the quality factor decreases with reduced device dimensions as depicted by the dashed line in Fig. 3.3.

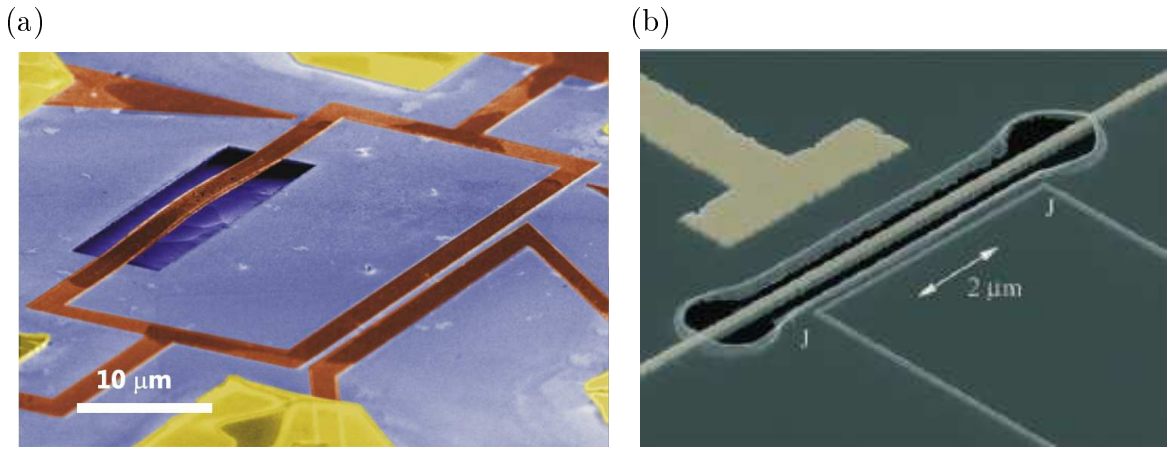

Figure 3.1: Conventional NEMS: False color SEM image of a (a) 2 MHz flexural resonator ($L = 50\mu$m) embedded in a DC SQUID (red structure). Figure from [1, 62]. (b) 19.7 MHz SiN resonator (8μm x 200 nm x 100 nm) covered by 20 nm of Au coupled to a superconducting single electron transistor. Figure from [1, 63].

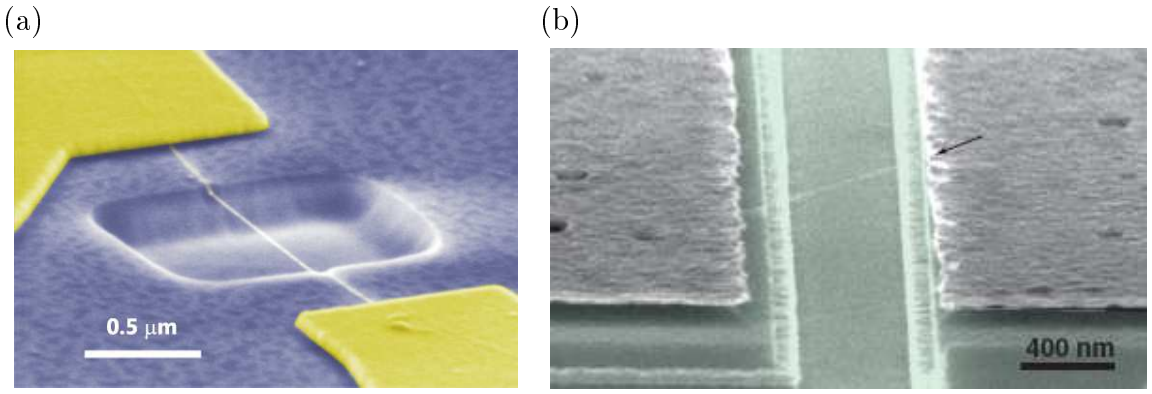

Figure 3.2: Carbon nanotube NEMS: False color SEM image of a (a) Top-down carbon nanotube NEMS [1, 64]. The carbon nanotube is clamped by Au electrodes (yellow) and subsequently suspended by etching the underlying silicon oxide (blue). (b) Bottom-up ultraclean carbon nanotube NEMS [1, 61]. The carbon nanotube is grown by CVD over the prefabricated junction in the last step of the process (see Chapter 4 for details).

Carbon nanotube NEMS can be obtained in a similar top-down approach by etching the nanotube's underlying substrate (Fig. 3.2a). The resonance frequency of flexural modes is indeed larger than in conventional NEMS, due to the lower mass and higher Young's modulus E (Fig. 3.4). Additionally, the quality factors on the order of 100-1000 deviate from the expected trend for conventional NEMS (black dots in Fig. 3.3).

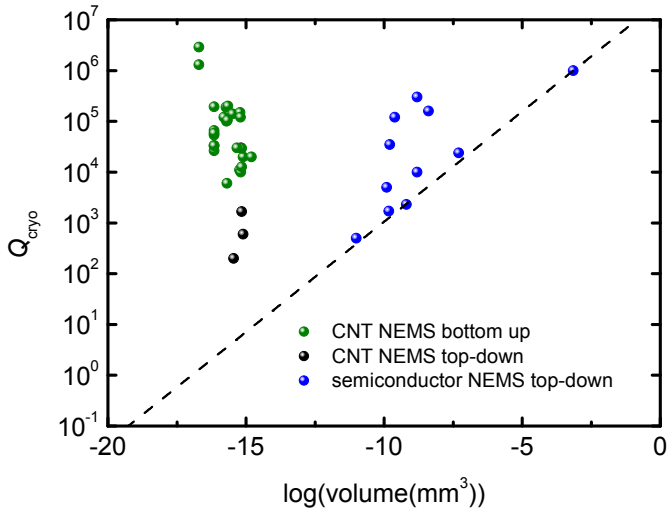

Figure 3.3: Quality factor Q_{cryo} at cryogenic temperatures ($T < 4$K) as a function of the NEMS' volume. The quality factors for conventional (blue dots) and carbon nanotube (black dots) top-down NEMS were extracted from [1]. Quality factors for bottom-up carbon nanotube NEMS (green dots) were compiled from [1, 19, 65, 66]. The dashed line represents the expected trend of the Q factors of top-down conventional NEMS upon reduction of their dimensions.

Alternatively, carbon nanotube NEMS are obtained from a bottom-up fabrication process (see Chapter 4 and Fig. 3.2b). In such bottom-up devices, carbon nanotubes are grown on a 'back-bone' metal junction by chemical vapor deposition (CVD) in the very last step of the fabrication process, thus avoiding contamination of the carbon nanotube by residual resist, solvents or chemical etching procedures [1, 61]. In consequence, the quality factors of these ultraclean bottom-up carbon nanotube NEMS can reach values up to 10^6 for flexural modes at cryogenic temperatures (Fig. 3.3 and 3.4). As expected, the resonance frequencies of flexural modes in bottom-up carbon nanotube devices range from 100 MHz to a few tens of gigahertz (Fig. 3.4) [1].

In the following section, we will discuss the state of the art for high frequency mechanical bending modes in carbon nanotube NEMS with large Q-factors obtained from such an ultraclean bottom-up fabrication approach (Section 3.2).

Due to their geometry, carbon nanotube NEMS can also exhibit high energy longitudinal streching modes (LSM) or radial breathing modes (RBM) in addition to transversal bending modes (Fig. 3.5). We will discuss quantized longitudinal stretching modes which occur due to a strong electron-phonon coupling in carbon nanotubes (Section 3.3). We will not discuss radial breathing modes (RBM) as they are beyond the scope of this thesis.

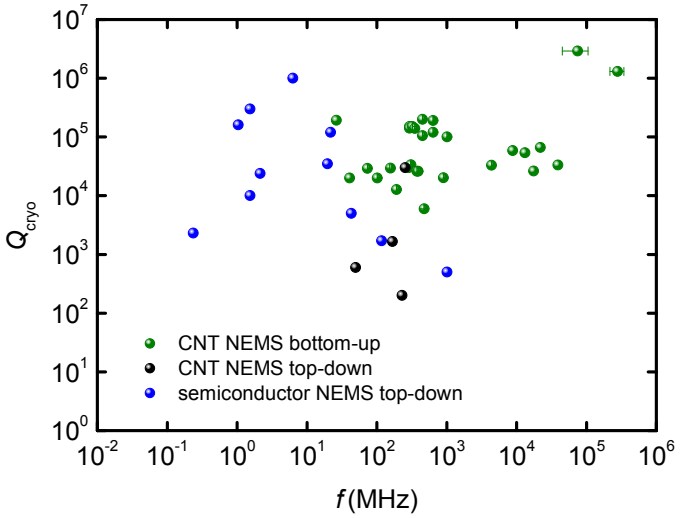

Figure 3.4: Quality factor Q_{cryo} at cryogenic temperatures as a function of the NEMS' resonance frequency. The values for conventional (blue dots) and carbon nanotube (black dots) top-down NEMS were extracted from [1]. Quality factors and frenquencies for bottom-up carbon nanotube NEMS (green dots) were compiled from [1, 19, 65, 66].

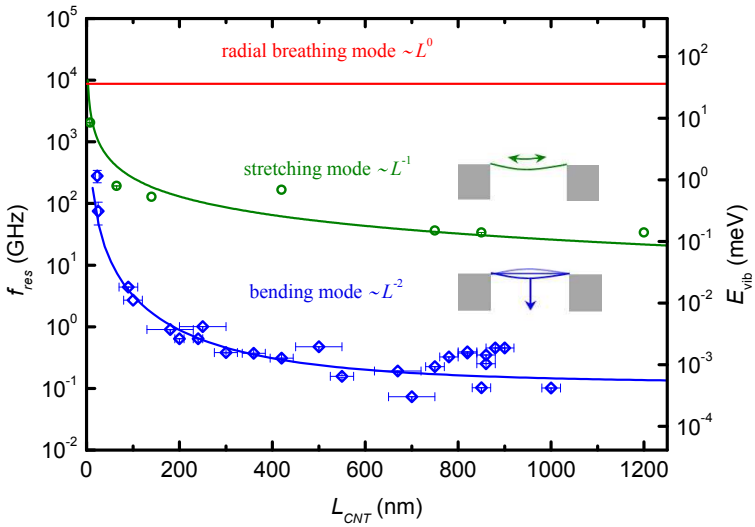

Figure 3.5: Vibrational modes in a carbon nanotube NEMS: Transversal bending modes (blue), longitudinal stretching modes (green) and radial breathing modes (red) as function of the nanotube's length. Bending mode frequencies (blue open squares) are compiled from [1, 19, 65, 66], LSM frequencies (green circles) from [66, 67, 20, 68]. The solid lines correspond to the calculated length dependance as described in [68].

As described in the previous section, we aim at probing the magnetization of single magnetic molecules at low temperature with the carbon nanotube's mechanical motion (see Section 2.3 and 6). In the following, we will therefore restrict the discussion of a carbon nanotube NEMS mechanical behavior to the low temperature regime. A detailed description of a carbon nanotube NEMS at room temperature can be found elsewhere [70].

3.2 High-Q mechanical bending modes in ultraclean carbon nanotube NEMS

3.2.1 Carbon nanotube beam mechanics: Linear harmonic oscillator

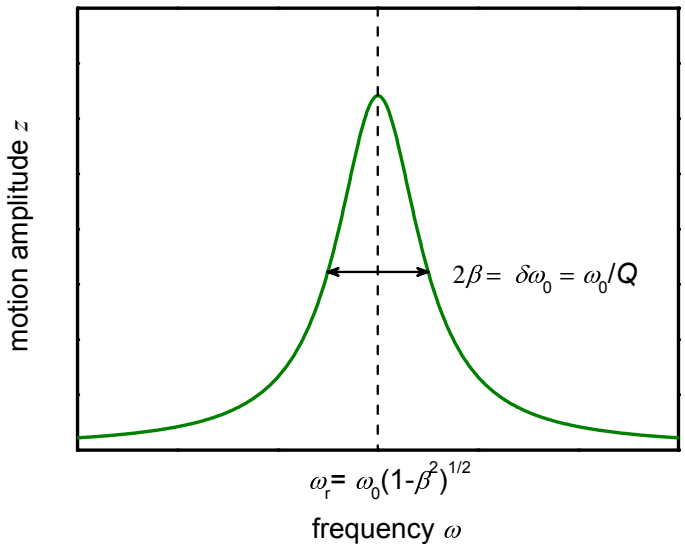

Figure 3.6: Mechanical response of a damped harmonic oscillator to an external oscillating force.

Doubly clamped carbon nanotube beam

A doubly clamped carbon nanotube beam can be described by a dampened harmonic oscillator actuated by a small oscillating driving force [69]. The equation of motion of such a system is given by

$$m\ddot{z}(t) + b\dot{z}(t) + kz(t) = F_0 cos(\omega t) \tag{3.1}$$

The steady state solution of eq. 3.1 then yields

$$z(t) = \frac{F_0/m}{\sqrt{\left(\omega_0^2 - \omega^2\right)^2 + 4\omega^2\beta^2}} cos(\omega t - \phi) \tag{3.2}$$

$$\phi = arctan\left(\frac{\omega_0^2 - \omega^2}{2\omega\beta}\right) \tag{3.3}$$

with the damping term $\beta = b/2m$ and the resonance frequency of the free harmonic oscillator $\omega_0 = \sqrt{k/m}$.

The amplitude of motion $z(t)$ therefore exhibits a Lorentzian lineshape with a resonance frequency $\omega_r = \omega_0\sqrt{1-\beta^2}$ and a linewidth given by ω_0/Q, where Q is the quality factor of the system given by $Q = \omega_0/(2\beta) = \omega_0/\delta\omega_0$ (Fig. 3.6).

Doubly clamped carbon nanotube beam under tension

We now consider a tension T induced by a constant force on the carbon nanotube beam. The carbon nanotube beam is oriented along the x-axis with y and z-axis perpendicular to it (Fig. 3.7). For simplicity we consider only bending mode vibrations and external forces applied in the x-z plane.

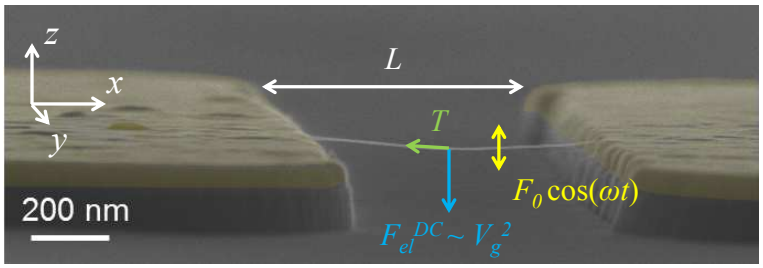

Figure 3.7: Suspended carbon nanotube beam driven by an oscillating force $\vec{F}_0 cos(\omega t)$ (yellow). A tension $\vec{T}$ (green) is induced in the beam by an constant force $\vec{F}_{el}^{DC}$, in this case an electrostatic force generated by the Si backgate (blue).

The elastic potential energy of the carbon nanotube beam is then given by [70, 71]

$$U = \frac{1}{2}\int_0^L \left(EI\frac{\partial^2 z}{\partial x^2} + T_0 + \frac{1}{2}EA\left(\frac{\partial z}{\partial x}\right)^2 + Kz\right) dx \tag{3.4}$$

where E is the Young's modulus, I the moment of inertia, A the beam's cross sectional area of the carbon nanotube and K a constant downward force in the x-z plane. Minimizing the potential energy U leads to the following equilibrium equation:

$$EI\frac{\partial^4 z}{\partial x^4} - T\frac{\partial^2 z}{\partial x^2} - K = 0 \tag{3.5}$$

where the tension is given by $T = T_0 + \frac{EA}{2L}\int_0^L \left(\frac{\partial z}{\partial x}\right)^2 dx$ [70, 71]. Equation 3.5 can then be solved in two different limits.

In the so called *bending* limit, the tension is small compared to the flexural rigidity of the beam $EI \gg T$ and the resonance frequency of the fundamental mode is given by

$$\omega = \frac{22.4}{L^2}\sqrt{\frac{EI}{\mu}} + 0.28T\sqrt{\frac{1}{\mu EI}} \tag{3.6}$$

where L is the length and μ the linear mass density of the nanotube beam [70, 71]. In this limit, the resonance frequency of mechanical bending mode follows a $1/L^2$ dependance, as depicted in Fig. 3.5.

In the *tension* limit, the tension is large compared to the flexural rigidity $EI \ll T$ and the resonance frequency holds

$$\omega = \frac{\pi}{L}\sqrt{\frac{T}{\mu}} + \frac{2\pi}{L^2}\sqrt{\frac{EI}{\mu}} \tag{3.7}$$

where L is the length and μ the linear mass density of the nanotube beam [70, 71].

In a suspended carbon nanotube resonator as depicted in Fig. 3.7, the tension can be due to an *in-biult* tension T_0 occuring during the fabrication process of the sample. Tension can also arise from a DC gate potential V_g^{DC} and the associated electrostatic force

$$F_{el}^{DC} = \frac{1}{2}C'_{\mathrm{g}}\left(V_{\mathrm{g}}^{DC} - V_0\right)^2 \tag{3.8}$$

with V_0 being the charge neutrality voltage of the carbon nanotube. The resulting tension T is then given in good approximation by $T \approx F_{el}^{DC}/\sqrt{24s}$, where s is the slack[1] in the carbon nanotube beam [70].

For small gate voltages V_{g}^{DC} we have $F_{el}^{DC} \ll EI/L^2$ ($V_0 = 0$). Thus, the tension is small compared to the flexural rigidity and the resonator is in the *bending* regime. From equation 3.6 with determine

$$\omega_{bend} \sim T \sim V_{\mathrm{g}}^{DC^2} \tag{3.9}$$

For large gate voltages V_{g}^{DC} we have $F_{el}^{DC} \gg EI/L^2$. The resonator is in a *catenary tension* regime and from equation 3.7 we deduce

$$\omega_{cat} \sim \sqrt{T} \sim V_{\mathrm{g}}^{DC} \tag{3.10}$$

[1] The slack s is given by the ratio $\frac{L-L_0}{L}$, where L is the length of the beam and L_0 the distance between the clamping points.

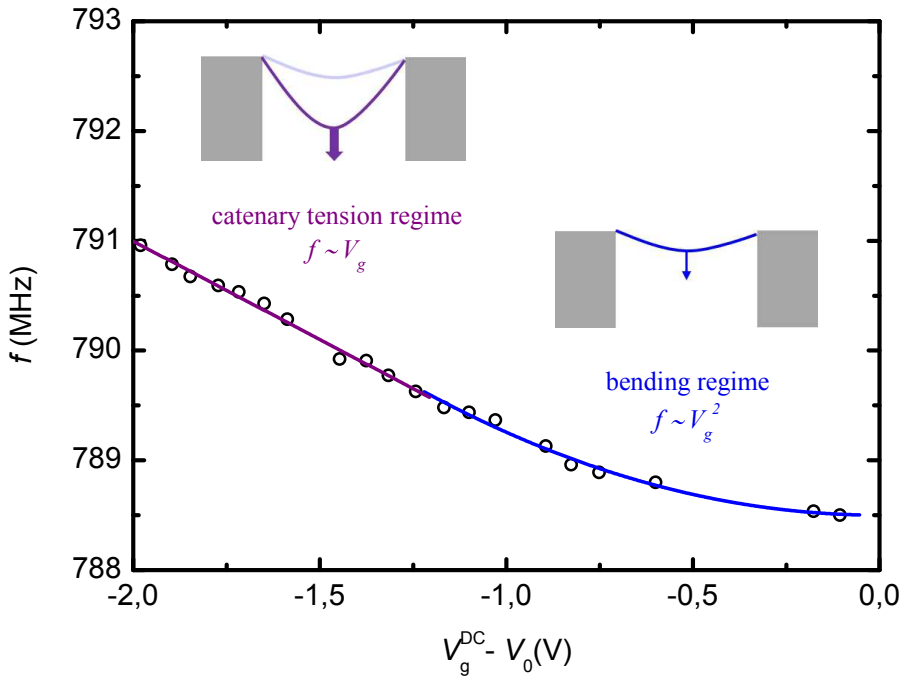

Figure 3.8: Frequency dispersion of a carbon nanotube NEMS at $T = 20$ mK. In the bending regime (blue segment), the applied force to the nanotube is small and the frequency follows a quadratic dependance on the gate voltage. In the catenary tension regime (purple segment), the force becomes large and the frequency depends linearly on the gate potential.

The transition between the two regimes occurs for $T = EI/L^2$ and a crossover gate voltage V_g^* [70]

$$V_g^* = \sqrt{\frac{2EI\sqrt{24s}}{C_g'}} \tag{3.11}$$

Fig. 3.8 displays the frequency dispersion of a carbon nanotube resonator under such a gate dependant tension.

Harmonic frequency spectrum

Eventually, one can observe higher mechanical modes in a carbon nanotube NEMS [70, 65, 72] as depicted in Fig. 3.9a. As expected for a carbon nanotube beam under tension, the higher mode frequencies f_n are integer multiple of the fundamental resonance frequency f_0 (Fig. 3.9b). For a true harmonic spectrum, the relation f_n/nf_0 equals 1 (Fig. 3.9c) [65].

Recently, Laird *et al.* [65] observed fractional resonance modes in carbon nanotube resonators at cryogenic temperatures ($n = 1/4, 1/2, 3/2$), which can be attributed to parametric driving of higher integer resonance modes (see Fig. 3.9c) (see [65] for details).

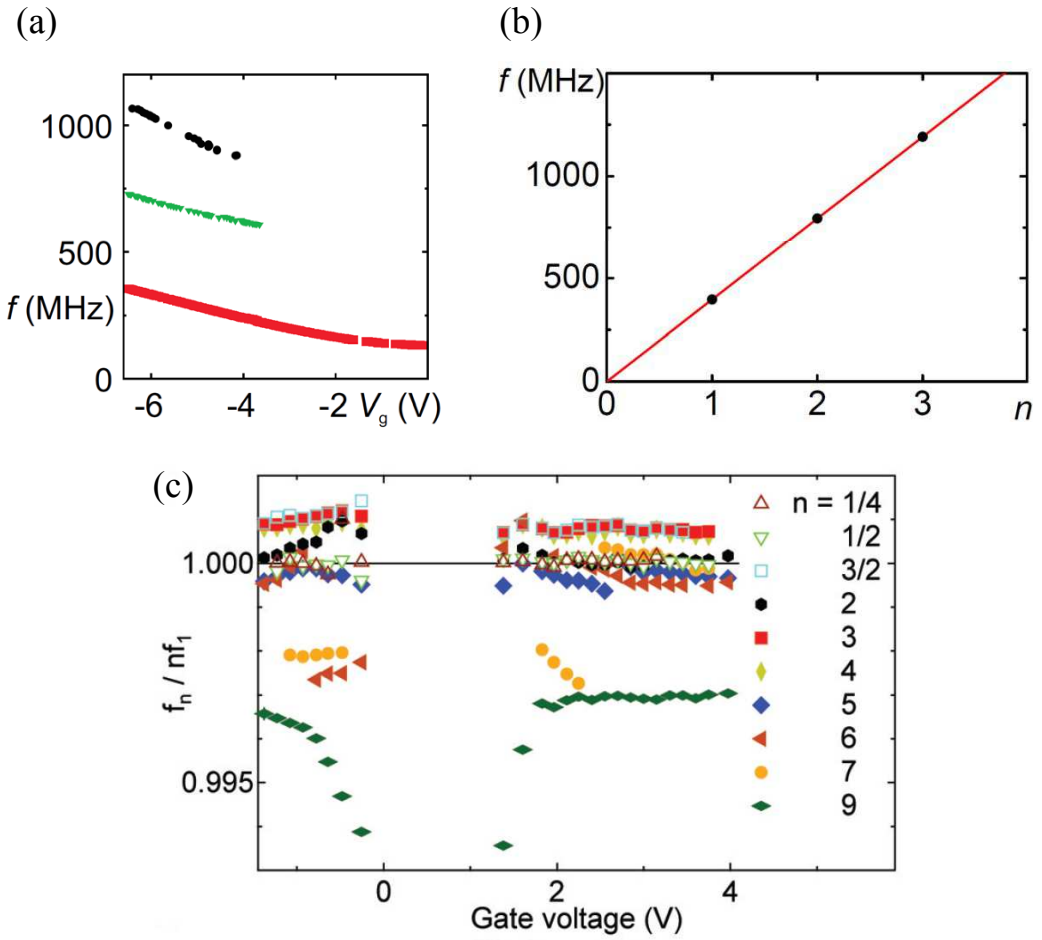

Figure 3.9: Integer and fractional mechanical modes in carbon nanotube resonators: (a) Frequency dispersion for the first three integer modes under gate dependant tension at $T = 20$ mK. Modified figure from [72]. (b) Mode frequency as function of the mode number n for $V_g = -6.29$ V in (a). Modified figure from [72]. (c) Normalized resonance frequency f_n/nf_0 as a function of the gate voltage for different modes at $T = 100$ mK. Fractional modes appear, which are attributed to parametric driving of integer resonance modes. Figure from [65].

3.2.2 Carbon nanotube beam mechanics: Nonlinear Duffing oscillator

At large amplitude of motion, the carbon nanotube NEMS exhibits a nonlinear mechanical behavior attributed to additional restoring forces in the beam. The mechanical motion is then described by a Duffing oscillator yielding the following equation of motion:

$$\ddot{z}(t) + \frac{\omega_0}{Q}\dot{z}(t) + \omega_0^2 z(t) + \alpha z^3(t) = \frac{F_0}{m}cos(\omega t) \tag{3.12}$$

where α is the so called Duffing parameter.

At low driving forces (power), equation 3.12 reduces to equation 3.1 and we obtain a Lorentzian resonance lineshape. However, upon increasing the driving force (power) the resonance peak is pulled towards higher frequencies (lower frequencies) if the Duffing parameter α is positive (negative) (Fig. 3.10a). In this bistable state, a hysteretic switching develops between different metastable modes in addition to the frequency pulling (Fig. 3.10b) and one observes an asymetric lineshape, with a sharp edge on the high (low) frequency side for a positive (negative) Duffing parameter α (Fig. 3.10c). The hysteresis between upwards and downwards frequency sweep becomes larger with an increased driving force on the beam.

The nonlinearity is typically associated with an elastic deformation of the carbon nanotube beam with a Duffing parameter $\alpha_m = \frac{E}{18\rho}\left(\frac{2\pi}{L}\right)^4$, where ρ is the density of the carbon nanotube.

It was recently suggested [70], that such nonlinear behavior could also arise from a direct dependance of the resonance frequency on the driving force. Since the carbon nanotube resonance can be tuned and is actuated by a gate voltage (see Section 3.2.1 and 3.2.3, respectively), the driving power modulates the frequency and thus the spring constant in the beam, leading to a bistability in the system. The motion is then described by a modified version of eq. 3.12

$$\ddot{z}(t) + \frac{\omega_0}{Q}\dot{z}(t) + \omega_0^2\left(F_0 cos(\omega t)\right) z(t) = \frac{F_0}{m}cos(\omega t) \tag{3.13}$$

At very low temperature, an additional nonlinearity is induced in carbon nanotube NEMS by charge quantization effects [61, 73, 74]. Carbon nanotube resonators behave as a quantum dots and exhibit Coulomb blockade at cryogenic temperatures, where the electron transport is governed by a quantized charge transport known as single-electron tunneling. Single-electron tunneling modulates the nanotube's spring constant due to the strong coupling between the charge transport and mechanical motion. The resulting current-dependant nonlinearity is much larger than nonlinearities arising from elastic deformation of the beam (see Section 3.2.4 for details).

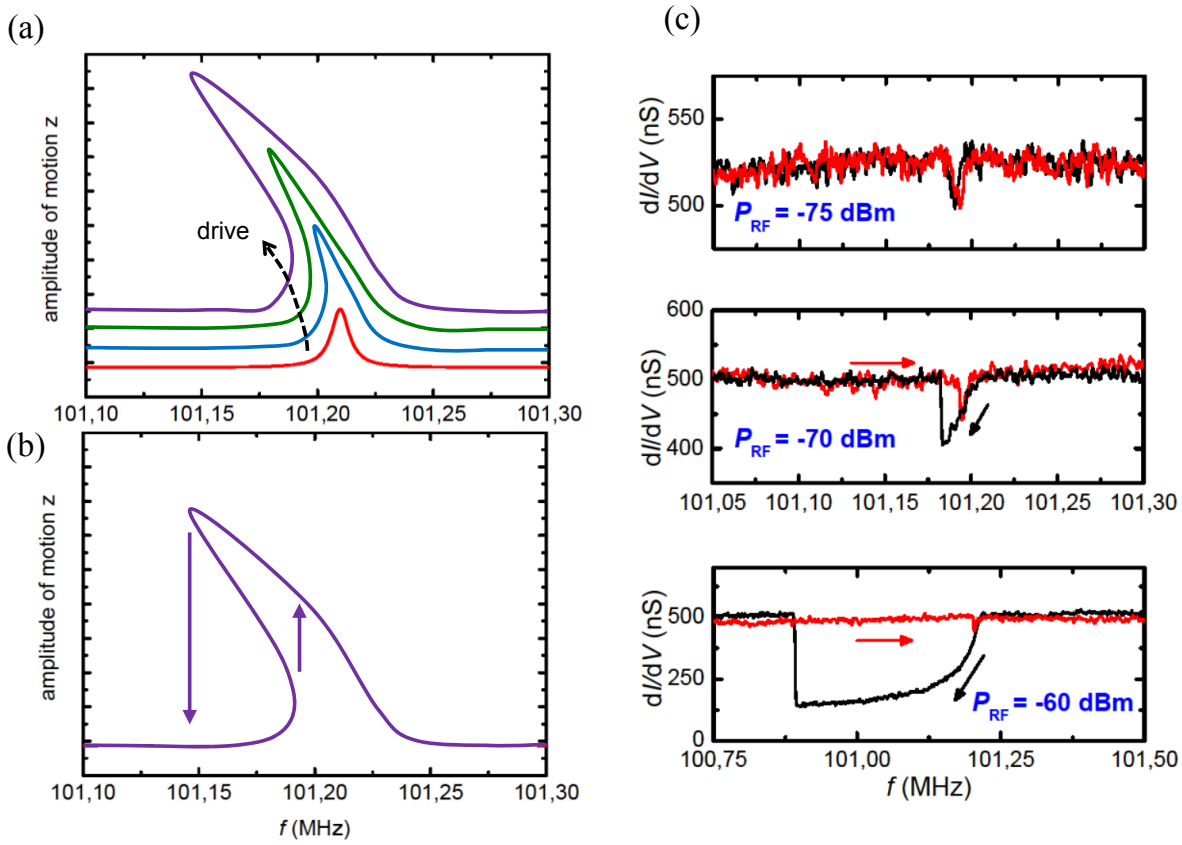

Figure 3.10: Nonlinear behavior in carbon nanotube Duffing oscillators: (a) Increasing drive pulls the resonance peak towards lower frequencies for $\alpha < 0$. (b) Hysteretic switching between upwards and downwards frequency at large driving powers for $\alpha < 0$. (c) Evolution of the lineshape with different driving powers and $\alpha < 0$. At low drive, we observe a Lorentzian lineashape. Upon increasing the drive, an asymetric lineshape with increasing hysteresis develops. Red and black curves correnspond to upwards and downwards frequency sweeps, respectively. The measurement was performed at $T = 20$ mK.

3.2.3 Actuation and detection principle

Huettel *et al.* proposed an electronic actuation and detection scheme for a carbon nanotube's mechanical motion at low temperature ($T < 4$ K). The readout is based on the nonlinear gate dependance of the current in a carbon nanotube NEMS at cryogenic temperatures and the coupling between its charge transport and mechanical motion [73, 75].

As the carbon nanotube is driven into resonance, it oscillates with a frequency ω_r and a finite amplitude $u(t) = u_0 cos(\omega_r t)$. The mechanical motion periodically modulates the gate capacitance C_g in the resonator by $\delta C_g = \partial C_g / \partial u \cdot u$ and therefore the gate

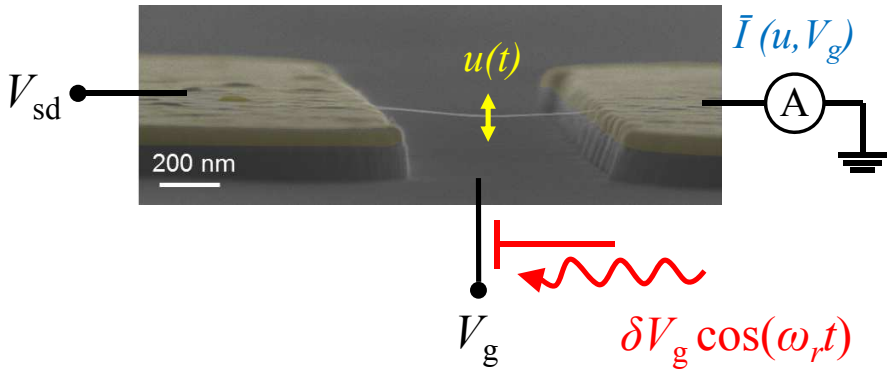

Figure 3.11: Electrostatic actuation scheme of carbon nanotube NEMS

induced charge $q_c = C_g V_g$ on the resonator. Hence the oscillating gate capacitance is equivalent to an effective oscillating voltage $\delta V_g = V_g \delta C_g / C_g$ applied to the gate electrode. The corresponding time-dependant current is then obtained in a Taylor expansion of $I(V_g + \delta V_g)$ around $\delta V_g = 0$.

It should be noted that the mechanical resonance frequency is much larger than the measurement bandwidth of the setup (see Section 4.4). In consequence, we only measure time-average DC currents yielding

$$\bar{I}(u_0, V_g) = I(V_g) + \frac{u_0^2}{4} \left(\frac{V_g}{C_g} \frac{\partial C_g}{\partial u} \right)^2 \frac{\partial^2 I}{\partial V_g^2} + o\left(u^4\right) \tag{3.14}$$

Due to averaging, only even powers of u_0 contribute to the average current $\bar{I}$. Fig. 3.12a compares the time average current $\bar{I}$ (blue curve) with the static current I (black curve). The time average current $\bar{I}$ is numerically calculated from the measured static current I for a motion amplitude on resonance $u_0 = 5$ nm, gate capacitance $C_g = 9$ aF and $\partial C_g / \partial u = 10^{-12}$ F/m using eq. 3.14.

The current change $\Delta I = \bar{I} - I$ induced by the mechanical motion thus follows the local curvature $\partial^2 I / \partial V_g^2$ of the static current $I(V_g)$ in the carbon nanotube NEMS (Fig. 3.12b). On a Coulomb blockade peak the curvature is negative, i.e. $\bar{I} < I$, resulting in a current dip at the resonance frequency of the carbon nanotube (Fig. 3.12c). On the sidewalls of the Coulomb peak however the curvature is positive, i.e. $\bar{I} > I$, which manifests as a current peak at the resonance frequency (Fig. 3.12d).

The method therefore exploits the nonlinear gate dependance of the current in a suspended carbon nanotube quantum dot by detecting second or higher order current changes. As such, the method differs from the conventional mixing technique, which only probes linear changes of current in the carbon nanotube NEMS [70, 73].

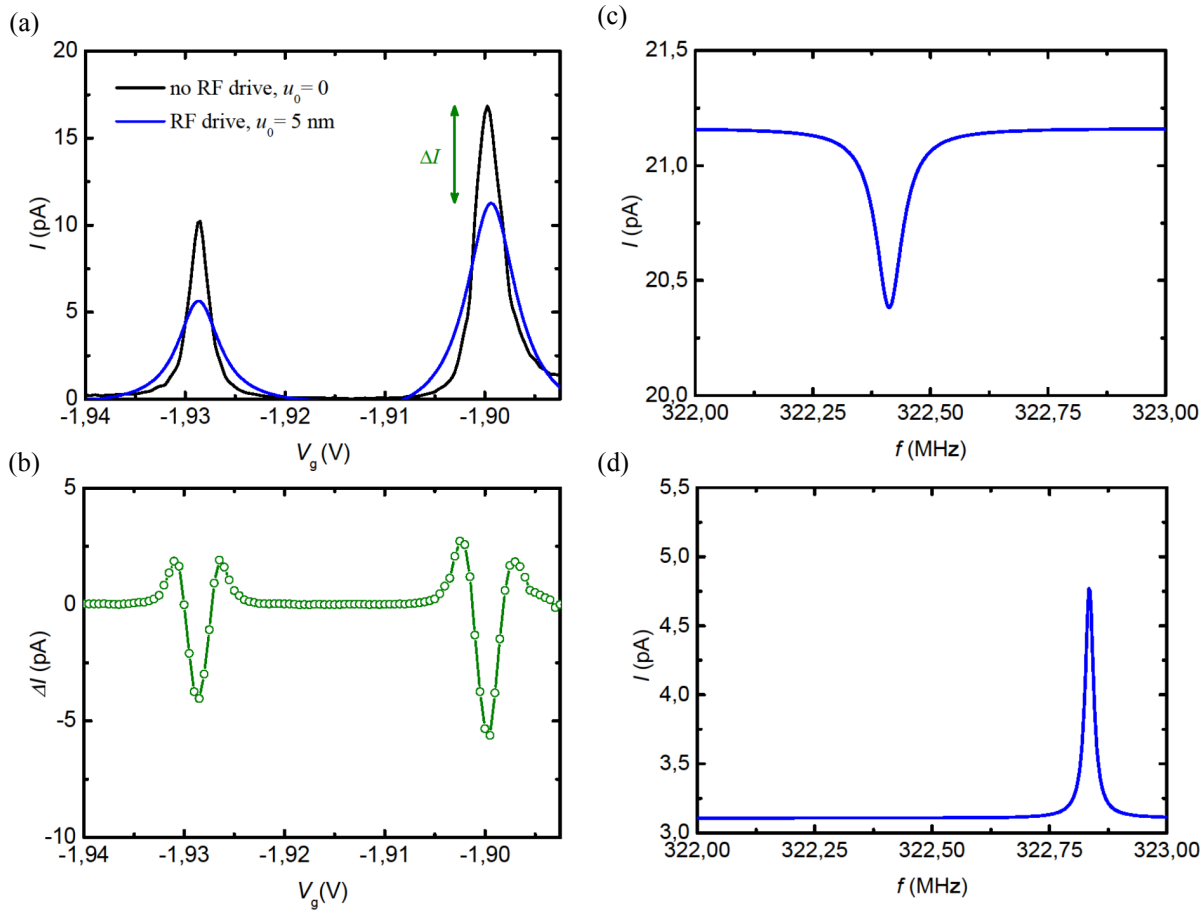

Figure 3.12: Current detection scheme of carbon nanotube NEMS at cryogenic temperatures: (a) Calculated time average $\bar{I}(V_g)$ (blue curve) and measured static current $I(V_g)$ (black curve) as function of the gate voltage. The average current is obtain from the static current and Eq.3.14 for $u_0 = 5$ nm [70], $C_g = 9$ aF and $\partial C_g/\partial u = 10^{-12}$ F/m [70]. (b) Difference ΔI between average and static current as a function of gate voltage. The curve follows the curvature of the static current $\partial^2 I/\partial V_g^2$. (c)(d) Measured current as a function of frequency for $V_g = -1.8983$ V and $V_g = -1.904$ V showing the sign change of the current modulation ΔI. The observed frequency shift is due to single-electron fluctuations (see Section 3.2.4). All measurements were performed at $T = 20$ mK.

3.2.4 Strong coupling between single-electron tunneling and mechanical bending modes

At cryogenic temperatures, a carbon nanotube NEMS is in a regime of Coulomb blockade and the electronic transport is governed by single-electron tunneling (SET). In the previous section, we showed the influence of the nanotube's mechanical motion in the

electronic transport enabling its detection. In this section we will describe the inverse effect, i.e. the impact of the SET on the nanotube's mechanical motion.

SET in a CNT NEMS-QD can be considered as an external perturbation to the CNT mechanical motion, and vice versa. This perturbation can be described as an electrodynamic force acting on the CNT. The contribution of this force, which is in phase with the mechanical motion, is responsible for a frequency modulation Δf, whereas a contribution of the force which is out of phase with mechanical motion induces a modification of the dissipation and the quality factor Q. The model and the experimental data presented in the following section, were first published by Lassagne *et al.* [74] and by Steele *et al.* [61] in 2009.

First we consider the mechanical response of a CNT NEMS-QD, i.e. the frequency shift due to SET. The electrostatic force acting on a CNT quantum dot is given by

$$F_{\mathrm{el}} = \frac{1}{2}C_{\mathrm{g}}'\left(V_{\mathrm{g}}^{\mathrm{DC}} - V_{\mathrm{dot}}\right)^2 \approx \frac{1}{2}C_{\mathrm{g}}'\left(V_{\mathrm{g}}^{\mathrm{DC}^2} - 2V_{\mathrm{dot}}V_{\mathrm{g}}^{\mathrm{DC}}\right) + o(V_{\mathrm{dot}}^2) \tag{3.15}$$

where V_{dot} is the electrostatic potential on the quantum dot yielding

$$V_{\mathrm{dot}} = \frac{-Pe}{C_{\mathrm{dot}}} + \frac{C_{\mathrm{g}}V_{\mathrm{g}}^{\mathrm{DC}}}{C_{\mathrm{dot}}} \tag{3.16}$$

with the control charge $q_{\mathrm{c}} = C_{\mathrm{g}}V_{\mathrm{g}}^{\mathrm{DC}}$, the charge on the dot $q_{\mathrm{dot}} = -Pe$ and the dot capacitance C_{dot}.

The relevant electrodynamic force related to SET is described by the second term in Eq. 3.15 and reads:

$$F = -\frac{C_{\mathrm{g}}'V_{\mathrm{g}}^{\mathrm{DC}}}{C_{\mathrm{dot}}}\left(q_{\mathrm{dot}} - q_{\mathrm{c}}\right) \tag{3.17}$$

If the CNT is driven into mechanical motion by an oscillating field with the frequency f and a drive amplitude δz_0, the amplitude of motion is given by

$$\delta z = \delta z_0 e^{i2\pi ft} \tag{3.18}$$

As a consequence, the distance between the CNT and gate and hence the CNT-gate capacitance and the control charge oscillate as

$$\delta C_{\mathrm{g}} = C_{\mathrm{g}}'\delta z = C_{\mathrm{g}}'\delta z_0 e^{i2\pi ft} \tag{3.19}$$

$$\delta q_{\mathrm{c}} = \delta C_{\mathrm{g}}V_{\mathrm{g}}^{\mathrm{DC}} \tag{3.20}$$

The charge on the quantum dot q_{dot} exhibits staircase dependance on the control charge q_{c} (Fig. 3.13). In consequence the charge on the quantum dot also oscillates in response to the mechanical motion and the oscillation can be written as

$$\delta q_{\mathrm{dot}} = e\delta P = e\frac{dP}{dq_{\mathrm{c}}}\delta q_{\mathrm{c}} \tag{3.21}$$

where P is the occupation probability of the quantum dot. The steps are broadened by charge fluctuations induced by thermal activation or a bias voltage (dashed curve Fig. 3.13).

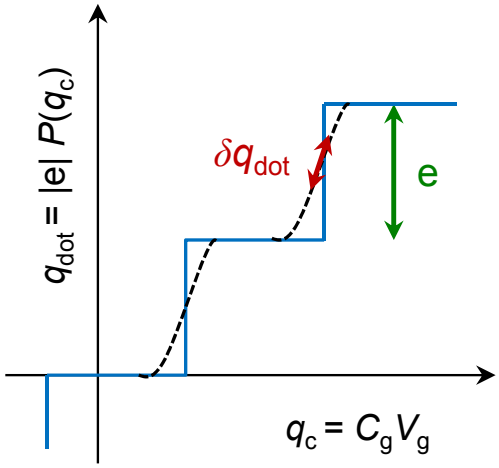

Figure 3.13: Electrostatic charge on the quantum dot q_{dot} as a function of the control charge q_{c}. The blue staircase depicts the charge q_{dot} at $T = 0$ K and the dashed line depicts the charge at finite temperature or bias.

In a regime of Coulomb blockade, the occupation probability can be related to the conductance G of the dot and the tunnel rate at the contacts Γ *via* [74, 76]

$$G = \frac{dP}{dq_{\mathrm{c}}} eC_{\mathrm{dot}} \frac{\Gamma}{2} \tag{3.22}$$

Therefore, the quantum dot charge fluctuation holds $\delta q_{\mathrm{dot}} = e\delta P = e\frac{2G}{C_{\mathrm{dot}}\Gamma}\delta q_{\mathrm{c}}$ and the force oscillation δF yields

$$\delta F = -\frac{C_{\mathrm{g}}' V_{\mathrm{g}}^{\mathrm{DC}}}{C_{\mathrm{dot}}} \left(\delta q_{\mathrm{dot}} - \delta q_{\mathrm{c}}\right) = \frac{\left(C_{\mathrm{g}}' V_{\mathrm{g}}^{\mathrm{DC}}\right)^2}{C_{\mathrm{dot}}} \left(\frac{2G}{C_{\mathrm{dot}}\Gamma} - 1\right) \delta z_0 e^{i2\pi f t} \tag{3.23}$$

Since the force is proportional to the motion amplitude $\delta F = \delta k \delta z$ it can be seen as a spring force, changing the CNT's resonance frequency by

$$\Delta f = -\frac{f_0}{2}\frac{C_{\mathrm{g}}'^2}{k}\frac{V_{\mathrm{g}}^2}{C_{\mathrm{dot}}} \left(\frac{2G}{C_{\mathrm{dot}}\Gamma} - 1\right) \tag{3.24}$$

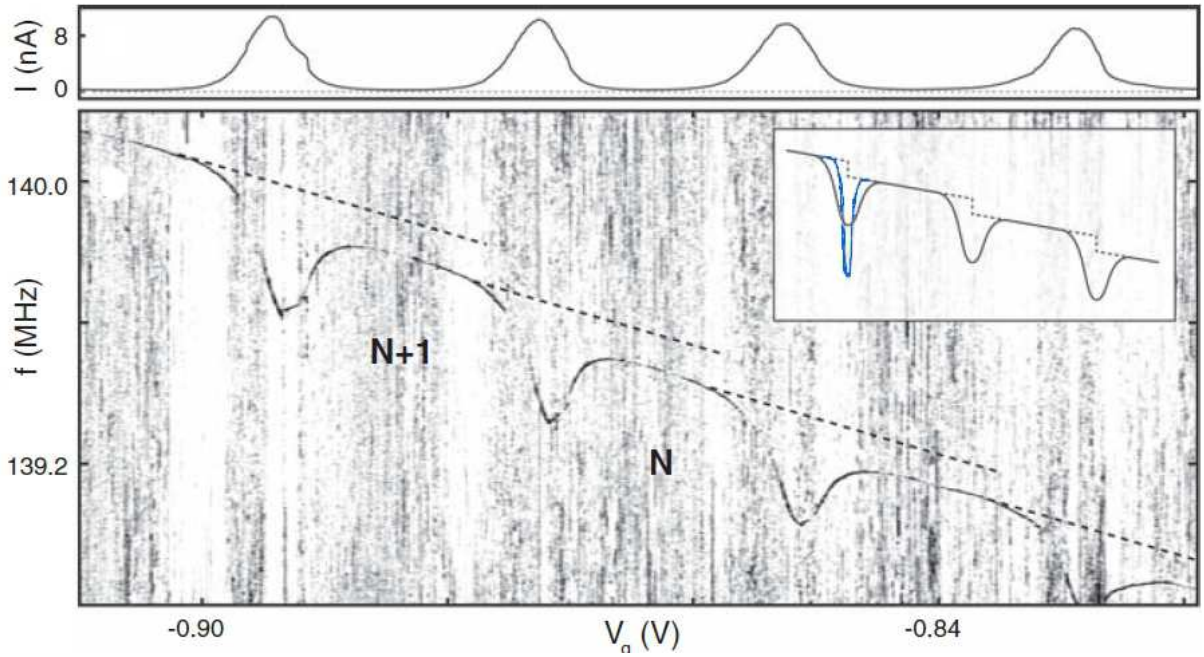

Figure 3.14: Mechanical response of a carbon nanotube NEMS to single-electron tunneling: Resonance frequency and the current of the carbon nanotube NEMS as a function of the gate voltage. The measurement is performed at actuation power of -38 dBm and a small bias $V_{sd} = 1.5$ mV. The inset depicts the expected frequency behavior for zero bias (blue line) and large bias (black line). Modified figure from Ref. [61]

In consequence, a decrease of the resonance frequency occurs for an increased current through the quantum dot (Fig. 3.14). For the carbon nanotube NEMS parameters $C_{\mathrm{dot}} = 30$ aF, $\Gamma \sim 75$ GHz, $C_{\mathrm{g}}' = 10^{-12}$ F/m, $k = 10^{-3}$ N/m and $f \sim 140$ MHz the frequency shift yields $\delta f \sim -0.5$ MHz [61]. The frequency drop eventually corresponds to a softening of the nanotube's spring constant by $\delta k = \frac{\delta f}{f} k \sim -10^{-6}$ N/m.

If the gate potential of the quantum dot is tuned from one Coulomb valley to another, the (static) charge q_{dot} on the nanotube increases by one electron. As the electrostatic force acting on the nanotube is proportional to q_{dot}^2, the additional electron causes a change of the electrostatic force and thus a discrete shift in the resonance frequency. This frequency shift is indicated by the offset between the dashed lines in Fig. 3.14 and is on the order of 0.1 MHz.

Finally, the observed frequency dip becomes broader and shallower if a bias voltage is applied to the quantum dot (Fig. 3.15 and inset of Fig. 3.14). The bias voltage causes a broadening of the quantum dot charge steps $q_{\mathrm{dot}}(q_{\mathrm{c}})$ as depicted in Fig. 3.13 (dashed curve). Thus, $\frac{dP}{dq_{\mathrm{c}}}$ becomes smaller and the step width increases, which accounts for the observed broadening and flattening of the frequency dip.

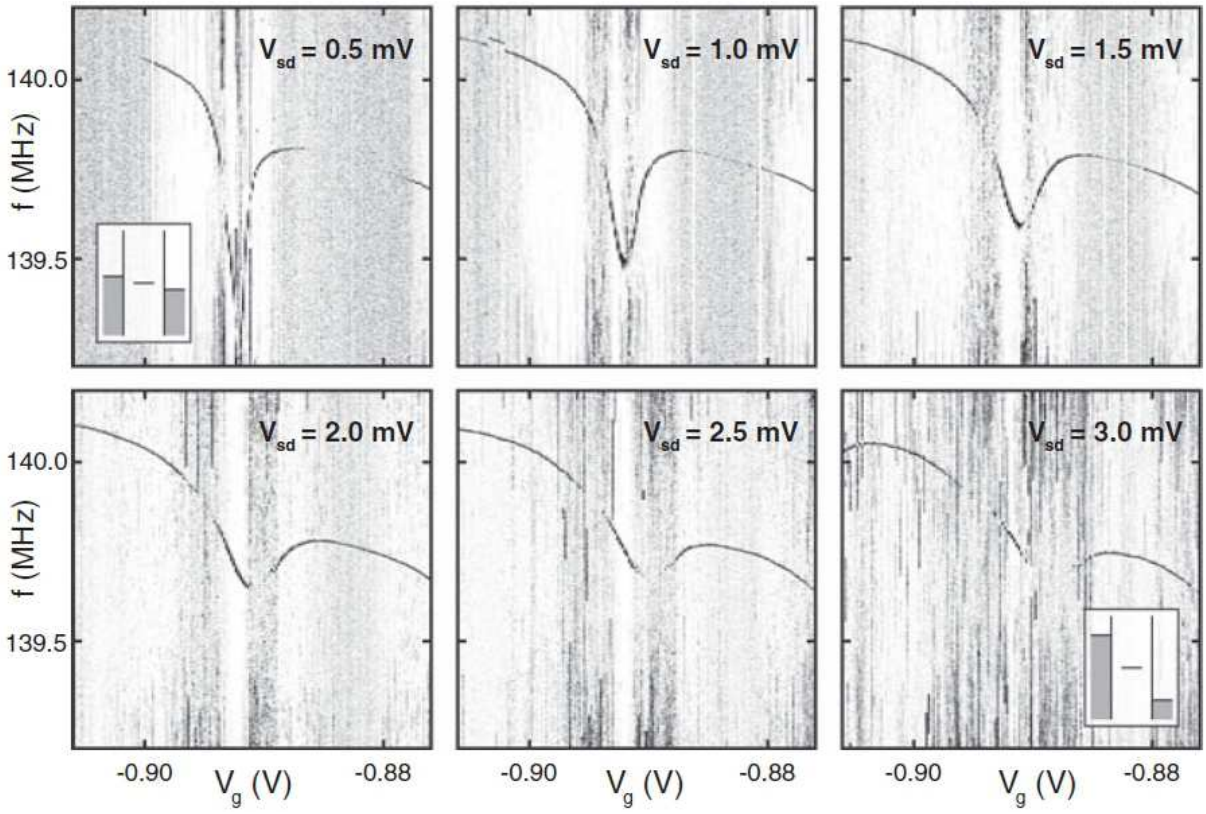

Figure 3.15: Bias dependance of the mechanical response of a carbon nanotube NEMS to single-electron tunneling. The insets show the quantum dot's energy diagram for small and large bias. Figure from Ref. [61]

We now discuss the dissipation induced by SET in the carbon nanotube NEMS. The oscillating charge δq_{dot} flows through the tunnel barrier, i.e. the tunnel resistance at the nanotube-metal interface with a current

$$\delta I_{\mathrm{dot}} = 2\pi f \delta q_{\mathrm{dot}} = 2\pi f e \frac{2G}{C_{\mathrm{dot}}\Gamma}\delta q_{\mathrm{c}} = 2\pi f e \frac{2G}{C_{\mathrm{dot}}\Gamma} C_{\mathrm{g}}' V_{\mathrm{g}}^{\mathrm{DC}} \delta z_0 e^{i2\pi f t} \tag{3.25}$$

The corresponding energy loss during an oscillation period is given by

$$E_{\mathrm{diss}} = \int_0^{1/f} \frac{1}{G}\delta I_{\mathrm{dot}}^2 dt = \frac{4\pi^2 f}{G}\left(\frac{2G}{C_{\mathrm{dot}}\Gamma} C_{\mathrm{g}}' V_{\mathrm{g}}^{\mathrm{DC}} \delta z_0\right)^2 \tag{3.26}$$

The quality factor is given by the ratio of the energy loss and the total mechanical energy stored in the resonator $E_{\mathrm{tot}} = \frac{1}{2}k\delta z_0^2$ and yields

$$\frac{1}{Q} = \frac{1}{2\pi}\frac{E_{\mathrm{diss}}}{E_{\mathrm{tot}}} = 2\pi f \frac{C_{\mathrm{g}}'^2}{k}\left(\frac{2V_{\mathrm{g}}^{\mathrm{DC}}}{C_{\mathrm{dot}}\Gamma}\right)^2 G \tag{3.27}$$

Therefore, a current increase results in stronger dissipation at the carbon nanotube-metal interface and a decrease of the quality factor Q as depicted in Fig. 3.16 and 3.18.

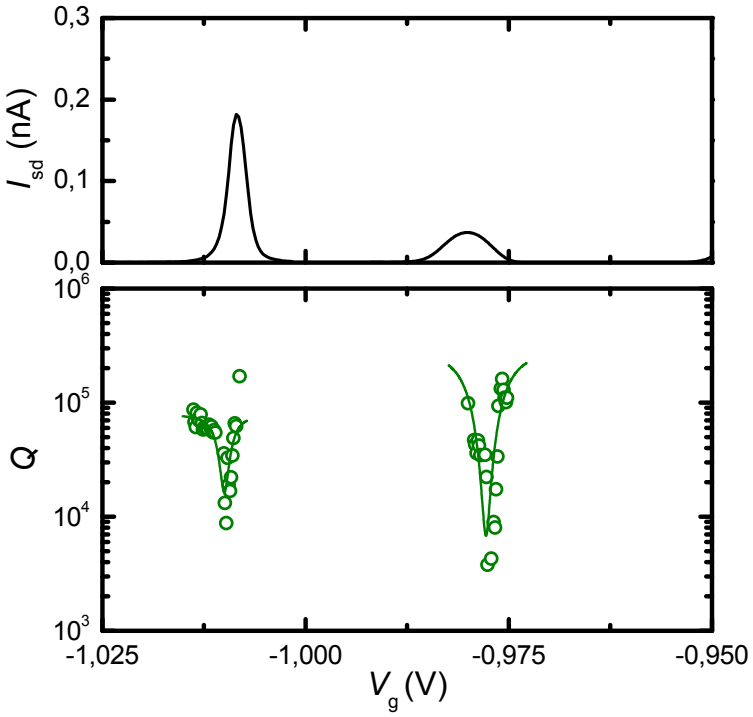

Figure 3.16: Dissipation induced by single-electron tunneling in a carbon nanotube NEMS. The measurement is performed under zero bias and a driving power of -60 dBm. Due to very strong Coulomb blockade, no resonance was observe and therefore no quality factor calculated in the Coulomb valley. The green lines are fits with equation 3.27.

Finally, SET affects the nonlinearity in a carbon nanotube NEMS. If the carbon nanotube NEMS is driven at higher power, the resonance peak becomes asymmetric and shows a significant hysteresis between upward and downward frequency sweeps (see Section 3.2.2). In such a Duffing oscillator, the spring constant k is modulated by the large mechanical displacement u yielding $k' = k + \alpha u^2$, with α being the Duffing parameter. For a spring hardening $\alpha > 0$, the resonance exhibits a sharp edge on the high frequency side, whereas for a spring softening $\alpha < 0$ the sharp edge of the resonance is found on the low frequency side [61].

The SET Duffing parameter α_{SET} can be determined from the third derivative of the driving force.

$$\alpha_{SET} = -\frac{d^3F}{dz^3} = \frac{d^2}{dz^2}\delta k = \frac{V_g^2}{C_g^2}\frac{k}{f}\left(\frac{dC}{dz}\right)^2\frac{d^2\delta f}{dV_g^2} \tag{3.28}$$

Therefore, the sign of α_{SET} follows the sign of the curvature of δf, leading to a spring

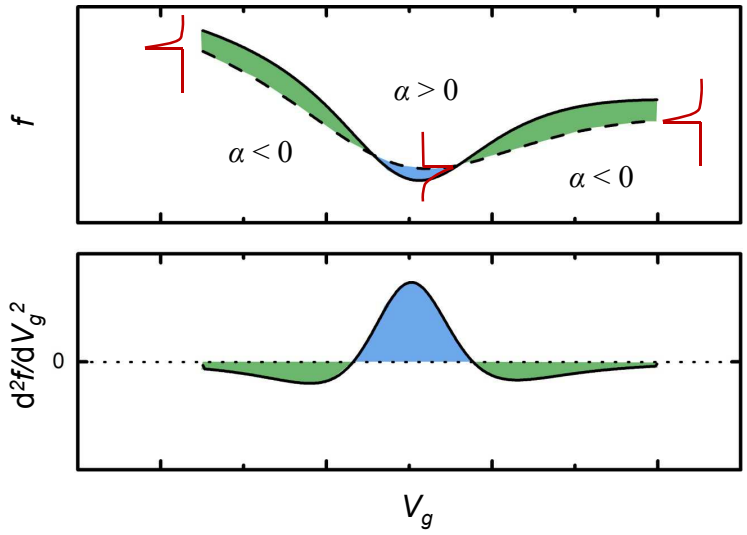

Figure 3.17: Nonlinearity modulation by single-electron tunneling in a carbon nanotube NEMS. The sign of α_{SET} follows the curvature $\frac{d^2f}{dV_g^2}$ of the frequency modulation induced by SET.

softening $\alpha_{SET} < 0$ in the Coulomb valley and a spring hardening $\alpha_{SET} > 0$ on the Coulomb peak (Fig. 3.17 and 3.18 c-d).

At even higher driving amplitudes (Fig. 3.18), a substructure appears in the resonance lineshape indicating transistions between different metastable states of motion (see Ref. [61] for more details).

The modulation of the carbon nanotube's nonlinearity by SET indicates that the associated Duffing parameter α_{SET} is much larger than its counterpart for mechanical deformation α_m, i.e. $\alpha_{SET} \gg \alpha_m$. The SET nonlinearity dominates over the geometric nonlinearity in the carbon nanotube resonator at cryogenic temperatures [61].

The here described strong coupling between the charge transport and mechanical motion in a carbon nanotube NEMS is observed only in a regime of Coulomb blockade and charge quantization. However, charge quantization is destroyed by temperature or by quantum fluctuations on the charge [77]. In consequence, the single electron effects on the mechanical motion are absent at high temperature $k_BT > E_C$ [70] or in Fabry Perot regime dominated by ballistic transport $R_{CNT} < e^2/h$ [77].

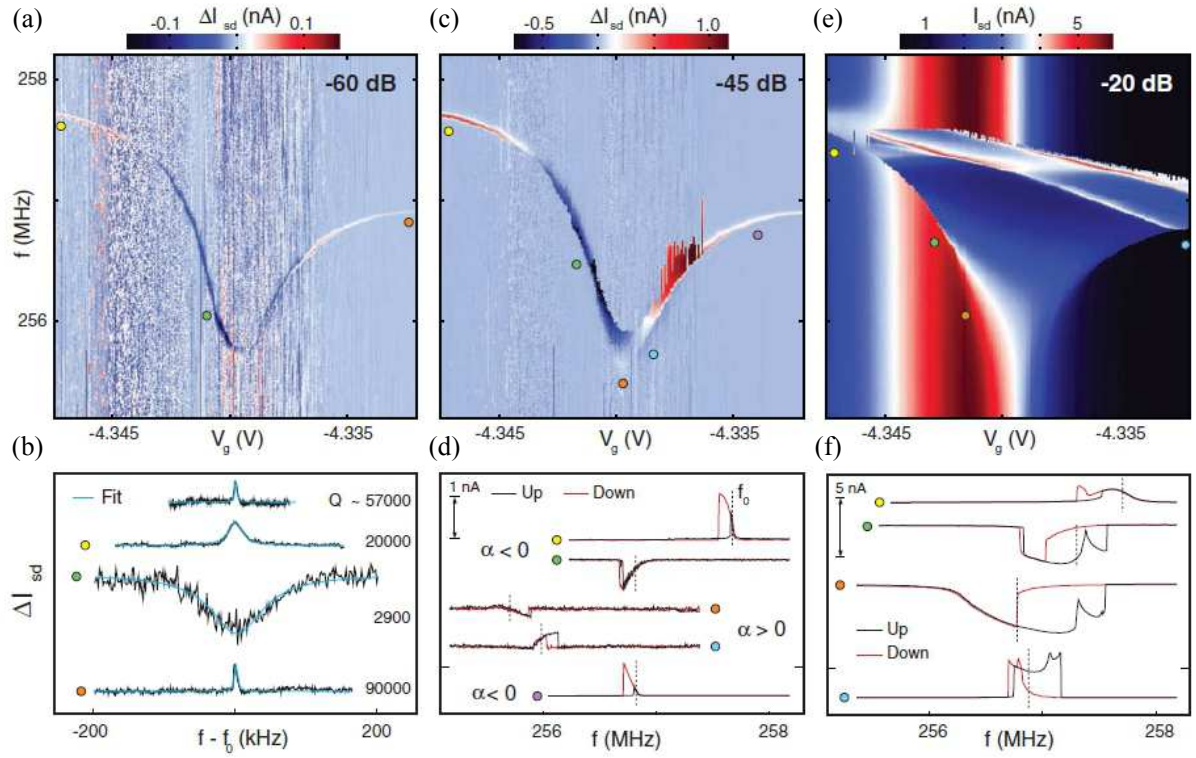

Figure 3.18: Evolution of a carbon nanotube NEMS resonance from linear to nonlinear driving regime. (a-b) Linear driving regime at -60 dBm showing the frequency modulation and the evolution of the Q factor by SET. (c-d) Onset of Duffing-like drive regime at -45 dBm demonstrating the evolution of the Duffing nonlinearity with SET. (e-f) At even higher drive power of -20 dBm, a substructure appears in the resonance lineshapes indicating a switching between several metastable modes. Figure from Ref. [61].

3.3 Quantized longitudinal stretching modes in ultra-clean carbon nanotube NEMS

In the previous section, we reported the influence of single-electron tunneling on the mechanical bending mode in a carbon nanotube NEMS. According to the Franck-Condon model, a single-electron tunneling onto the carbon nanotube quantum dot can also induce a mechanical displacement along the carbon nanotube's axis, so called longitudinal stretching modes (LSM) [67, 68]. The magnitude of this LSM depends on the (dimensionless) electron-phonon coupling g in the resonating beam. In conventional NEMS, the electron-phonon coupling is usually very weak and $g \ll 1$ due to the bulk character of those systems. Carbon nanotubes however can exhibit a strong electron-phonon coupling and $g \geq 1$ [67, 68, 78]. In the following section, we will discuss the appearance of longitu-

dinal stretching modes in carbon nanotube NEMS for different electron-phonon coupling regimes.

3.3.1 Weak and intermediate coupling $g \leq 1$: Quantized longitudinal stretching modes

The Franck-Condon principle postulates, that single-electron tunneling on the carbon nanotube quantum dot shifts the equilibrium position of the carbon nanotube along the nanotube's axis by an amount

$$l_{\text{mech}} = \sqrt{2g} l_{\text{osc}} \tag{3.29}$$

where g is the dimensionless electron-phonon coupling and $l_{\text{osc}} = \sqrt{\hbar/M\omega}$ the quantum mechanical oscillator length [67, 68, 78].

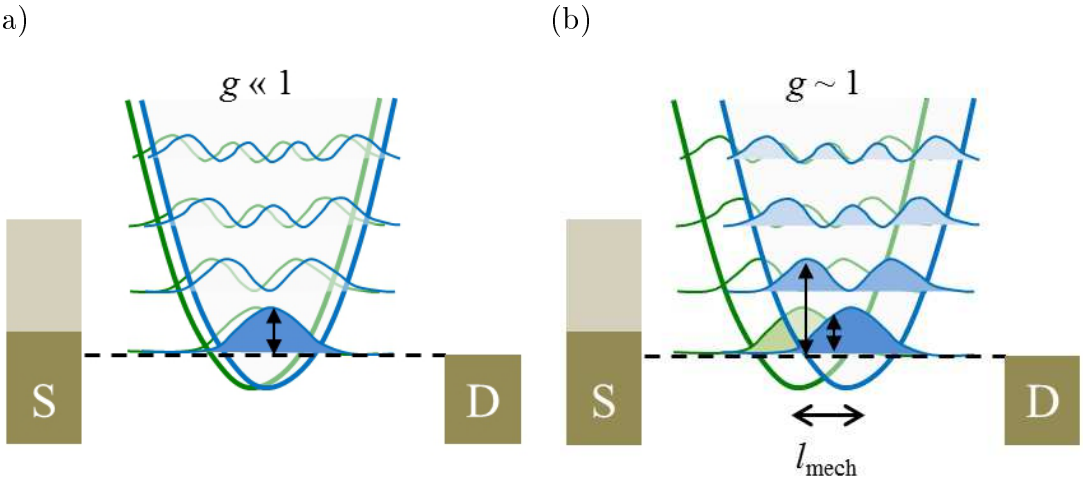

Figure 3.19: Franck-Condon principle for weak and intermediate electron-phonon coupling in carbon nanotube NEMS. The green (blue) curve corresponds to N ($N+1$) electrons on the dot. (a) For $g \ll 1$ the shift of the vibron potential is small and only ground-state-to-ground-state transitions are allow. (b) For $g \sim 1$ the shift of the vibron potential is such that transitions into higher excited states are allowed. The transitions are depicted by the black arrows and a high (low) transition probability corresponds to the dark blue (light blue) area under the wavefunction traces.

The coupling parameter g depends on the phonon mode and is sample specific. The parameter g strongly depends on the geometric radius and length of the carbon nanotube and is sensitive to the location of the quantum dot on the carbon nanotube and the strain profile of the phonon mode [78]. Despite the sample dependance we can estimate a value

of the coupling constant g for the lowest LSM mode using the Anderson-Holstein model which is given by

$$g^{\mathrm{LSM}} \approx \frac{2.25}{L_{\perp}[nm]} \tag{3.30}$$

where $L_{\perp}$ is the circumference of the nanotube [78].

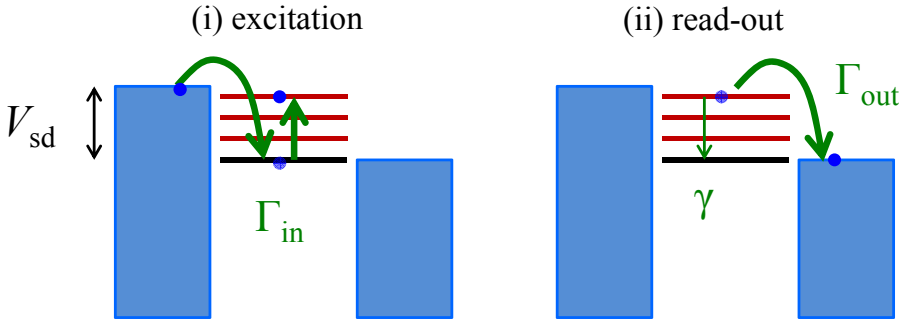

Figure 3.20: Electronic actuation and readout of longitudinal stretching modes: (i) Single-electron tunneling onto the suspended CNT shifts the equilibrium position of the CNT along his axis and proportional to the electron-phonon coupling g, leaving the electron in an excited vibrational state (red). (ii) If $\Gamma_{\mathrm{out}} > \gamma$, the electron tunnels out of the dot, resulting in equidistant excited states running parallel to the edge of the Coulomb diamond.

For very weak coupling $g \ll 1$, the shift of the associated vibron potential is negligeable which enables ground-state-to-ground-state transitions, where the transition probability is given by the overlap between the wavefunction for N and $N+1$ (Fig. 3.19a). On the other hand, the ground state is orthogonal to all excited states and the transitions into/from higher excited vibrational states are supressed. Therefore no vibrational mode is generated in the carbon nanotube.

For an electron-phonon coupling on the order of $g \sim 1$, the shift of the vibron potential enables transitions into higher excited states in addition to ground-state-to-ground-state transitions (Fig. 3.19b). The electron therefore effectively tunnels into an excited vibrational state (red in Fig. 3.20 (i)). If the tunnel rate out of the dot Γ_{out} is larger than the relaxation rate γ into the vibrational ground state, the electron tunnels out of the dot (Fig. 3.20 (ii)), resulting in equidistant excited states in the region of SET, running parallel to the edge of the Coulomb diamond (black arrows in Fig. 3.21a).

The average energy level separation ΔE_{vib} corresponds to the phonon energy and is given by

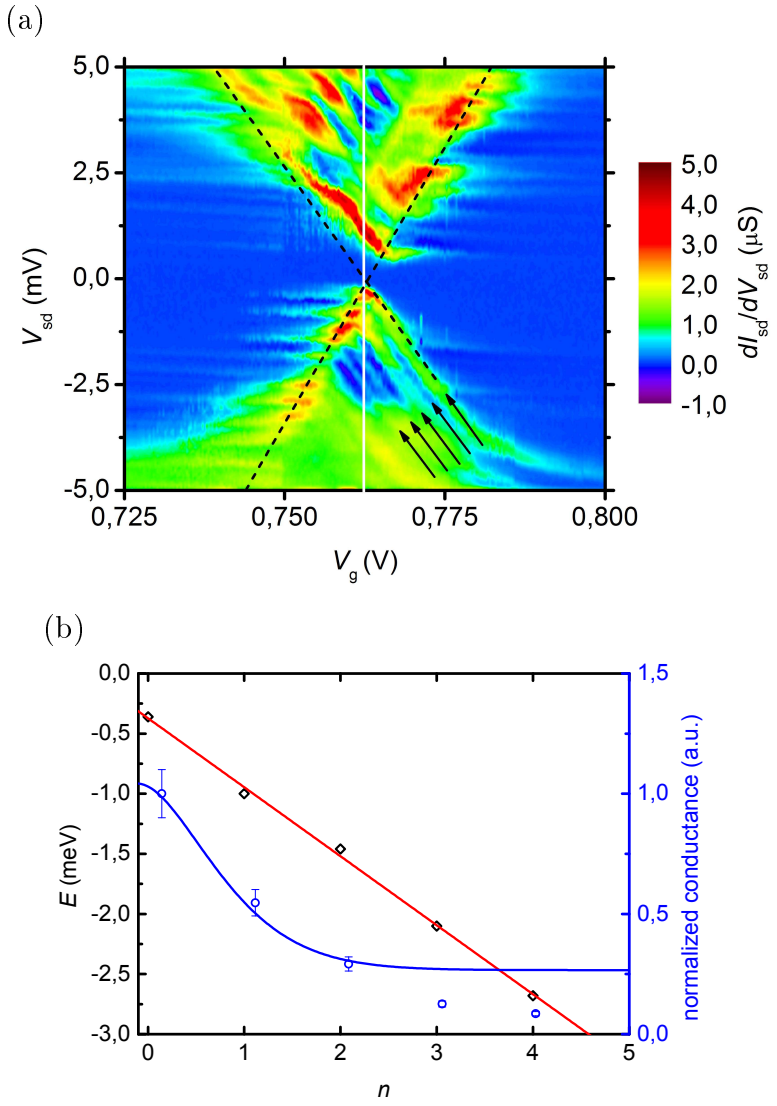

Figure 3.21: Quantized longitudinal stretching mode phonons in carbon nanotube NEMS at $T = 20$ mK ($L_{\mathrm{CNT}} = 250$ nm, $d_{\mathrm{CNT}} = 2$ nm). (a) Stability diagram of the CNT showing the differential conductance as a function of gate and bias voltages at 20 mK. The black arrows indicate the excited vibrational states attributed to a LSM, as described above. The dashed lines delimit the Coulomb diamond. (b) Energy of excited vibrational states (black squares) and normalized currrent intensity (blue dots) vs. the excitation line number n at $V_g = 0.762$ V (white line in (b)). A linear fit suggests a LSM phonon energy of $\Delta E_{\mathrm{vib}} = 575$ μeV, in agreement with the carbon nanotube length of $L_{\mathrm{CNT}} = 250$ nm. From the normalized current intensity (blue dots) of the excited vibrational states we can estimate the LSM electron-phonon coupling factor to $g = 0.35 \pm 0.075$.

$$\Delta E_{\mathrm{vib}} = \frac{nh\sqrt{E/\rho_m}}{L} \sim \frac{110\mu\mathrm{eV}}{L\,(\mu m)} \tag{3.31}$$

where $E = 1$ TPa is the Young's modulus, $\rho_m = 1.3$ g/cm^3 the mass density, L the nanotube length and n the vibrational quantum number [68, 69]. In Fig. 3.21(a) and (b), we observe a longitudinal stretching mode phonon with an energy of $\Delta E_{\mathrm{vib}} = \hbar\omega_{\mathrm{ph}} = 575$ μeV, which corresponds to a nanotube length of $L \approx 250$ nm. As expected for a quantized longitudinal phonon mode in the carbon nanotube resonator, the phonon energy is much larger than the temperature $T = 20$mK $\approx 1\mu$eV and the thermal occupation $\bar{n} = k_{\mathrm{B}}T/\hbar\omega_{\mathrm{ph}} \approx 0.002$ smaller than 1. The resonator mode should therefore be in its quantum mechanical ground state most of the time [1].

We can estimate the magnitude of the electron-phonon coupling from the normalized conductance intensity of the excited vibrational states in the SET region [67]. For equilibrium phonons, the normalized conductance follows a Poisson distribution and is given by

$$\left(\frac{dI_{\mathrm{sd}}}{dV_{\mathrm{sd}}}\right)_n^{\mathrm{norm}} \sim \frac{e^{-g}g^n}{n!} \tag{3.32}$$

where n is the mode number and g the electron-phonon coupling. In Fig. 3.21b, fitting the normalized intensity with equation 3.32 yields a coupling factor of $g = 0.35 \pm 0.075$. Using equation 3.30 we find a carbon nanotube diameter of $d_{\mathrm{CNT}} = 2$ nm, which is in agreement with the diameter distribution ($d_{\mathrm{CNT}} = 1.6 \pm 0.6$ nm) of carbon nanotubes grown from Fe/Mo catalyst and a methane feedstock (see Section 4.3.2).

Finally one can deduce a lower boundary for the quality factor Q of LSM phonons [79]. The quality factor is given by $Q = \omega/(2\pi\gamma)$, where γ is the relaxation rate into the ground state. In order for the vibrational states to be visible in a SET, we should have $\Gamma_{\mathrm{out}} > \gamma$. The tunnel current at the edge of the Coulomb diamond I gives an approximation of the tunneling rate $\Gamma_{\mathrm{out}} = I/e$. The quality factor therefore yields

$$Q > \frac{\omega_{\mathrm{ph}}}{2\pi\Gamma_{out}} \tag{3.33}$$

In Fig. 3.21, the tunnel current at the diamond edge holds $I = 66$ pA and a tunneling rate $\Gamma_{\mathrm{out}} \approx 410$ MHz. The quality factor thus yields $Q \approx 340$.

3.3.2 Strong coupling $g \gg 1$: Franck-Condon blockade

For strong electron-phonon coupling $g \gg 1$, the shift of the vibron potential is large, which supresses ground-state-to-ground-state transitions but strongly enhances transitions into higher excited vibrational states [67] (Fig. 3.22a).

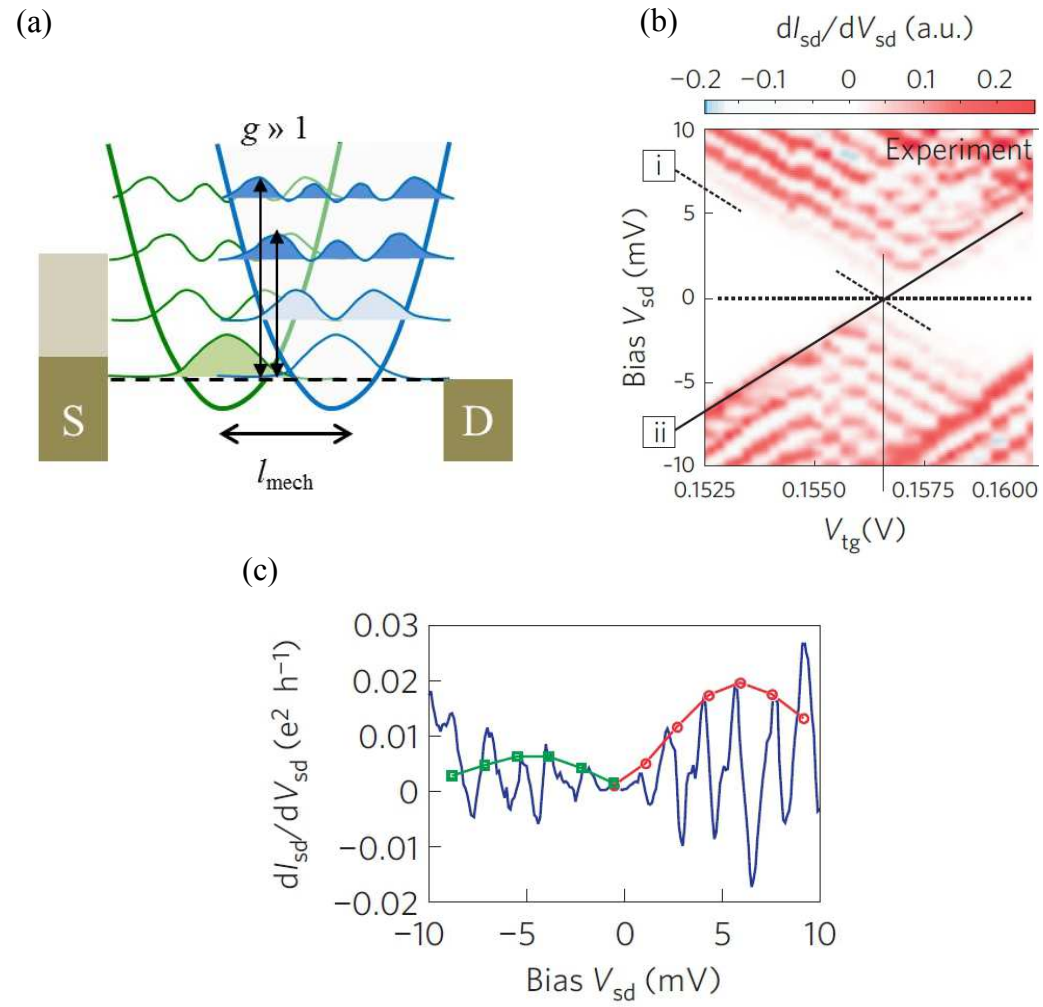

Figure 3.22: Franck-Condon blockade for strong electron-phonon coupling in carbon nanotube NEMS. (a) For $g \gg 1$, the shift of the vibron potential is such that transitions into higher excited states are strongly enhanced, whereas ground state transitions are forbidden. The green (blue) curve corresponds to N ($N+1$) electrons on the dot. The transitions are depicted by the black arrows and a high (low) transition probability corresponds to the dark blue (light blue) area under the wavefunction traces. (b) Stability diagram for a suspended carbon nanotube NEMS at 1.3 K showing the current suppresion at low bias (dotted line labeled i) and enhanced current in the high bias regime. Figure from [67]. (c) Differential conductance as function of bias voltage at $V_{tg} = 0.1570$ V (solid vertical line in (b)). From the maxima of the conductance peaks (red circles, green squares), one can extract an electron-phonon coupling $g = 4.5$ (positive bias) and $g = 3$ (negative bias) using equation 3.32. Figure from [67]

The effect known as Franck-Condon blockade, results in a current suppresion at low bias (dotted line (i) in Fig. 3.22b). In the same time, the tunneling current through higher excited vibrational states is strongly enhanced in the high bias regime [67] (Fig. 3.22b and c). From Fig. 3.22c, the magnitude of the electron-phonon coupling can be estimated with equation 3.32 to $g = 3$ and $g = 4.5$ for negative and positive bias, respectively.

3.4 Outlook

In this chapter, we described the fingerprint like characteristics of *transverse bending modes* (Section 3.2) and *longitudinal stretching modes* (Section 3.3) in a carbon nanotube NEMS.

In the following chapter 4, we will describe the ultraclean bottom-up nanofabrication process of such a carbon nanotube NEMS as well as the experimental setup used to probe the nanotube's mechanical motion at cryogenic temperatures.

In Chapter 5 we present a systematic study of the *transverse bending mode vibration* in a carbon nanotube NEMS. We demonstrate that the response and dissipation of a carbon nanotube's bending mode vibration to single-electron tunneling through the carbon nanotube NEMS-quantum dot critically depends on the dot's electronic environment, i.e. the capacitance, the tunnel coupling to the metal leads, the current and temperature. The findings suggest that one could achieve quality factors of 10^6 or higher by choosing appropriate gate dielectrics and/or by improving the tunnel coupling to the leads. Owing to these large and highly tunable quality factors, a carbon nanotube NEMS therefore represents an ideal plateform for magnetic torque detection, with a maximum sensitivity of $1\mu_B$ as described in section 2.3 [19].

In Chapter 6 on the other hand, we present the strong interaction of a *quantized longitudinal streching mode vibration* with a single molecule magnet, which allows for instance the detection of a single nuclear spin. The magnitude of the observed interaction suggests the possiblity of quantum entanglement between a single nuclear spin (or electronic spin) and single phonon mode. Moreover the coupling indicates that a carbon nanotube NEMS functionalized with single molecule magnets can be the first experimental realization of a supramolecular torque magnetometer with single molecule sensitivity [20].

Chapter 4

Nanofabrication and characterisation of carbon nanotube based NEMS and molecular spintronic devices

---

In this section we will present the complete nanofabrication and characterization process of a high-Q carbon nanotube NEMS. It was recently demonstrated, that such high-Q carbon nanotube NEMS can be obtained from a bottom-up fabrication process, where carbon nanotubes are grown on a 'back-bone' metal junction by chemical vapor deposition (CVD) in the very last step of the fabrication process, thus avoiding contamination of the carbon nanotube by residual resist, solvents or chemical etching procedures [80, 81, 1, 61, 65].

Such a process needs to be performed in a clean environment, in our case the CNRS clean room facility 'Nanofab' in Grenoble. Moreover, the 'back-bone' structure has to withstand the extreme temperatures of 800° reached during a CVD growth, which typically requires the use of materials such as platinum or tungsten. Finally, one needs to have a good control on CVD growth conditions, in order to obtain a reproducible process and a good yield of working carbon nanotube resonators. In the following we will describe an ultraclean, bottom-up fabrication process for carbon nanotube NEMS with quality factors as high as 10^5 and a yield of working devices around 5%.

The fabrication starts from a degeneratly p-doped silicon 2" wafer covered by a layer of dry chlorinated thermal SiO_2, serving as gate dielectric (Section 4.1). Using state of the art lithography techniques, we pattern the back-bone junction for the carbon nanotube NEMS with a standard Si backgate (Section 4.2.2) or a high efficiency local gate (Section 4.2.3). After extensive cleaning of this back-bone structure in an oxygen plasma, carbon nanotubes are grown by CVD at 800°C from a CH_4 carbon feedstock and iron based catalyst island patterned on the source-drain electrodes next to the junction (Section 4.3). Using the real-time data acquisition system ADWIN (Section 4.4), the devices are then characterized by electric transport measurements at room temperature, in order to select the best devices prior to a cooldown to cryogenic temperatures (Section 4.5). Finally, real-time measurements *via* ADWIN of the nanotube's nanomechanical motion are carried out in a $^3He/^4He$ dilution refrigerator at a base temperature of 30 mK. The NEMS actuation and detection scheme used in our experiment is similar to the one used by Steele and co-workers [61, 75]. As the induced mechanical motion changes the charge

flow through the CNT quantum dot and vice versa, we can detect the CNT resonance through a change in zero bias conductance (Section 4.6).

Ultimately, a high-Q carbon nanotube NEMS ought to be a suitable building block for molecular spintronic devices. In the last section 4.7 of this chapter, we will describe the solution based grafting of $TbPc_2$ single molecule magnets on a carbon nanotube NEMS. The presented method conserves both the mechanical properties of the resonator and the magnetic properties of the $TbPc_2$ and is therefore a crucial step towards the development of a carbon nanotube based molecular spintronic device.

4.1 Substrate selection

The starting point for a carbon nanotube NEMS is a silicon wafer covered by a layer of silicon dioxide (SiO_2). The silicon (Si) crystal wafer is grown in a so called Czochralski process, which allows heavy doping by phosporus (n-doping) or boron atoms (p-doping) of the silicon [82]. As a consequence the Si becomes conductive down to very low temperatures and can be used as a backgate electrode for our carbon nanotube NEMS. The SiO_2 serves as gate dielectric and is obtained by thermal oxidation of the Si wafer in a pure oxygen atmosphere (dry oxidation) or under water vapor/steam (wet oxidation) as described below.

During a "wet oxidation" process, the Si wafer is heated between 600°C and 1200°C using water vapor or pyrogenic steam as an oxidation agent. SiO_2 will then form according to the following equation [82]:

$$Si + H_2O \rightarrow SiO_2 + 2H_2 \tag{4.1}$$

Due to the fast kinetics of this reaction, one can grow SiO_2 layers up to a thickness of 15 μm [83]. However, this process leaves a high density of dangling bonds at the Si/SiO_2 interface due to the lattice mismatch between Si and SiO_2. These structural defects are likely to act as charge trap states and cause leakage currents in a carbon nanotube NEMS patterned on such a substrate. Moreover, these dangling bonds induce mechanical stress in the SiO_2 layer [84, 85]. Upon heating the substrate up to 900°C during the CVD growth, this mechanical stress is realeased into its surroundings, causing extensive damage to the carbon nanotube NEMS (hillock and hole formation on the Pt electrodes as depicted Fig. 4.1a). Such damage can be avoided by using dry oxidized Si/SiO_2 substrates with a much smaller defect density (Fig. 4.1b) and/or by covering the SiO_2 with a "buffer" layer of aluminum oxide Al_2O_3 grown by atomic layer deposition (Fig. 4.1c).

In a "dry oxidation" process, the Si wafer is oxidized between 950°C and 1150°C in pure oxygen atmosphere. SiO_2 will then form according to the following equation [82]:

$$Si + O_2 \rightarrow SiO_2 \tag{4.2}$$

By adding a chlorine source (anhydrous HCl or (1,2) trans-dichloroethylene) during the oxide growth, one can remove any kind of metal impurity in the oxide [82, 83]. After the oxidation, the wafer is annealed in a so called forming gas (H_2/N_2) in order to passivate the dangling bonds at the Si/SiO_2 interface [82, 83]. As a consequence, the density of electronic trap states as well as the mechanical stress and the resulting damage to the CNT NEMS are considerably reduced compared to wet thermal SiO_2 layers (Fig. 4.1b). Due to the very slow kinetics of reaction 4.2 however, the thickness of a dry chlorinated SiO_2 layer does not exceed 500 nm.

In order to obtain high-Q carbon nanotube NEMS, it is therefore essential and strongly recommended to use doped Si wafers covered with a layer of dry chlorinated SiO_2. Such wafers were purchased from NOVA Electronic Materials [86] and characteristics summarized in Table 4.1.

Si (100)	
diameter	2"
doping	p-type Bo
resistivity	0.001-0.005 Ω·cm
thickness	275-325 μm
process	Czochralski
SiO_2	
thickness	$285 \pm 15nm$
process	dry chlorinated oxidation + forming gas annealing

Table 4.1: Characteristics of Si/SiO_2 wafers purchased from NOVA Electronic Materials.

4.2 Nanofabrication of the 'back-bone' junction for a carbon nanotube NEMS

In the following section, we will describe the fabrication of different 'back-bone' metal junctions for the carbon nanotube NEMS. First, we will briefly recall the principles of optical contact lithography (Section 4.2.1) and describe the fabrication process for a back-bone junction with a Si backgate as depicted in Fig.4.1b (Section 4.2.2). However the efficiency of a Si backgate is limited by the distance between the carbon nanotube and the backgate $t = 500$ nm and by the dielectric constant $\varepsilon = 3.7-3.9$ of the SiO_2 [81]. In order to improve the gate efficiency for a carbon nanotube NEMS, one has to replace the SiO_2 by a high-κ dielectric and reduce the distance between the CNT and the gate. This can be achieved by patterning an additional metal gate covered by Al_2O_3 ($\varepsilon = 7-8$) directly into the gap of the back-bone junction as in Fig. 4.1c (Section 4.2.3). We will show

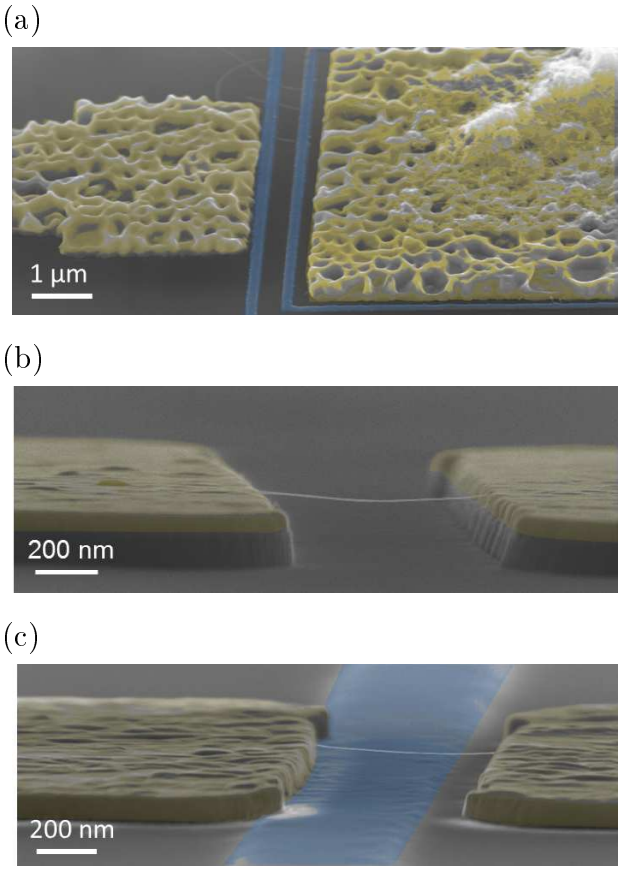

Figure 4.1: Impact of substrate quality on carbon nanotube NEMS: False color SEM image (side view) of a CNT NEMS on a (a) wet thermal SiO_2 layer ; (b) dry chlorinated thermal SiO_2 layer; (c) dry chlorinated thermal SiO_2 layer covered by an alumina "buffer" layer obtained by atomic layer deposition. Mechanical stress in wet oxide layers (a) is released during the CVD growth at 900°C, causing hole and hillock formation in Pt electrodes (yellow) of the CNT NEMS. Due to the extensive damage to the electrodes, the CNT are not suspended. This effect can be avoided by using (b) dry oxide layers with a much smaller defect density and/or (c) by covering the SiO_2 with a "'buffer"' layer of alumina grown by atomic layer deposition. The blue electrodes correspond to local metallic gates (see Section 4.2).

in Chapter 5, that the total capacitance and ultimately the Q-factor of such a carbon nanotube NEMS increase by an order of magnitude, due to the higher efficiency of the Al_2O_3 covered localgate.

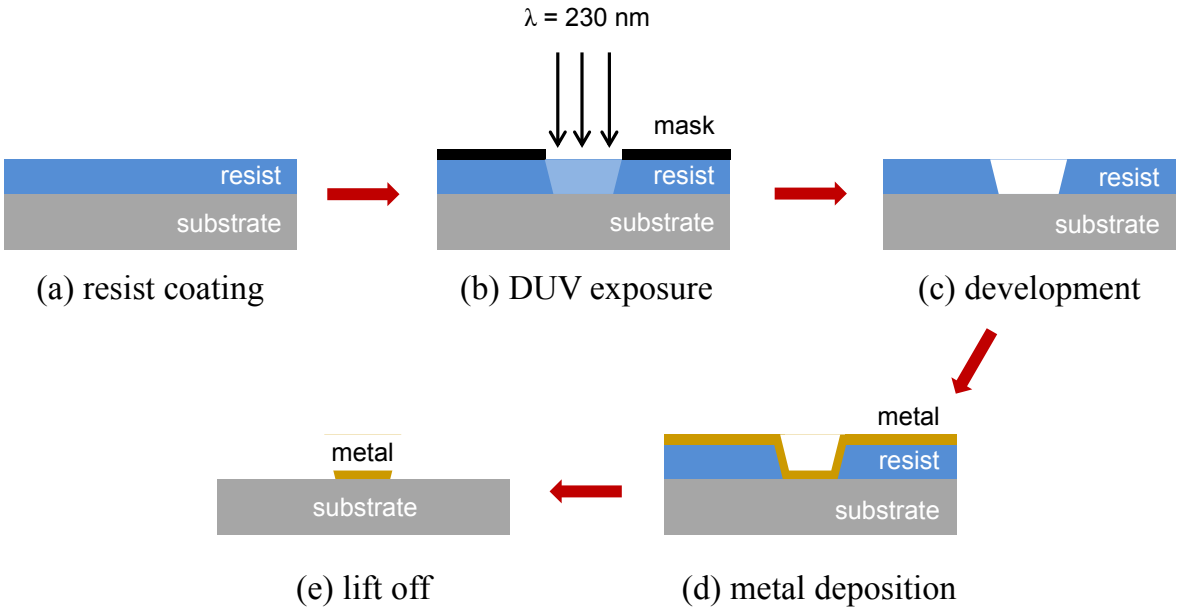

Figure 4.2: Principal of optical contact lithography: (a) Spin coating of photosensitive resist. (b) Contacting with optical mask and exposure to UV radiation $\lambda = 230$ nm. A good contact is essential, as the resolution of the process is proportional to the gap size between the mask and the coated substrate (see text). (c) Removal of exposed resist regions in a developper solution. (d) Metal coating and (e) lift off.

4.2.1 Optical contact lithography

The concept of optical contact lithography (Fig. 4.2) shares some fundamental principles with photography [87]. A layer of positive, organic photoresist is deposited on a substrate and brought in close mechanical contact with an optical mask yielding the negative of desired pattern (Fig. 4.2a). The photoresist is then exposed through the optical mask with UV radiation ($\lambda = 230$ nm). The UV radiation causes a breakdown of the chemical bonds in the exposed parts of the photoresist (light blue, Fig. 4.2b). The exposed regions can then be removed by an appropriate developper leaving the desired pattern "imprinted" into the photoresist (Fig. 4.2c). A layer of metal is then deposited onto the "imprinted" photoresist (Fig. 4.2d). By dissolving the rest of the photoresist, the excess metal is *lifted off* and leaving only the desired pattern on the substrate (Fig. 4.2e).

The imprinted feature size is limited by diffraction, thus by the wavelength λ of the incident radiation, and by the gap size g between the photoresist and the optical mask. The maximal resolution is given in good approximation by $d = (\lambda g)^{1/2}$ [88]. The short radiation wavelength and a good mechanical contact between the photoresist and the mask, i.e. a small gap size g, are therefore crucial for a high resolution optical lithography.

4.2.2 Junctions with a Si backgate

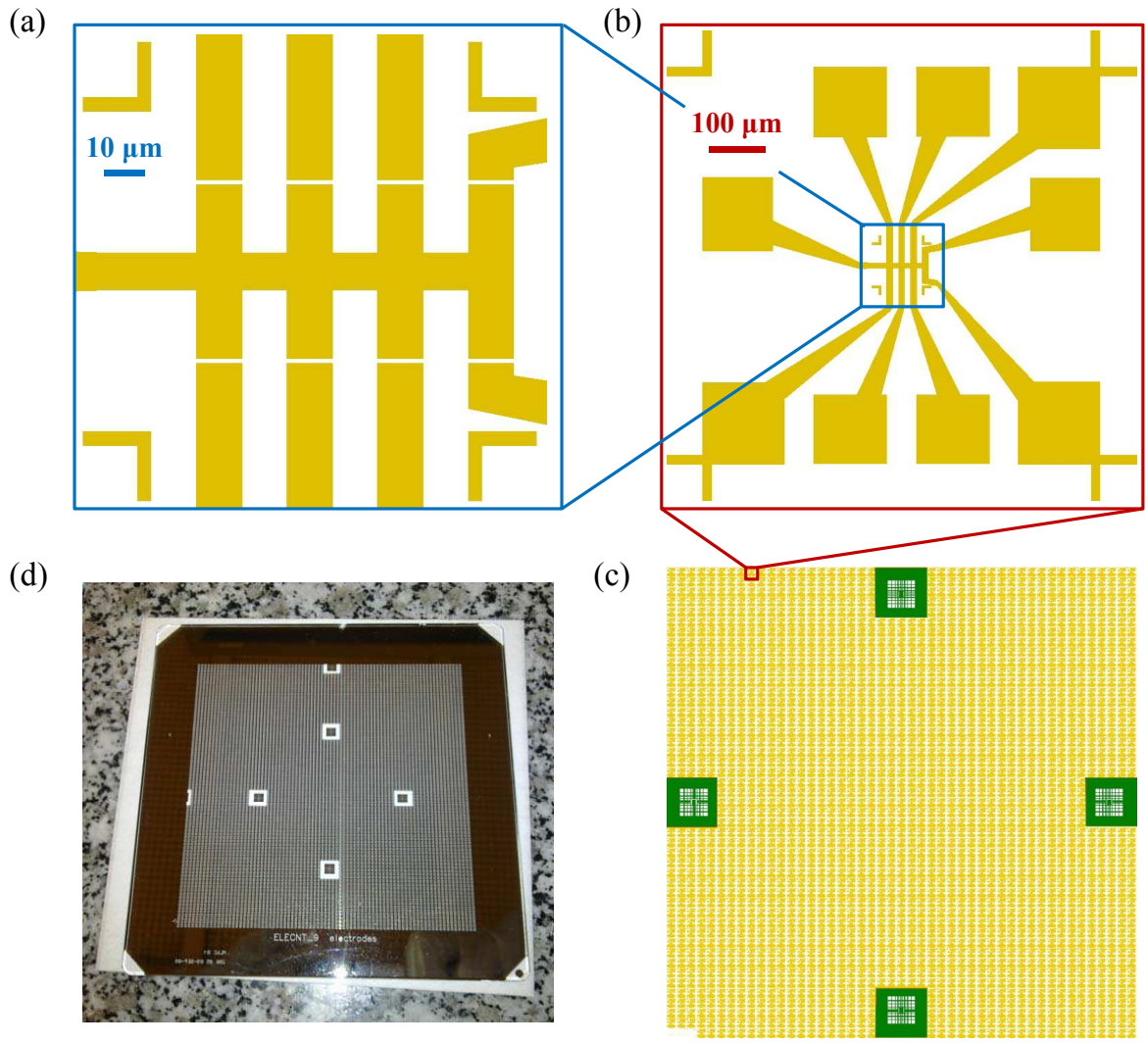

Figure 4.3: Pattern for backbone junction with a Si backgate: (a) 50x50 μm^2 central writefield, displaying 8 electrode pairs with a gap of 1 μm each. (b) 0.5x0.5 mm^2 writefield, displaying the junction array with the bonding pads designed for electrical connection. (c) 2"x2" matrix of junction arrays with 4 markers (green) designed for the alignement of additional layers in subsequent lithography steps. (d) Mask for optical UV lithography: The pattern is etched into a chromium layer covering a 3"x3" quartz substrate. The quartz is transparent at short UV wavelength.

The pattern for the NEMS back-bone junction was designed by Jean-Pierre Cleuziou at Neel Institute and is depicted in Fig. 4.3. It consists of 8 electrode pairs, each with

a gap of 1 μm (Fig. 4.3a). The electrodes are connected to 100x100 μm^2 pads designed for electrical connection (Fig. 4.3b). This junction array is reproduced and arranged in a matrix, including 4 alignement markers (green) for following lithography steps (Fig. 4.3c). This matrix is then patterned and etched into a chromium layer covering a 3"x3" quartz substrate in order to obtain the optical mask depicted in Fig. 4.3d.

As described in the previous section, we will use a 2" Si wafer (p-doped) covered with 285 nm of dry chlorinated SiO_2 (Section 4.1). After a cleaning step in an oxygen plasma, the wafer is coated with two layers of photoresist LOR3A (bottom layer) and UV3 (top layer). The coated substrate is then exposed to UV radiation ($\lambda = 230$ nm) through the optical mask in a Suess MJB3 mask aligner. After a post exposure bake, the exposed regions of the resist are removed in a developper solution (MF 26A). The developer is then neutralized in distilled water. It should be noted that without the post exposure bake, the development would be impossible or only occur at strongly reduced rate.

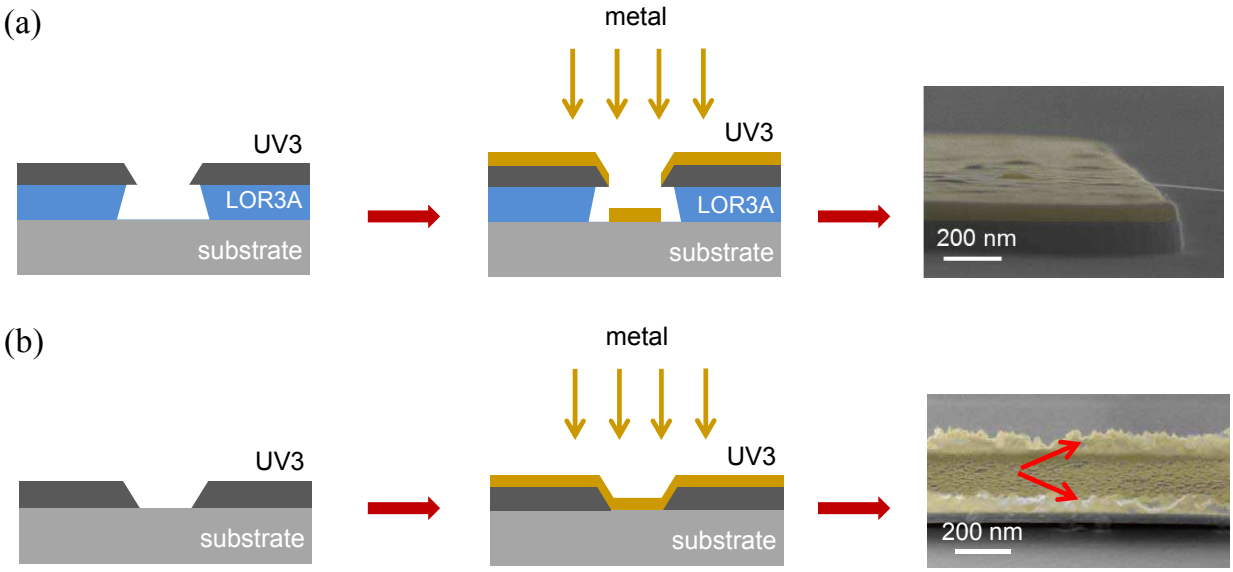

Figure 4.4: (a) Bilayer resist vs. (b) monolayer resist: The undercut formed during the development in the bilayer resist and the directional deposition via electron beam evaporation prevents the metal deposition on the sidewalls of the resist and thus the formation of fence-like structures after lift off, which usually occurs with monolayer resist (red arrows in (b)).

Metal is then deposited *via* electron beam evaporation followed by a lift off in hot acetone and the LOR3A removal with PG remover. It should be noted, that the bottom LOR3A layer is more reactive to the developper and thus an undercut forms in the bilayer resist during the development. This undercut and the directional deposition by

electron beam evaporation prevents the metal deposition on the sidewalls of the resist and thus the formation of fence-like structures on the deposited junction after lift off (Fig. 4.4a), which typically occurs with monolayer resist (Fig. 4.4b). Such fences would be detrimental to successfull growth of carbon nanotubes. Also, among the available metals for evaporation, only platinum can withstand the extreme conditions of a CVD growth and provides a good electrical contact with a carbon nanotube. However, platinum has a poor adhesion to SiO_2 and it is therefore required to deposit a thin "adhesion" layer prior to/for the platinum. This adhesion layer should also consist of materials with extremely high melting points, such as molybdenum or tungsten.

Finally, we etch 150 nm of SiO_2 in a CHF_3 plasma (8 min at 50W in 15cc CHF_3) in order to ensure the suspension of the carbon nanotube after CVD growth. The detailed process is summarized in Table 4.2. A top view photography of a junction array is represented in Fig. 4.5 and a side view of a single junction (after CVD) recorded *via* SEM is depicted in Fig. 4.1b. We can achieve a maximal resolution of approximately 500 nm. This process was developped at the Nanofab clean room facility at Institut Neel with the help of Bruno Fernandez.

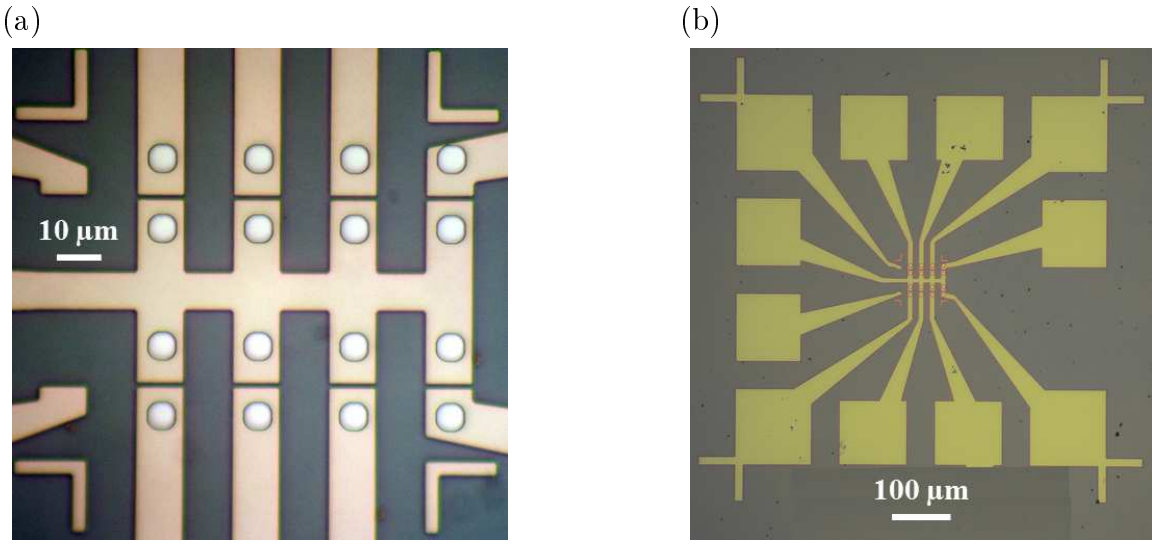

Figure 4.5: Photography of the backbone junction array for carbon nanotube NEMS displaying (a) eight electrode pairs with a gap of 1 μm each and (b) linked with bonding pads designed for electrical connection.

As mentionned earlier, the efficiency of the Si backgate will be limited by the CNT-gate distance, which we estimate to 500 nm (300 nm of SiO_2 and 200 nm of electrode thickness), and by the dielectric constant of the SiO_2 ($\varepsilon = 3.7 - 3.9$) [81]. The efficiency

Step	description	equipement	parameters, comments
0	cleaning	O_2 plasma, RIE	10 min at 50W, 20 cc O_2
1	coating of LOR3A resist	spin coater	2000 rpm, 2000rpm/s for 30s thickness 450 nm
2	LOR3A softbake	hotplate	60s at 170°C
3	coating of UV3 resist	spin coater	4000 rpm, 2000rpm/s for 30s thickness 450 nm
4	UV3 softbake	hotplate	60s at 130°C
5	UV exposure	MJB3 mask aligner	$\lambda = 230$ nm 5.3s at 30 mW/cm^2
6	post exposure bake	hotplate	60s at 130°C
7	development	MF 26A	45s-60s until alignement marks are clear of resist
8	developper neutralization	DI water	60s
9	removing residual resist	O_2 plasma, RIE	40s at 50W, 20 cc O_2
10	metal depostion	ebeam evaporator PLASSYS	20 nm Mo or W (adhesion layer) 160 nm Pt
11	metal lift off	acetone	5 min at 45°C until excess metal is removed
12	LOR3A removal	PG remover	75°C for a few hours

Table 4.2: Fabrication process for carbon nanotube NEMS backbone junction with a Si backgate *via* optical lithography.

can be enhanced by reducing the CNT-gate distance and by replacing SiO_2 with a high-κ dielectric such as Al_2O_3 ($\varepsilon = 7 - 8$). As described in the next section, one could for example pattern a local metallic gate covered by a high-κ dielectric into the gap of the here described backbone junction. We will demonstrate in Chapter 5, that the enhanced gate efficiency in such a device results in a 10-fold increase of the carbon nanotube NEMS' total capacitance (Section 5.1.3) and consequently in an enhanced quality factor Q (Section 5.3).

4.2.3 Junctions with a high efficiency local gate

In the following section, we will describe how to pattern a high efficiency, metallic "local" gate into the gap of the backbone junction described in the previous section using optical contact lithography.

First lithography: Metallic localgate

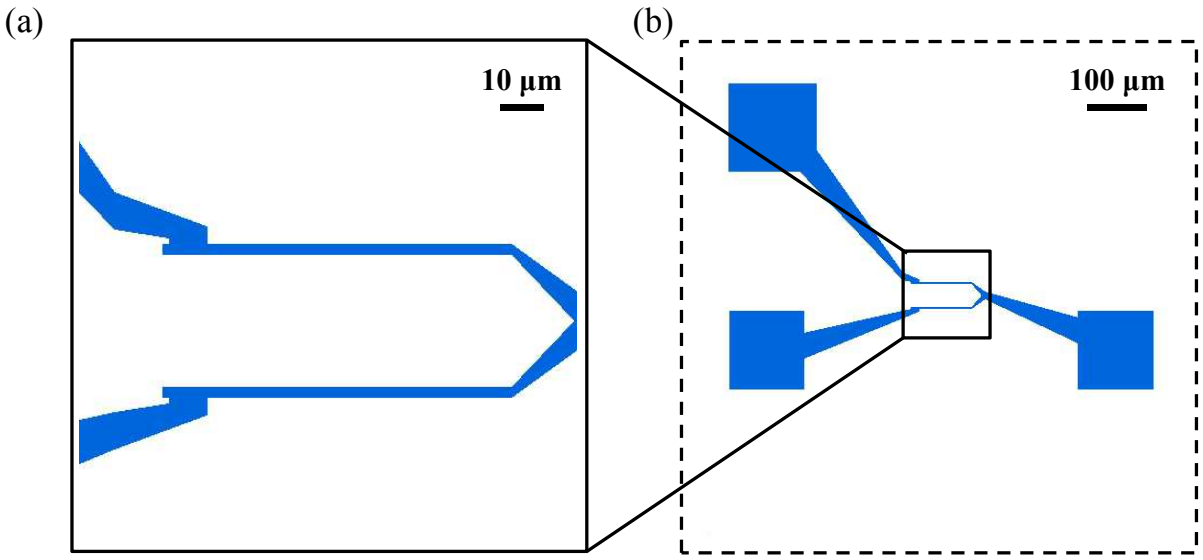

Figure 4.6: Pattern of a localgate for the backbone junction of a CNT NEMS: (a) 50x50 μm^2 central writefield, displaying two gate electrodes with a width of 2 μm each. (b) 0.5x0.5 mm^2 writefield including the central writefield and connection pads designed for microbonding.

For pratical reasons, we first pattern a 2"x2" matrix of the local gate design depicted in Fig. 4.6 together with four alignement marks (blue marks in Fig. 4.8c) onto a 2" Si/SiO_2 wafer using the same lithography process as in Table. 4.2. In order to withstand the extreme temperatures during the CVD growth, the local gates are made from molybdenum with a thickness of 30 nm. The fabrication of the corresponding optical mask is identical to the one described in Section 4.2.2.

After a cleaning step in an oxygen plasma, the complete wafer is covered with a high-κ gate dielectric *via* atomic layer deposition (ALD) as described below.

Atomic layer depostion of high-κ dielectric

Atomic layer deposition allows the conformal deposition of dielectric thin films on a substrate with atomic layer control using the sequential, self-limiting surface reactions of two precursor materials [89]. The conformal and self-limiting nature of the deposition results in dielectric layers with almost no defects and therefore with a higher dielectric constant compared to other deposition techniques (see also Table.4.3 for the case of Al_2O_3).

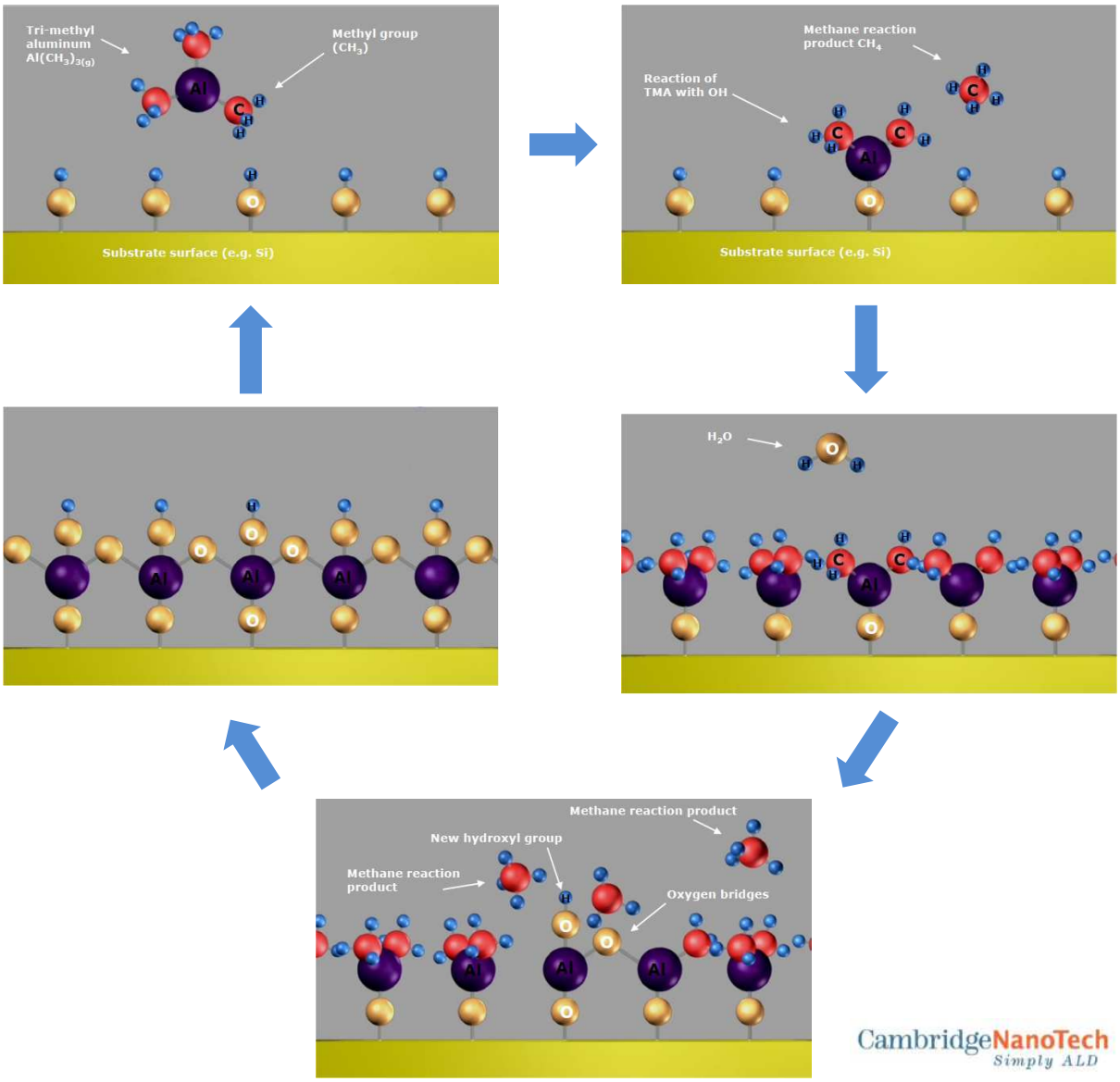

Figure 4.7: Atomic layer deposition cycle of aluminium oxide gate dielectric: The TMA precursor is pulsed into the chamber and reacts with the hydroxyl groups at the surface until the latter is passivated with single atomic layer. Then water vapor is pulsed into the reactor, reacting with the dangling methyl groups and forming aluminium-oxygen bridges as well as new surface hydroxyl groups. After the full passivation of the surface, one obtains a atomic monolayer of Al_2O_3 with a thickness of 1.08 Å. The images are courtesy of Cambridge Nanotech [90].

We used a *Savannah* ALD reactor (Cambridge Nanotech) [90] in order to deposit a

layer of aluminium oxide Al_2O_3 on the first lithography layer. In a process developped by Cambridge Nanotech and Laurent Cagnon at Neel Institute, the wafer is placed in the reactor chamber and heated to 200°C (see Fig. 4.7). First, the precursor Trimethyl Alumimum $Al(CH_3)_{3(g)}$ (TMA) is pulsed (τ_{TMA} = 15 ms) in its gaseous form into the chamber. The TMA reacts with the hydroxyl groups (OH) at the surface of the wafer, forming methane as reaction product. As the TMA cannot react with itself, this reaction will be terminated once the surface is passivated with a single atomic layer of TMA. Next, water vapor is pulsed (τ_{H2O} = 15 ms) into the reaction chamber. The water reacts with the dangling methyl groups (CH_3) forming surface hydroxyl groups and aluminium-oxygen bridges until the reaction is again terminated after a full surface passivation. We obtain a monolayer of aluminium oxide Al_2O_3 with a thickness of 1.08 Å [90].

The cycle was then repeated 1000 times in order to obtain a layer thickness of approximately 108 nm. The dielectric constant of such an ALD grown alumina layer is approximately $\varepsilon = 7 - 8$ and therefore higher than in layers obtained from other deposition techniques (Table 4.3).

Deposition technique	Depostion temperature (°C)	Dielectric constant	References
ALD	30-200	7-8	[89]
Sputtered	not given	~ 5.1	[91]
Anodized	20	~ 4.2	[91]

Table 4.3: Comparison of different deposition processes for aluminium oxide Al_2O_3.

In order to further increase the dielectric constant and the gate efficiency, one could turn to other dielectric materials such as hafnium oxide (HfO_2, $\varepsilon = 15 - 20$). Unlike aluminium oxide however, hafnium oxide crystalizes during the CVD growth, therefore loosing its dielectric properties.

Second lithography: Source-drain junctions

Finally, we align 180 nm thick Mo/Pt source-drain junctions above the localgates in a second optical lithography step (Fig. 4.8a and 4.8b). The alignement can be performed with a MJB3 mask aligner using specifically designed alignement marks. As depicted in Fig. 4.8c, the alignement markers on the optical mask used for the 2^{nd} layer (source-drain junction layer, golden) have to be superimposed with the marks of the first layer (localgate layer, blue), already patterned on the wafer. At least three marks are necessary for an accurate alignement. The lithography recipe is completely identical to Table 4.2.

After CVD growth, we will finally obtain a CNT NEMS with a localgate covered by 110 nm of Al_2O_3 ($\varepsilon = 7 - 8$) and separated from the nanotube by 300 nm, thus yielding a much higher efficiency than a standard Si backgate described previously.

Figure 4.9 shows a top view photography of the final backbone structure. A side view SEM image of a single carbon nanotube NEMS after CVD is represented in Fig. 4.1c.

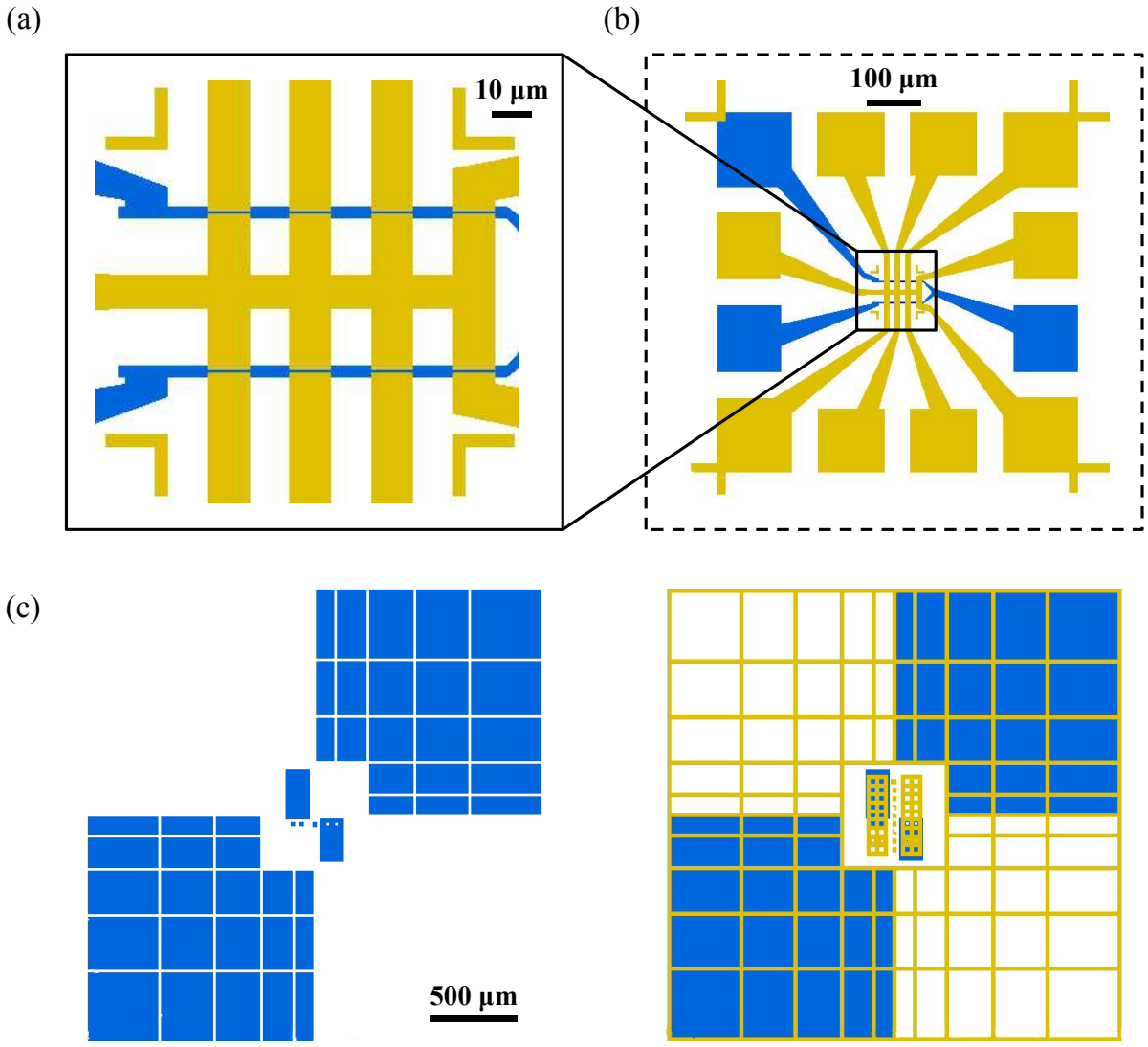

Figure 4.8: Pattern of the backbone junction with a high efficiency local gate: (a)+(b) The source-drain junctions (golden) are aligned above the localgate (blue) using specifically designed alignement marks (c).

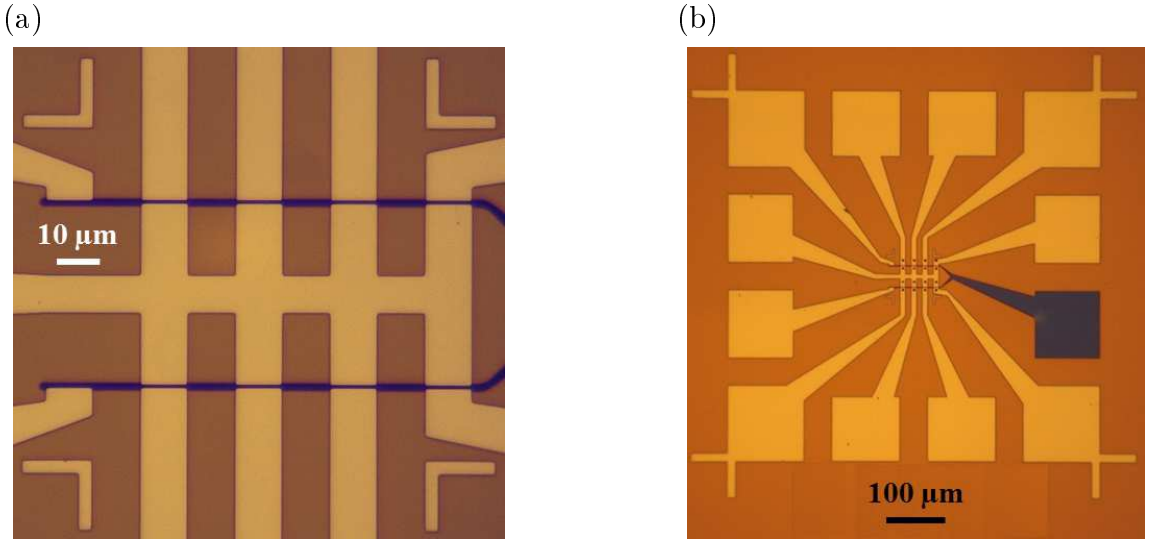

Figure 4.9: Photography of the backbone junction array for carbon nanotube NEMS displaying (a) eight electrode pairs with a gap of 1 μm each aligned over a localgate (blue) and (b) linked with bonding pads designed for electrical connection.

4.3 Ultraclean on-chip growth of carbon nanotube NEMS *via* chemical vapor deposition

In the last step of the nanofabrication process, the carbon nanotubes are grown by chemical vapor deposition (CVD) across the previously patterned backbone junctions ("On-chip ultraclean growth") [80, 81]. During a CVD growth, a carbon rich precursor gas is decomposed at very high temperature on the surface of catalyst particles, where the resulting carbon radicals can then reorganize to the more stable form a carbon nanotube. The obtained ultraclean carbon nanotube NEMS are free from fabrication-related contaminations and yield ultrahigh quality factors of 10^5 [1, 61, 65].

In the following section, we will described the ultraclean, on-chip growth of carbon nanotubes at 800°C from a methane feedstock and iron/molybdenum catalyst particles, which was developped at Neel Institute by Jean-Pierre Cleuziou and Viet Ngoc-Nguyen [92].

4.3.1 Catalyst deposition

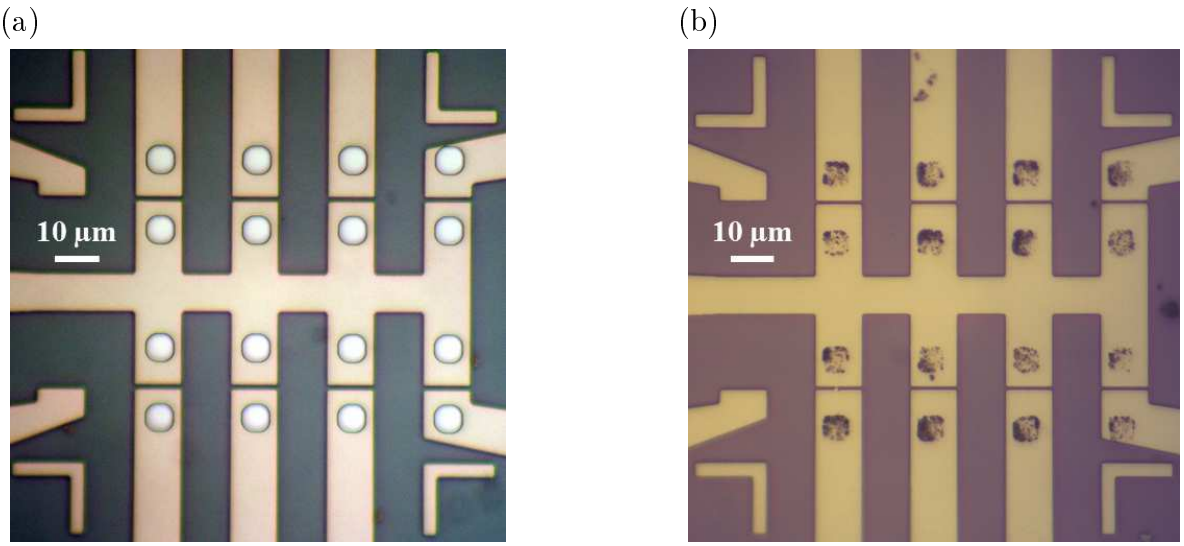

Figure 4.10: Photography of the backbone junction array for carbon nanotube NEMS (a) after lithography and (b) after catalyst deposition.

For this purpose, the wafer is coated again with a bilayer LOR3A/UV3 resist. In another optical lithography step (see Table 4.4), we then align and imprint 5μm x 5μm squares into the photoresist covering the electrodes, at 5 μm from the gap of the junction (Fig. 4.10a). After lithography, the wafer is cut into small chips, each one holding 4x4 junction arrays, i.e. 128 junctions.

The Fe/Mo catalyst particles (ratio 1:0.08 atomic percent) are precipitated in a porous alumina matrix and suspended in a methanol solution [92]. A drop from this suspension is subsequently spin-coated onto a chip, in order to fill the 5μm x 5μm square "holes" imprinted into the photoresist with catalyst particles. Depending on the desired concentration of catalyst, this process has to be repeated several times. After a liftoff, we then obtain square shaped catalyst islands in close proximity to the junction, as depicted in Fig. 4.10b. Finally, the chip is cleaned for 20 minutes in an oxygen plasma to remove all eventual organic residue prior to the CVD. This step is crucial, as any residual organic material will lead to the formation of amorphous carbon and thus to a contamination and degradation of the suspended carbon nanotubes.

Step	description	equipement	parameters, comments
0	cleaning	O_2 plasma, RIE	10 min at 50W, 20 cc O_2
1	coating of LOR3A resist	spin coater	1000 rpm, 1000 rpm/s for 30s thickness 600 nm
2	LOR3A softbake	hotplate	60s at 170°C
3	coating of UV3 resist	spin coater	4000 rpm, 2000rpm/s for 30s thickness 450 nm
4	UV3 softbake	hotplate	60s at 130°C
5	UV exposure	MJB3 mask aligner	$\lambda = 230$ nm 5.3s at 30 mW/cm^2
6	post exposure bake	hotplate	60s at 130°C
7	development	MF 26A	45s-60s until alignement marks are clear of resist
8	developper neutralization	DI water	60s
9	removing residual resist	O_2 plasma, RIE	40s at 50W, 20 cc O_2
10	catalyst deposition	spin coater	3000 rpm, 1000 rpm/s for 20s repeated 2 times (*low density*) repeated 4 times (*high density*)
11	post deposition bake	hotplate	60s at 120°C
12	Catalyst liftoff	PG remover	75°C for a few hours
13	Pre-CVD cleaning	O_2 plasma, RIE	20 min at 50W, 20 cc O_2
14	CVD growth	EasyTube 2000 CVD system	770°C-800°C, 1.2 L/min CH_4, 0.8 L/min H_2 12 min

Table 4.4: Catalyst deposition and ultraclean CVD growth of carbon nanotube NEMS

4.3.2 Growth condition

The chip with the deposited catalyst is then introduced into the reaction chamber of an EasyTube 2000 CVD system (Fig. 4.11) at 770°C to 800°C (so called "hotload" procedure). The carbon nanotubes are grown under a methane flux of 1.2 L/min and hydrogen flux of 0.8 L/min during 12 minutes. Methane serves as carbon feedstock whereas hydrogen prevents the formation of amorphous carbon on the sample. Those growth conditions were optimized by Viet Ngoc-Nguyen during his PhD thesis at Neel Institute and produce essentially single wall, large diameter ($d = 1.6 \pm 0.6$ nm) carbon nanotubes [92].

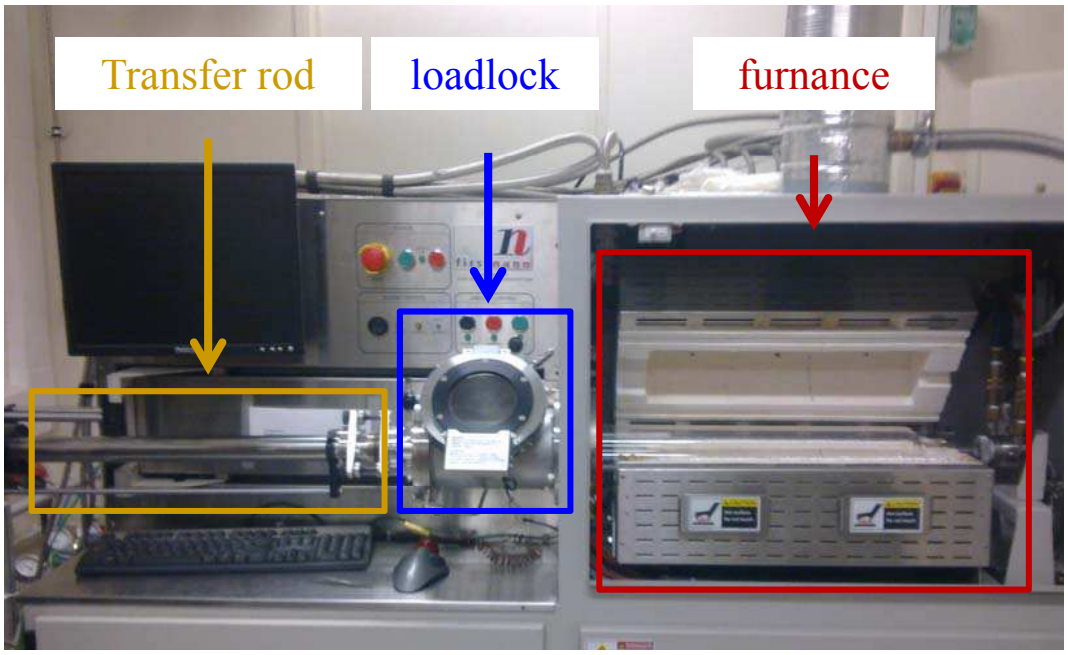

Figure 4.11: EasyTube 2000 CVD system: The sample is introduced into a loadlock (blue) and subsequently transfered into the CVD furnance (red) using a magnetic transfer system (golden).

The yield of single, suspended carbon nanotube devices η_1 on a chip will depend essentially on the density of the deposited catalyst. A low catalyst density leads almost exclusivly to single, suspended carbon nanotube devices, but with an extremely low yield of $\eta_{\mathrm{tot}} \sim \eta_1 \sim 1\%$ (Fig. 4.12a). On the other hand a very high catalyst density will increase the yield of single suspended tube devices (η_1 ~5%), but also the yield of multiple tube junctions (Fig. 4.12b) and the overall yield of suspended carbon nanotube devices η_{tot}. The remaining 1-η_{tot} junctions on a chip are either *not bridged* by a nanotube or connected with one or more *non-suspended* nanotube(s).

Moreover the yield of single carbon nanotube devices η_1 also depends on the growth

temperature. Below 770°C, the grown carbon nanotubes are too short to bridge the junction, which reduces the yield of working single tube devices almost to zero. On the other hand, increasing the temperature will results in longer carbon nanotubes and an increased yield of suspended single tube devices. However, aluminum oxide starts to crack due to mechanical stress that builts up in the surrounding metal gate and electrodes. We are therefore limited to a growth temperature window between 770°C and 800°C.

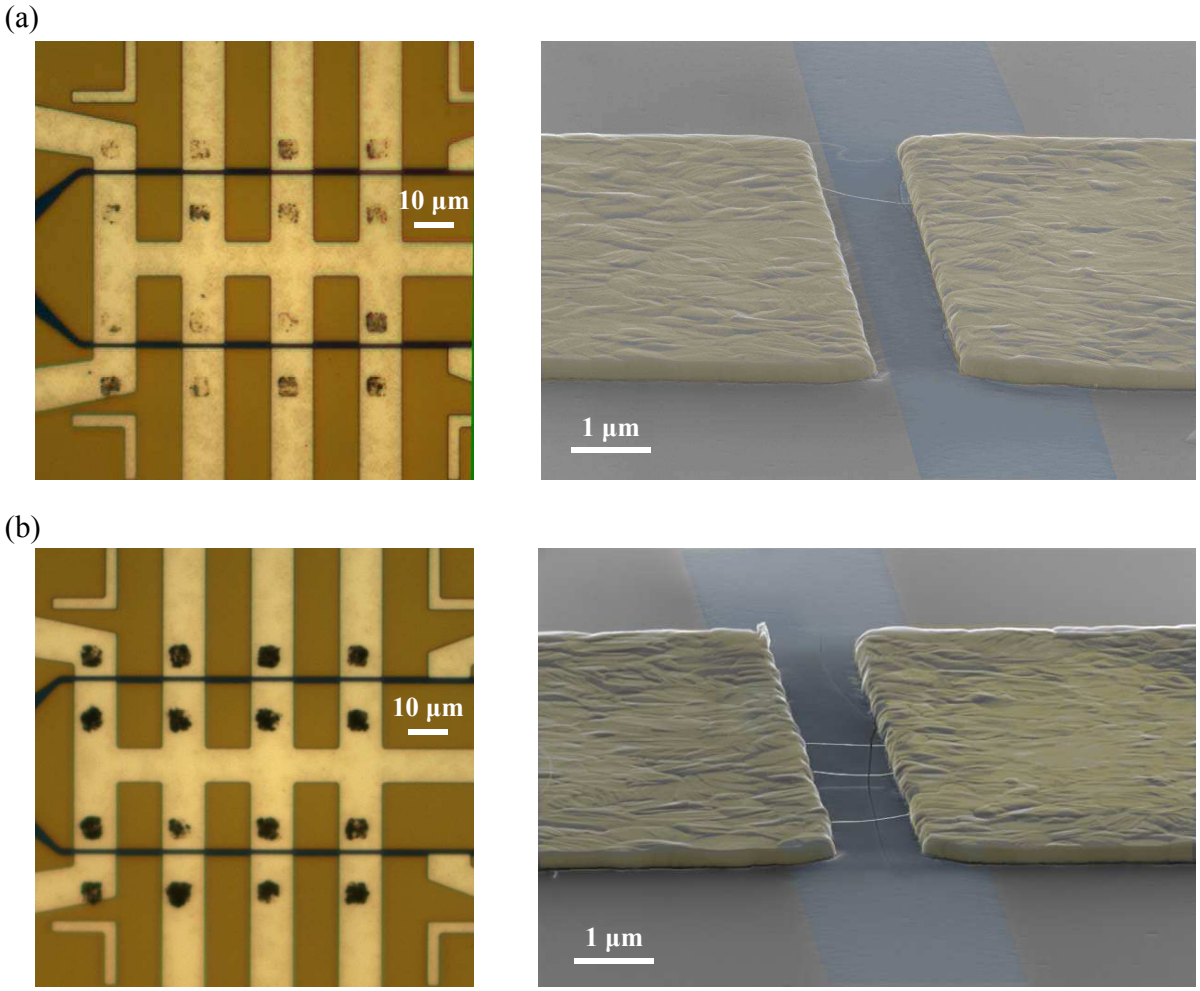

Figure 4.12: Impact of catalyst concentration: (a) Low catalyst density results almost exclusivly in single tube devices, but to a very low yield of $\eta_{\mathrm{tot}} \sim \eta_1 \sim 1\%$. (b) Higher catalyst density increases the yield for single tube devices $\eta_1 \sim 5\%$, but also results in multiple tube devices and a higher overall yield of η_{tot}. The images in the right column are false color SEM images with the localgate colored in blue and the source-drain junction in gold. The contrast was enhanced for better visibility of the carbon nanotubes.

The highest possible yield of single, suspended tube devices ($\eta_1 \sim 5\%$) was achieved

with a high catalyst density as in Fig. 4.12b and the above mentionned growth conditions. The complete fabrication process is is summarized in Table 4.4.

The yield of suspended carbon nanotube junctions was determined by SEM imaging of each junction on a chip. However, scanning the carbon nanotube with an electron beam ($E = 1 - 20$ keV) leads to the deposition of amorphous carbon on the nanotube [93, 94], resulting in a degradation of the mechanical and eletronic properties of the latter. As a consequence, SEM imaging is only performed *after* a complete characterisation of the sample at low temperature.

Upon completion of the nanofabrication process, the carbon nanotube devices will be subjected a thorough selection process in order to elucidate the best candidates for a characterization of their nanoelectromechanical properties at cryogenic temperatures (Section 4.6). The selection will be performed on the basis of electron transport measurements at room temperature (Section 4.5), using a real-time data acquisition system ADWIN (Section 4.4) as described in the following sections.

4.4 Real-time data acquisition system for nanoelectronics

During this thesis, we will for instance demonstrate the detection of a nanotube's mechanical motion or the magnetization reversal of single molecule magnet grafted to a carbon nanotube through electron transport measurements. For this purpose, we will have to monitor a low intensity current I or differential conductance dI/dV of a carbon nanotube as function of different external parameters such as gate voltage, bias voltage, RF signal or magnetic field.

In the following we will describe a low noise data acquisition system ADWIN which can perform these tasks in real-time, in combination with a home-made control program NanoQt [95, 96, 57].

4.4.1 ADWIN automate and NanoQt control interface

The ADWIN automate consist of a 16-bit D/A converter with 8 output channels capable of generating voltages of $\pm$ 10V with a stepsize of $20/2^{16} = 305$ μV/bit. An 18-bit A/D converter with 8 input channels is used to readout voltages between -10V and +10V with a resolution of $20/2^{18} = 76$ μV/bit (Fig. 4.13).

Input and output ports are controlled by an integrated Digital Signal Processor (DSP) with a frequency of 300 MHz. The processor's period of 3.3 ns provides the necessary time reference frame for so called *real time* measurements. In contrast to plateforms designed to perform multiple tasks in parallel without time constraints like a computer

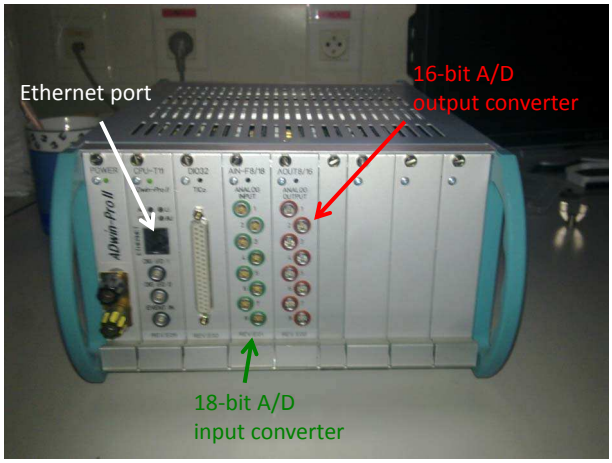

Figure 4.13: ADWIN automate with a 16-bit D/A converter for the signal output and a 18-bit A/D converter for the signal readout.

operating system (typical cycle times are on the order of 10 ms), one can perform a task with a time precision smaller than 1 μs with an ADWIN automate [95, 57].

A computer interface called *NanoQt* was designed by Raoul Picquerel, Christophe Thirion and Edgar Bonet at Neel Institute in order to control the ADWIN automate.

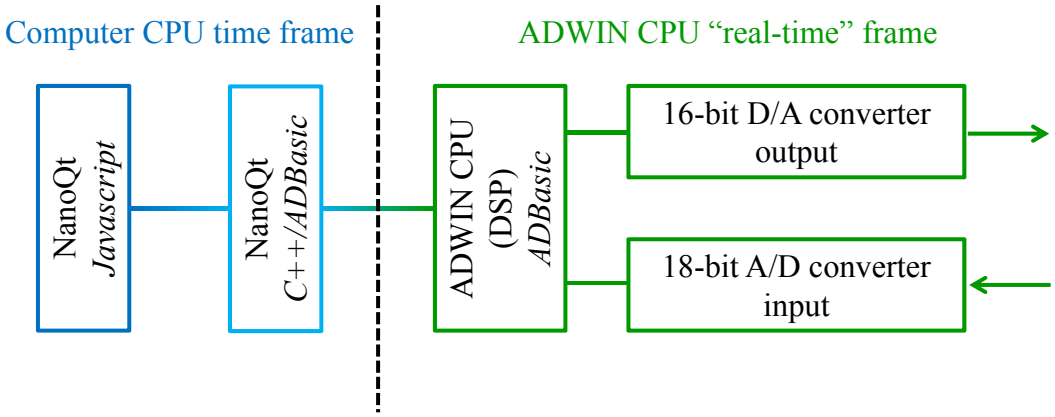

Figure 4.14: Schematic representation of the real-time data acquisition system: A measurement procedure can be impleted in Javascript in NanoQt and sent to digital signal processer (DSP) of the ADWIN in the form of a sequence of ADBasic instructions. The DSP will carry out those instructions within the reference time frame given its frequency (300 MHz).

The user can define series of instructions in a *Javascript* code, which are then interpreted into *ADbasic*, the programming language of the ADWIN DSP. The commands

are sent via an ethernet connection to the DSP, which will generate the desired signals according to its own time reference (Fig. 4.14). The sample's response to the generated signals is recorded by the DSP and the data are sent back to the NanoQt computer interface, where they can be stored, treated and displayed within the time reference of the computer's CPU (Fig. 4.15).

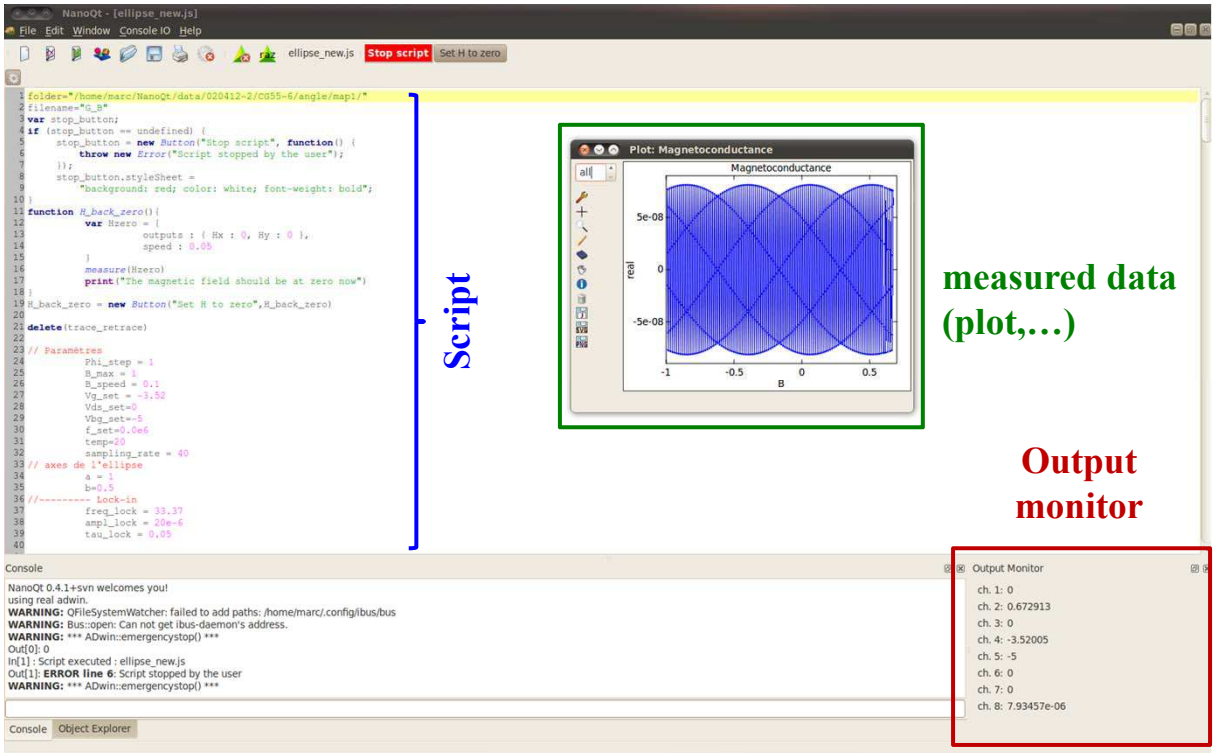

Figure 4.15: User interface NanoQt: A measurement sequence is defined in a script (Javascript) and sent to the ADWIN DSP which generates the desired signals. The output can be monitored in real time. The response of the sample is recorded by the ADWIN and the data sent back to the NanoQT interface, where it is displayed in real time in a separate graph window (green).

4.4.2 Advantages of real-time measurement system

First, the presented real-time data acquisition system allows to generate multiple signals with a single piece of equipment, which significantly reduces the number of ground loops and therefore the signal noise compared to a standard setup with multiple generators interfaced in parallel.

In addition one can generate a periodic signal with frequencies between 10 Hz and 10 kHz. This enables the implementation of a numerical lock-in detection and makes a

physical lock-in detector unnecessary. This further reduces the number of ground loops and the signal noise in the system (Fig. 4.16).

Moreover, the system enables a *bit by bit* ramping of a signal parameter which also reduces the signal noise generate in the setup. Due to the fast response time of the DSP, one can reduce the measurement time by a factor of 1000 compared to a standard setup controlled by a computer plateform.

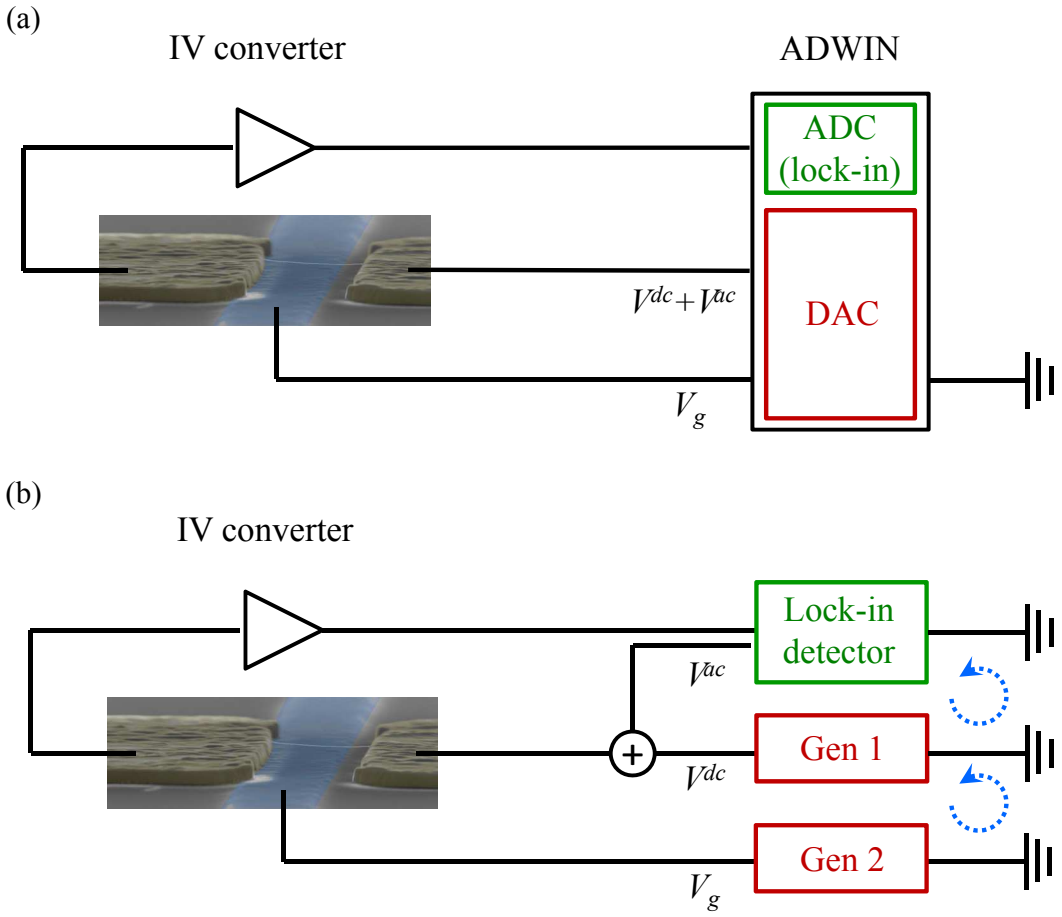

Figure 4.16: ADWIN setup vs. standard setup: (a) All generators and detectors are integrated into the ADWIN and have the same ground. (b) A lock-in detector and two signal generators are linked through the mass, resulting in two ground loops (blue dotted lines).

4.5 Selection of carbon nanotube NEMS at room temperature

In this section, we propose a selection procedure that allows us to determine and retain only single suspended carbon nanotube device of the highest quality for the characterization at cryogenic temperatures. As mentionned in the previous section, single suspended carbon nanotube devices can be selected by electron microscopy. However, the electron beam can induce a substantial amount of electronic defects to the carbon nanotube and render it useless for subsequent measurements. Moreover, the suspended carbon nanotube devices should have clean electron transport properties for the electronic readout of the mechanical motion. As a consequence, the selection process is performed on the basis of electron transport measurements, in particular of the differential conductance vs. gate voltage characteristics $dI/dV\,(V_g)$. The selection procedure was confirmed and validated by SEM imaging after low temperature measurements.

Based on these $dI/dV\,(V_g)$ characteristics recorded at zero source-drain DC bias by lock-in detection (Section 4.5.1), one has first to discriminate suspended from non-suspended carbon nanotube devices (Section 4.5.2). In the same way, one can also seperate single from multiple suspended tube devices. Finally, one has to discard all contaminated devices .

4.5.1 Lock-in detection and measurement setup

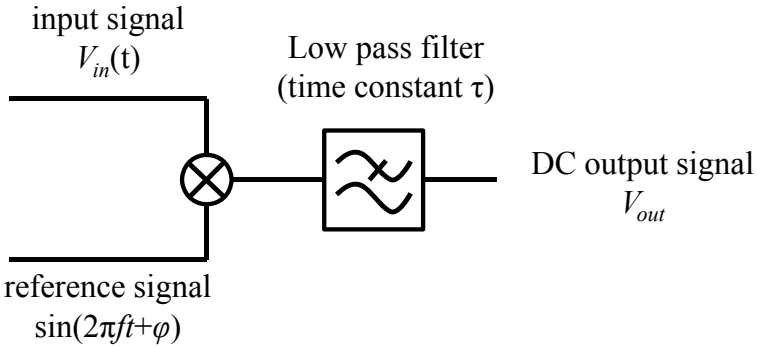

Figure 4.17: Lock-in amplifier: The measuring signal $V_{in}(t)$ is mixed with a low frequency reference signal $\sin(2\pi ft + \varphi)$ and sent through a low pass filter with a time constant τ.

A lock in amplifier mixes the input signal $V_{in}(t)$ with a low frequency, sinusoidal reference signal $\sin(2\pi ft + \varphi)$ and integrates the mixed signal in a low pass filter (integration time τ). For integration times τ longer than the period of the input and reference signal, the output signal will be a DC signal given by equation 4.3.

$$V_{out} = \frac{1}{\tau}\int_{t-\tau}^{t} \sin(2\pi f t' + \varphi) V_{in}(t') dt' \tag{4.3}$$

A lock-in amplifier is essentially a narrow band pass filter centered around the reference frequency, i.e. only frequency components matching the reference frequency (within the bandwidth $1/\tau$) will contribute to the output DC signal. Also the signal-to-noise ratio of the output signal is strongly enhanced, as most of the signal noise is also eliminated by the lock-in amplifier. It is therefore ideal to detect very weak signals in extremely noisy environments, like the current in a carbon nanotube transistor.

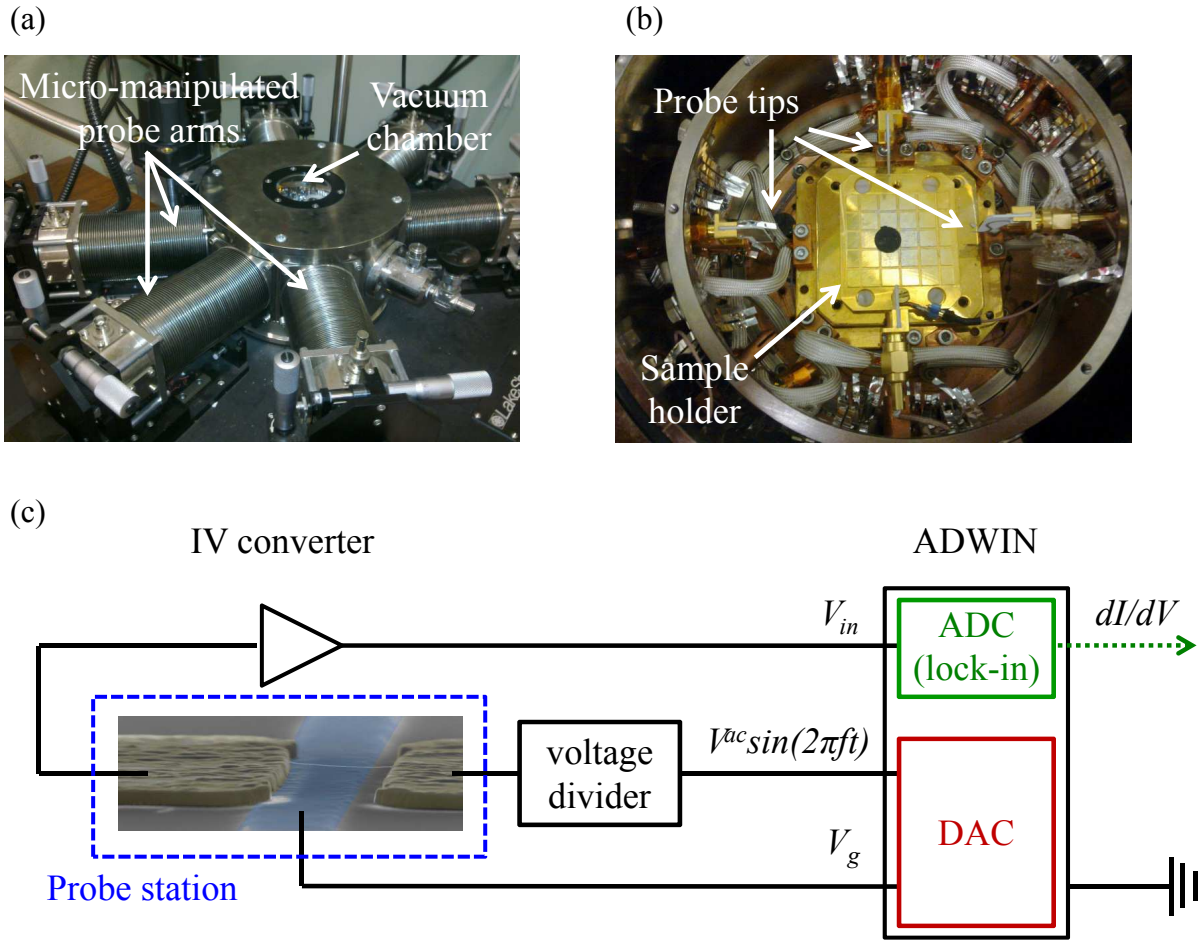

Figure 4.18: Room temperature electron transport measurement setup: (a) Vacuum probe station *Lakeshore TTPX*. (b) Inside of the vacuum test chamber with tungsten probe tips. (c) Schematic view of measurement setup with an ADWIN connected to a sample mounted in the probe station. A numerical lock-in detection provides directly the differential conductance of the probed device at zero DC bias.

In order to perform a lock-in current detection, an AC voltage $V^{ac}\sin(2\pi ft)$ is applied to the carbon nanotube device with $f = 33.37$ Hz and $V^{ac} = 20\mu$V (Fig. 4.18c). A voltage divider will be necessary to apply the desired voltage, as the minimal output voltage of the ADWIN 16-bit DAC is $20/2^{16} = 305$ μV. The resulting current $I(t) = \frac{dI}{dV}V^{ac}\sin(2\pi ft)$ through the carbon nanotube is amplified and converted to a voltage V_{in} using an IV converter. This voltage will be recorded by the ADWIN and yields:

$$V_{in} = R\frac{dI}{dV}V^{ac}\sin 2\pi ft \tag{4.4}$$

where R is the amplification factor of the IV converter.

The numerical lock-in detector implemented in the ADWIN DSP will mix the recorded voltage V_{in} with a sinusoidal reference signal at the same frequency f and integrate it in low pass filter with a time constant $\tau \sim 0.2s$. The resulting output signal

$$V_{out} = \frac{1}{\tau}\int_{t-\tau}^{t} V^{ac}R\frac{dI}{dV}\sin^2(2\pi ft')dt' = \frac{1}{2}V^{ac}R\frac{dI}{dV} \tag{4.5}$$

will be a DC signal and directly proportional to the differential conductance dI/dV of the probed carbon nanotube device.

Electron transport measurements are performed under vacuum ($p = 10^{-4}$ mbar) in a *Lakeshore TTPX* probe station at room temperature and zero DC bias (Fig. 4.18).

4.5.2 Selection procedure for carbon nanotube NEMS at room temperature

Suspended vs. non suspended carbon nanotube devices

In theory, a small bandgap (large diameter) non-suspended carbon nanotube contacted by Pt electrodes should exhibit an ambipolar conductance-gate voltage characteristic dI/dV (V_g) at room temperature under vacuum. In practice however, the electron conduction (n-type) branch of the carbon nanotube is completely suppressed by a oxygen-water redox couples, which occur in the thin water film covering the substrate's surface [97]. This results in a characteristic p-type behaviour for non-suspended carbon nanotubes. A suspended carbon nanotube however is not in contact with the substrate and remains unaffected by those surface oxygen-water redox couples. As a carbon nanotube is also intrinsically hydrophobic [98], we therefore recover the ambipolar behaviour in suspended carbon nanotubes [81].

Hence, we attribute p-type behaviour to non-suspended carbon nanotubes and ambipolar dI/dV characteristics to suspended carbon nanotube devices as depicted in Fig. 4.19. By those means, we can discard all non-suspended and retain only suspended tube device for the next step of the selection process. In addition, we also discard all non-connected devices and device with no gate dependance ("flat" dI/dV characteristics).

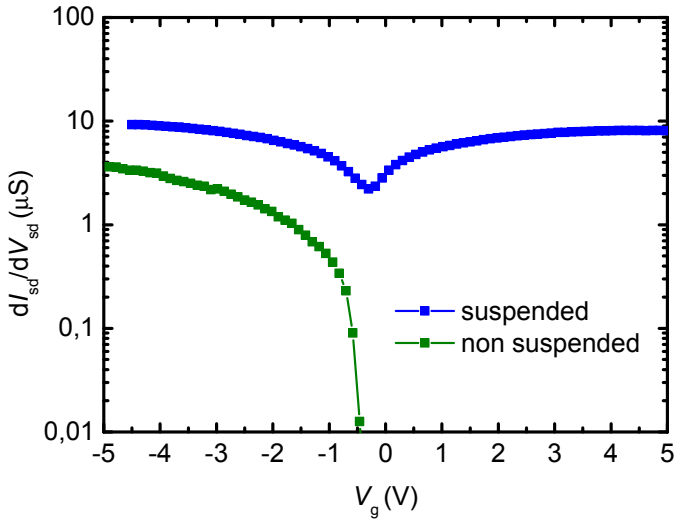

Figure 4.19: Room temperature zero bias dI/dV characteristics for suspended (blue) and non-suspended (green) carbon nanotube devices.

Single tube vs. multiple tube junction

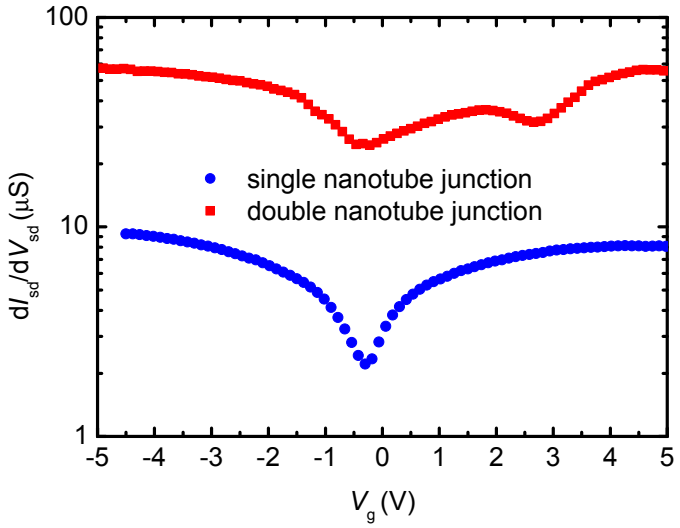

Figure 4.20: Room temperature zero bias dI/dV characteristics for single (V-shape, blue) and double (W-shape, red) suspended carbon nanotube devices.

As demonstrated in the previous section, the CVD growth conditions produce both single and multiple suspended tubes devices. A single suspended nanotube device should exhibit the V-shaped dI/dV characteristic, typical for an ambipolar device (Fig. 4.19

and 4.20, blue curve). If two or more carbon nanotubes grow in parallel on the same junction (Fig. 4.12b), the resulting dI/dV characteristic of the junction ought to be a superposition of the individual dI/dV characteristics from each nanotube. For example, a double tube junction would exhibit a W-shaped dI/dV characteristic as in Fig. 4.20 (red curve).

Moreover multiple tube junctions typically exhibit are higher differential conductance ($dI/dV > 30\mu$S) than single tube devices ($1\mu\text{S} < dI/dV < 30\mu$S).

By those means, we can differentiate single from multiple suspended tube devices, and retain only the former for the last step of the selection process.

Discarding contaminated devices

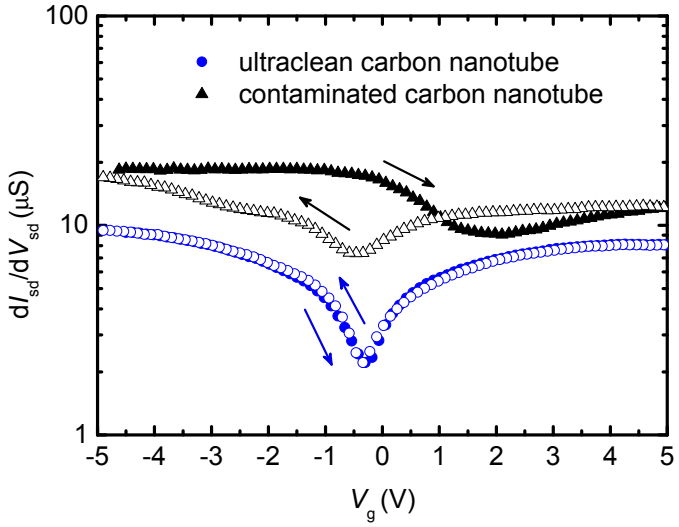

Figure 4.21: Room temperature zero bias dI/dV characteristics for an ultraclean suspended carbon nanotube (hysteresis-free, blue curve) and a contamined suspended carbon nanotube (large hysteresis, black curve). Full (open) symbols represent the upwards (downwards) sweep of the gate voltage, as indicated by the arrows.

Among the retained devices, we finally have to discard all devices with a large hysteresis between the up- and downward sweep of the gate voltage (Fig. 4.21, black curve). Generally, gate-induced hysteresis in carbon nanotube transistors is believed to originate from a charge transfer from the nanotube into the adjacent gate dielectric [99], a surface bound water layer [100] or molecules adsorbed to the nanotube's sidewall which results in an effective screening of the gate potential.

For suspended carbon nanotubes a charge transfer to the gate dielectric and surface bound water molecules can be ruled out. In this case, a large hysteresis can for instance be attributed to strongly adsorbed species on the suspended carbon nanotube. Such

adsorbates would cause electronic defects and lead to a reduced quality factor of the mechanical motion. As a consequence, we will only retain "hysteresis-free"' or "small-hysteresis" devices for the measurements a cryogenic temperatures, to ensure the high quality of the carbon nanotube NEMS.

The yield of single suspended tube devices obtained by this procedure ranges 3% and 8%, depending on the sample and the amount of catalyst used for the CVD growth. The results are consistent with SEM characterization mentionned in Section 4.3.

4.6 Probing nanomechanical bending modes in carbon nanotube NEMS at cryogenic temperature

In Sections 4.6.2 and 4.6.3, we will describe the practical realization of an actuation and detection scheme for mechanical bending modes in carbon nanotube NEMS at cryogenic temperatures, as proposed by Steele and co-workers [61] (see Section 3.2.3 for further details).

The measurements at cryogenic temperatures are carried out in an *inversed* ^{3}He/^{4}He dilution refrigerator ("Sionludi") with a base temperature of 30 mK. This peculiar cryostat design, where the coldest point is located on top of the cryostat outside a helium dewar, was developped by Alain Benoit and co-workers at Neel Institute for the joint NASA/ESA Planck satellite project. The cryostat was designed to operate in a zero gravity environment and provide the millikelvin temperatures necessary to run the two instruments aboard the satellite. In the following we will give a brief description of this particular cryostat (Section 4.6.1).

4.6.1 Inverse dilution refrigerator

A Sionludi consists of five thermalisation levels, with decreasing temperature from bottom (80K) to top (20 mK). Each stage is protected with an aluminium screen to block out radiation (however screens for the 50 mK and 1K stage are *optional*). The cryostat is sealed by a metal shield fixed to the 300K stage and a vacuum is created inside the shield.

The first step in the cooldown of such a cryostat is the pre-cooling of all stages to 4K. For this purpose, He_4 is directly injected at high flow rates into the 4K pod, which is in thermal contact with the 4K stage. The He_4 then flows out of the cryostat in a spiral tube and thermalizing the 20K and 80K levels on the way (green circuit in Fig. 4.22). Subsequently, a He_4/He_3 mixture circuit is used to thermalise the upper levels of the cryostat.

First, a small amount of He_4/He_3 mixture is injected at 4 bars into 12 capillaries mounted inside the spiral tube for the He_4 back flow. As the mixture flows up in the spiral tube, it is cooled by the He_4 counterflow and will have reached a temperature of 4K

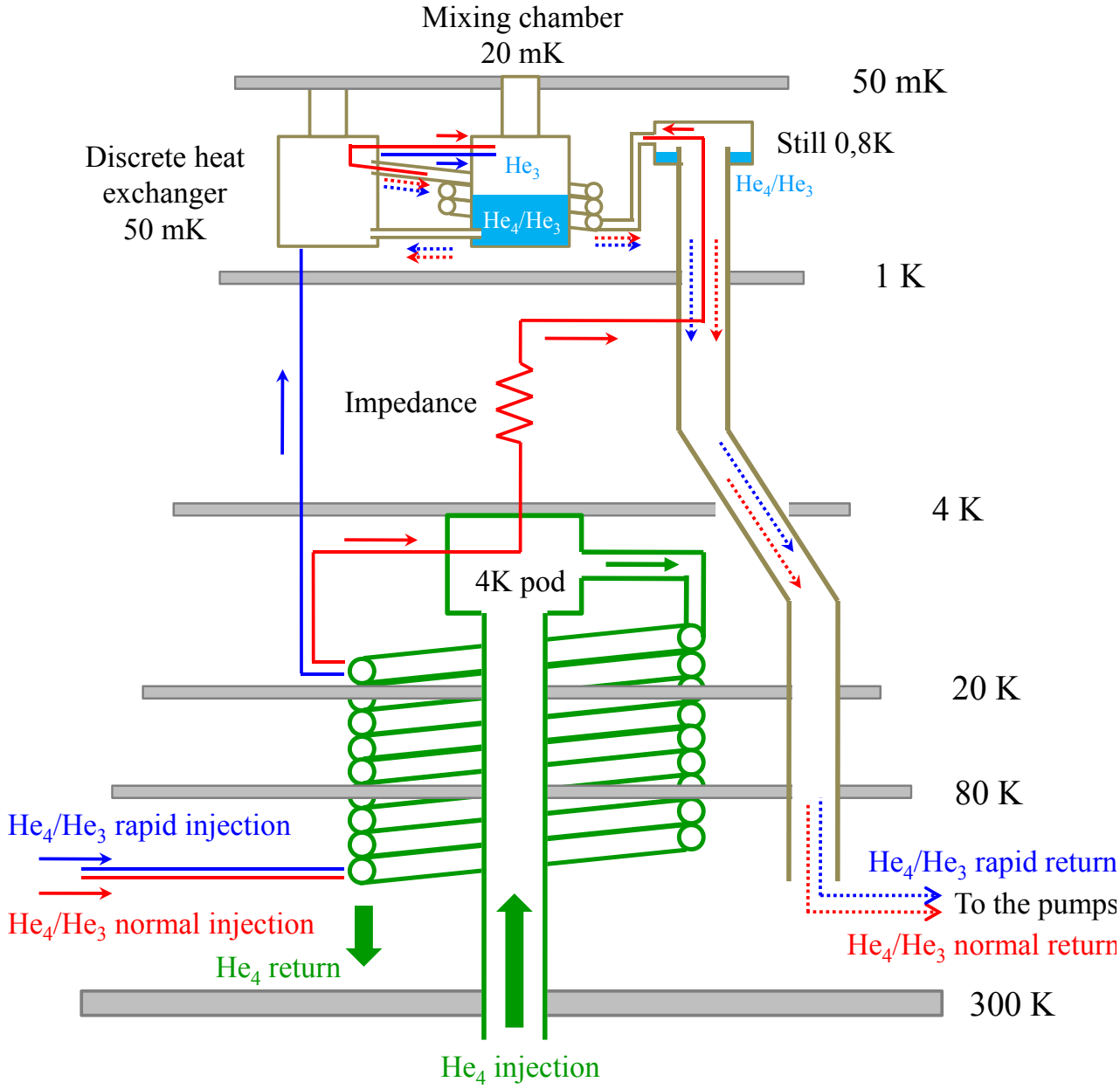

Figure 4.22: Inversed dilution refrigerator: The He_4 circuit (green) is precooling the mixture and the lower levels to 4K. A rapid injection circuit (blue) is used to cool the upper stages to 1K. The main dilution circuit (red) is used to reach and maintain a temperature of 20 mK in the mixing chamber. The dashed arrows represent the mixture flow from the mixing chamber back to the pump. Details see text.

upon emerging on the 4K stage. From this point, eleven of these capillariess are directly connected to the 1K stage and mixing chamber on the last level. As the mixture flows

through this rapid injection circuit (blue circuit in Fig. 4.22), the upper levels can be cooled to 4K. The remaining capillary leads through a Joule-Thomson impedance into the still, thermalized to the 1K stage, and from there into the mixing chamber through two heat exchangers (a countinuous counterflow and a discrete exchanger). This normal injection capillarity is the main dilution circuit of the cryostat (red circuit in Fig. 4.22). From the mixing chamber both circuits flow back through the heat exchangers, the still and out of the cryostat (dashed arrows). A primary pump and a compressor ensures the circulation of the mixture.

Once all stages have reached a temperature of 4K, an additional roots pump is turned on in order to enhance the vacuum in the dilution circuit. The circulating mixture will undergo an expansion at the Joule-Thomson impedance and cool to approximately 1K. As the mixture starts to condense in the still and the mixing chamber, the rapid injection circuit is closed.

Once a temperature of 800 mK is reached in the circuit, the phase separation of He_4 and He_3 will start in the mixing chamber. The continuous pumping with the primary and the roots pump, will extract He_3 from the consended mixture in the still and reinject it into the mixing chamber through the dilution circuit. The He_3 will then diffuse through the phase boundary from He_3-rich phase into the He_4-rich phases. This diffusion draws heat energy from its surroundings which results in a cooling of the mixing chamber. This so called dilution process will provide the necessary cooling power to reach a base temperature of 20 mK. This process sustains itself, as long as there is enough He_4 in the precooling circuit.

4.6.2 Measurement setup

After the fabrication and selection process is completed, the sample is mounted in the cryostat for low temperature measurement.

For this purpose, the sample is fixed on a specifically designed sampleholder using silver conductive paint. The selected carbon nanotube junctions on the sample are connected to Au strip lines integrated into the sampleholder by microbonded Al wires. The sampleholder yields 24 Au strip lines in total, with 12 lines embedded into the sampleholder re-emerging above the sample (DC lines 1-12 Fig. 4.23) and 12 embedded lines re-emerging below the sample (DC lines 13-24 Fig. 4.23). Among the latter, four are also connected to Au strip lines patterned on the surface, which are highlighted in blue in Fig. 4.23. Each strip line is connected to a Au contact pad at the bottom of the sampleholder. The embedded Au lines are used to contact the gate and the source-drain electrodes of each selected device and perform DC current measurement. The four strip lines at the surface (blue in Fig. 4.23) are used to inject a RF microwave signal to the gate of the selected devices and actuate the carbon nanotube resonator.

The sampleholder is subsequently mounted on a copper support above the mixing chamber in the cryostat, which will provide the necessary thermal contact between the

sample and the mixing chamber. Electrical connection wires were drawn from 300K to the 50 mK stage, where they can be connected to the Au contact pads on the sampleholder by a plug-in connector. At 300K the wires exit the cryostat through a π-filter before being connected to the ADWIN measurement setup.

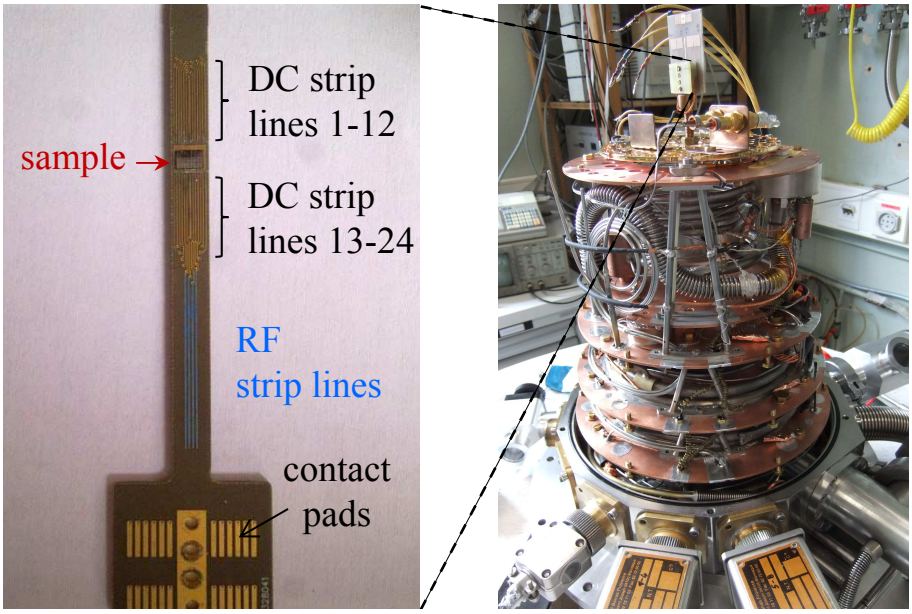

Figure 4.23: Sampleholder for low temperature measurements yielding 24 Au embedded strip lines (12 below and 12 above the position of the sample) designed for DC electron transport measurements. Four lines are connected to RF strip lines (blue) on the surface of the sampleholder, which will serve for the injection of a microwave into the gate and the actuation of the carbon nanotube resonators. The sampleholder is then mounted onto the mixing chamber of the dilution refrigerator (right panel).

A coaxial cable is drawn from the 300K stage to the 50 mK stage to guide an RF signal from the outside of the cryostat to the sample. The bare end of the coaxial cable, which will serve as RF antenna, is mounted in close proximity to the four RF strip lines on the sampleholder. A *Rhode&Schwarz SMA 100 A* signal generator, controlled by the ADWIN, is used to generate the RF signal at the antenna. The signal is injected into the RF strip lines through capacitive coupling (like in a *bias-T*) and then through the bonding wire into the gate of the adressed NEMS. The design of the sampleholder will prevent the injection of the RF signal into the source or the drain of the NEMS, thus avoiding a signal mixing in the carbon nanotube and an increased current noise. The oscillating potential on the gate of the NEMS will then actuate the nanotube's mechanical motion. As described in Section 3.2.3, the induced mechanical motion changes the charge flow through the CNT quantum dot and vice versa. Hence, we can detect the carbon

nanotube resonance through a change in zero bias differential conductance, which is recorded by a lock-in detection.

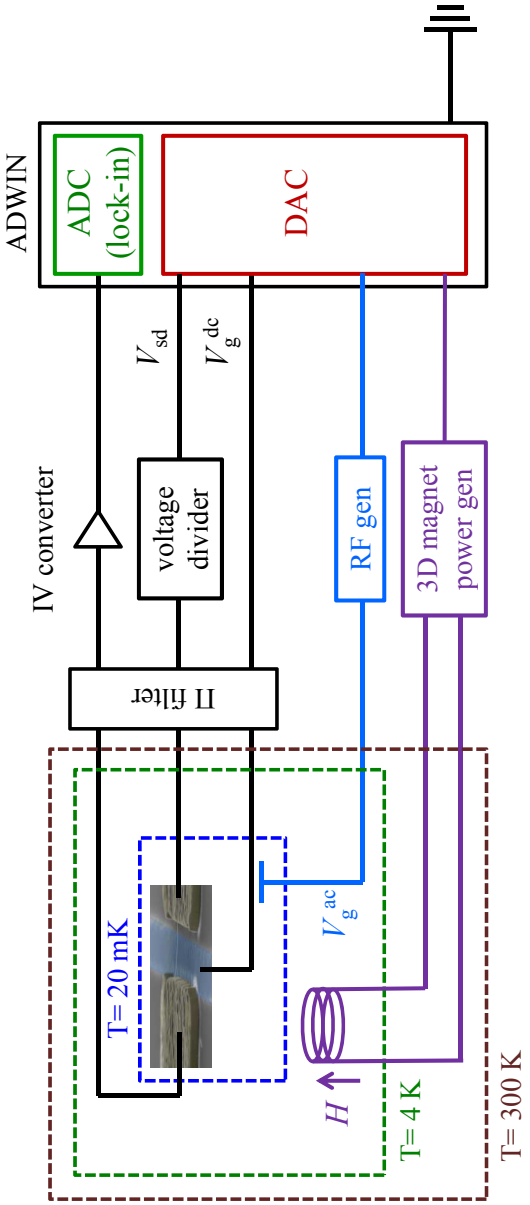

Figure 4.24: Schematic representation of the cryogenic measurement setup: Electron transport measurement on the carbon nanotube NEMS are performed by lock-in detection with the ADWIN (black circuit). The actuation signal for the carbon nanotube NEMS is generated by a RF signal generator and injected in the gate of the NEMS through a home-built bias-T (blue circuit). A 3D superconducting vector magnet can be mounted to perform magnetic measurements (purple circuit).

For magnetic measurement, a 3D superconducting vector magnet is installed in the cryostat. The magnet consists of a central solenoid coil and two Helmholtz coil pairs, aligned orthogonal to one another. The coils are capable of generating a magnetic vector field of 1.4T x 0.5T x 0.15T. The sampleholder was designed to fit inside the solenoid, such that the sample would be located exactly at the center of the 3D vector magnet. Each superconducting coil is powered by an independant current source, which can be controlled by ADWIN.

A (simplified) schematic representation of the measurement setup can be found in Fig. 4.24.

4.6.3 Detection procedure for nanomechanical bending modes at cryogenic temperature

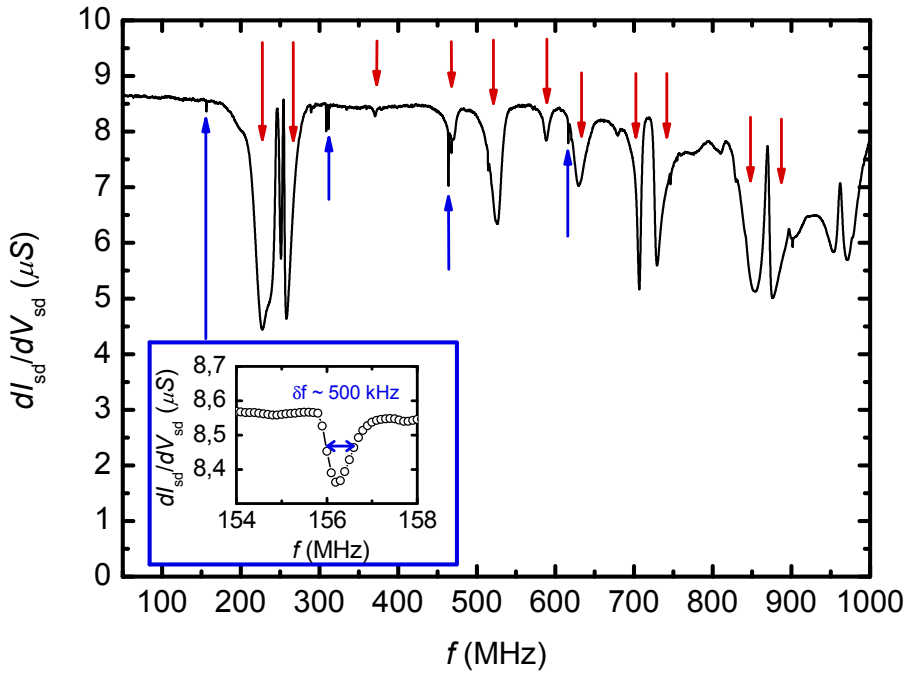

Figure 4.25: Carbon nanotube's differential conductance vs. actuation frequency at actuation power of $P_{RF} = -45$ dBm. Blue arrows indicate potential carbon nanotube resonances, red arrows resonances from the measurement setup. The inset depicts a *potential* carbon nanotube resonance at $f = 156$ MHz with a linewidth of $\delta f \sim 500$ kHz.

At cryogenic temperatures, the carbon nanotube NEMS is in a regime of Coulomb blockade. In order to perform the current detection of the resonance frequency (see Section 3.2.3 and 4.6.2), we have to tune the quantum dot to a regime of single electron tunneling, i.e. set the gate voltage close to a charge degeneracy point.

A RF actuation signal is injected into the gate of the corresponding NEMS. As described in Section 3.2, the resonance frequency of the mechanical bending mode from a carbon nanotube resonator is on the order of a few hundred MHz for nanotube length's between 500 nm and 1 μm. In order to find the nanotube's resonance frequency, we therefore sweep the RF frequency between 50 MHz and 1 GHz, while monitoring the conductance of the carbon nanotube NEMS recorded by lock-in detection. The output power of the signal generator is set between -40dBm and -50 dBm, to generate a large motion amplitude and thus facilitating its detection. An example of such a sweep is depicted in Fig. 4.25.

In Fig. 4.25, one will notice wide resonance features with a FWHM of a few tens of MHz. Those low-Q resonances ($Q \sim 10-100$) can be attributed for instance to resonances in the measurement setup itself (RF coax cable, etc...) and shall be disregarded in the following (red arrows in Fig. 4.25).

More interestingly, one can observe sharp conductance peaks ($\Delta dI/dV > 0$) or dips ($\Delta dI/dV < 0$), with a FWHM of a few hundred kHz and a relative amplitude change of $|\Delta dI/dV|/|dI/dV| \approx 5\%$ at those RF power settings (blue arrows and inset Fig. 4.25). Those high-Q resonance lines ($Q \sim 1000$) are a first strong indication for a mechanical bending mode in the resonator.

However, one has to the confirm the nature of those resonances using a set of "fingerprints" unique to mechanical bending modes in carbon nanotube NEMS which we introduced in chapter 3.

Driving power and high quality factor Q

According to Section 3.2, a first characteristic fingerprint of a carbon nanotube resonance is its dependance on the actuation power. At high driving power, a carbon nanotube resonator exhibits a strongly nonlinear behavior. Upon decreasing the driving power, the resonator is evolving from a Duffing-like oscillator to a harmonic oscillator (Fig. 4.26a). The resonance eventually vanishes, once the driving power drops below a threshold value, which is typically on the order of -80 dBm for our devices.

At a driving power just above threshold, the resonator behaves as a harmonic oscillator and exhibits a typical Lorentzian line shape. The corresponding quality factor is on the order of $Q \sim 10^4-10^5$ (Fig. 4.26b) which is to be expected for ultraclean carbon nanotube NEMS (Section 3.2).

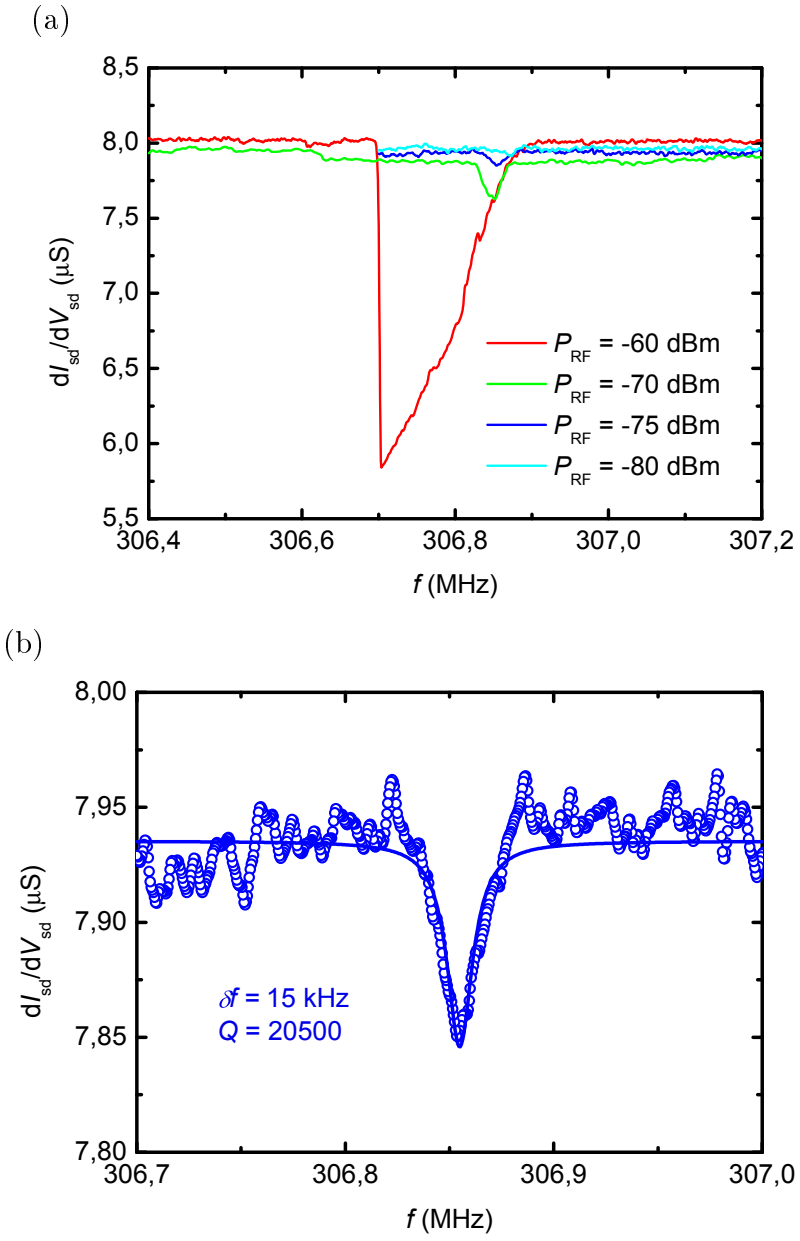

Figure 4.26: Bending mode resonance "power" fingerprint: (a) At high driving power, the resonator shows the characteristic asymetric line shape of a Duffing oscillator (red). At low driving, the resonator evolves into a harmonic oscillator with a typical Lorentzian line shape (green and blue). The resonance disappears if the power drops below a threshold value (light blue). (b) We calculate a quality factor of 20000 in the linear driving regime at $P_{RF} = -75$ dBm.

Single electron modulation

A second fingerprint is the evolution of the resonance frequency with respect to the gate voltage at low driving power. As described in Section 3.2.4, upon tuning the gate voltage through a degeneracy point, a softening of the resonance frequency due to single electron fluctuation as well as a sign change of $\Delta dI/dV$ will occur (Fig. 4.27).

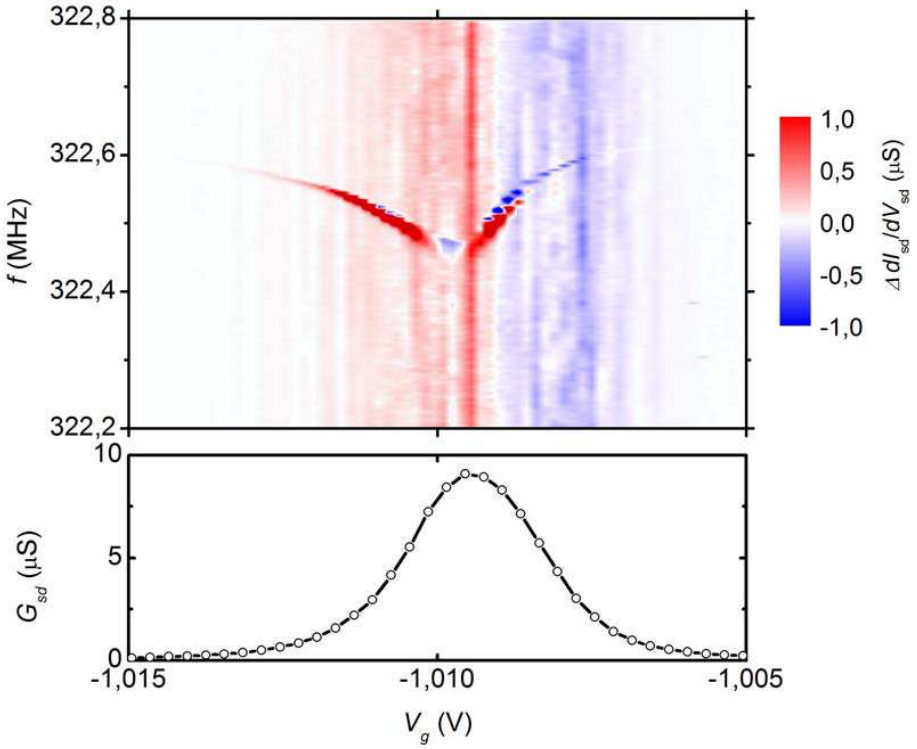

Figure 4.27: Bending mode resonance "SET" fingerprint: The upper panel depicts the change in conductance $\Delta dI/dV$ incuded by mechanical motion as function of the frequency and the gate voltage at $P_{RF} = -70$ dBm. The bottom panel depicts conductance as a function of the gate voltage.

Harmonic frequency spectrum

Finally, the bending mode resonance of a carbon nanotube should exhibit a harmonic frequency spectrum. For a harmonic spectrum, the n^{th} resonance mode is given by $f_n = nf_0$, where $n \in \mathbb{N}$ and f_0 the frequency of the fundamental mode (Fig. 4.28). The normalized mode frequency f_n/nf_0 should therefore be equal to 1, with error margin of 1% (inset Fig. 4.28).

It should be noted that a harmonic spectrum like in Fig. 4.28 is usually difficult to observe, since the signal amplitude decreases as n^{-4}. In most cases only the fundamental

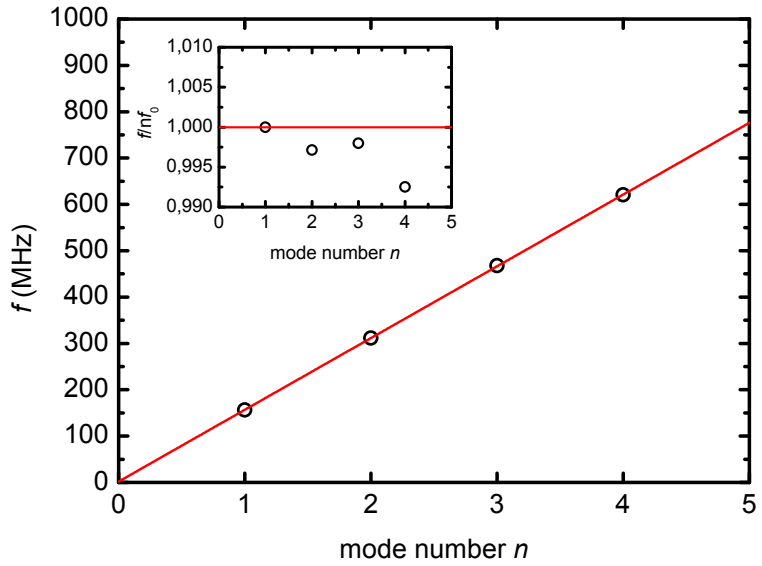

Figure 4.28: Harmonic frequency spectrum of a mechanical bending mode: The resonance frequency is directly proportional to the mode number. The inset shows the normalized frequency f_n/nf_0 as a function of the mode number.

and the first harmonic are observed, which is not sufficient to prove the harmonic nature of the frequency spectrum.

As a consequence, the high quality factor $Q \sim 10^4 - 10^5$ together with the described drive power and SET dependance are considered sufficient evidence for a bending mode resonance in the carbon nanotube NEMS.

4.7 Functionnalization of carbon nanotube NEMS with Single Molecule Magnets

In the following section, we will demonstrate the grafting of $TbPc_2$ single molecule magnets (see Section 2.2) to carbon nanotube NEMS by drop casting from solution and subsequent supercritical point drying. We will show that solution based grafting conserves the magnetic properties of the Tb^{3+} and the mechanical properties of the carbon nanotube NEMS for a very low density of grafted $TbPc_2$. The latter point is key to the fabrication of carbon nanotube NEMS based molecular spintronic devices.

4.7.1 Grafting $TbPc_2$ single molecule magnets to carbon nanotube NEMS

The $TbPc_2$ single molecule magnet introduced in Section 2.2 was synthesized at the Karlsruhe Institute of Technology by Mario Ruben and Svetlana Klyatskaya [37]. It consists of a single Tb^{3+} ion bearing an uniaxial anisotropic spin $J = 6$ sandwiched between two organic phthalocyanine (Pc) ligand planes (Fig. 6.2). The $TbPc_2$* has a $S = 1/2$ radical delocalized over the Pc ligand planes. Due to π-π interaction, this radical can hybridize with the π-electrons of any form of sp_2-carbon without affecting the magnetic properties of the Tb^{3+} ion, thus promoting the grafting to a carbon nanotube [37, 48].

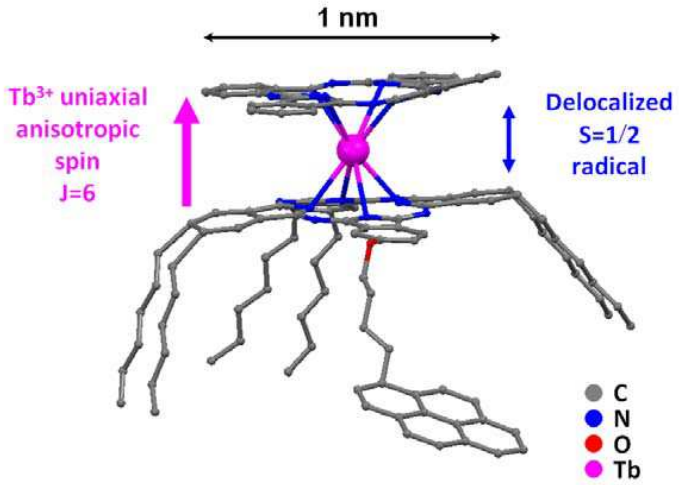

Figure 4.29: $TbPc_2$* Single Molecule Magnet: A Tb^{3+} ion with an uniaxial anisotropic spin $J = 6$ is sandwiched by two phthalocyanine ligand planes. A pyrene arm and six hexyl groups significantly increase the grafting efficiency of the SMM to sp_2 carbon systems.

The pyrene arm and the six hexyl groups added to one of the Pc planes are known for an attractive van der Waals interaction with sp_2-carbon and further enhance the grafting efficiency [37, 48]. Moreover the hexyl groups induce a steric hindrance in the molecule which prevents the reaggregation of the $TbPc_2$* in a solution and the formation of $TbPc_2$* clusters on the sidewall of the carbon nanotube [48].

The $TbPc_2$* molecules were synthesized in form of a dark green powder and dissolved in dichloromethane. The suspension is then drop casted on the sample after the selection process of the carbon nanotube NEMS (see Section 4.5). The sample is rinsed in dichloromethane and isopropanol for 5 minutes each. The rinsing should remove all non or weakly grafted molecules from the nanotubes and the surface of the sample.

The final and most critical part of this deposition is removing of the remaining iso-

propanol drop after the rinsing. One could remove the drop under a flow of nitrogen or by evaporating the remaining solvent. However, as the meniscus of the drop moves across the suspended carbon nanotube during the drying, the carbon nanotube is ripped apart by the surface tension of the drop (Fig. 4.30a).

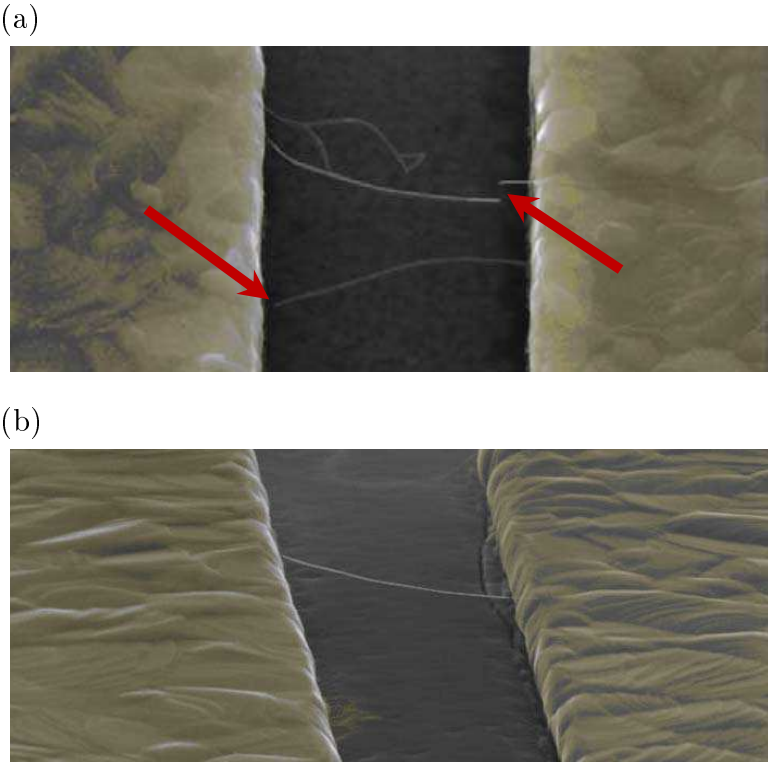

Figure 4.30: Carbon nanotube NEMS after $TbPc_2$ deposition (false color SEM image): (a) Classical drying (N_2 blow, heating) results in capillarity forces along the sample surface which tear the carbon nanotubes apart. The rupture is indicated by the red arrows. (b) Supercritical point drying prevents the rupturing of suspended carbon nanotube.

Such capillarity effects can be avoided by using a process known as supercritical point drying. The liquid is first placed into a region of the (p, T) phase diagram above the critical point, without crossing the liquid-gas phase boundary (Fig. 4.31a). In this *supercritical* state, a liquid and a gas can no longer be distinguished. As a consequence the meniscus separating the liquid from the gas vanishes and no capillarity forces will act on the suspended carbon nanotube upon the return into the gas phase (Fig. 4.31a). The carbon nanotube remains intact upon completion of the process (Fig. 4.30b).

We performed a supercritical point drying in a *Tousimis Autosamdri 815* (Fig. 4.31b). The sample is transfered into the chamber, which was previously filled with isopropanol. The chamber is cooled to 270 K and the alcohol is replaced by liquid CO_2. As a consequence, the pressure rises to 80 bar and the chamber is heated to 310 K, above the

(a)

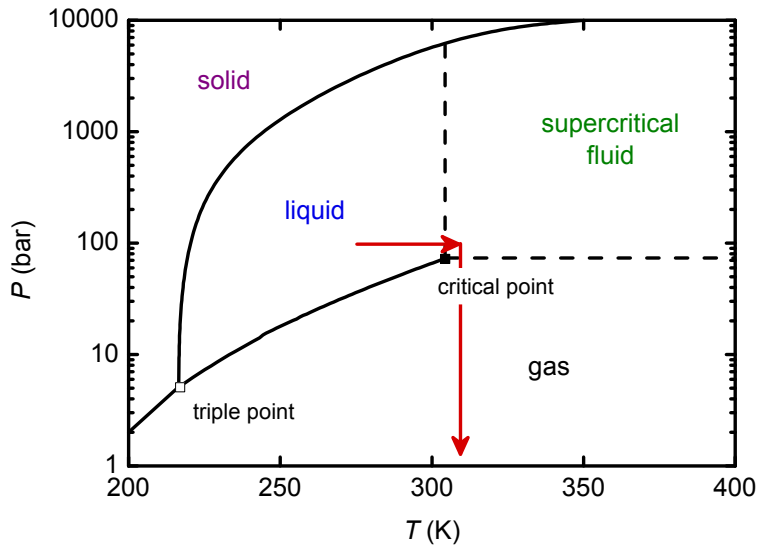

(b)

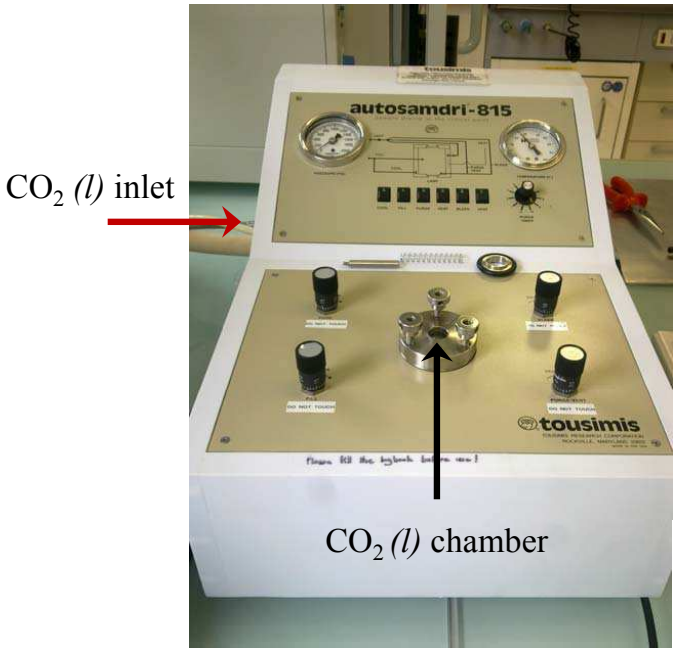

Figure 4.31: Critical point drying: (a) CO_2 phase diagram. A supercritical point drying (red path) allows to perform a liquid-gas phase transition without crossing the phase boundary. (b) *Tousimis Autosamdri 815* critical point dryer.

critical point of CO_2 ($p_c = 73.8$ bar, $T_c = 304.5$ K). Upon reducing the pressure, the CO_2 turns into a gas and can be purged from the chamber.

4.7.2 Conservation of the NEMS's mechanical and the $TbPc_2$ magnetic properties

We performed depositions of $TbPc_2$* molecules on carbon nanotube NEMS from solutions with $TbPc_2$* concentrations ranging from 10^{-7} to $5 \cdot 10^{-6}$ mol/L. The functionnalized carbon nanotube NEMS are cooled down to temperatures of 20 mK to characterize the $TbPc_2$* magnetic properties and the NEMS mechanical motion.

Magnetic fingerprint

It was previously demonstrated, that the van der Waals interaction between the $TbPc_2$* Pc ligand planes and the sidewall of the carbon nanotube leaves the magnetism of the Tb^{3+} ion intact [37, 48]. As described in Section 2.3.2, a characteristic spin valve behavior is observed in the electronic transport of carbon nanotube quantum dots functionnalized with $TbPc_2$*. It was demonstrated that the magnetic anisotropy of this spin valve effect is in very good agreement with the uniaxial anisotropy of the Tb^{3+} spin and therefore provides a magnetic fingerprint for the $TbPc_2$* SMM [48].

We observe this magnetic fingerprint on 100 % of the carbon nanotube devices after grafting, indicating a highly efficient grafting process which conserves the magnetic properties of Tb^{3+} ion as demonstrated in previous works [37, 48]. We performed magnetic field sweeps (trace and retrace) at different field orientations. Fig. 4.32 depicts the difference in conductance between trace and retrace, i.e. the magnetic hysteresis as a function of the magnetic field angle for two $TbPc_2$* concentrations. At high $TbPc_2$* concentration of $5 \cdot 10^{-6}$ mol/L one observes at least two easy axis of magnetization corresponding to two $TbPc_2$* SMM's with different orientations (Fig. 4.32a). One can subsequently reduce the $TbPc_2$* concentration until one easy axis of magnetization attributed to a single $TbPc_2$* molecule remains (Fig. 4.32b).

Mechanical fingerprint

The mechanical motion of the carbon nanotube resonator is characterized as described in Section 4.6.3.

For a concentration of $TbPc_2$* of 10^{-7} mol/L in solution, we observe a mechanical resonance with a frequency around 100 MHz and a quality factors on the order of $Q \sim 6000$ for low drive power (Fig. 4.33a). The drive power and the gate dependances are consistent with the mechanical bending mode of a carbon nanotube NEMS (Fig. 4.33 b and c, respectively).

The observed quality factor at low drive power is at least an order of magnitude smaller than for ultraclean carbon nanotube NEMS. The result indicates that the grafted $TbPc_2$* molecules induce additional dampening to the mechanical motion of the nanotube. Indeed a $TbPc_2$* SMM grafted to the sidewall of a carbon nanotube can be considered as two-level system (TLS) and induce additional dissipation in the NEMS (see Section 5.4 for details

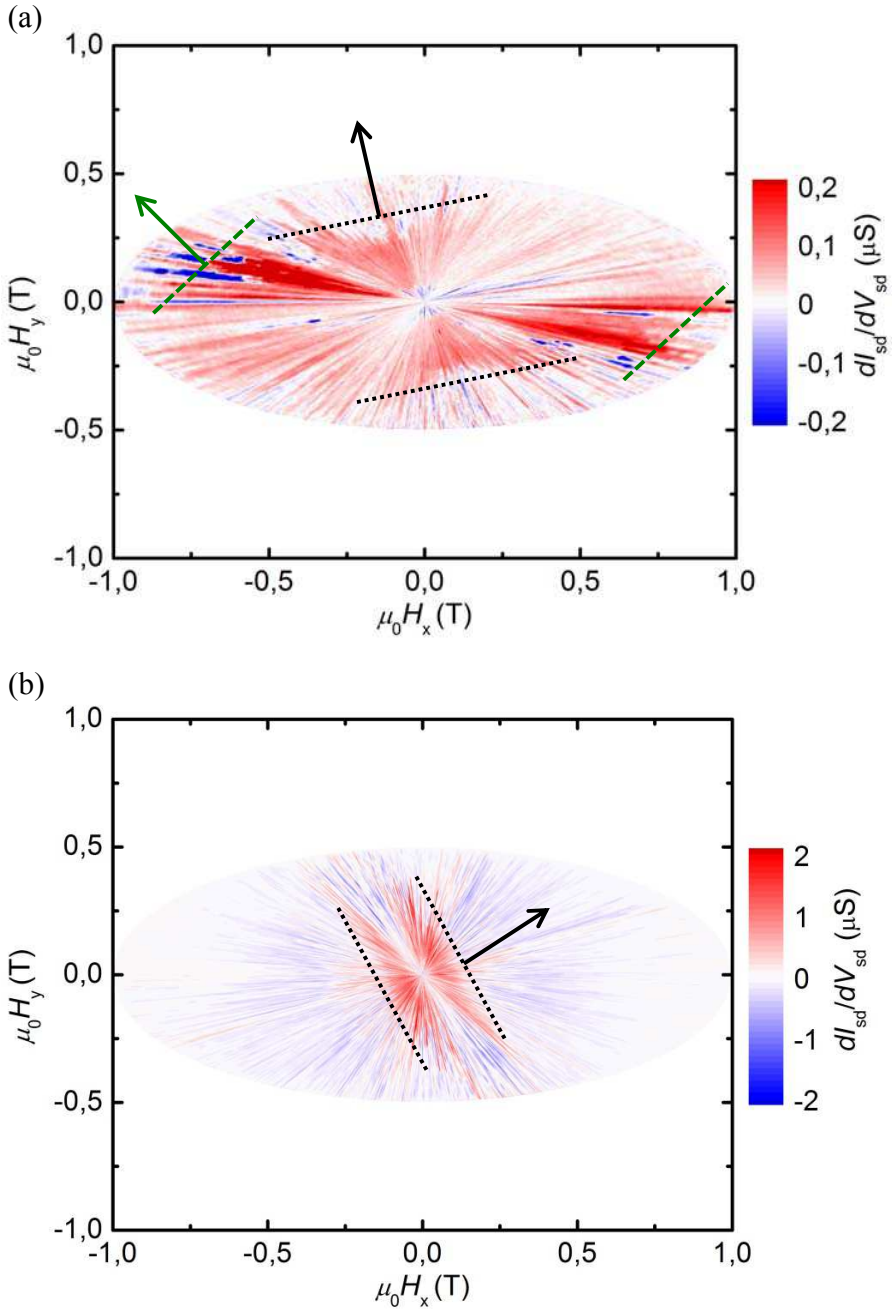

Figure 4.32: Magnetic fingerprint for $TbPc_2$* SMM at solution concentrations of (a) $5 \cdot 10^{-6}$ mol/L and (b) $5 \cdot 10^{-7}$ mol/L. The arrows depict to the easy axis of the respective molecule whereas the dashed lines indicate the corresponding switching fields. The white color code indicates a region of zero magnetic hysteresis, whereas the blue or red color code corresponds to a bistable region.

on dissipation processes in carbon nanotube NEMS). The additional $TbPc_2$* mass load also reduces the resonance frequency and hence the quality factor. It should be noted that we cannot determine the exact change of the resonance frequency. In order to assess the frequency shift due to the mass load, the carbon nanotube motion has to be characterized at cryogenic temperature before and after the deposition. However, this implies a thermal cycling of the sample, which proved to be detrimental to the quality of the sample and making any assessment impossible.

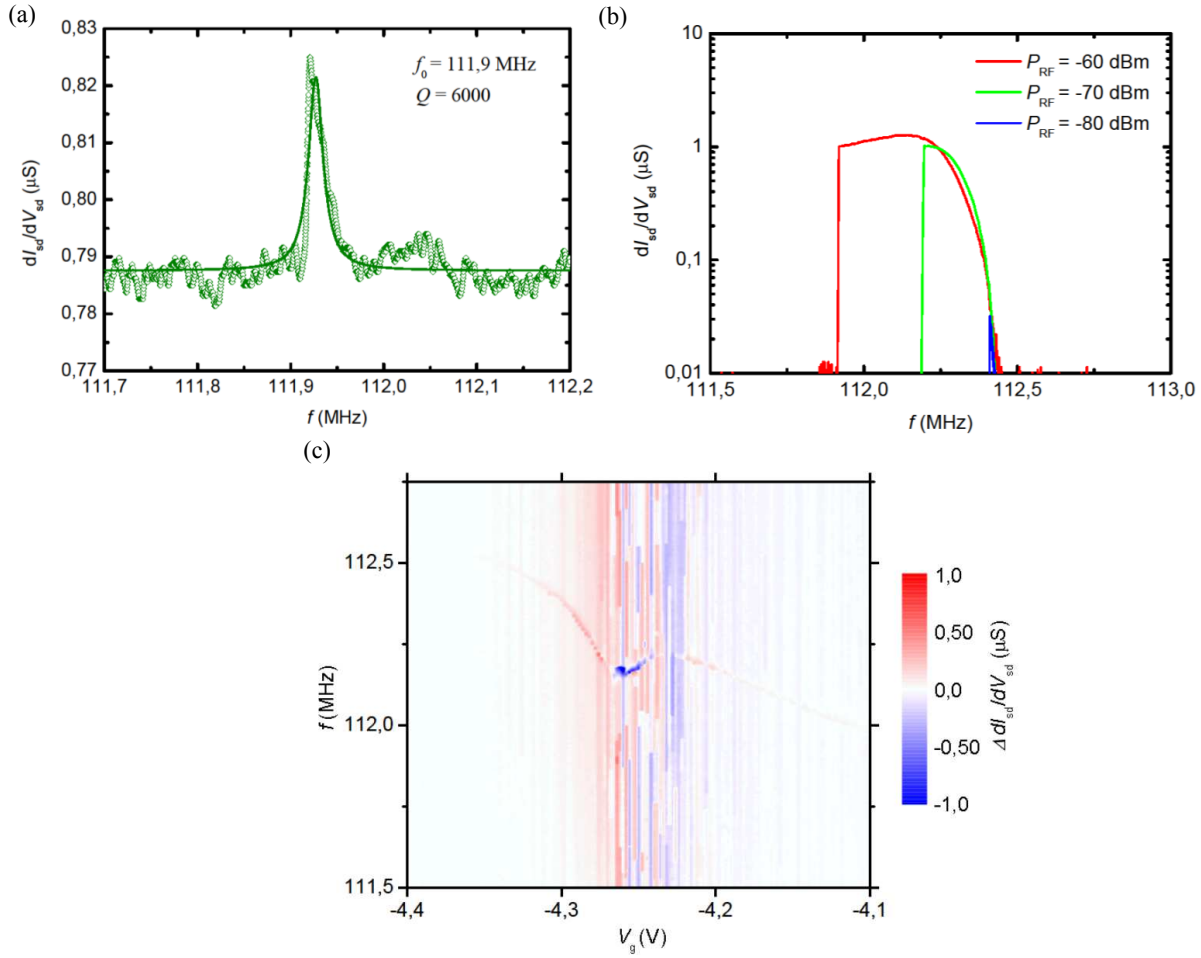

Figure 4.33: Fingerprint of nanomechanical bending mode in carbon nanotube NEMS functionalized with $TbPc_2$* SMM. The $TbPc_2$* concentration in solution is 10^{-7} mol/L. (a) Quality factor of nanomechanical bending mode in carbon nanotube NEMS at minimum drive. (b) Drive power dependance and (c) gate dependance of the resonance frequency.

Increasing the $TbPc_2$* concentration in solution by at least an order of magnitude results in a higher density of grafted $TbPc_2$* on the carbon nanotube. This considerably

increases the number of two level systems as well as the mass load and therefore the dissipation. Indeed, no carbon nanotube resonance was detected for $TbPc_2$* concentrations in solution higher than 10^{-7} mol/L.

We can conclude, that grafting $TbPc_2$* single molecule magnets from low concentration $TbPc_2$* solution onto carbon nanotube NEMS conserves both the magnetic properties of the $TbPc_2$* (chapter 2) and the mechanical properties of the resonator (described in chapters 3&5) and is therefore a key component for the fabrication of carbon nanotube supramolecular spintronic device.

Chapter 5

Dynamics and dissipation induced by SET in carbon nanotube NEMS

In section 3.2.4 we demonstrated that a CNT NEMS' nanomechanical motion at very low temperature (i.e. in Coulomb blockade regime) is strongly affected by the electronic transport through the CNT quantum dot (QD), and vice versa: For instance, single-electron tunneling (SET) caused a frequency softening and increased dissipation when tuning the CNT dot's potential through a Coulomb peak [74, 61, 75].

Here we demonstrate that the response and dissipation of a CNT NEMS at very low temperature induced by zero bias SET through the CNT NEMS-QD critically depends on the dot capacitance, the tunnel coupling to the metal leads and temperature. We studied the frequency and dissipation response of nanomechanical bending modes to zero-bias SET in suspended CNT devices with tunable tunnel couplings and different gate dielectrics, i.e. different dot capacitance. We observe that SET causes a frequency softening for small dot capacitance and/or tunnel coupling, whereas a frequency hardening or no frequency modulation is observed for large dot capacitance and/or tunnel coupling (section 5.2). We show that the dissipation of the CNT NEMS is mainly dominated by the capacitance, when electron tunneling through the dot is suppressed (i.e. in the Coulomb valley), whereas it is limited by the mean tunneling rate Γ and the conductance, when electron tunneling through the dot is allowed (i.e. on a Coulomb peak) (section 5.3). Finally we demonstrate that the tunnel current is the dominant dissipation mechanism in CNT NEMS at low temperature (section 5.4). Our findings, published in Physical Review Letters [19], are in fair agreement with a theoretical model provided previously [74, 61] (section 5.1).

5.1 Introduction

In this section, we recall briefly the fabrication of single gated, suspended CNT devices with tunable tunnel couplings on different gate dielectrics, i.e. with different dot capacitances (see Sections 4.2.2 and 4.2.3), as well as the the model describing the SET backaction on the nanomechanical motion of a carbon nanotube resonator, which was presented in Section 3.2.4 of this manuscript and the work of Lassagne *et al.* and Steele *et al.* [74, 61].

5.1.1 Nanofabrication

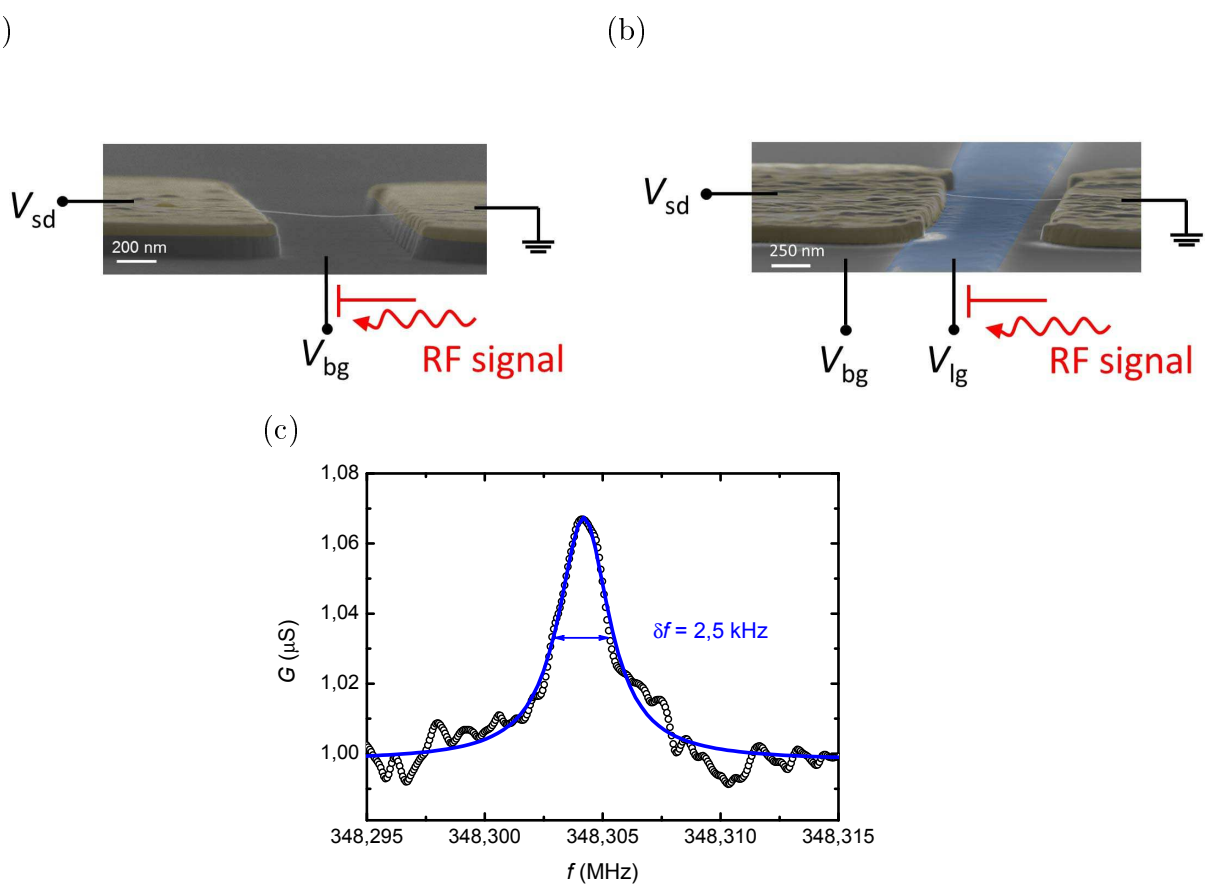

Figure 5.1: False color SEM image of **(a)** a low capacitance device based on a SiO_2 covered Si backgate (grey color) and **(b)** a high capacitance device based on an Al_2O_3 covered local metallic gate (blue). The RF actuation signal is injected into the local metallic gate and Si backgate, respectively, through a home-built bias-T. As the induced mechanical motion changes the charge flow through the CNT quantum dot and vice versa, we can detect the CNT resonance through a change in zero-bias conductance. **(c)** Mechanical resonance of a typical CNT NEMS at low driving power $P_{\mathrm{RF}} = -100$ dBm. The resonance width $\delta f = 2.5$ kHz leads to a quality factor of $Q \approx 140000$.

Low capacitance CNT quantum dots ($C_{\mathrm{dot}} \approx 20$ - 40 aF) were obtained by using silicon dioxide as gate dielectric (Fig. 5.1a). First, source-drain electrodes are patterned by optical deep UV lithography ($\lambda \sim 240$ nm) and electron-beam evaporation of Mo (20 nm) and Pt (160 nm) on 500 nm of thermal SiO_2. To ensure the suspension of the CNT, 150 nm of SiO_2 are dry etched in CHF_3 plasma.

High capacitance CNT quantum dots ($C_{\mathrm{dot}} \approx 160$ - 260 aF) are obtained with high-κ

gate dielectrics Al_2O_3 (Fig. 5.1b). First, a 1 μm-wide metallic local gate is patterned by optical deep UV lithography and electron-beam evaporation of Mo (20 nm) on 300 nm of thermal SiO_2. A layer of 100 nm of Al_2O_3 is then deposited by atomic layer deposition. Using optical deep UV lithography and electron-beam evaporation of Mo (20 nm) and Pt (160 nm), source-drain electrodes are aligned above the local gate. Suspended CNT's are finally grown by chemical vapor deposition at 800°C from a CH_4 feedstock and Fe/Mo catalyst spots patterned on the source-drain electrodes next to the junction. The CNT device length is approximately 800 nm ($\pm$ 50 nm) and the dot capacitances are deduced from the dot's charging energy at low temperature. The spread in capacitance values of nominally identically fabricated devices is due to variations in the nanotubes length and slack (see Section 5.1.3).

The measurements are carried out in a ^{3}He/^{4}He dilution refrigerator with a base temperature of 30 mK. The NEMS actuation and detection scheme used in our experiment is similar to the one used by Steele and co-workers [61, 75]. The RF actuation signal is injected into the gate electrode via a home-built bias T. As the induced mechanical motion changes the charge flow through the CNT quantum dot and vice versa, we can detect the CNT resonance through a change in zero-bias conductance. The actuation power is kept to a minimum ($P_{\mathrm{RF}} \approx$ -100 dBm) in order to ensure a quasi-linear regime of the oscillator and a high Q lorentzian resonance shape (Fig. 5.1c). All measurements were done under zero bias with a standard lock-in technique.

5.1.2 SET backaction on a carbon nanotube NEMS's mechanical motion

SET in a CNT NEMS-QD can be considered as an external perturbation to the CNT mechanical motion, and vice versa. This perturbation can be described as an electrodynamic force acting on the CNT. The contribution of this force, which is in phase with the mechanical motion, is responsible for a frequency modulation Δf, whereas a contribution of the force which is out of phase with mechanical motion induces a modification of the dissipation and the quality factor Q. Δf and Q can be expressed as follows [74]

$$\Delta f = -\frac{f_0}{2}\frac{C_{\mathrm{g}}'^2}{k}\frac{V_{\mathrm{g}}^2}{C_{\mathrm{dot}}}\left(\frac{2G}{C_{\mathrm{dot}}\Gamma} - 1\right) \tag{5.1}$$

$$\frac{1}{Q} = 2\pi f\frac{C_{\mathrm{g}}'^2}{k}V_{\mathrm{g}}^2\left(\frac{2}{\Gamma C_{\mathrm{dot}}}\right)^2 G \tag{5.2}$$

Where Γ is the mean tunnel coupling of the dot to the leads, yielding $\Gamma = (\Gamma_{\mathrm{d}} + \Gamma_{\mathrm{s}})/2$, and C_{dot} is the total dot capacitance. As we will show in the following sections, we can estimate the dot capacitance C_{dot} from the charging energy (see Section 5.1.3) and the tunnel coupling Γ from the line shape of the Coulomb blockade peaks (see Section 5.1.4). Eqs. 5.1 and 5.2 are valid in the regime of Coulomb blockade and if $\Gamma \gg f_0$.

5.1.3 Estimating the quantum dot capacitance of carbon nanotube NEMS

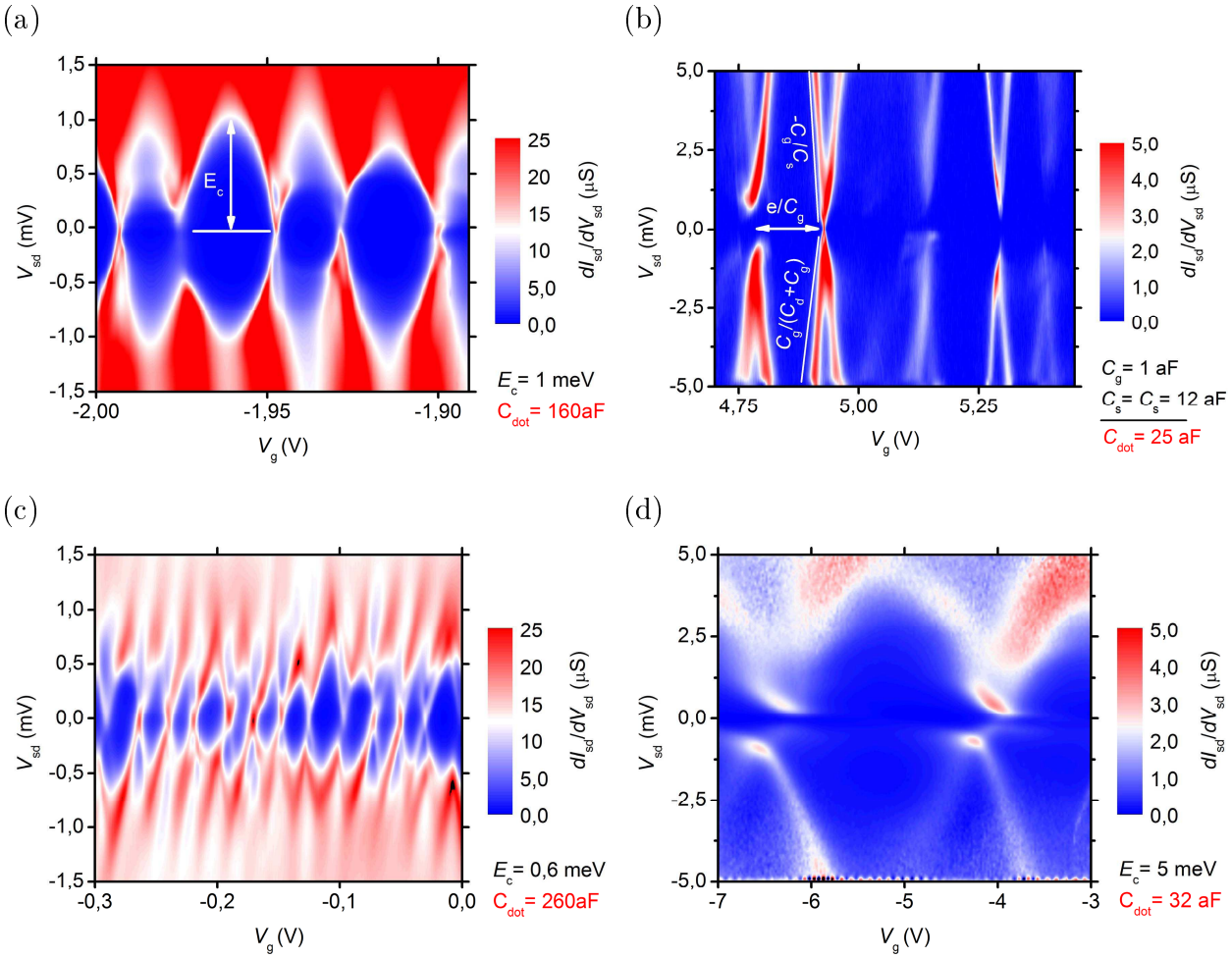

Figure 5.2: Estimating the dot capacitance via bias spectroscopy: (a)(c) Coulomb diamonds for two Al_2O_3 based devices with a length of 780 nm and 820 nm, respectively. (b)(d) Coulomb diamonds for two SiO_2 based devices.

The total dot capacitance is obtained from bias spectroscopy measurements. The total dot capacitance C_{dot} is related to the charging energy E_c of the dot via $C_{dot} = e/E_c$. The charging energy is deduced from the size of the Coulomb diamonds (Fig. 5.2a). Alternatively one can determine the capacitances C_s and C_d from the slope of the diamond edges and the gate capacitance C_g from the distance between 2 degeneracy points (Fig 5.2b). The total dot capacitance then yields $C_{dot} = C_s + C_d + C_g$.

For SiO_2 based devices we obtain capacitance between 20 and 40 aF, whereas for Al_2O_3 based devices the values range from 160 aF to 260 aF. The spread in capacitance

values for nominally identically fabricated devices can mainly be attributed to different device lengths (ranging from 700 nm to 850 nm) and therefore to variations in charging energies. Electron microscopy revealed slack on most devices, suggesting a low built-in tension which is characteristic for CVD grown CNT's [61, 75]. As the slack may be a different for each device, the distance between the CNT and the gate can vary from one device to another, which would also contribute to the spread in capacitance values.

5.1.4 Estimating the tunnel coupling Γ in CNT quantum dot

In the regime of Coulomb blockade, the energy level broadening in the carbon nanotube quantum dot is given by the electronic temperature T and the tunnel couplings Γ_s and Γ_d to the leads. The electronic temperature in our system is around 150 mK, therefore at least an order of magnitude smaller than the average tunneling rate $\Gamma = (\Gamma_\mathrm{s} + \Gamma_\mathrm{d})/2$ in carbon nanotube junctions $\Gamma \gg kT$. In this limit of tunnel broadened Coulomb blockade, the Coulomb peak line shape is given by [101, 102]:

$$G = \frac{2e^2}{h}\frac{4\Gamma_\mathrm{s}\Gamma_\mathrm{d}}{\Gamma^2}\int_{-\infty}^{\infty} d\omega \left(-\frac{df(\omega)}{d\omega}\right)\frac{(\Gamma/2)^2}{(\omega-\varepsilon)^2 + (\Gamma/2)^2 (1+f(\omega))^2} \tag{5.3}$$

where ε is the level energy and $f(\omega) = 1/(\exp(\omega/k_\mathrm{B}T)+1)$ the Fermi function.

At very low temperature $\Gamma \gg kT$, the integral yields [101, 102]

$$G = \frac{e^2}{h}\frac{2\Gamma_\mathrm{s}\Gamma_\mathrm{d}}{\varepsilon\Gamma}\tan^{-1}\left(\frac{\varepsilon\Gamma}{\Gamma^2+2\varepsilon^2}\right) \tag{5.4}$$

This expression can be written in very good approximation as a Lorentzian and by defining $\varepsilon = \alpha(V_\mathrm{g} - V_{\mathrm{g},0})$ and $G_\mathrm{max} = \frac{e^2}{h}(4\Gamma_\mathrm{s}\Gamma_\mathrm{d})/\Gamma^2$, we finally obtain:

$$\frac{G}{G_\mathrm{max}} = \frac{(\Gamma/2)^2}{\alpha^2 (V_\mathrm{g} - V_{\mathrm{g},0})^2 + (\Gamma/2)^2} \tag{5.5}$$

where $\Gamma = (\Gamma_s + \Gamma_d)/2$ is the mean tunneling rate through the quantum dot, $V_{\mathrm{g},0}$ the center of the Coulomb peak and α an energy scaling factor given by:

$$\alpha = \frac{1}{1.36}\frac{\partial V_\mathrm{sd}}{\partial V_\mathrm{g}} = \frac{1}{1.36}\frac{C_\mathrm{g}}{C_\mathrm{s} + C_\mathrm{d} + C_\mathrm{g}} \tag{5.6}$$

where C_s, C_d and C_g correspond to the source, drain and gate capacitance of the CNT quantum dot, respectively. One can estimate the dot capacitances and the energy scaling factor α via bias spectroscopy, as described in the previous section 5.1.3.

Hence, by fitting the Coulomb blockade peaks with Eq. 5.5 (Fig. 5.3), we obtain a good approximation of the tunneling rate Γ through the corresponding energy levels of the CNT quantum dot.

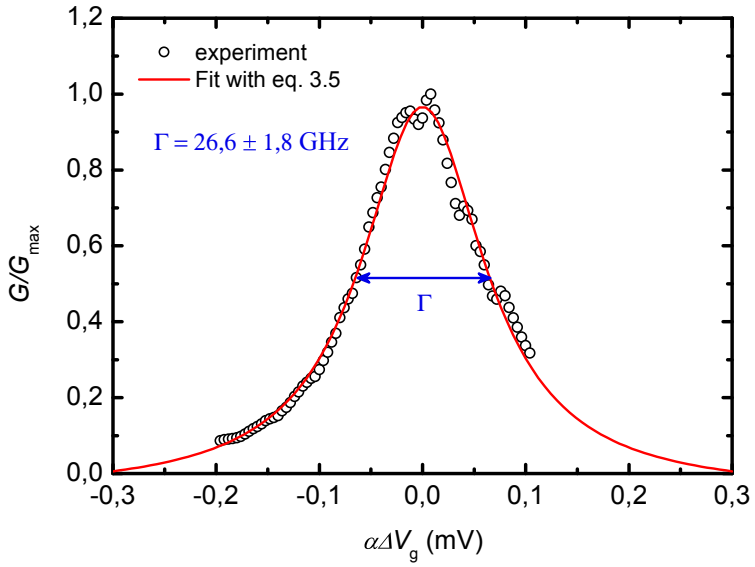

Figure 5.3: Estimating the tunnel coupling Γ of carbon nanotube quantum dot: In a regime of Coulomb blockade, the Coulomb peak line shape is given in very good approximation by a Lorentzian line shape, with a full width at half maximum (FWHM) corresponding to the tunneling rate Γ. A fit of the experimental data with equation eq. 5.5 therefore gives a good approximation of the tunneling rate Γ.

5.2 Frequency shift induced by SET in carbon nanotube NEMS

First, we compare the frequency shift induced by SET Δf (scaled with $1/f \cdot V_g^2$) of devices with different dot capacitances C_{dot}. We studied the frequency response for comparable Coulomb peaks height, i.e. for comparable conductance $G\,(V_{\mathrm{g}}) \approx 20\ \mu$S. As depicted in Fig. 5.4a, we observe a strong frequency softening for small dot capacitances, whereas for high dot capacitances a frequency hardening or no modulation is observed. As shown in Fig. 5.4b, the experimental data are in fair agreement with the model. A fit with Eq. 5.1 yields fitting parameters $C_{\mathrm{g}}'^2/k = 8 \cdot 10^{-22}$ F^2/Nm and $\Gamma \approx 10$ GHz, which are in rather good agreement with previous experiments [74, 61, 103].

Fig. 5.5a shows the frequency shift Δf (scaled with $1/f \cdot V_g^2$) for different Coulomb peaks and tunneling rates Γ on a given device (device 1). One can tune a CNT quantum dot from a Coulomb blockade regime to a regime of strong tunnel coupling by simply changing the CNT's gate potential [104, 105]. Hence, we can change the tunnel coupling Γ by tuning the gate voltage of CNT device 1 and estimate the values of Γ from the Coulomb peak line shape using Eq. 5.5 (Fig. 5.5b). The dot capacitance $C_{\mathrm{dot}} = 260$ aF remain unchanged by tuning the gate voltage. As Γ increases, the CNT becomes

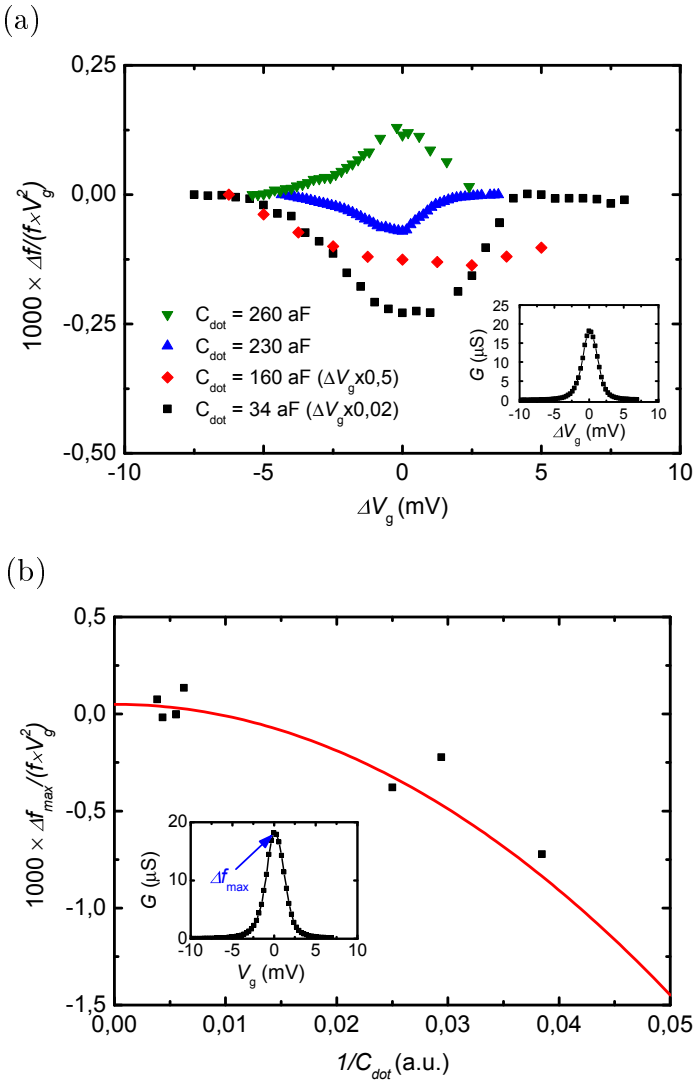

Figure 5.4: Modulation of the resonance frequency *via* dot capacitance C_{dot}: (a) Scaled frequency shift $\Delta f/\left(f \cdot V_g^2\right)$ for different dot capacitance C_{dot}, with comparable tunneling rates Γ. The inset shows a typical Coulomb peak centered at $\Delta V_{\mathrm{g}} = 0$; (b) Maximum scaled frequency shift $\Delta f_{\mathrm{max}}/\left(f \cdot V_g^2\right)$ at maximum tunnel current G_{max} $(\Delta V_g = 0)$ vs. the inverse dot capacitance $1/C_{\mathrm{dot}}$ for all measured devices. The solid red line corresponds to the fit using eq. 5.1 with $C_{\mathrm{g}}^{'2}/k = 8 \cdot 10^{-22}$ F^2/Nm and $\Gamma \approx 10$ GHz. The data are in fair agreement with the model.

stiffer, resulting in a sign change of Δf and the transition from a frequency softening to frequency hardening, in qualitative agreement with Eq. 5.1 (Fig. 5.5a).

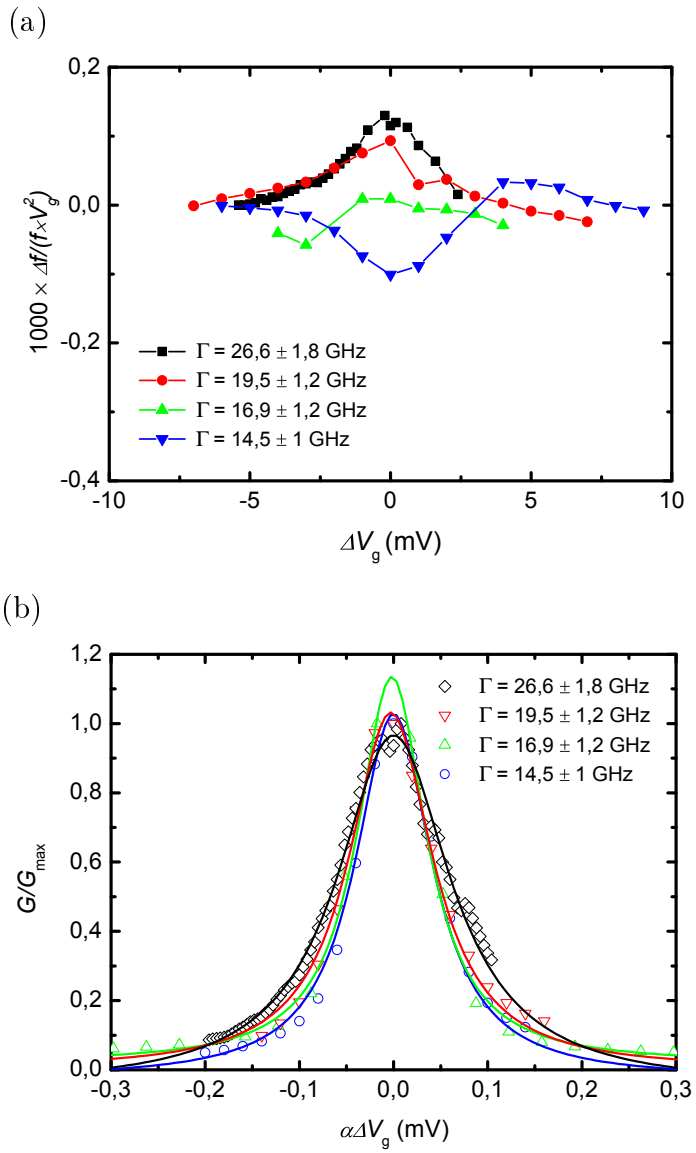

Figure 5.5: Modulation of the resonance frequency *via* tunneling rate Γ: (a) Scaled frequency shift $\Delta f / \left(f \cdot V_g^2\right)$ for different Coulomb peaks, i.e. tunneling rates Γ, with a fixed dot capacitance $C_{\mathrm{dot}} = 260$ aF (device 1). The tunneling rates Γ are estimated from the lineshape of the respective Coulomb peaks using Eq. 5.5 (b).

5.3 Dissipation induced by SET in carbon nanotube NEMS

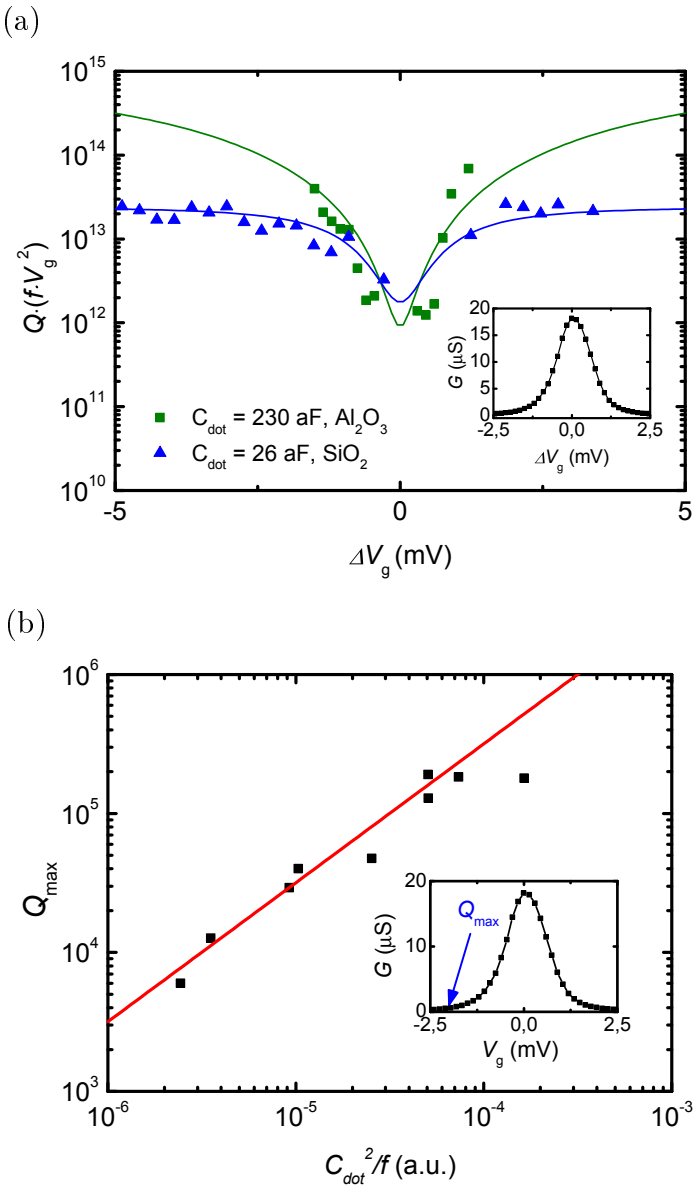

Figure 5.6: Modulation of the Q-factor *via* dot capacitance C_{dot}: (a) Scaled quality factor $Q \cdot f \cdot V_g^2$ for different dot capacitances, with comparable tunneling rates Γ. The solid lines are guide to the eye and the inset shows a representative Coulomb peak centered at $\Delta V_{\mathrm{g}} = 0$. (b) Maximum quality factor Q_{max} at minimal tunnel current G ($|\Delta V_{\mathrm{g}}| \gg 0$) vs. C_{dot}^2/f for all measured devices. The solid red line represents the fit with eq. 5.2 with $C_{\mathrm{g}}'^2/k = 1 \cdot 10^{-21}$ F^2/Nm and $\Gamma \approx 10$ GHz. Our findings are in good agreement with the model.

Fig. 5.6a depicts the effect of SET on the dissipation of the CNT NEMS, i.e. the Q factor (scaled with $f \cdot V_g^2$), for devices with different dot capacitances. From Eq. 5.2, we expect an increase of the Q factor with increasing capacitance in the limit of suppressed SET through the dot. Indeed, in a region of suppressed SET ($|\Delta V_g| \gg 0$),the Q factor is larger for devices with higher dot capacitance (Fig. 5.6a). The tunnel coupling $\Gamma \approx 10$

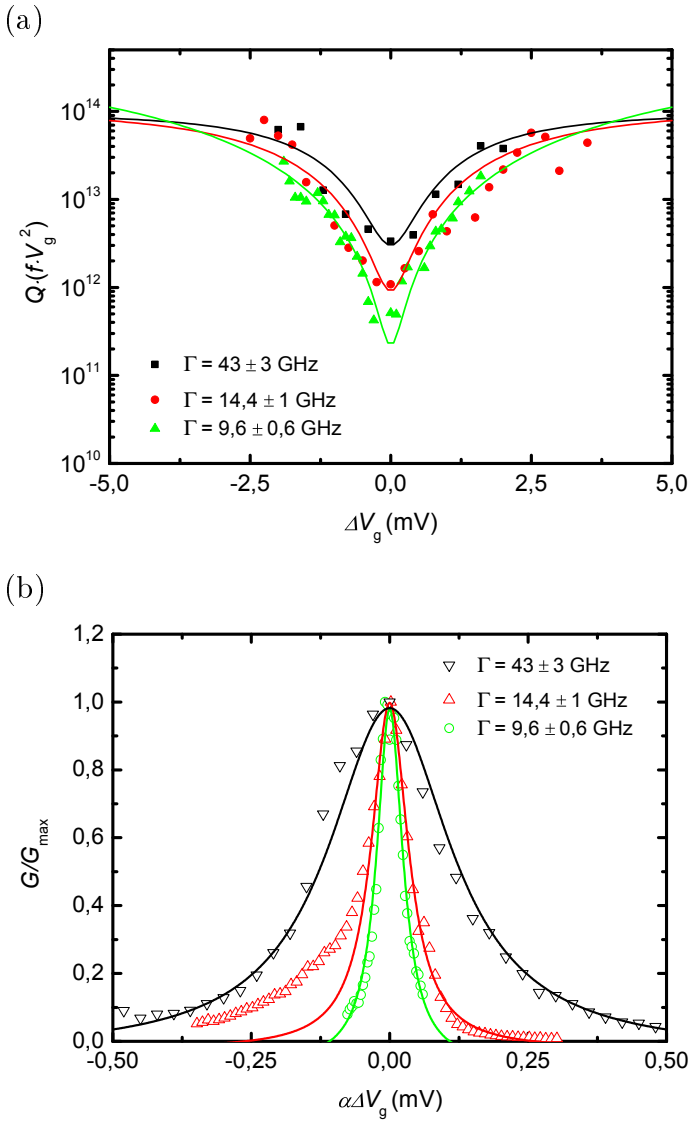

Figure 5.7: Modulation of the Q-factor *via* tunneling rate Γ: (a) Scaled quality factor $Q \cdot f \cdot V_g^2$ for different Coulomb peaks, i.e. different tunneling rates Γ, with a fixed dot capacitance $C_{\mathrm{dot}} = 160$ aF (device 2). The solid lines are guide to the eye and the tunnel coupling Γ is estimated from the lineshape of the respective Coulomb peaks using Eq. 5.5(b).

GHz and the conductance $G(V_g) \approx 18$ μS are comparable for both traces. Fig. 5.6(b) shows the Q factor in the limit of suppressed SET ($|\Delta V_g| \gg 0$) as a function of C_{dot}^2/f for all measured devices. The fit with Eq. 5.2 yields $C_g'^2/k = 1 \cdot 10^{-21}$ F^2/Nm and $\Gamma \approx$ 10 GHz which is consistent with the fitting parameters of Fig. 5.4b and previous experiments [74, 61, 103].

Moreover, we expect from Eq. 5.2 and previous experiments [74, 61] an enhanced electromechanical dissipation in a given device if the conductance G (i.e. the tunnel current) and the tunnel resistance at the nanotube-electrode interface $R \sim 1/\Gamma_d$ are increased, in analogy to the current dissipation in a simple resistance. Indeed we observe increased dissipation (decreased Q factor) when tuning the gate voltage through a Coulomb peak (Fig. 5.6a and 5.7a). In Fig 5.7a (device 2), this effect becomes more pronouced as we move to gate voltage regions with a smaller tunneling rate Γ, i.e. larger tunnel resistance at the nanotube-electrode interface, where we estimate the tunneling rate Γ from the lineshape of the respective Coulomb peaks (Fig. 5.7b). The dot capacitance C_{dot} yields 160 aF for this device and the height of the Coulomb peak are comparable for all traces ($G \approx 7$ μS).

Therefore, the CNT capacitance is the limiting factor for the dissipation in regions of suppressed SET, whereas the mean tunnel coupling and the tunneling current itself define the dissipation in regions of strong SET. Our results indicate that the current dissipation at the CNT-electrode interface is the dominant loss mechanism in our system.

5.4 Dissipation mechanisms in carbon nanotube NEMS

In the previous section, we described the effect of SET on the resonance frequency and the dissipation of a carbon nanotube NEMS at very low temperature. In the following we discuss the different dissipation mechanisms in a carbon nanotube NEMS. We will demonstrate that the current dissipation at the CNT-electrode interface is the dominant loss mechanism in such a system at cryogenic temperatures and that other mechanisms can be neglected (clamping losses, thermoelastic damping or interacting two level systems).

For this purpose, we study the frequency response and the dissipation induced by SET as a function of temperature for our carbon nanotube NEMS. Fig. 5.8a depicts the frequency shift Δf_{max} for $G_{max} = G(\Delta V_g = 0)$ whereas Fig. 5.8b shows the quality factor Q_{max} for $G_{min} = G(|\Delta V_g| \gg 0)$ as function of temperature. We find the following temperature dependance for both parameter:

$$\Delta f_{max} \sim T \tag{5.7}$$

$$Q_{max}^{-1} \sim T \tag{5.8}$$

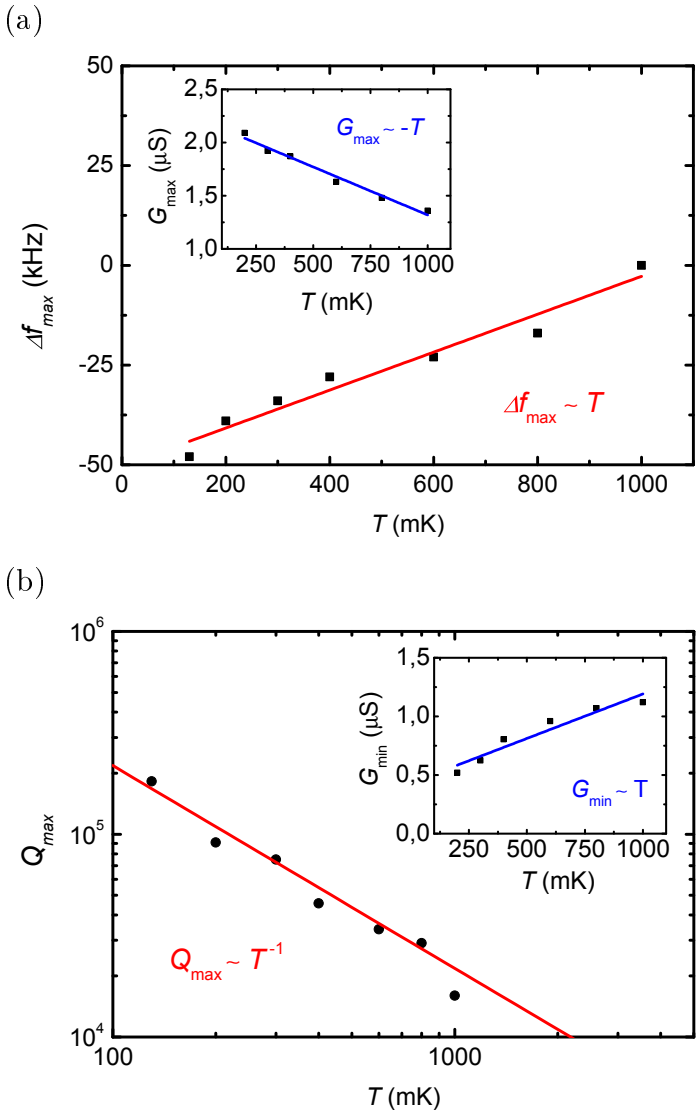

Figure 5.8: Temperature dependance: (a) Maximum frequency shift $\Delta f_{\max}$ at maximum tunnel current $G_{\max}$ ($\Delta V_g = 0$) vs. temperature for a device yielding $C_{\rm dot} = 160$ aF (device 2). The inset shows the evolution of $G_{\max}$ as a function of temperature.(b) Maximum quality factor $Q_{\max}$ at minimal tunnel current $G_{\min}$ ($|\Delta V_{\rm g}| = 1$mV) vs. temperature for a device yielding $C_{\rm dot} = 160$ aF (device 2). The inset shows the evolution of $G_{\min}$ as a function of temperature.

These observation however do not agree with previous experiments on carbon nanotube NEMS [75], lattice matched GaAs/InGaP/GaAs MEMS [106] and silicon single crystal NEMS [107] at cryogenic temperatures:

They reported a weak power law dependance for the quality factor yielding

$$Q^{-1} \sim T^{1/3} \tag{5.9}$$

which is in very good agreement with the quantum dissipation arising from interacting two-level systems (TLS) [108]. Moreover, resonant interactions between two-level systems (TLS) also lead to a shift of the resonance frequency, which reads [106, 107]

$$\frac{\Delta f}{f} \sim \log T \tag{5.10}$$

This suggests that the main dissipation mechanism in our suspended carbon nanotube resonators does not arise from quantum friction between interacting TLS.

Clamping losses, due to a transfer of strain energy from the double-clamped carbon nanotube beam into its supporting structure, are described by

$$Q^{-1}_{clamping} \approx \frac{dt^4}{L^5} \tag{5.11}$$

with the CNT diameter d, the CNT length L and the base thickness t (i.e. the thickness of the electrodes) [70].

Those losses are temperature independant and for the values $d \approx 1$ nm, $L \approx 1$ μm and $t \approx 100$ nm, we obtain $Q^{-1}_{clamping} \approx 10^{-7}$, which is at least two orders of magnitude smaller than the observed dissipation in our NEMS. We can therefore exclude clamping losses as main dissipation mechanism.

We now consider thermoelastic damping in a suspended CNT resonator. Mechanical vibrations can for instance induce a local change in volume of the CNT, creating localized expanded and contracted regions on the CNT. As a consequence of thermoelastic coupling a temperature gradient develops and a heat transfer from the expanded to the contracted regions occurs. The associated dissipation of the CNT resonator is then given by

$$Q^{-1}_{thermoelastic} \approx \frac{\alpha^2 T E}{C}\left(\frac{\omega\tau}{1+(\omega\tau)^2}\right) \tag{5.12}$$

with the temperature T, the Young's modulus E, the heat capacitance C, the thermal expansion coefficient α, the NEMS resonance frequency ω and the timescale τ of the heat transfer from hot to cold region, i.e. from expanded to contracted regions of the beam [70].

At temperatures around 1K, the heat capacitance evolves as $C \sim T$ [70, 109] and the thermal expansion coefficient yields $\alpha \approx -3 \cdot 10^{-7}\mathrm{K}^{-1} \cdot T$ [70, 110]. Therefore we have the following temperature dependance for thermoelastic damping at low temperature:

$$Q^{-1}_{thermoelastic} \sim T^2 \tag{5.13}$$

Moreover we have at $T = 1$ K, $E = 1$ TPa [70], $C \approx 10^{-5}$ J/Km^3 [70, 109], $\alpha \approx -3 \cdot 10^{-7}$ K^{-1} [70, 110], $\omega = 400$ MHz and $\tau \approx 4 \cdot 10^{-11}$ s [70]. Finally we have $Q^{-1}_{thermoelastic} \approx 10^{-6}$, which is at least an order of magnitude smaller than the dissipation observed in Fig. 5.6. Hence, thermoelastic damping cannot account for the observed temperature dependance and dissipation.

Last, we discuss the dissipation arising from SET through the CNT-electrode interface. As temperature increases the Coulomb blockade peak broadens and becomes smaller (Fig. 5.9). As a result $G_{\max} = G(\Delta V_g = 0)$ decreases whereas $G_{\min} = G(|\Delta V_g| = 1\text{mV})$ increases with temperature, as depicted in the insets of Figs. 5.8a and 5.8b. From the data fit we obtain $G_{\max} \sim -T$ and $G_{\min} \sim T$.

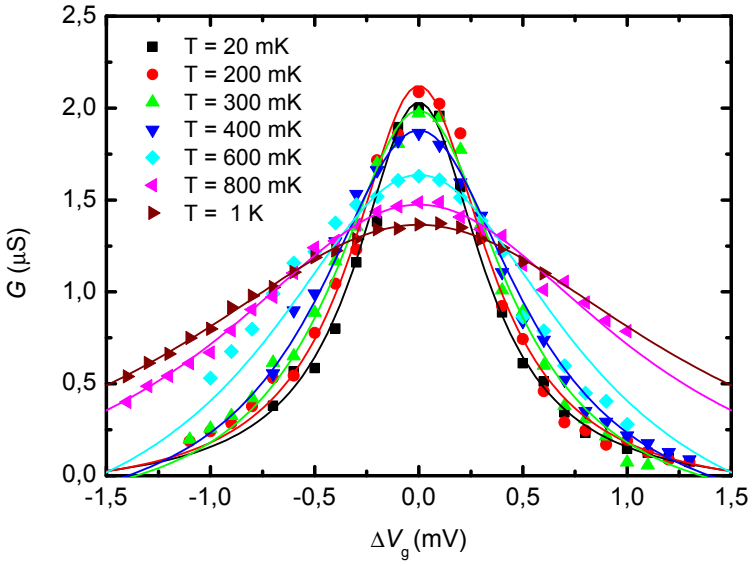

Figure 5.9: Evolution of the Coulomb blockade peak studied in Fig. 5.8(a) and 5.8(b) as a function of temperature

It was previously demonstrated that carbon nanotubes show Luttinger liquid behavior [111, 112, 113], where the conductance follows a characteristic power law dependence as a function of temperature

$$G(T) \sim T^{\alpha} \tag{5.14}$$

α being related to the Luttinger parameter g by $\alpha = (g-1+g-2)/2$ [111, 112]. We find $\alpha \approx 1$ and a Luttinger parameter of $g = 0.1$, which is close to previous measurements [111] and theoretical predictions [112, 113]. Comparing the temperature dependance of the conductance, the quality factor and the frequency shift we finally obtain

$$\Delta f_{\max} \sim -G_{\max} \tag{5.15}$$

$$Q^{-1}_{\max} \sim G_{\min} \tag{5.16}$$

which is in full agreement with Eqs. 5.1 and 5.2.

We can conclude that SET is the dominant dissipation mechanism for carbon nanotube based NEMS in a Coulomb blockade regime at cryogenic temperatures.

5.5 Conclusion and Outlook

Despite the good agreement between theory and experiment, we observe deviations from the model for some devices in Fig. 5.4b and 5.6b, which we attribute to variations in $C_g'^2/k$ and the tunneling rates Γ.

According to ref. [103], a good approximation for $C_g'^2/k$ is given by

$$C_g'^2/k \approx \left(C_g/Z\right)^2/k \tag{5.17}$$

with C_g being the gate capacitance, Z the CNT-gate distance and k the CNT's spring constant.

We studied two different device layouts: Single gated SiO_2 based CNT QD with an average gate capacitance of $C_g = 2 \pm 1$ aF and $Z = 700$ nm and single gated Al_2O_3 based CNT QD with an average gate capacitance of $C_g = 3 \pm 1$ aF and $Z = 300$ nm. C_g is estimated from the voltage separation of two adjacent Coulomb peaks (see Fig. 5.2) and Z is given by the sum of the oxide thickness and thickness of the metal electrodes (see section 5.1). With an average spring constant $k = 10^{-3}$ N/m (value extracted from ref. [74] and [103]) we obtain values for $C_g'^2/k = (6 \pm 2) \cdot 10^{-21}$ F^2/Nm, which is close to values obtained from the fit in Fig. 5.4b and 5.6b.

The above estimation shows that we indeed have variations in $C_g'^2/k$, caused by a small spread in capacitance values C_g and CNT-gate distance Z, which leads to deviations of some devices from the model fit.

Moreover we have to consider an uncertainty in the estimation of the tunneling rates Γ. Although Eq. 5.5 provides a good approximation for Γ, we obtain an uncertainty of $\delta\Gamma \approx 7\%$, which could also account for the above mentionned deviation from the model.

We have demonstrated that single-electron tunneling causes a modulation of the resonance frequency (Section 5.2) and the dissipation (Section 5.3) in carbon nanotube NEMS at low temperature, depending on the dot capacitance and the tunnel coupling to the leads [19]. The experimental data are in close agreement with theoretical predictions [74, 61]. Based on this evidence one could significantly increase the quality factor Q up to 10^6, by choosing high-κ dielectrics (HfO_2 or ZrO_2) and improving the tunnel contact to the metal leads.

A study as a function of temperature reveals that single-electron tunneling is the dominant loss mechanism at low temperature for carbon nanotube NEMS (Section 5.4), which stands in contrast to previous experiments [75, 106, 107] were dissipation is due to interacting two-level systems (TLS) [108].

It was proposed in theoretical calculation that one can use such high$-Q$ CNT NEMS as magnetic torque or force detectors for nanoparticles [18] or single molecule magnets [114, 115] grafted to the CNT NEMS. In principle one can achieve a sensitivity of one μ_{B} at low temperature, whereas the best magnetometers, for instance the micro-SQUID, only have a sensitivity of 10^3 μ_{B} [54]. Finally, such molecular quantum spintronic device would allow single spin manipulation on a molecular level.

Chapter 6

Strong Spin-Phonon Coupling of a Single Molecular Spin to a Carbon Nanotube NEMS

The magnetization reversal of a single spin at low temperature is mediated by the exchange of an energy quantum between the spin system and a thermal reservoir. Such magnetic relaxation processes were first discussed for a crystal of paramagnetic transition ions [50]. It was suggested that mechanical vibrations of the crystal lattice ('phonons') modulate the crystal electric field of the magnetic ion, thus inducing a so called 'direct' relaxation between two different spin states [50, 116, 117]. Direct relaxation has also been predicted for single molecule magnets (SMM) with a large spin and a high magnetic anisotropy [50, 36, 118, 119, 120] and was first demonstrated in a Mn12 acetate crystal [121]. The spin-lattice relaxation time for such a direct transition is essentially limited by the phonon density of states at the spin resonance and the spin-phonon coupling [50]. In a macroscopic 3D system, like a SMM crystal, the phonon energy spectrum is continuous whereas in a 1D system, like a suspended carbon nanotube (CNT), the energy spectrum is discrete and can be engineered to an extremely low density of states [122]. An individual SMM, coupled to a suspended carbon nanotube, should therefore exhibit extremely long relaxation times [122] and the reduced size and dimensionality of the system should result in a strongly enhanced spin-phonon coupling [114, 115]. In this section, we will provide the first experimental evidence for a strong spin-phonon coupling between a single molecule spin and a carbon nanotube resonator. This could ultimately enable coherent spin manipulation and quantum entanglement [114, 115].

Carbon nanotubes (CNT) have become an essential building block for nanoelectromechanical systems (NEMS). Their low mass and high Young's modulus give rise to high oscillation frequencies for transverse [65, 123] and longitudinal modes [68, 79, 67], therefore enabling ground state cooling with state of the art cryogenics and a large zero point motion in the quantum regime [1]. Moreover, the strong coupling between nanomechanical motion and single-electron tunneling in high-Q CNT NEMS allows an electronic actuation and detection of its nanomechanical motion [19, 74, 61, 75]. As such, a CNT NEMS can be used for ultrasensitive mass sensing [124, 125, 5] or as magnetic torque detectors for single spin systems [18].

A single spin, strongly coupled with a CNT NEMS in the quantum regime, could serve as elementary qubit in quantum information processing. It has been recently suggested that a strong coupling between a quantum CNT NEMS and a single electron spin would enable basic qubit control and the implementation of entangled states [122]. In this framework, coupling a single-molecule magnet (SMM) to the quantized nanomechanical motion of a CNT NEMS is a very attractive alternative [11]. Chemical engineering allows the synthesis of perfectly identical SMM's and integration into nanoscale devices such as electromigrated junctions [126, 127, 47] or carbon nanotube transistors [48]. A large magnetic moment and a strong, uniaxial magnetic anisotropy enable for instance quantum tunneling of magnetization [128, 129] or quantum phase interference [42], and yields coherence times on the order of seconds in crystalline form [43]. Moreover, it was recently predicted that the spin-phonon coupling between an SMM and a quantum CNT NEMS is strong enough to perform coherent spin manipulation and quantum entanglement of a spin and a resonator [114, 115].

In this chapter, we first present the spin relaxation in a $TbPc_2$ SMM coupled to a carbon nanotube (Section 6.2) and provide evidence for a quantized longitudinal stretching mode in carbon nanotube NEMS (Section 6.3). We then establish a strong spin-phonon coupling between both systems, that is, between an individual $TbPc_2$ SMM and the quantized high-Q longitudinal stretching mode (LSM) of the CNT resonator (Section 6.4). The strong spin-phonon coupling presented here would enable the quantum control of magnetization at a single-phonon level [122, 114] and the entanglement of a single spin with quantized mechanical motion [122, 115].

6.1 Nanofabrication and measurement setup

Here we will briefly recall the fabrication of high capacitance carbon nanotube resonators (see Section 4.2.3 for details) and the grafting procedure for $TbPc_2$* SMM (see Section 4.7 for details).

A 1 μm-wide metallic local gate is patterned by optical deep ultraviolet (DUV) lithography and subsequent e-beam evaporation of Mo (20 nm) on a degenerately p-doped silicon wafer with a 300 nm thick layer of thermal SiO_2. A layer of 100nm of Al_2O_3 is then deposited by atomic layer deposition. Using optical DUV lithography and e-beam evaporation of Mo (20nm) and Pt (160nm), source-drain electrodes are aligned above the local gate. Suspended CNT's are finally grown by CVD at 800°C from a CH_4 feedstock and Fe/Mo catalyst spots patterned on the source-drain electrodes next to the junction (Section 4.2.3). The CNT device length is approximately 800 nm.

The pyrene-substituted $TbPc_2$* were synthesized as reported in Ref. [37]. The $TbPc_2$ powder was dissolved in a solution of dichloromethane with a $TbPc_2^*$ concentration of 10^{-7} mol/L and drop casted onto the sample. The droplet was subsequently dried in

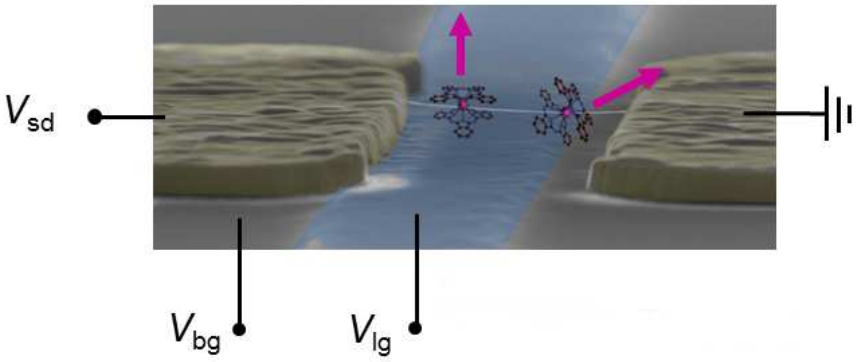

Figure 6.1: $TbPc_2$* Single Molecule Magnet grafted to a carbon nanotube NEMS (device *LSM-hybrid*)

a critical point dryer, to avoid destruction of the suspended CNT's through capillarity effects (Section 4.7). In following we will study a hybrid carbon nanotube-molecule device designed by those means labeled *LSM-hybrid*.

Conductance measurements on the device *LSM-hybrid* were carried out in He_3/He_4 dilution refrigerator with a base temperature of 20 mK. The refrigerator is equipped with a 3D vector magnet, generating up to 1.4 T and up to 0.5 T in the plane of the sample, with a maximum sweep rate of 250 mT/s, and an out-of-plane field of 0.15 T. The transport measurements were made with an ADWIN real-time data acquisition system (Section 4.6.2).

6.2 Spin-lattice relaxation in $TbPc_2$* SMM coupled to a carbon nanotube

6.2.1 Magnetization reversal in a $TbPc_2$* SMM

We study the magnetization reversal of a pyrene-substituted bis(phthalocyaninato) terbium(III) SMM (also $TbPc_2$* SMM, Fig. 6.2) grafted to a CNT resonator [37]. The $TbPc_2$* is a rare earth SMM in which the magnetic moment is carried by a single Tb^{3+} ion sandwiched between two organic phthalocyanine (Pc) ligand planes [49]. The $TbPc_2$* has a $S = 1/2$ radical delocalized over the Pc ligand planes. Due to π-π interaction, this radical can easily hybridize with the π-electrons of any form of sp_2-carbon without affecting the magnetic properties of the Tb^{3+} ion [48, 37, 38]. The highly anisotropic $4f$ shell of the Tb^{3+} ion and its intrinsically strong spin-orbit coupling results in a magnetic ground state of $J = 6$ and a pronounced uniaxial magnetic anisotropy, with an easy axis perpendicular to the Pc planes (Fig. 6.2a).

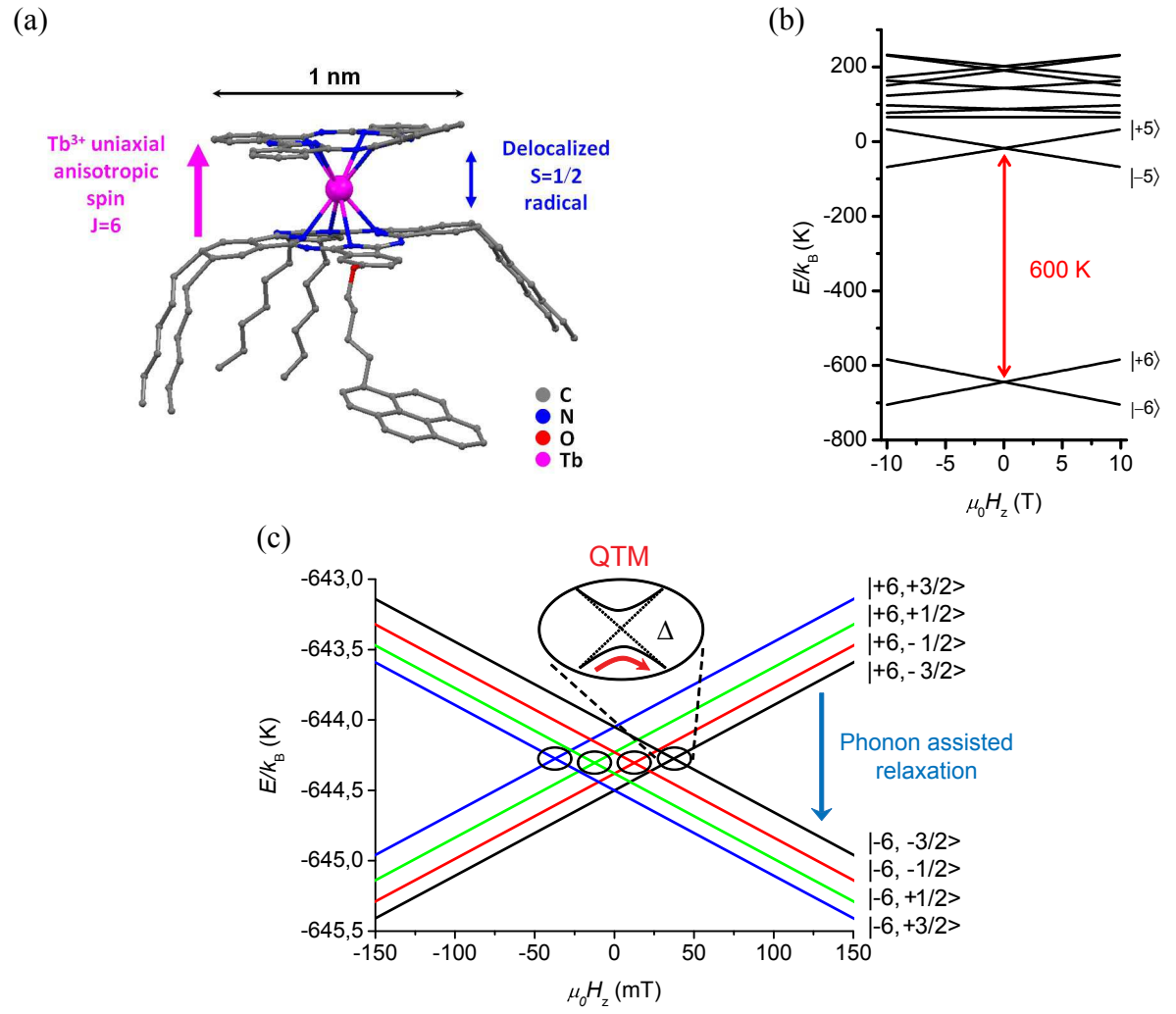

Figure 6.2: $TbPc_2$* Single Molecule Magnet: (a) Schematic representation of a pyren-substituted $TbPc_2$* SMM. A Tb^{3+} ion (pink) is sandwiched between two organic phthalocyanine (Pc) ligand planes. The oxidation state of the Tb^{3+} ion generates a spin $S = 1/2$ radical delocalized over the phthalocyanine planes which can interact with any kind of sp_2 carbon via π-π interaction. A pyrene arm and six hexyl groups further enhance the grafting efficiency (b) Full Zeeman diagram of the $TbPc_2$* SMM. Due to the highly anisotropic $4f$-shell of the Tb^{3+} ion and a strong spin-orbit coupling, the $TbPc_2$* can be considered as an Ising like spin system, with a high magnetic anisotropy and a ground state doublet $J_z = \pm 6$. Modified figure from [48] (c) Zeeman diagram of the $TbPc_2$* SMM's ground state doublet. The strong hyperfine coupling with the nuclear spin $I = 3/2$ in the Tb^{3+} ion, splits the ground state doublet $J_z = \pm 6$ into four states each.

The ground state doublet $J_z = \pm 6$ is separated from the excited states by several hundreds of Kelvin (Fig. 6.2b), which makes the $TbPc_2$* an Ising like spin system at low temperature ($T < 5$ K) and small magnetic field ($B < 10$ T) [49]. A strong hyperfine interaction with the nuclear spin $I = 3/2$ of the Tb^{3+} ion, splits the ground state doublet $J_z = \pm 6$ into four states each (Fig. 6.2c). Finally, the ligand field generates a small transverse magnetic anisotropy resulting in avoided level crossings (black circles in Fig. 6.2c) [49].

At cryogenic temperatures, the magnetization reversal can occur via two different processes (Section 2.2). Around zero magnetic field, the avoided level crossings allow for quantum tunneling of magnetization $|J_z, I_z\rangle \rightarrow |-J_z, I_z\rangle$ [48, 49]. At high magnetic fields the magnetization reverses through a direct relaxation process involving non-coherent tunneling events combined with the emission or absorption of phonons [48] (Fig. 6.2c).

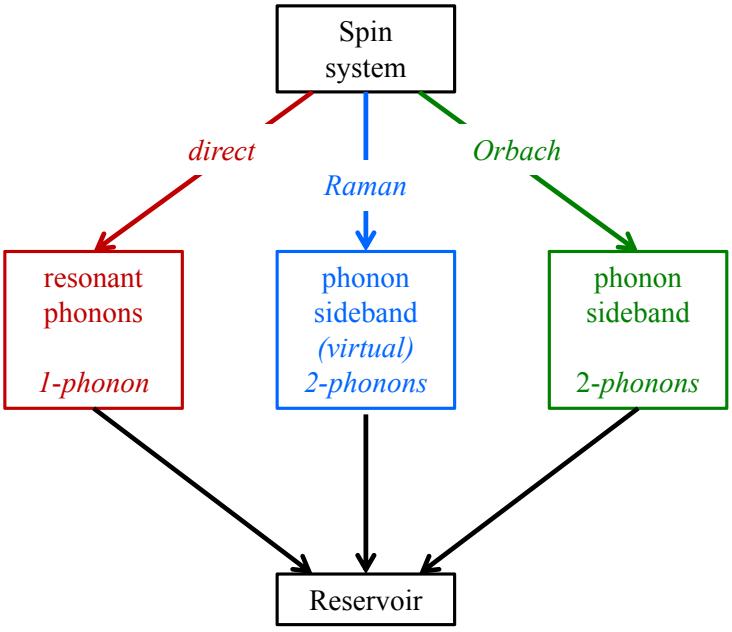

Figure 6.3: Spin-phonon relaxation processes in $TbPc_2$* single molecule magnets: A *direct* one-phonon process dominates at lowest temperatures, whereas two-phonon *Orbach* and *Raman* processes take over as the temperature increases. The phonon energy is then transfered to a thermal reservoir. The arrows indicate the direction of the energy transfer. Figure inspired from [50].

Spin-phonon relaxation processes in $TbPc_2$* SMM are due to a modulation of the molecule's crystal electric or ligand field by the motion of charged ions in a surrounding lattice, so called phonons. Due to strong spin-orbit interactions in the Tb^{3+} ion, the fluctuating ligand field can induce transitions between different spin states. Different

transition mechanisms can contribute to the molecule's magnetization reversal, involving the emission or absorption of one or two phonons as depicted in Fig. 6.3. At the lowest temperature, the spin-lattice relaxation is typically dominated by the one-phonon *direct* process. As the temperature increases, higher order two-phonon *Orbach* and *Raman* processes, involving a real and virtual excited state (or phonon sideband) respectively, contribute to the magnetic relaxation (see Section 2.2 and [50]). In the following we will now discuss the time scale for spin-lattice relaxation in the case of a *direct* transition in a $TbPc_2$* SMM coupled to a carbon nanotube.

6.2.2 Spin-lattice relaxation time for a *direct* process

The spin relaxation time associated to a *direct* transition is essentially given by the phonon energy and the phonon density of states at the spin resonance as well as the spin-phonon coupling (see Section 2.2.3 and [50]). The transition probability $1/\tau$ yields

$$\frac{1}{\tau} \sim |\mathcal{H}_{\mathrm{lf}}^{1}|^2 D(\omega) \left[1 + exp\left(\frac{\hbar\omega}{k_{\mathrm{B}}T}\right)\right] \tag{6.1}$$

where $|\mathcal{H}_{\mathrm{lf}}^{1}|$ is the matrix element coupling the spin states to the phonons and $D(\omega)$ the phonon density of states at the phonon frequency ω. The relaxation time strongly depends on the dimension of the associated phonon bath, as we will describe in the following.

3D phonons

In a $TbPc_2$* coupled to a non-suspended carbon nanotube, the direct relaxation is mainly enabled by 3D bulk phonons in the amorphous SiO_2 [48, 130]. The coupling is mediated by the carbon nanotube, which is mechanically coupled to the $TbPc_2$* spin and is in thermal contact with the SiO_2 phonons [130]. The energy distribution of 3D bulk phonons in SiO_2 is continuous and the density of states (DOS) for a longitudinal acoustic phonon mode is given in the Debye approximation by

$$D\left(\omega\right) = \frac{\hbar\omega^3}{2\pi^2 v_l^3 \left[\exp\left(\frac{\hbar\omega}{k_{\mathrm{B}}T}\right) - 1\right]} \tag{6.2}$$

where v_l is the group velocity of a longitudinal phonon. Therefore, one observes a finite phonon DOS in SiO_2 at all energies (Fig. 6.4a) and the rate for a direct relaxation in the $TbPc_2$* follows the relation derived in Section 2.2

$$\frac{1}{\tau} \sim \left(\hbar\omega\right)^3 coth\left(\frac{\hbar\omega}{2k_{\mathrm{B}}T}\right) \sim H^3 coth\left(\frac{\beta H}{2k_{\mathrm{B}}T}\right) \tag{6.3}$$

with the phonon energy $\hbar\omega = g\mu_0\mu_B\Delta m_J H_z = \beta H$ and H the magnetic switching field.

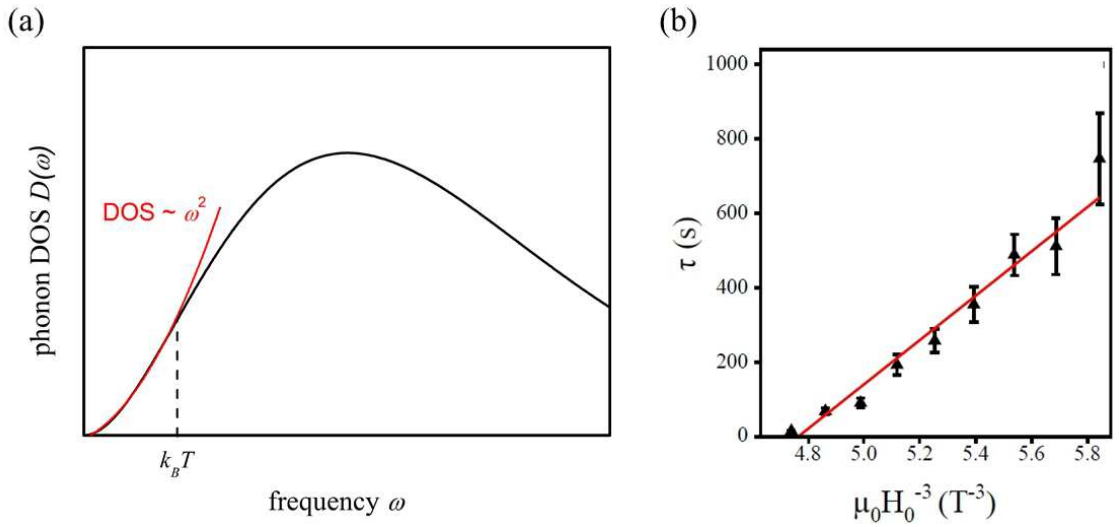

Figure 6.4: Spin-phonon relaxation processes in a $TbPc_2$* coupled to a non-suspended carbon nanotube (3D phonons): (a) Phonon density of states for a longitudinal phonon mode in a bulk material (b) Relaxation time measured as a function of the magnetic switching field H_0, i.e. the phonon energy $\hbar\omega$. Figure extracted from [130]

As demonstrated by Urdampilleta et al. [130], the relaxation time of a $TbPc_2$* coupled to a non-suspended carbon nanotube indeed follows the expected H^{-3} dependance at very low temperature given by equation 6.3 (Fig. 6.4b).

1D phonons

An individual $TbPc_2$* SMM grafted on a suspended CNT however is physically decoupled from the bulk phonons in the substrate. As a consequence the $TbPc_2$* SMM can only couple to the one-dimensional phonons of the carbon nanotube. Phonons in a carbon nanotube typically exhibit a discrete energy spectrum (Fig. 6.5b) which can be engineered to a very low density of states at the spin resonance [122].

It has been recently demonstrated that high frequency transverse [65, 66] and longitudinal phonon [68, 79, 67] modes in a carbon nanotube are quantized at cryogenic temperatures and can be found in their quantum mechanical ground state if the average thermal occupation $\tilde{n} = k_B T/\hbar\omega_R$ becomes smaller than 1, i.e. for $\hbar\omega_R > k_B T$ (Fig. 6.6).

In thermal equilibrium, the quantized energy levels of such a harmonic oscillator have an occupation probability given by [1]

$$P_n = \left(e^{-\frac{\hbar\omega_r}{k_B T}}\right)^n \left(1 - e^{-\frac{\hbar\omega_r}{k_B T}}\right) \tag{6.4}$$

where n is the oscillator's quantum number.

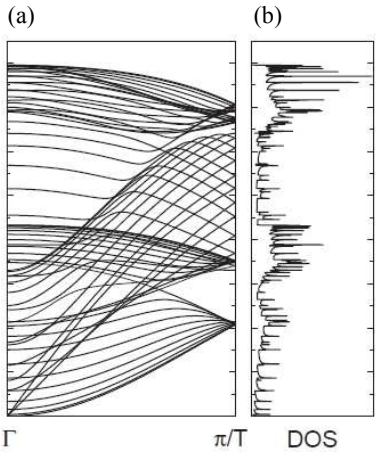

Figure 6.5: Phonon dispersion relation (a) and density of states (b) in an armchair (10,10) carbon nanotube. Figure extracted from [131]

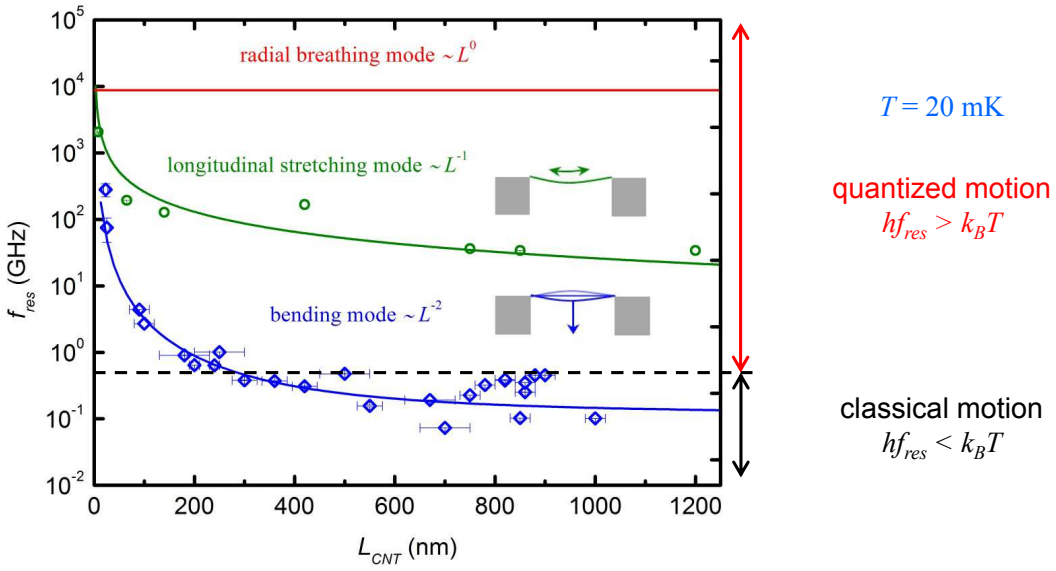

Figure 6.6: Vibrational modes in a carbon nanotube resonator as a function of the device length L at $T = 20$ mK. For $\hbar\omega_R > k_B T$, mechanical modes reach a quantum state of motion and can be found in their quantum mechanical ground state. Upon this "ground-state cooling", excited vibrational states become depleted, thus yielding an extremely low density of states. Bending mode frequencies (blue open squares) are compiled from [1, 19, 65, 66], LSM frequencies (green circles) from [66, 67, 20, 68]. The solid lines correspond to the calculated length dependance as described in [68].

According to equation 6.4, as the harmonic oscillator reaches the ground state for $\hbar\omega_R > k_B T$, excited vibrational states ($n \geq 1$) become almost depleted, which results in an extremely low density of states (Fig. 6.7). In consequence, one can expect strongly enhanced spin relaxation time for a single $TbPc_2$* SMM coupled to such quantized mechanical mode of motion in a suspended carbon nanotube.

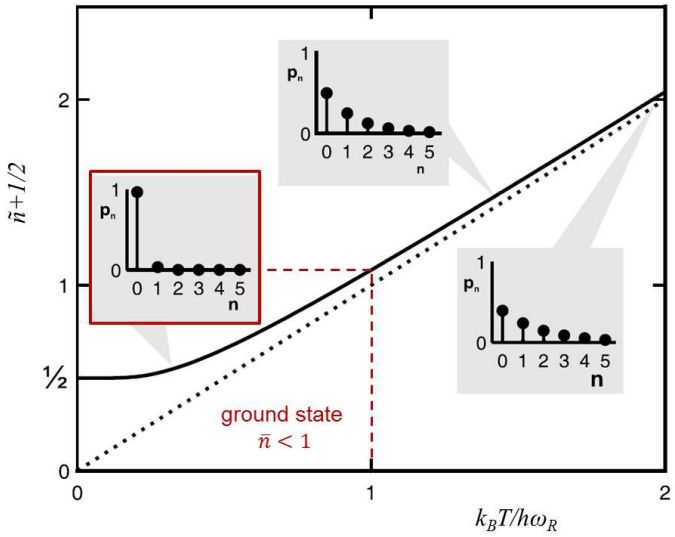

Figure 6.7: Average thermal occupation $\tilde{n} + \frac{1}{2}$ vs temperature T. The inset show the occupation probability P_n for $k_B T/\hbar\omega_R = 0.3$, 1.44 and 2. Figure from [1]

In the following sections, we will provide evidence for a longitudinal stretching mode vibration in its quantum mechanical ground state (Section 6.3) and establish a strong coupling between the latter and the spin of a single $TbPc_2$* SMM grafted to the suspended carbon nanotube (Section 6.4).

6.3 Evidence for quantized longitudinal stretching modes in carbon nanotube NEMS

In this section we will provide evidence for a longitudinal stretching mode in the hybrid nanotube-molecule device *LSM-hybrid* (Fig. 6.8). We will probe its phonon energy, linewidth as well as the electron-phonon coupling.

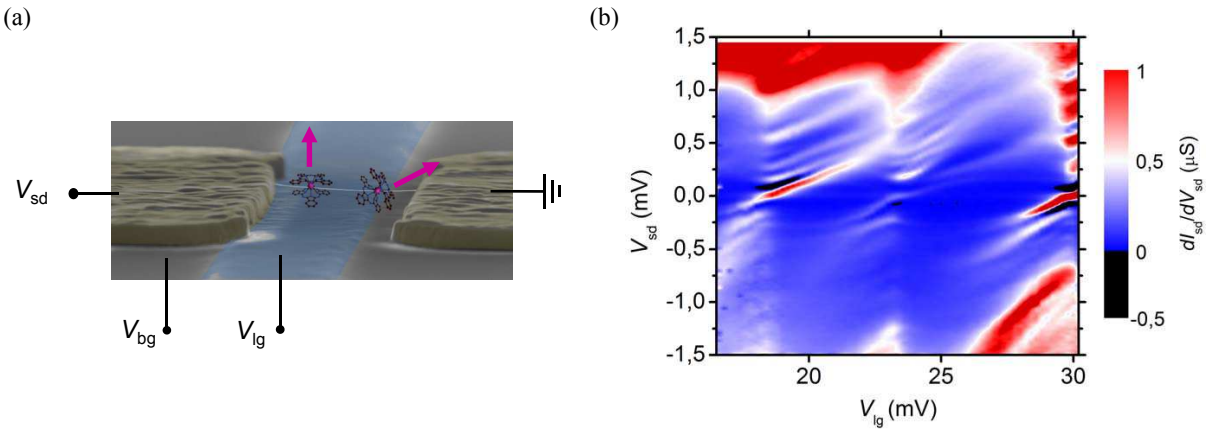

Figure 6.8: Hybrid nanotube-molecule device *LSM-hybrid*. (a) False color SEM image and (b) stability diagram of the hybrid nanotube-molecule device in the few electron regime at a temperature $T = 20$ mK and a magnetic field along the the nanotube's axis of $H_x = 1.4T$.

6.3.1 Electronic actuation and detection for longitudinal stretching modes

Single-electron tunneling (SET) onto the CNT quantum dot shifts the equilibrium position of the CNT along the CNT's axis by an amount proportional to the electron-phonon coupling g [68]. For an intermediate electron-phonon coupling $g \sim 1$, the electron therefore effectively tunnels into an excited vibrational state (Fig. 6.9). If the tunnel rate Γ_{out} is larger than the relaxation rate γ into the vibrational ground state, the electron tunnels out of the dot, resulting in equidistant excited states in the region of SET, running parallel to the edge of the Coulomb diamond (black arrows Fig. 6.10) [68, 79].

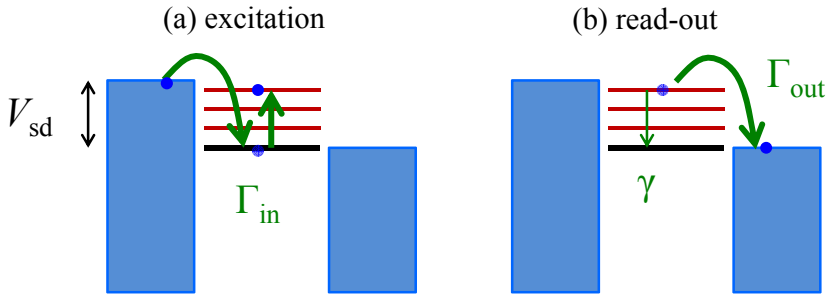

Figure 6.9: Electronic actuation and readout of longitudinal stretching modes (see text and section 3.3.1).

For large electron-phonon coupling $g \gg 1$, one observes additionally a current sup-

pression at low bias, a phenomenon known as Franck-Condon blockade [67]. It was also demonstrated, that one can pump excited vibrational states in a Coulomb-blockade regime by higher-order co-tunneling processes [79].

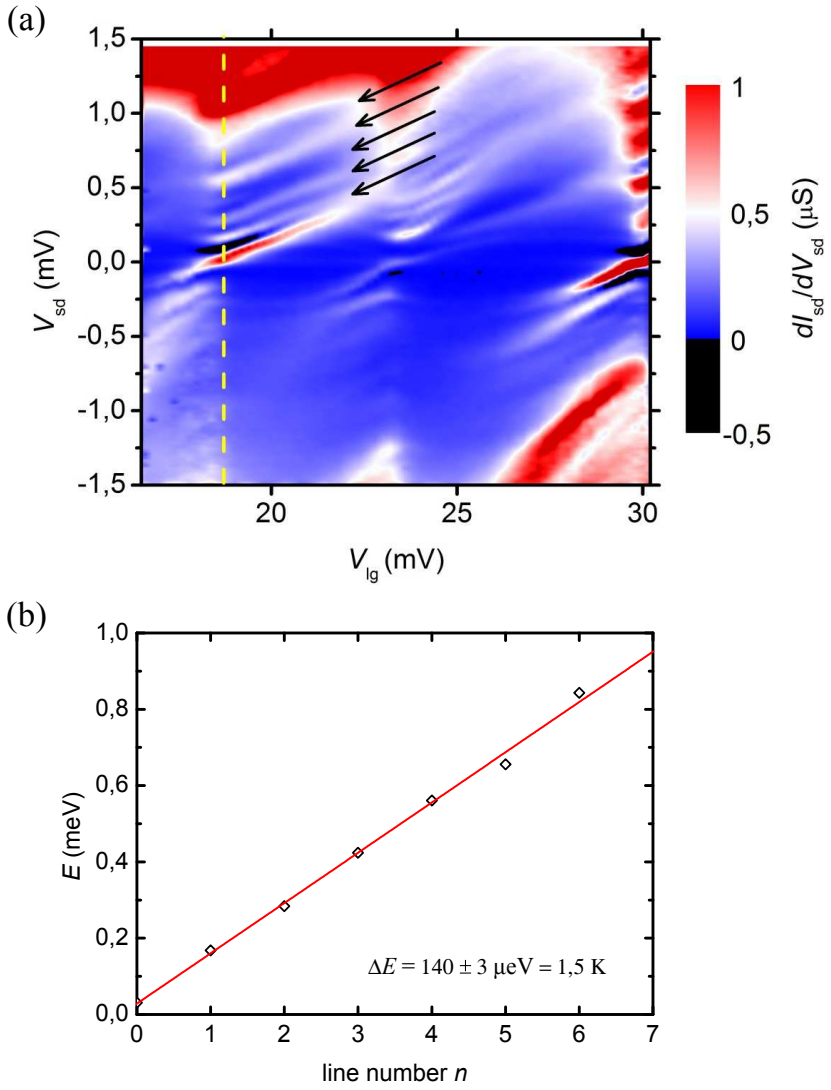

Figure 6.10: Phonon energy and linewidth of a LSM mode in device *LSM-hybrid*: (a) Stability diagram of the CNT showing the differential conductance as a function of gate and bias voltages at $T = 20$ mK and a longitudinal magnetic field of $H_x = 1.4$ T. The black arrows indicate the excited vibrational states attributed to a LSM, as described above. (b) Energy of excited vibrational states (black squares) vs. the excitation line number n at $V_{\mathrm{lg}} = 18$ mV (dashed yellow line). A linear fit suggests a LSM frequency of $\Delta E_{\mathrm{vib}} = 140\mu$eV, which is consistent with the measured CNT length of $L = 800$ nm.

6.3.2 Phonon energy and linewidth

For the device presented in this chapter (Fig. 6.8a), we observe a spectrum of equidistant excited states in the region of SET (black arrows in Fig. 6.10a) with an average energy separation and phonon energy of $\hbar\omega_{\mathrm{ph}} = 140\mu\mathrm{eV} = 1.5$ K (Fig. 6.10b). In order to reduce the current noise induced by the motion of $TbPc_2$* SMM's grafted to the resonator, the measurement was performed in a magnetic field along the nanotube axis of $H_x = 1.4$ T to "pin" the molecules magnetic moments. According to equation 3.31, $\hbar\omega_{\mathrm{ph}} = 110\ \mu\mathrm{eV/L}\ [\mu\mathrm{m}]$, the obtained phonon energy corresponds to a carbon nanotube length $L_{\mathrm{CNT}} = 850$ nm, which is consistent with the *measured* carbon nanotube length $L_{\mathrm{CNT}}^{\mathrm{meas}} = 800$ nm (Fig. 6.8a). From the average thermal occupation of this harmonic oscillator mode $\tilde{n} = k_{\mathrm{B}}T/\hbar\omega_R \approx 0.013$, we can deduce that the resonator is in its quantum mechanical ground state. As such, we expect a very low energy density of states for excited vibrational states with $n \geq 1$.

The quality factor is given by $Q = \omega/(2\pi\gamma)$, where γ is the relaxation rate into the ground state. In order for the vibrational states to be visible in SET, we should have $\Gamma_{\mathrm{out}} > \gamma$. The tunnel current at the edge of the Coulomb diamond I gives an approximation of the tunneling rate $\Gamma_{\mathrm{out}} = I/e$. For tunnel current at the edge of the Coulomb diamond of $I \approx 50$ pA, we find a tunneling rate $\Gamma_{\mathrm{out}} \approx 310$ MHz. We can determine a lower boundary for the quality factor $Q > \omega_{\mathrm{ph}}/2\pi\Gamma_{out} \approx 110$ (see Section 3.3.1), equivalent to an upper boundary for the linewidth of excited phonon states of $\delta E_{\mathrm{ph}} \lesssim 15$ mK. The quality factor Q exceed values from earlier measurements by a factor of 3 [79] and are the highest values reported in literature.

6.3.3 Electron-phonon coupling

We can estimate the magnitude of the electron-phonon coupling from the normalized conductance intensity of the excited vibrational states in the SET region (see Section 3.3.1 and [67]). For equilibrium phonons, the normalized conductance follows a Poisson distribution and is given by

$$\left(\frac{dI_{\mathrm{sd}}}{dV_{\mathrm{sd}}}\right)_n^{\mathrm{norm}} \sim \frac{e^{-g}g^n}{n!}$$

where n is the mode number and g the electron-phonon coupling.

In Fig. 6.11, fitting the normalized intensity with equation 3.32 yields a coupling factor of $g = 0.45 \pm 0.2$. Using equation 3.30 we find a carbon nanotube diameter of $d_{\mathrm{CNT}} \approx 1.6$ nm, which is in perfect agreement with the mean diameter $d_{\mathrm{CNT}}^{mean} \approx 1.6$ nm of carbon nanotubes grown from Fe/Mo catalyst and a methane feedstock (see Section 4.3.2).

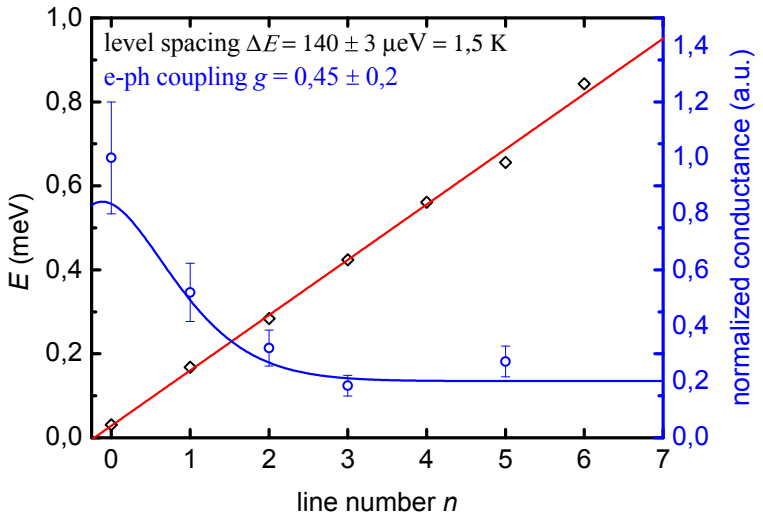

Figure 6.11: Electron-phonon coupling for a LSM phonon in th device *LSM-hybrid*: Normalized conductance (blue dots) of excited vibrational states vs. the excitation line number n at $V_{lg} = 18$ mV (dashed yellow line in Fig. 6.10a). From a fit with equation 3.32, we deduce an electron-phonon coupling of $g = 0.45 \pm 0.2$.

We now demonstrate that this high-Q longitudinal phonon mode enables the magnetization reserval of a single $TbPc_2$ and thus revealing a strong spin-phonon coupling.

6.4 Strong coupling of a single $TbPc_2$* spin to a quantized longitudinal resonator mode

In this section, we will demonstrate the coupling of the spin of a $TbPc_2$* to the quantized longitudinal motion of the carbon nanotube by magnetoconductance measurements in the device *LSM-hybrid* depicted in Fig. 6.12. We will first describe the mechanism coupling the spin to the quantized longitudinal motion (Section 6.4.1) and describe the current detection of the $TbPc_2$* magnetization reversal developped by Urdampilleta *et al* [48, 130] (Section 6.4.2). We then report on the nuclear spin dependent magnetization reversal of a single $TbPc_2$* spin induced by the strong coupling with a quantized longitudinal stretching mode (Section 6.4.3). We finally assess the magnitude of this coupling, which could enable the entanglement of a single (nuclear) spin and quantum harmonic oscillator (Section 6.4.4).

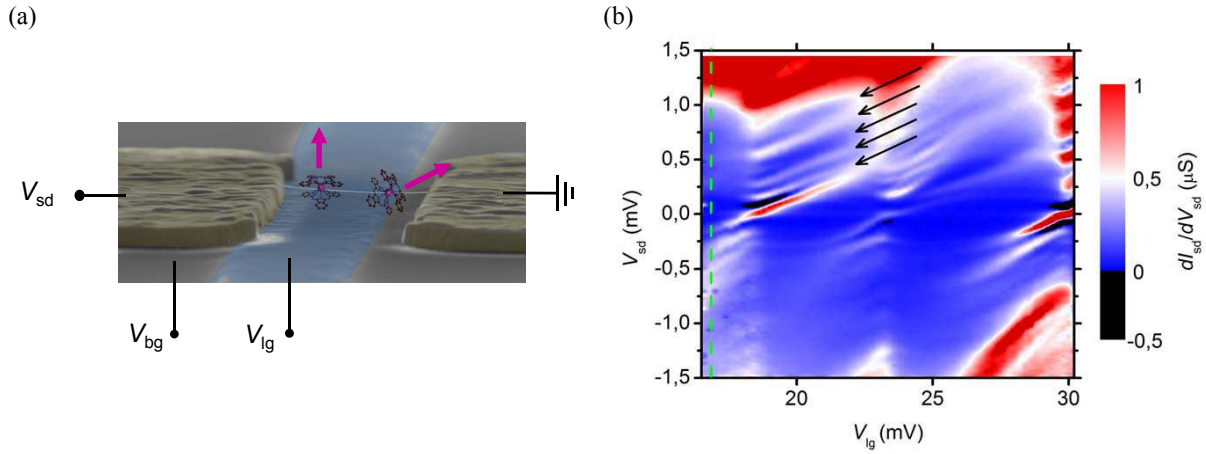

Figure 6.12: Hybrid nanotube-molecule device *LSM-hybrid*. (a) False color SEM image and (b) stability diagram of the hybrid nanotube-molecule device in the few electron regime at $T = 20$ mK and $H_x = 1.4T$. The black arrows depict excited vibrational states associated with the LSM phonon described in the previous section and the green dashed depicts the working point for the measurements shown in section 6.4.3.

6.4.1 Coupling mechanism between a single $TbPc_2$* spin to a quantized longitudinal resonator mode

First, we tune our CNT quantum dot to a regime of Coulomb blockade ($V_{\mathrm{lg}} = 16.5$ mV, green dashed line in Fig. 6.12b). In the case of a strong spin-phonon coupling, the magnetization reversal of an individual $TbPc_2$ SMM via *direct* transition can induce the excitation of the longitudinal stretching mode phonon described in the previous section 6.3 (Fig. 6.13).

An upper boundary for the linewidth of an excited LSM phonon state was estimated to $\delta E_{\mathrm{ph}} \lesssim 15$ mK (Section 6.3) and is therefore smaller than the energy level spacing $\Delta E_{\mathrm{I}} = 120, 150, 180$ mK between the nuclear spin states of the Tb^{3+} ion [47, 49]. Sweeping the magnetic field from negative to positive values, we should thus observe four different transitions matching the phonon energy $\hbar\omega_{\mathrm{ph}} = 140\mu$eV $= 1.5$ K and corresponding to the different nuclear spin states of the Tb^{3+} ion as depicted by the colored arrows in Fig. 6.13.

We can evaluate the magnetic field associated with each transition, the so called switching field $\mu_0 H_{\parallel,\mathrm{sw}}$, from the Zeeman energy difference between the spin states $|m_{\mathrm{J}} = +6, m_{\mathrm{I}}\rangle$ and $|m'_{\mathrm{J}} = -6, m_{\mathrm{I}}\rangle$

$$\Delta E_z = \left(g\mu_{\mathrm{B}}\mu_0 H_{\parallel,\mathrm{sw}} + A m_I\right) \Delta m_J \tag{6.5}$$

where $g = 3/2$ is the gyromagnetic factor of the Tb^{3+} ion, $\mu_{\mathrm{B}} = 0.673$ K/T the Bohr

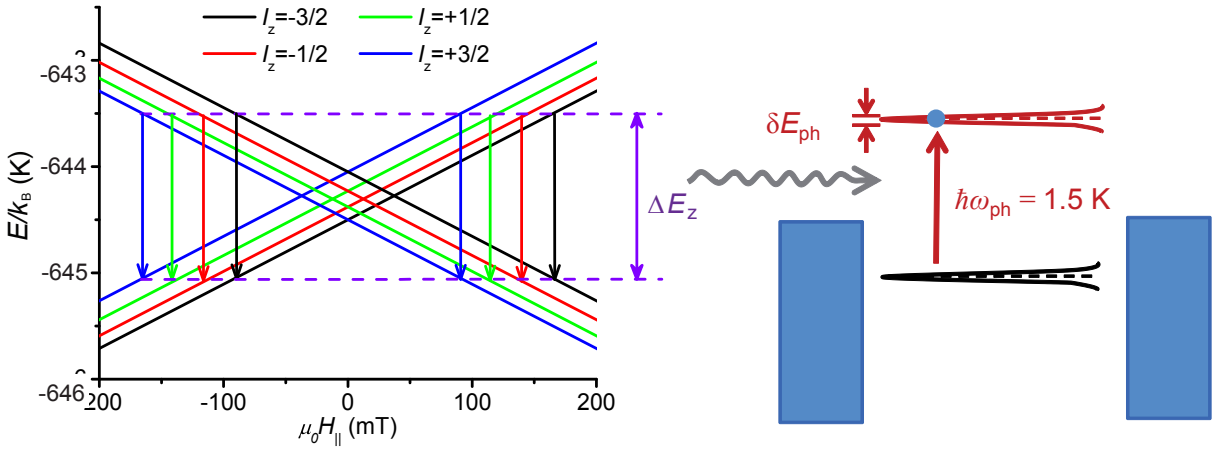

Figure 6.13: Coupling mechanism between a single $TbPc_2$* spin to a quantized longitudinal resonator mode: The magnetization reversal of the $TbPc_2$ via *direct* transition results in the excitation of the electron into a vibrational LSM state in the carbon nanotube resonator. In contrast to bulk phonons, the energy spectrum of a LSM phonon in 1D carbon nanotubes is discretized and yields high quality factors around $Q \sim 100$. The corresponding phonon linewidth $\delta E_{\mathrm{ph}} \approx 15$ mK is smaller than the energy separation between the Tb^{3+} nuclear spin states $\Delta E_{\mathrm{I}} > 120$ mK. Hence, we observe four different transitions, corresponding to the four nuclear spin states as depicted by the colored arrows.

magneton, $A = 24.5$ mK the hyperfine constant, m_I the nuclear spin's quantum number, $\Delta m_J = m_{\mathrm{J}} - m'_{\mathrm{J}} = 12$ and $\mu_0 H_{\parallel,\mathrm{sw}}$ the switching field along the easy axis of the $TbPc_2$* SMM. From equation 6.5 we can deduce the switching field

$$\mu_0 H_{\parallel,\mathrm{sw}}(m_I) = \left(\frac{\Delta E_z}{\Delta m_J} - A m_I \right) \frac{1}{g \mu_{\mathrm{B}}} \tag{6.6}$$

For a Zeeman energy difference matching the phonon energy $\Delta E_z = \hbar\omega_{\mathrm{ph}} = 1.5$ K, we indeed obtain four different switching fields of $\mu_0 H_{\parallel,\mathrm{sw}} = 89, 113, 137, 161$ mT for the respective nuclear spin states $m_I = +3/2, +1/2, -1/2, -3/2$ of the Tb^{3+} ion. Reversing the sweep direction will result in a magnetization reversal at switching fields of $\mu_0 H_{\parallel,\mathrm{sw}} = -89, -113, -137, -161$ mT for the respective nuclear spin states $m_I = -3/2, -1/2, +1/2, +3/2$ of the Tb^{3+} ion.

6.4.2 Current detection of a $TbPc_2$* magnetization reversal

We perform magnetoconductance measurements on the hybrid $TbPc_2$*-carbon nanotube device *LSM-hybrid*. Starting at a magnetic field of $H_x = -1.4$ T applied along the carbon nanotube axis, we sweep the magnetic field towards a positive field of 1.4T. We observe a first abrupt jump in conductance to its minimum value around 0.5 T and a second jump

back to higher conductance around 1 T (red trace Fig. 6.14). Sweeping the field back to -1.4 T, we observe a "down"-jump around -0.5 T and an "up"-jump at -1 T (blue retrace Fig. 6.14). We obtain a hysteresis loop which is characteristic for a spin valve device. This spin valve behaviour was first observed in non-suspended carbon nanotube-SMM hybrids by Urdampilleta *et al* [48, 130] and was introduced in section 2.3.2.

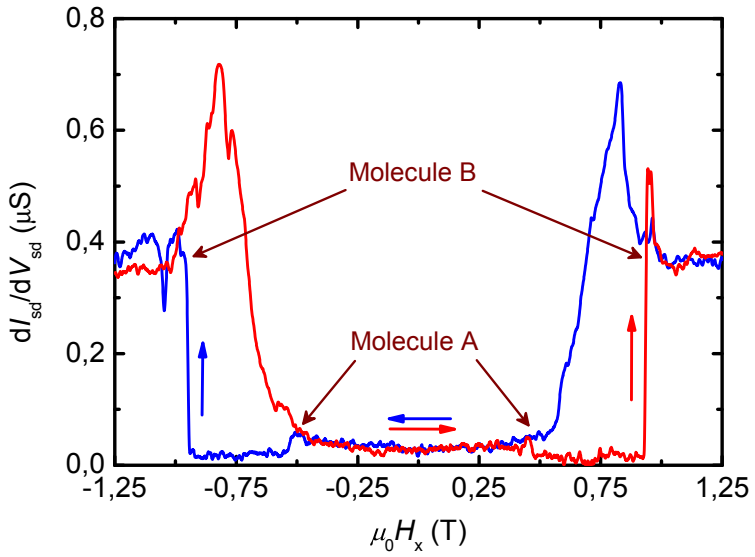

Figure 6.14: Supramolecular spin valve in the hybrid nanotube-molecule device *LSM-hybrid*. Hysteresis loop at $T = 20$mK and a magnetic field H_x applied along the carbon nanotube axis. The red (blue) curve correspond to up(down)-wards magnetic field sweeps. The device exhibits a strong change in magnetoconductance.

Urdampilleta *et al* [48, 130] proposed a simple model, where two molecules A and B grafted to the carbon nanotube act as localized spin polarizer and analyzer on the nanotube's electronic transport. Due to a hybridization between the electronic systems of the nanotube and the molecules, each molecule can induce a localized spin polarized dot in the carbon nanotube (Fig. 6.15). A strong exchange interaction between the molecular spin and the conduction electrons on the nanotube, mediated by the π electrons in the Pc ligand, lifts the spin degenaracy in the carbon nanotube, thus inducing spin polarized states in the localized dot (Fig. 6.15a). A detailed description can be found in [48, 130].

At the saturation field of -1.4T both molecule are in a parallel spin configuration. Localized states with equal spin are aligned and enable a high conductance regime in the nanotube (Fig. 6.15a). Upon increasing the field, molecule A switches its magnetization at a given value of magnetic field, the so called *switching field* around 0.5T, resulting in an inversion of the two spin states in the dot A and an anti-parallel spin configuration. The resulting energy mismatch between levels with same spin induces a current blockade in the carbon nanotube (Fig. 6.15b). The differential conductance in

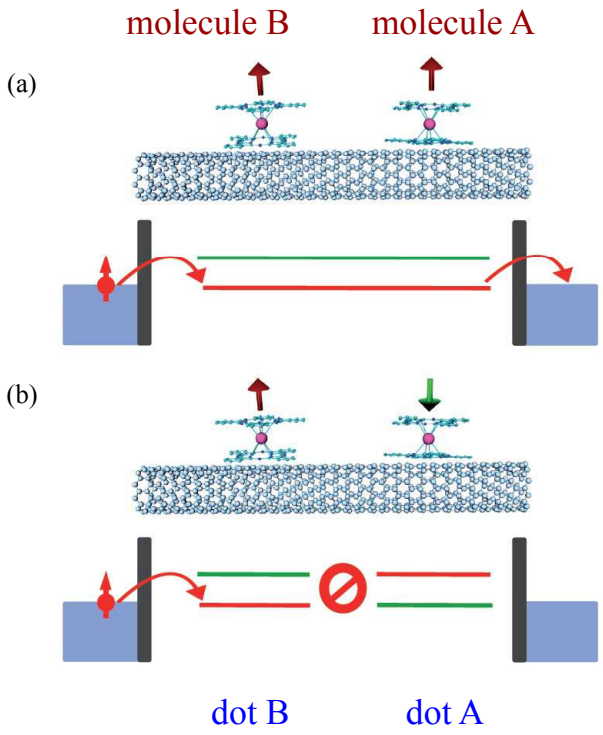

Figure 6.15: Multidot model for a supramolecular spin valves. (a) Parallel spin configuration for both molecules A and B. Energy levels with same spin are aligned allowing electron transport through the carbon nanotube. (b) Antiparallel spin configuration. The spin states are inversed in the dot A and the energy mismatch between levels with identical spin results in a current blockade. Modified figure from [48, 130]

the carbon nanotube thus transits abruptly to a minimum value at the switching field of molecule A (Fig. 6.14). Upon driving the field to positive saturation of 1.4T, the second molecule B reverses its magnetization, restoring the parallel configuration (Fig. 6.15a). The differential conductance in the carbon nanotube then transits back to a higher value, at the switching field of molecule B (Fig. 6.14). We can thus determine the switching field of each molecule, by probing the corresponding abrupt transitions in the nanotube's differential conductance. In the following, we will now focus our discussion on the current switching and magnetization reversal dynamics of molecule B.

Due to the strong magnetic anisotropy of the $TbPc_2$* SMM, the observed spin valve behaviour and current switching should exhibit a pronounced magnetic anisotropy and a strong dependance on the magnetic field orientation. Therefore, the hysteresis cycle is repeated for different orientations of the magnetic field in the plane of sample. The switching field of molecule B is extracted from each hysteresis loop as described above

and plotted as a function of the in-plane magnetic field angle (Fig. 6.16a). The switching fields strongly depend on the orientation of the in-plane magnetic field and follow four parallel, straight lines in the field plane for both up- and downwards magnetic fields sweeps (dashed lines in Fig. 6.16a). The projection of these switching fields on the "easy axis" is constant, which is consistent with the uniaxial magnetic anisotropy of the Ising-like Tb^{3+} ion.

As we will demonstrate in the following section 6.4.3, the four observed transitions are in fact consistent with the nuclear spin-resolved phonon-assited the magnetization reversal of the $TbPc_2$* molecule B.

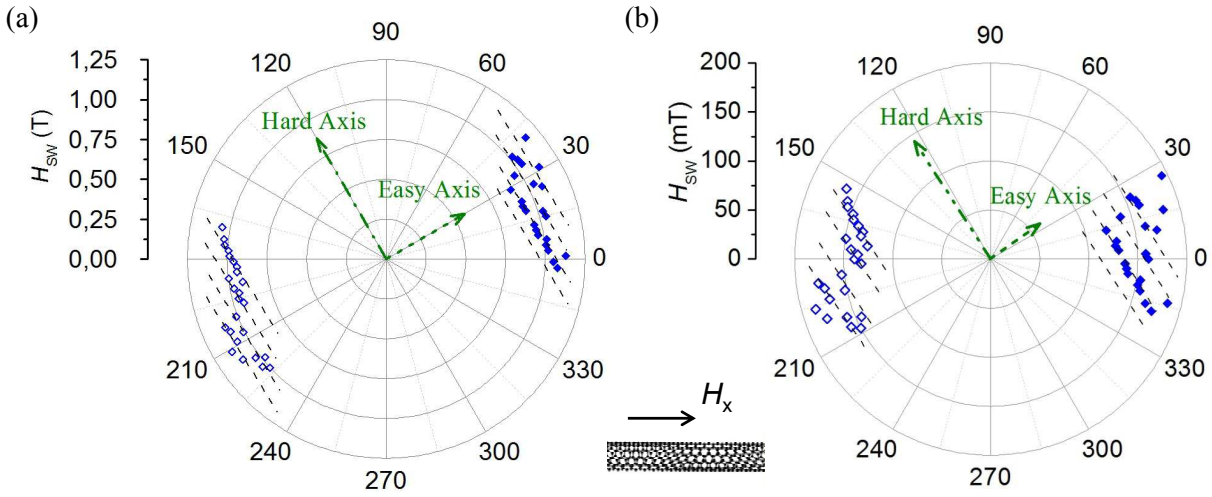

Figure 6.16: Magnetic anisotropy of $TbPc_2$ molecule B in the hybrid nanotube-molecule device *LSM-hybrid*. (a) Switching fields for upwards (full dots) and downwards (open dots) sweeps as a function of the angle of the magnetic field in the sample plane. The dashed lines are guide to the eye. (b) Switching fields as a function of the in-plane magnetic field angle corrected for the out-of-plane misalignement β of the molecule.

Using Fig. 6.16a, we can determine the *in the plane* orientation of the easy axis for molecule B (i.e. in the sample plane). The easy axis is oriented perpendicular to the four highlighted transition lines, thus having an angle of $\alpha \sim 28°$ with the nanotube axis H_x.

We can also determine the *out-of-plane* orientation of the SMM's easy axis using the equation

$$cos\beta = \frac{\delta H_{\parallel}}{\delta H} \tag{6.7}$$

where $\delta H_{\parallel} = 23$ mT is the magnetic field separation between the nuclear spin states for a field oriented parallel to the SMM's easy axis and δH the magnetic field separation between the nuclear spin states for a field applied along the projection of the easy axis

into the sample plane. In our case, we obtain an out-of-plane angle of $\beta \sim 74° \pm 5°$. With our 3D vector magnet we are not able to compensate for this out-of-plane orientation. However, for the sake of clarity, this misalignment was numerically corrected for all data presented in the following. Fig. 6.16b represents the switching fields as a function of the in plane magnetic field angle, but corrected for the out-of-plane misalignement β.

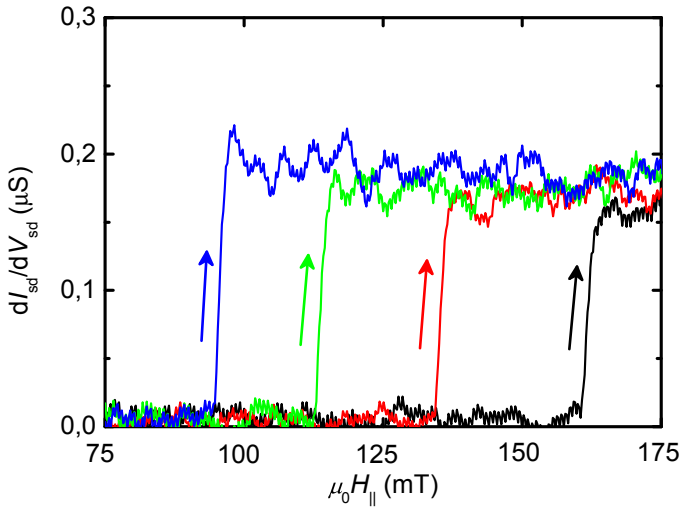

Figure 6.17: Magnetoconductance measurements $dI/dV\left(\mu_0 H_\parallel\right)$ along the easy axis of the $TbPc_2$ molecule B in the hybrid nanotube-molecule device *LSM-hybrid*. Four distinct switching fields are observed, which are attributed to the nuclear spin resolved phonon-assisted magnetization reversal described in section 6.4.1.

We can now perform magnetoconductance measurements along the easy axis of the molecule B. Fig. 6.17 shows four consecutive upwards sweeps of the magnetic field along the easy axis of molecule B. We observe current switching events at four distinct switching fields, which can indeed be attributed to the nuclear spin resolved phonon-assisted magnetization reversal (Section 6.4.1), as we will describe in the following section 6.4.3.

6.4.3 Nuclear spin-resolved phonon-assisted magnetization reversal of a single $TbPc_2$* spin coupled to a CNT NEMS

Transverse magnetic field dependance

Magnetoconductance measurements as depicted in Fig. 6.17 are performed at different values of a magnetic field $H_\perp$, transverse to the field sweep direction which is aligned with molecule B's easy axis $H_\parallel$. The switching fields $H_{\parallel,sw}$ are recorded and plotted as a

function of the transverse magnetic $H_\perp$ (Fig. 6.18).

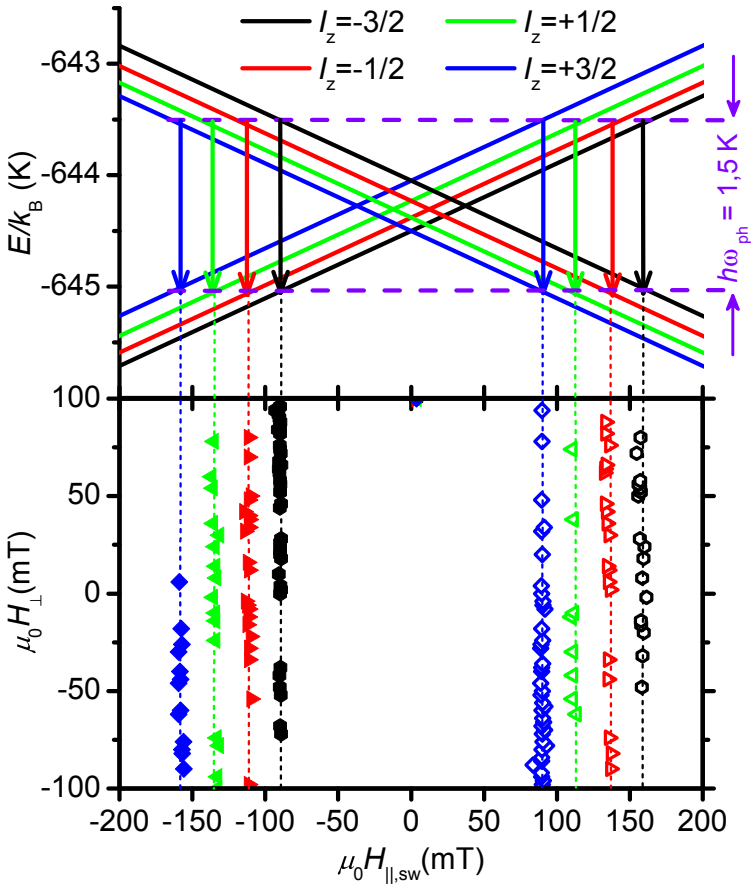

Figure 6.18: Switching field $H_{\parallel,sw}$ as a function of the transverse magnetic field $H_\perp$ at $T = 20$ mK and a sweep rate of 50 mT/s. Open (full) symbols correspond to a switching on the upwards (downwards) sweep of the parallel field component $H_\parallel$. The Zeeman diagram depicts the phonon-assisted transition associated with each switching event.

By sweeping the parallel magnetic field $H_\parallel$ from negative to positive values (trace), we observe four narrow transitions for molecule B at $H_{\parallel,sw} = 90, 111, 134, 158$ mT (open symbols in Fig. 6.18). By reversing the sweep direction for $H_\parallel$ (retrace), we observe four narrow transitions at $H_{\parallel,sw} = -90, -112, -135, -157$ mT (full symbols in Fig. 6.18). The switching field values are in perfect agreement with the predictions for a nuclear spin resolved magnetization reversal assisted by a LSM phonon with an energy of 1.5 K. We can attribute each switching field to one nuclear spin state as depicted in Fig. 6.18.

Moreover, the energy of a direct transition in a $TbPc_2$* molecule as well as the phonon energy does not the depend on the transverse magnetic $H_\perp$. In consequence the switching field should be independant from the transverse magnetic field $H_\perp$. Indeed, the transi-

tions for both trace and retrace do not depend on the transverse magnetic field $H_\perp$ and are perfectly symmetric with respect to $H_\parallel = 0$.

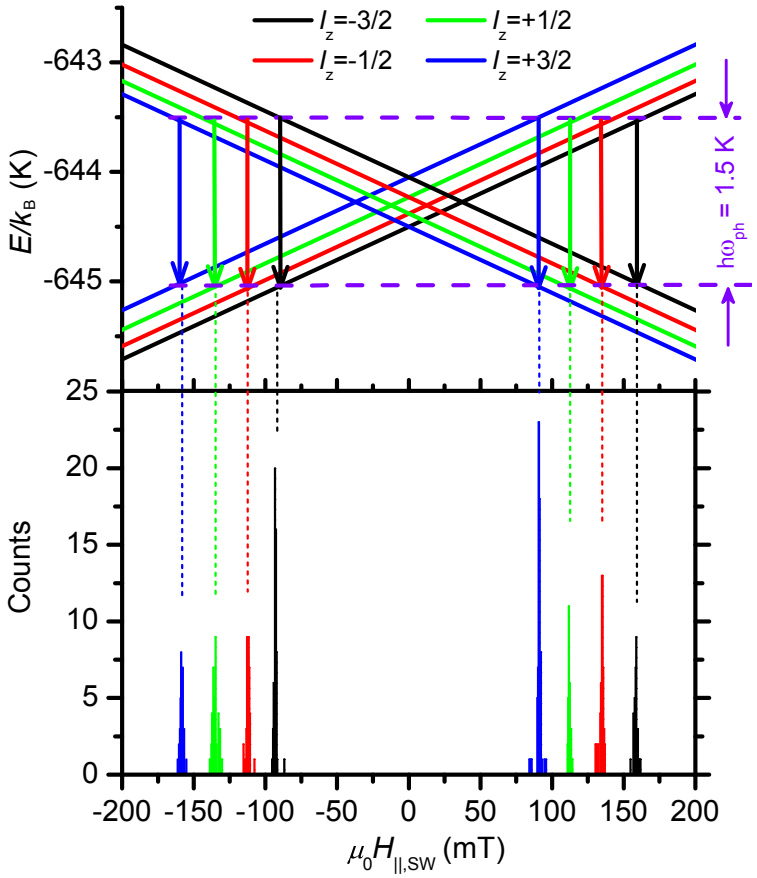

Figure 6.19: Switching field $H_{\parallel,sw}$ histogram for $H_\perp = 0$ at $T = 20$ mK and a sweep rate of 50 mT/s. The Zeeman diagram depicts the phonon-assisted transition associated with each switching event.

In order to obtain a magnetization reversal statistic, we performed 200 hysteresis loops at zero transverse magnetic field $H_\perp = 0$. All switching fields were recorded and compiled in a histogram depicted in Fig. 6.19. The histogram shows four dominant transition events at $H_{\parallel,sw} = 90, 112, 134, 158$ mT for the trace and four dominant transitions at $H_{\parallel,sw} = -90, -112, -134, -158$ mT on the retrace, with an average FWHM of about $\delta H_{\parallel,sw} = 2$ mT.

The model described in Section 6.4.1 predicts that in case of a strong coupling between the $TbPc_2$ spin and the quantized longitudinal phonon mode in the CNT (energy $\hbar\omega_{\rm ph} = 1.5$ K and linewidth $\delta E_{\rm ph} = 15$ mK), the magnetization reversal of the $TbPc_2$ will indeed occur from the four nuclear spin states of the Tb^{3+} ion at magnetic fields of

$\mu_0 H_{\parallel,\mathrm{sw}} = 89, 113, 137, 161$ mT for an upwards magnetic field sweep (and at $-\mu_0 H_{\parallel,\mathrm{sw}}$ for a downwards magnetic field sweep).

The Zeeman energy δE_z corresponding to the FWHM of each switching event in Fig. 6.19 is approximately 30 mK, which is in close agreement with the phonon linewidth of $\delta E_{\mathrm{ph}} = 15$ mK determined in the previous section. Moreover, all four switching events in the $TbPc_2$ can be associated with a transition energy of $\Delta E_{\mathrm{z}} = 1.5$ K, which is in perfect agreement with phonon energy of $\hbar\omega_{\mathrm{ph}} = 1.5$ K. The experimental findings are thus in excellent agreement with the provided model. The strong interaction between the molecular $TbPc_2$ spin and the quantized longitudinal phonon is further supported by the magnitude of the spin-phonon coupling, which we will evaluate in Section 6.4.4.

The transverse field dependance and the statistics of the magnetization reversal of molecule B provides a strong evidence for a phonon-assisted and nuclear spin-resolved magnetic relaxation process in a $TbPc_2$*. We will now demonstrate that the observed magnetization reversal indeed follows the sweep rate and temperature dependance expected for a Tb^{3+} nuclear spin.

Sweep rate dependance

We performed magnetization reversal statistics at sweep rates of the magnetic field of 10, 50, 100 and 150 mT/s (Fig. 6.20).

At a sweep rate of 150 mT/s, the magnetization reversal essentially occurs from the nuclear spin ground state at a switching field $H_{\parallel,sw} = \pm 160$ mT (Fig. 6.20a). Fig. 6.21a depicts the integrated number of counts as a function of the magnetic field for an upwards magnetic field sweep. We can deduce the occupation probability of a nuclear spin state from the corresponding step height in the integrated histogram (Fig. 6.21a). Indeed, the occupation probability of the nuclear spin states follows a Maxwell Boltzmann distribution $P = P_0 exp(-E/k_{\mathrm{B}}T_{\mathrm{N}})$, with a strong population of the nuclear spin ground state (blue fit curve in Fig. 6.21b). We determine an upper boundary of nuclear spin temperature of $T_{\mathrm{N}} = 150$ mK, which is on the order of the electronic temperature in the system, indicating that the nuclear spin is close to thermal equilibrium.

By reducing the sweeping rate (non-adiabatic sweep), the finite energy level lifetime of the nuclear spin states results in transitions from higher nuclear spin states and eventually in an inversion of the nuclear spin population. Indeed, for a sweep rate of 10 mT/s, the magnetic relaxation essentially occurs from the highest nuclear spin states at a switching field $H_{\parallel,sw} = \pm 90$ mT (Fig. 6.20d).

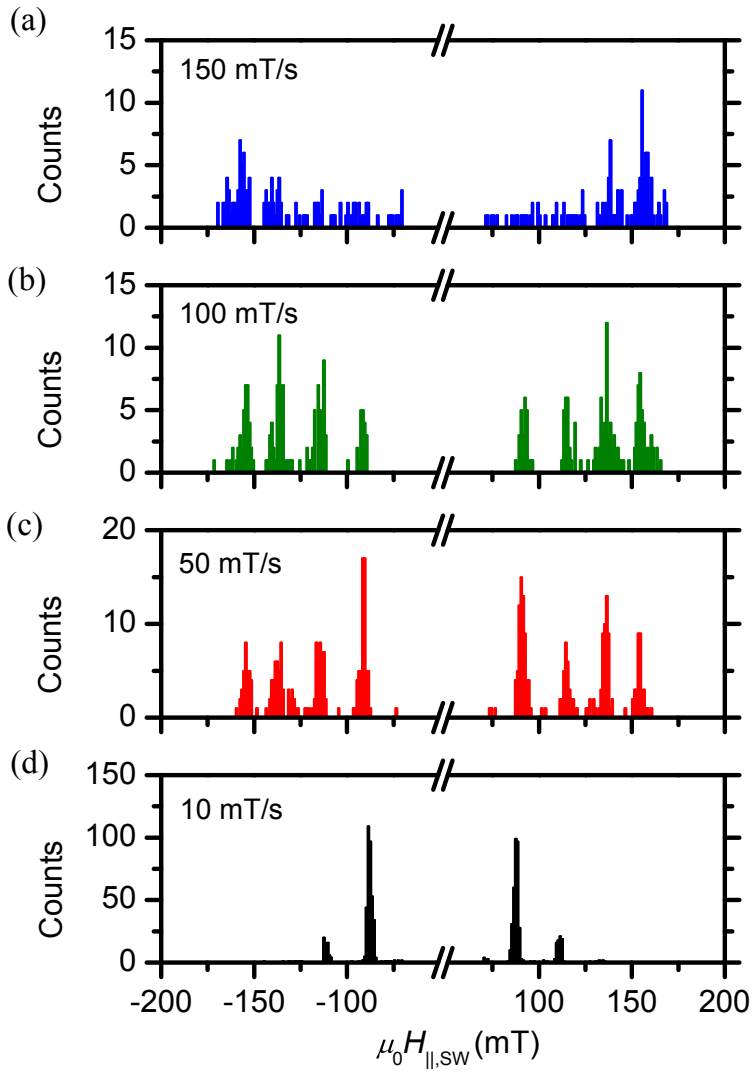

Figure 6.20: Switching field histograms at $T = 20$ mK for sweep rates of (a) $\nu = 150$ mT/s, (b) $\nu = 100$ mT/s, (c) $\nu = 50$ mT/s and (d) $\nu = 10$ mT/s. Switching events at positive fields correspond to sweep from negative to positive magnetic fields (trace), events at negative fields correspond to the reversed sweep direction (retrace). We observe an inversion of the nuclear spin population with the magnetic field sweep rate.

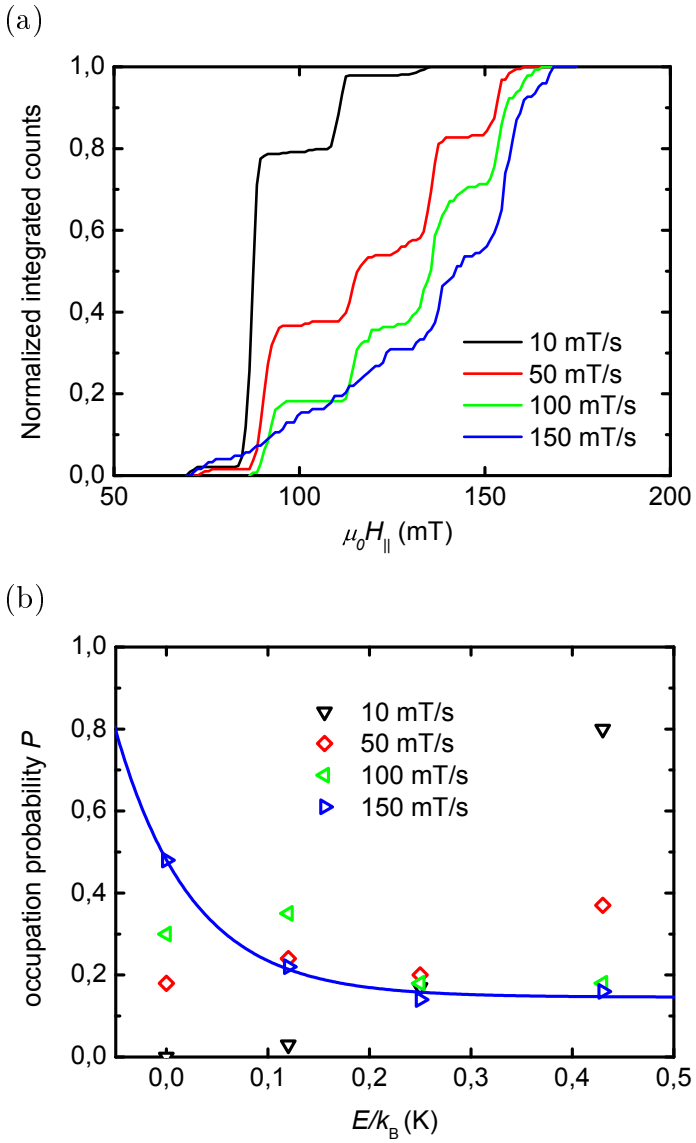

Figure 6.21: Nuclear spin temperature and occupation probability: (a) Integrated number of counts normalized with the total number of counts as a function of the parallel magnetic field for different sweep rates. The integrated counts correspond to switching events of the molecule on an upwards magnetic field sweep. (b) Occupation probability P of a nuclear spin state as function of his energy E_I with respect to the ground state (only for the upwards field sweep). The probability P corresponds to the step height extracted from the integrated histogram traces in (a). The blue curve corresponds to a fit with a Maxwell Boltzmann distribution $P = P_0 exp\,(-E_I/k_B T_N)$ and gives an effective nuclear spin temperature of $T_N = 150$ mK.

Temperature dependance

We performed 200 magnetic field sweeps (back and forth) at a rate of 150 mT/s for temperatures of 20, 300, 500, 700 mK. At the base temperature, the nuclear spin tends towards a thermal equilibrium with a large population of the nuclear spin ground (see previous section and Fig. 6.23). Increasing the temperature above the energy level separation of the nuclear spin states (120, 150, 180 mK starting from the ground state), leads to the population of higher nuclear spin states due to thermal activation (Fig. 6.23).

At $T = 700$ mK however, the hyperfine structure in the magnetization reversal vanishes and one observes a large switching field distribution with a FWHM of 50 mT, corresponding to a Zeeman energy of 750 mK (Fig. 6.23). In addition, the vibrational sidebands attributed to the quantized LSM phonon mode vanish in the nanotube's bias spectroscopy around $T = 900$ mK (Fig. 6.22). At $T = 900$ mK, the thermal energy is on the same order than the phonon energy $\hbar\omega_{\mathrm{ph}}$, which results in an average thermal occupancy $\bar{n} = \frac{kT}{\hbar\omega_{\mathrm{ph}}} \cong 1$. In consequence, the carbon nanotube resonator transits from a quantum state to a classical state of motion, which is consistent with the vanishing vibrational sidebands (Fig 6.22b) and thus with the quench of hyperfine structure in the reversal statistics above 700 mK (Fig. 6.23a).

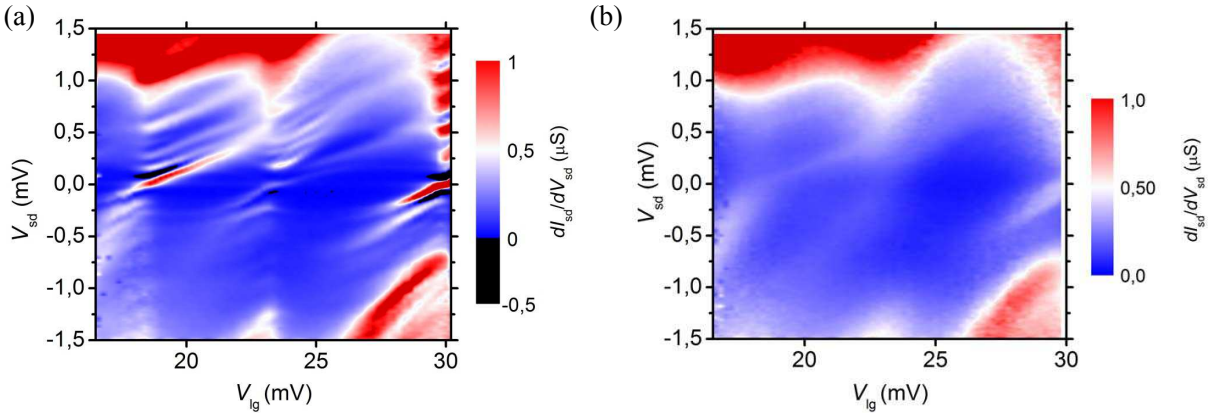

Figure 6.22: Longitudinal phonon mode vs. temperature. (a) Stability diagram at $T = 20$ mK at $H_x = 1.4$ T. (b) Stability diagram at $T = 900$ mK at $H_x = 1.4$ T. The excited states attributed to LSM phonons vanish as the resonators transits from a quantum to a classical state of motion. Features of negative differential conductance also vanish at higher temperature.

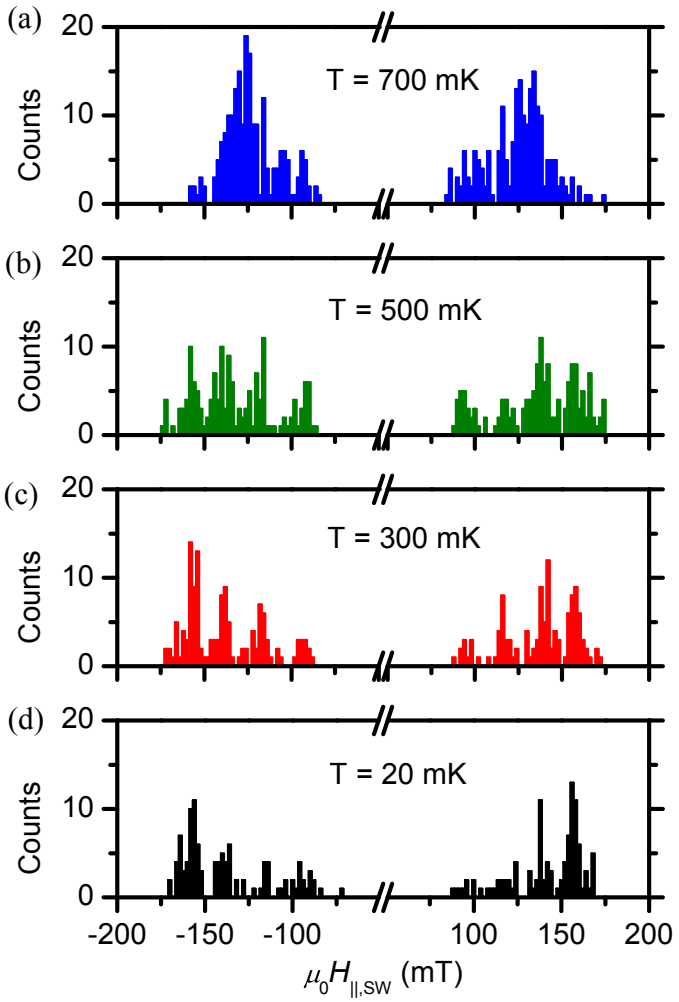

Figure 6.23: Switching field histogram recorded for a sweep rate of 150 mT/s at temperatures of (a) $T = 700$ mK, (b) $T = 500$ mK, (c) $T = 300$ mK, (d) $T = 20$ mK. For those sweep conditions, the nuclear spin tends towards a thermal equilibrium at the base temperature. Increasing the temperature above the energy level separation of the nuclear spin states (120, 150 and 180 mK, see main text) leads to an equal population of the four nuclear spin states (500 mK). At $T = 700$ mK, the hyperfine structure vanishes and we observe a large switching fields distribution for the Tb^{3+} ion.

6.4.4 Spin-phonon coupling between a molecular and quantized mechanical motion

Due to the strongly anisotropic $4f$ shell and a strong spin-orbit coupling in the Tb^{3+} ion, the TbPc$_2$* exhibits a magnetic ground state of $J = 6$ and a strong magnetic anisotropy, with an easy axis z perpendicular to the Pc ligand planes. The Hamiltonian for a TbPc$_2$* SMM's ground state multiplet $J = 6$ in a magnetic field is then written as

$$\mathcal{H}_{\mathrm{TbPc_2}} = \mathcal{H}_{\mathrm{B}} + \mathcal{H}_{\mathrm{cf}} \tag{6.8}$$

where the first term $H_{\mathrm{B}} = g\mu_{\mathrm{B}} B_z J_z$ corresponds to the Zeeman splitting in an external magnetic field. The latter term $\mathcal{H}_{\mathrm{cf}}$ describes the crystal electric field of the TbPc$_2$* and accounts for the magnetic anisotropy energy of the TbPc$_2$* [51]

$$\mathcal{H}_{\mathrm{cf}} = \alpha A_2^0 O_2^0 + \beta \left(A_4^0 O_4^0 + A_4^4 O_2^4\right) + \gamma \left(A_6^0 O_6^0 + A_6^4 O_6^4\right) \tag{6.9}$$

where O_q^k are the Stevens operators [52], α, β and γ the corresponding Stevens parameters and A_q^k the crystal field parameters [53] (see also Section 2.2 for a detailed description).

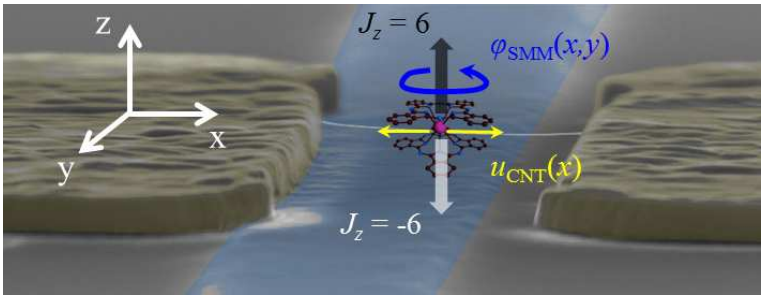

Figure 6.24: Single molecule magnet coupling to a carbon nanotube NEMS. The magnetization reversal of an TbPc$_2$* SMM from a spin state $J_z = +6$ to $J_z = -6$ results in a rotation of the SMM crystal lattice in the x-y plane. The rotation by an angle $\varphi_{\mathrm{SMM}}(x, y)$ TbPc$_2^*$ SMM of the generates a longitudinal stretching mode with an amplitude $u_{\mathrm{CNT}}(x)$.

We now consider a TbPc$_2$* SMM rigidly grafted to a suspended carbon nanotube NEMS. The magnetization reversal of the Tb^{3+} ion causes a rotation of the SMM crystal electric field and the crystal lattice by an angle $\hat{\varphi}_{\mathrm{SMM}}(\vec{r})$ in a (x-y)-plane perpendicular to its easy axis z, due to conservation of the total angular momentum (spin+lattice) [114, 132]. Due to the rigid grafting to the CNT, the SMM's rotation $\hat{\varphi}_{\mathrm{SMM}}(\vec{r})$ translates to a longitudinal stretching mode with an amplitude of $\hat{u}_{\mathrm{CNT}}(\vec{r})$ in the suspended CNT resonator beam (Fig. 6.24). We have [114, 132]

$$\hat{\varphi}_{\mathrm{SMM}}\left(\vec{r}\right) = \nabla \times \hat{u}_{\mathrm{CNT}}\left(\vec{r}\right) \tag{6.10}$$

$$\hat{u}_{\mathrm{CNT}}\left(\vec{r}\right) = \sqrt{\frac{\hbar}{2m\omega_l}} \int \frac{d^3k}{(2\pi)^3} e^{i\vec{k}\vec{r}} \left(a_{\vec{k}} + a^{\dagger}_{-\vec{k}}\right) \tag{6.11}$$

where ω_l is the frequency of the longitudinal phonon mode, m the resonator mass, $\vec{k}$ the quantization vector of the phonon and a and $a^{\dagger}$ the creation/annihilation operators. The Hamiltonian of the hybrid SMM-resonator can then be written as [114, 132]

$$\mathcal{H} = \mathcal{H}_{\mathrm{ph}} + \mathcal{H}_{\mathrm{B}} + e^{-iJ_z\hat{\varphi}}\mathcal{H}_{\mathrm{cf}}e^{iJ_z\hat{\varphi}} \tag{6.12}$$

where $\mathcal{H}_{\mathrm{ph}} = \hbar\omega_{\mathrm{l}}\left(a^{\dagger}a + 1/2\right)$ corresponds to the energy of the quantized phonon mode and $\mathcal{H}_{\mathrm{B}} = g\mu_{\mathrm{B}}B_zJ_z$ to the Zeeman energy of the $TbPc_2$*. The last term describes the modification of the crystal electric field of the $TbPc_2$* by the rotation of its crystal lattice. $\mathcal{H}_{\mathrm{cf}}$ corresponds to the unperturbed crystal electric field and $\hat{\varphi}$ to the rotation angle of the crystal lattice. In first order, the last term in equation 6.12 expands as

$$e^{-iJ_z\hat{\varphi}}\mathcal{H}_{\mathrm{cf}}e^{iJ_z\hat{\varphi}} \approx \mathcal{H}_{\mathrm{cf}} + i\left[\mathcal{H}_{\mathrm{cf}}, J_z\right]\hat{\varphi} = \mathcal{H}_{\mathrm{cf}} + \mathcal{H}_{\text{s-ph}} \tag{6.13}$$

We now evaluate the spin-phonon interaction Hamiltonian $\mathcal{H}_{\text{s-ph}}$. With equations 6.10 and 6.11 we evaluate the rotation angle in terms of the phonon creation and annihilation operators of longitudinal phonon generated in the carbon nanotube NEMS as follows

$$\hat{\varphi} = \frac{1}{2}\sqrt{\frac{2\hbar}{\omega_l I_z}}\left(a + a^{\dagger}\right) \tag{6.14}$$

with the moment of inertia I_z of the $TbPc_2$* and the phonon frequency ω_l [114].

Using equation 6.9 we can determine the commutator $[\mathcal{H}_{\mathrm{cf}}, J_z]$. From the Stevens operators and matrix elements determined in Ref.[52] and [53], we find that

$$\left[O^0_k, J_z\right] = 0\ ,\ k = 2, 4, 6 \tag{6.15}$$

$$A^4_6 = 0 \tag{6.16}$$

In consequence, the commutator $[\mathcal{H}_{\mathrm{cf}}, J_z]$ simplifies to $[\mathcal{H}_{\mathrm{cf}}, J_z] = \beta A^4_4\left[O^4_4, J_z\right]$ where $\beta A^4_4 = 1.8$ mK [53]. Using $O^4_4 = \frac{1}{2}\left(J^4_+ + J^4_-\right)$ [52] we then obtain

$$\begin{aligned}
\left[\mathcal{H}_{\mathrm{cf}}, J_z\right] &= \beta A^4_4\left[O^4_4, J_z\right] \\
&= \beta A^4_4\left[J^4_+, J_z\right] + \beta A^4_4\left[J^4_-, J_z\right] \\
&= -\frac{\hbar\beta A^4_4}{2}\left(J^4_+ - J^4_-\right) \\
&= -i\hbar\beta A^4_4 O^{-4}_4
\end{aligned} \tag{6.17}$$

Using equations 6.14 and 6.17 we obtain an interaction Hamiltonian

$$\mathcal{H}_{\text{s-ph}} = \frac{\hbar\beta A_4^4}{2}\sqrt{\frac{2\hbar}{\omega_l I_z}}\left(a + a^\dagger\right) O_4^{-4} \tag{6.18}$$

The total Hamiltonian thus reduces to a Jaynes-Cummings type equation as described in the following by

$$\mathcal{H} = \mathcal{H}_{\text{ph}} + \mathcal{H}_{\text{B}} + \mathcal{H}_{\text{cf}} + \hbar g_{\text{s-ph}}\left(a + a^\dagger\right) O_4^{-4} \tag{6.19}$$

where the spin-phonon coupling between the $TbPc_2$* spin and the carbon nanotube longitudinal phonon is given by

$$g_{\text{s-ph}} = \frac{\beta A_4^4}{2}\sqrt{\frac{2\hbar}{\omega_l I_z}} = 1.5 \text{ MHz} \tag{6.20}$$

with the SMM's moment of inertia $I_z = 10^{-42}$ kg $\cdot$ m^2, the phonon frequency $\omega_l = 34$ GHz and the crystal field parameter $\beta A_4^4 = 1.8$ mK.

A spin-resonator coupling of this magnitude could result in a suppression of quantum tunneling of magnetization (QTM) on the SMM by nanomechanical quantum interference effects [114], the creation of coherent magneto-mechanical oscillations [114] or the entanglement of a single spin with quantum mechanical oscillator [122, 115]. We would like to point out, that we did not observe quantum tunneling of magnetization in our spin-resonator system. Although the absence of QTM could be related to nanomechanical quantum interference effects, as stated above, we do not have sufficient evidence to support such a claim.

6.5 Conclusion and Outlook

In this chapter, we probed the magnetization reversal *via* an electronic readout of a $TbPc_2$* SMM coupled to the longitudinal streching mode vibration of a carbon nanotube resonator.

We find the longitudinal stretching mode vibration to be in its quantum mechanical ground state, thus yielding a quantized energy spectrum and very low density of states in excited vibrational states (Section 6.3). Upon coupling a $TbPc_2$* SMM to this longitudinal stretching mode phonon, the quantization of the latter enables the detection of the four nuclear spin states of the Tb^{3+} in magnetization reversal measurements (Section 6.4).

Moreover, we find a strong coupling between the the molecular spin and the quantized phonon mode on the order of 1 MHz. The value is comparable to the coupling strength predicted for a carbon nanotube based spin qubit coupled to a carbon nanotube's nanomechanical motion [122] or to a superconducting coplanar waveguide [133].

It has been predicted that a coupling of this magnitude would induce strong nonlinearities in a carbon nanotube's mechanical motion, which can for instance be used to enhance the sensitivity of carbon nanotube based magnetometers [122, 18]. A sensitivity of a few μ_B is to be expected, making this specific supramolecular spintronic device an ideal candidate for a torque magnetometer with molecule sensitivity [18].

In addition, the strong spin-phonon coupling would enable the electric manipulation of a single molecular spin via microwave irradiation [122]. Reciprocally, a strong spin-phonon interaction would allow a spin-based detection of the nanotube's mechanical motion or the ground state cooling of the resonator by manipulating the molecular spin via electron spin resonance [122]. Ultimately, our results open the path to the quantum entanglement of a single spin and a quantized mechanical motion.

Chapter 7

General conclusion and perspectives

The achievements in the field of molecular magnetism and spintronics proved to be milestones on the ambitious path towards the implementation of a quantum computer. The unique physical and chemical properties of molecular magnets provide a large variety of quantum mechanical effects ranging from tunneling processes, interference phenomena to large quantum coherence, making them an ideal candidate for a so called spin qubit system. In this manuscript, we proposed to couple the quantum magnetism of single molecule magnets to the quantum oscillation of a molecular resonator which would allow the detection and coherent manipulation of a single molecular spin or spin qubit by the resonators's quantum oscillation and *vice versa*. Such a supramolecular spintronic device could therefore be the first implementation of a so called supramolecular torque magnetometer with single molecule sensitivity.

In this work, we present the first experimental realization of such a *supramolecular quantum spintronic* device by coupling a rare earth single molecular magnet and a carbon nanotube nanoelectromechanical system (NEMS). Owing to their outstanding and electrically tunable mechanical properties, such as the high resonance frenquencies and quality factors, carbon nanotube NEMS represent the perfect building block for this kind of supramolecular quantum spintronic device.

We presented in chapter 4 an ultraclean bottom-up nanofabrication process for carbon nanotube NEMS, where carbon nanotubes are grown by CVD on a pre-fabricated metal 'backbone' junction in the very last step of the fabrication process. In contrast to top-down fabricated device, these carbon nanotube NEMS are mostly free from contaminants and defects, thus allowing a detailed study of their mechanical properties at cryogenic temperatures down to 20 mK.

Plateform for torque magnetometry: Transverse bending mode in carbon nanotube NEMS

In chapter 5, we discussed the dynamics and dissipation of *transverse bending* mode vibrations actuated by an oscillating gate potential and measured by an electronic readout at cryogenic temperatures. We demonstrated that the single-electron tunneling through the carbon nanotube quantum dot modulates the resonance frequency f_{bend} and the dissipation, i.e. the quality factor Q_{bend}, of a transverse bending mode vibration. We found that the frequency and quality factor modulation strongly depends on the electrostatic

environment of the carbon nanotube quantum dot, for instance on the current, the total capacitance, the tunnel resistance between the carbon nanotube and the metal leads and finally the temperature.

In particular, we can increase the quality factor by at least one order of magnitude by reducing the current, by reducing the tunnel resistance using a backgate voltage or by increasing the dot capacitance using a high-κ gate dielectric Al_2O_3 (chapter 5.3). We observe quality factors up to $Q_{\text{bend}} \sim 200000$ for resonance frequencies of a few hundred MHz, which is among the highest values in nanoscale resonators.

New carbon nanotube NEMS patterns are currently being developped at the institute (see appendix A.1) in order to further increase the NEMS resonance frequencies f_{bend} and quality factors Q_{bend}.

For instance, by choosing high-κ gate dielectrics such as HfO_2 or ZrO_2 or by tuning both tunnel barriers independantly *via* additional localized backgates (see Fig. 7.1 and appendix A.1 for fabrication details), one could eventually reach quality factors of $Q_{\text{bend}} \sim 10^6$.

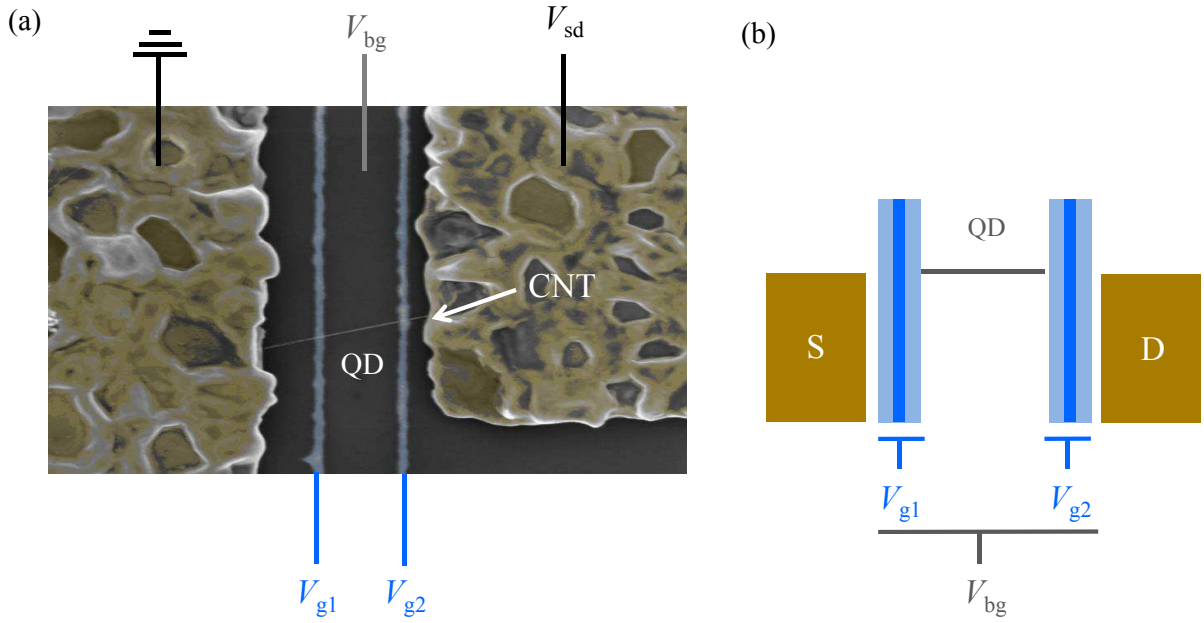

Figure 7.1: (a) False color SEM image of a carbon nanotube NEMS with two 50 nm wide metal gates, V_{lg1} and V_{lg2}, and Si++ backgate V_{bg}. (b) One can tune the tunnel barriers of the quantum dot independantly using the two local gate voltages. Light blue (dark blue) corresponds to an opaque (transparent) tunnel barrier.

In addition, the quality factor of a transverse bending mode is predicted to decay as $1/L^5$, where L is the length of the resonator [134]. Thus upon reducing the length

L of the resonator to a few tens of nanometer as depicted in Fig. 7.2 (see appendix A.2 for fabrication details), the quality factor can indeed exceed 10^6 [66]. Furthermore the resonance frequency f_{bend} decays as $1/L^2$, therefore reaching a few tens of GHz for resonator length's below 100 nm [66]. The resonance frequency and quality factor of the transverse bending mode from 27 measured carbon nanotube NEMS is depicted in Fig. 7.3 as a function of the resonator length (blue data points).

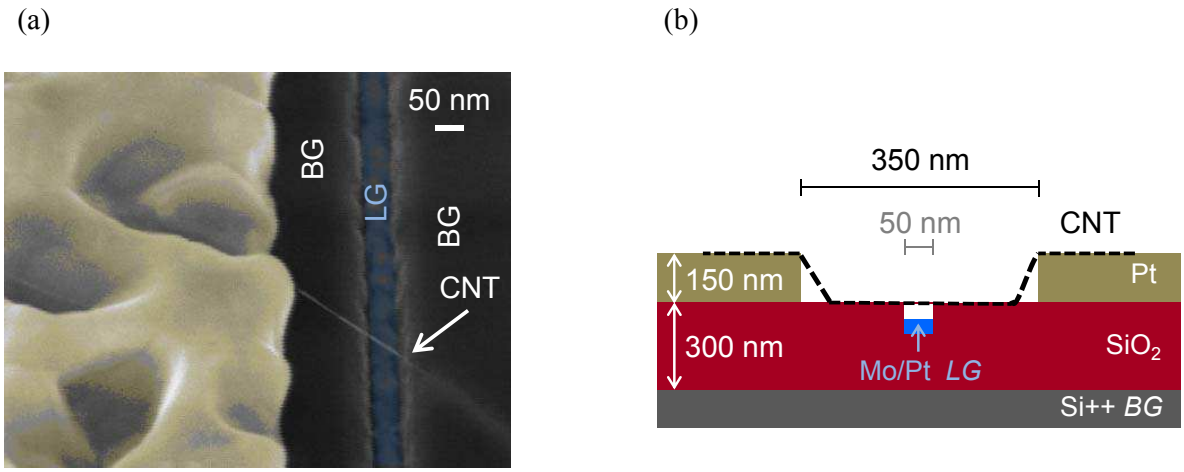

Figure 7.2: (a) False color SEM image of a carbon nanotube suspended over a localgate (blue) embedded in a 50 nm-wide trench in the SiO_2 (grey). The length of the suspended part is approximately 80 nm. (b) Cross section of device depicted in (a). The dashed line represents the carbon nanotube suspended over the embedded localgate

The high quality factors and resonance frequencies of this transverse bending mode would enable ultrasensitive torque and force detection. As described in chapter 2.3, the magnetization reversal of a single magnetic object grafted to the suspended carbon nanotube induces a shift of the bending mode's resonance frequency. The sensitivity of such a magnetic torque detector depends for instance on the mode's quality factor and the resonance frequency. For quality factors of $Q_{\text{bend}} \sim 10^6$ and resonance frequencies of $f_{\text{bend}} \sim 100$ GHz one obtains a sensitivity of approximately $1\mu_{\text{B}}$ using equation 2.16.

Although experimental evidence is so far elusive, a carbon nanotube NEMS based torque magnetometer therefore represents an ideal plateform for probing the magnetization dynamics of a single molecule magnet with the resonator's transverse bending mode.

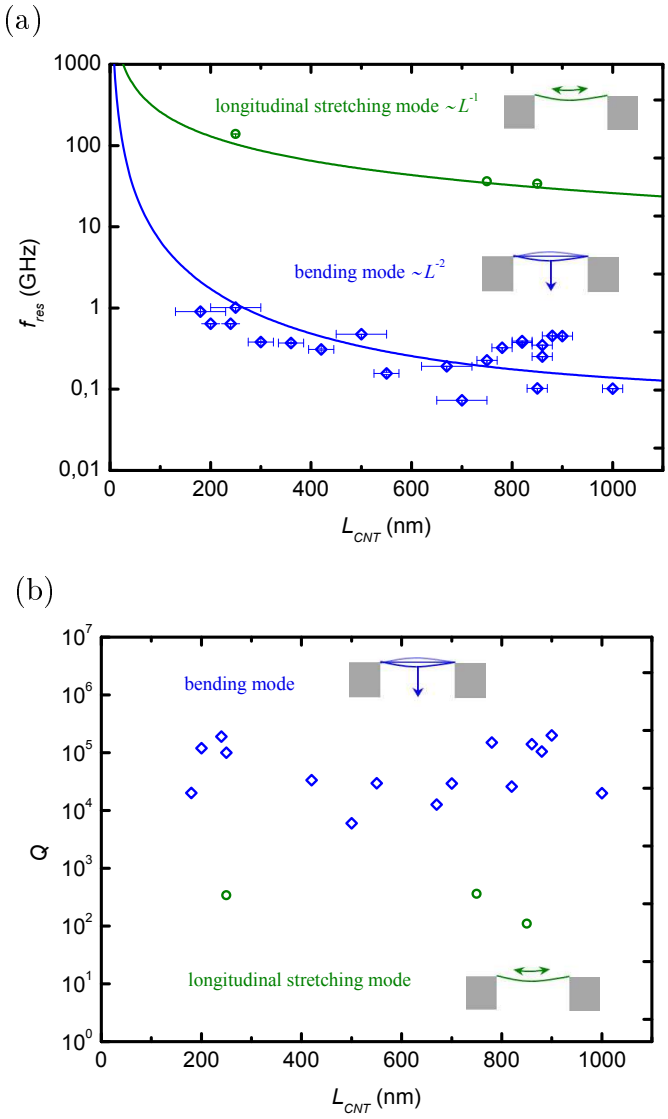

Figure 7.3: Summary of mechanical properties for 30 measured devices. (a) Resonance frequency of the fundamental transverse bending mode (blue) and longitudinal stretching mode (green) as a function of the resonator length. The experimental data follow the expected $1/L^2$ and $1/L$ dependancies, for bending and stretching mode respectively. Deviations can be attributed to different to variations of the electrostatic environment of the carbon nanotube quantum dot. The solid lines depict the expected L-dependance. (b) Quality factor Q of the transverse (blue) and longitudinal (green) stretching mode as function of the length. No clear length dependancy could be attributed. However, Q-factors for the longitudinal modes are 3 orders of magnitude smaller than for transverse bending modes as predicted in Ref [134].

A quantum harmonic oscillator: Longitudinal stretching mode in carbon nanotube NEMS

In chapter 3 and 6, we also presented evidence for a *quantized longitudinal stretching* mode vibration in the carbon nanotube NEMS at cryogenic temperatures. Due to the strong electron-phonon coupling in carbon nanotubes, longitudinal stretching modes can be actuated and detected by single-electron tunneling through the carbon nanotube. Indeed, a longitudinal stretching mode appears as a harmonic spectrum of excited vibrational states in the electron transport of the carbon nanotube NEMS at cryogenic temperatures. The observed resonance frequencies f_{long} range from 30 to 140 GHz and follow the expected $1/L$ dependance as depicted in Fig. 7.3a.

The quality factor Q_{long} of a quantized longitudinal vibration mode is given by the decay rate of the excited vibration mode and is typically on the order of 100, orders of magnitude smaller than in transverse bending mode (Fig. 7.3b).

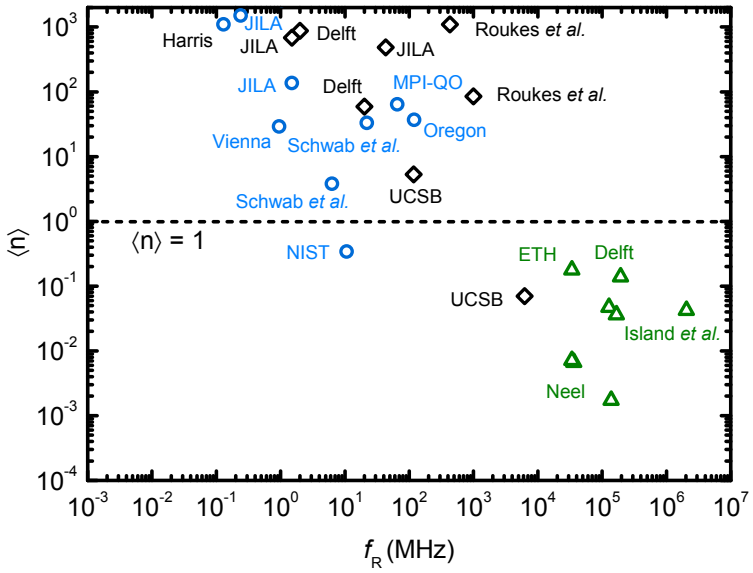

Figure 7.4: Average thermal occupation $\langle n \rangle$ of different resonator modes as function of the mode frequency. The blue circles correspond to resonator modes cooled by active feedback/sideband cooling [1], the black diamonds to resonators modes cooled by conventional cryogenic means [1] and the green triangles represent the longitudinal modes described in this manuscript and in ref. [66, 67, 68]. Modified figure from [1].

At cryogenic temperatures of $T = 20\text{mK}$, the energy of the longitudinal stretching mode $E_{\text{long}} = 140 - 575\ \mu\text{eV}$ is therefore much larger than the temperature $T = 1\mu\text{K}$ and the average level occupation of the resonator mode is on the order of $\langle n \rangle = 10^{-3}$. The quantized longitudinal stretching mode is therefore cooled into its quantum mechanical ground state $\langle n \rangle < 1$ with state of the art cryogenics, such as a dilution refrigerator.

In other terms, a longitudinal stretching mode can be seen as an experimental implementation of a quantum harmonic oscillator. Coupling such an oscillator to a "spin qubit", for example a single molecule magnet, would therefore enable the observation of quantum coherence in a "macroscopic" system.

Strong coupling between a single nuclear spin and a single quantum harmonic oscillator

In the last part of this manuscript (chapter 6), we finally presented the first experimental realization of a potential spin qubit, a $TbPc_2$ single molecule magnet, coupled to quantum harmonic oscillator, a longitudinal phonon mode in a carbon nanotube NEMS.

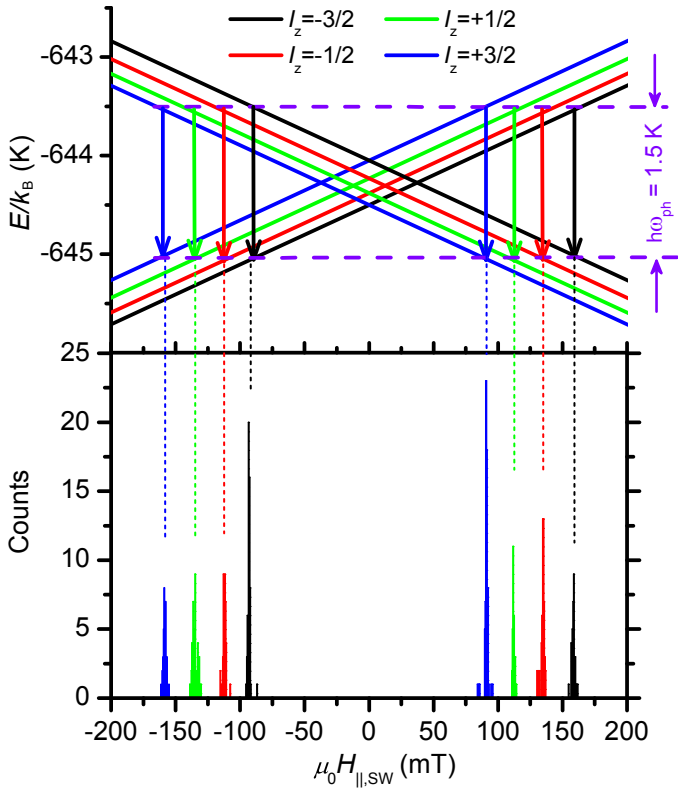

Figure 7.5: Switching field $H_{\parallel,sw}$ histogram for $H_\perp = 0$ at $T = 20$ mK and a sweep rate of 50 mT/s. The Zeeman diagram depicts the phonon-assisted transition associated with each switching event.

We successfully grafted $TbPc_2$ single molecule magnets on a carbon nanotube NEMS by drop casting from solution. Such a grafting process conserves both the magnetic properties of the single molecule magnet and the mechanical properties of the carbon nanotube resonator (see chapter 4.7).

Urdampilleta et al [48] recently demonstrated a supramolecular spin valve behaviour in a carbon nanotube functionnalized with single molecule magnets. It was shown that single molecule magnets act as polarizer and analyzer for the conduction electron in the carbon nanotube channel. In consequence the current depends on the relative spin orientation of the molecules, resulting a current jump as one of the molecules switches its magnetization. One can therefore determine the magnetic switching of a single molecule via the electronic transport in the carbon nanotube (chapter 2.3 and 6.4.2).

Using this electronic readout, we found that the magnetization reversal of the single molecule magnet is in fact enabled by a 1D quantized longitudinal stretching mode phonon in the carbon nanotube NEMS. As the decay rate or linewidth of an excited vibrational state of the phonon is smaller than the level-spacing between the nuclear spin states of the Tb^{3+} ion (chapter 6.3), one observes the magnetization reversal of the $TbPc_2$ from each of the four nuclear spin states of the Tb^{3+} ion, at four distinct values of magnetic field given by the energy of the longitudinal stretching mode phonon (Fig. 7.5).

By coupling a $TbPc_2$ single molecule magnet to a quantized phonon mode one can therefore probe the nuclear spin of an individual Tb^{3+} ion (chapter 6.4.3). Reciprocally, the same coupling also enables the readout of the energy and the frequency of the longitudinal stretching mode using the magnetization reversal of the molecule. This *spin based detection* of the resonance frequency could be extended to other vibrational modes in a carbon nanotube NEMS.

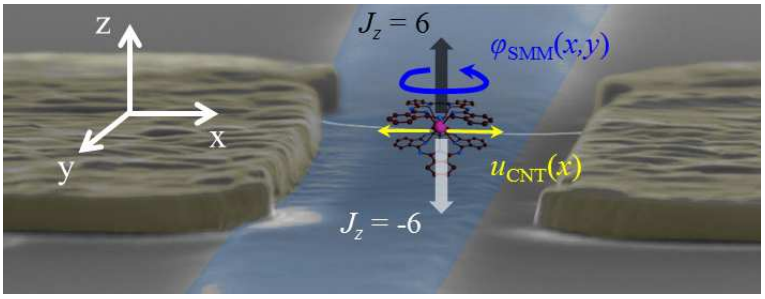

Figure 7.6: Single molecule magnet coupling to a carbon nanotube NEMS. The magnetization reversal of an $TbPc_2$ SMM from a spin state $J_z = +6$ to $J_z = -6$ results in a rotation of the SMM crystal lattice in the x-y plane. The rotation by an angle $\varphi_{\mathrm{SMM}}(x, y)$ $TbPc_2$ SMM of the generates a longitudinal stretching mode with an amplitude $u_{\mathrm{CNT}}(x)$.

We finally proposed a phenomenological explanation in order to assess the nature and the magnitude of the spin-phonon coupling. The magnetization reversal in a Tb^{3+} ion causes a rotation of the $TbPc_2$'s ligand lattice due to conservation of angular momentum. If the $TbPc_2$ single molecule magnet is rigidly grafted to the carbon nanotube, the rotation of $TbPc_2$ will generate a longitudinal stretching mode in the suspended carbon nanotube beam (Fig. 7.6). Using a Jaynes-Cummings formalism we determined a coupling strength

between the molecular spin and the quantized longitudinal motion on the order of 1 MHz (chapter 6.4.4). The magnitude of this coupling is similar to the predicted coupling in a carbon nanotube based spin qubit coupled to a carbon nanotube's nanomechanical motion [122] or to a superconducting coplanar waveguide [133]. Our findings suggest the possibility for coherent manipulation of the single molecular using the quantized mechanical motion of a carbon nanotube NEMS and *vice versa*.

Towards manipulation of a single spin and a single phonon

As demonstrated previously, the strong spin-phonon coupling enables the detection of a single nuclear/molecular spin with a quantized phonon and *vice versa*.

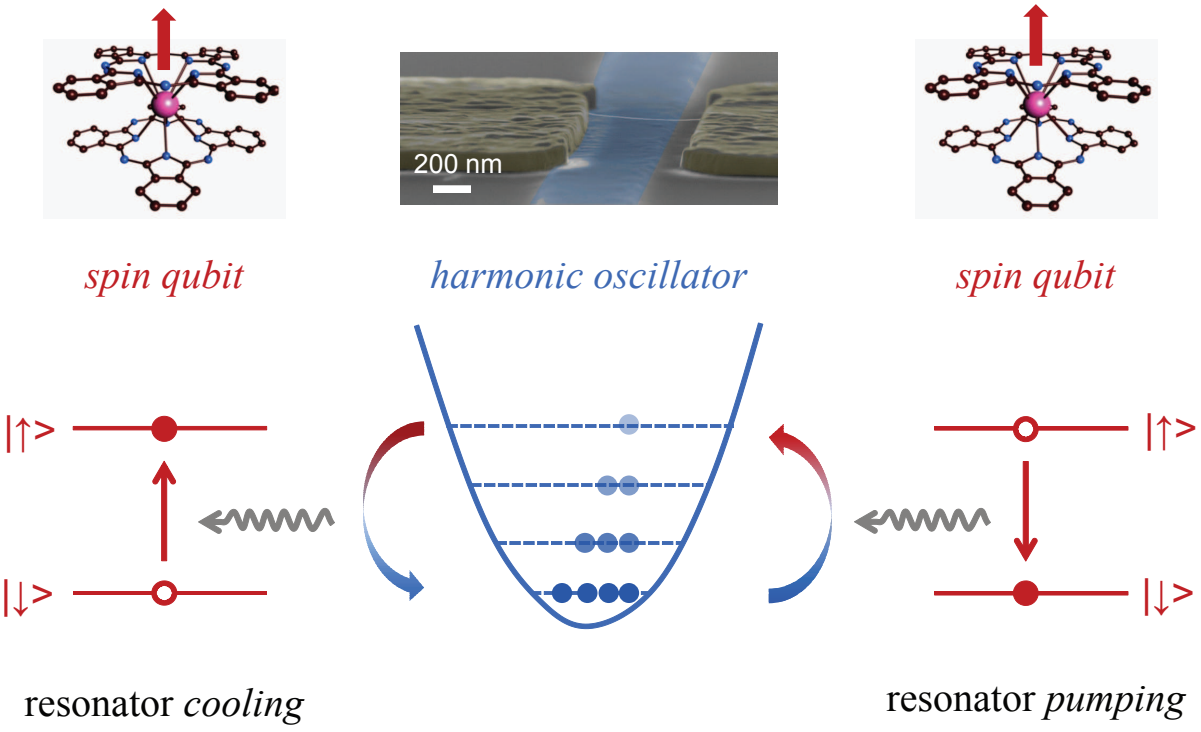

Figure 7.7: Coupling of a potential spin qubit and a harmonic oscillator. On the left hand side, the cooling of the oscillator via phonon absorption in the spin qubit is depicted. On the right hand side, the pumping of of higher excited quantum oscillation states *via* phonon emission of the spin qubit is depicted. A single molecule magnet and the longitudinal mode in carbon nanotube NEMS can be seen as potential a spin qubit and a harmonic oscillator, respectively.

Additionally, our findings suggest that one can manipulate a single molecular spin using the mechanical motion of a carbon nanotube NEMS. As we described in this

manuscript, the mechanical motion of a carbon nanotube NEMS can be controlled by static or oscillating electric fields due to strong coupling between the charge transport and mechanical motion in carbon nanotubes. Due to the strong coupling between the mechanical motion and the spin of the molecule, a modulation of the nanotube's mechanical properties, for example the resonance frequency, can therefore result in a modification of the molecule magnetization dynamics. Hence, the strong spin-phonon coupling would enable an electric control of magnetization dynamics of a single electronic or nuclear spin.

On the other hand, one can also manipulate the carbon nanotube's mechanical motion using the single molecular spin. For instance, one can use the magnetization reversal of the single molecule magnet to *pump* the excited states of the harmonic oscillator and control the phonon population. Reversely, phonons can be absorbed by the single molecule magnet resulting in a spin flip in the molecule and a cooling of the vibrational mode. Eventually one can reach the quantum mechanical ground state of the vibrational mode using this "magnetic cooling" (Fig. 7.7).

Coupling magnetism and mechanics on a molecular quantum level is therefore the next step towards coherent manipulation of a single spin or a single phonon and could open the path to quantum information processing in such a supramolecular quantum spintronic device.

Bibliography

[1] M. Poot and H. S. J. van der Zant, "Mechanical systems in the quantum regime", *Physics Report*, 511, 273-335, 2012. (Cited on pages 2, 35, 36, 37, 38, 58, 61, 75, 121, 127, 128, 129 et 155.)

[2] J. Teufel et al., "Sideband Cooling Micromechanical Motion to the Quantum Ground State", *Nature*, 475, 359-363, 2011. (Cited on pages 2.)

[3] A.D. O'Connell, M. Hofheinz, M. Ansmann, R.C. Bialczak, M. Lenander, E. Lucero, M. Neeley, D. Sank, H. Wang, M. Weides, et al., "Quantum ground state and single-phonon control of a mechanical resonator", *Nature*, 464, 697-700, 2010. (Cited on pages 2.)

[4] J. Chaste, A. Eichler, J. Moser, G. Ceballos, R. Rurali, and A. Bachtold "A nanomechanical mass sensor with yoctogram resolution", *Nature Nanotechnology*, 7, 301-304, 2012. (Cited on pages 2.)

[5] K. Jensen, K. Kim, and A. Zettl "An atomic-resolution nanomechanical mass sensor", *Nature Nanotechnology*, 3, 533-37, 2008. (Cited on pages 2 et 121.)

[6] A. Eichler, J.Moser, J. Chaste, M. Zdrojek, I. Wilson-Rae and A. Bachtold "Nonlinear damping in mechanical resonators made from carbon nanotubes and graphene", *Nature Nanotechnology*, 6, 339-342, 2011. (Cited on pages 2.)

[7] W. Wernsdorfer, "Molecular Nanomagnets : towards molecular spintronics", *Journal of Nanotechnology*, 7, 497, 2010. (Cited on pages 3.)

[8] P. Weiss "La variation du ferromagnetism en temperature", *Compte rendus*, 146, 1133-1149, 1906. (Cited on pages 2.)

[9] M. Jamet, W. Wernsdorfer, C. Thirion, D. Mailly, V. Dupuis, P. Mélinon, and A. Pérez "Magnetic Anisotropy of a Single Cobalt Nanocluster", *Physical Review Letter*, 86, 4676-4679, 1998. (Cited on pages 3.)

[10] E. C. Stoner and E. P. Wohlfarth, "A mechanism of magnetic hysteresis in heterogeneous alloys", *IEEE Transactions on Magnetics*, 27, 3475, 1991. (Cited on pages 3.)

[11] L. Bogani and W. Wernsdorfer, "Molecular spintronics using single-molecule magnets", *Nature Materials*, 7, 179-86, 2008. (Cited on pages 3, 7, 11, 12, 13, 15, 25, 26 et 122.)

[12] H. Mamin, D. Rugar, J. E. Stern, R. E. Fontana, and P. Kasiraj "Magnetic force microscopy of thin Permalloy films", *Applied Physics Letters*, 55, 318-321, 1989. (Cited on pages 4.)

[13] V. Puntes, P. Gorostiza, D. Aruguete, N. Bastus and P. Alivisatos "Collective behaviour in two-dimensional cobalt nanoparticle assemblies observed by magnetic force microscopy", *Nature Materials*, 7, 263-268, 2004. (Cited on pages 4.)

[14] A. Yamaguchi et al., "Real-Space Observation of Current-Driven Domain Wall Motion in Submicron Magnetic Wires", *Physical Review Letters*, 92, 077205, 2004. (Cited on pages 4.)

[15] D. Rugar, R. Budakian, H. J. Mamin and B. W. Chui "Single spin detection by magnetic resonance force microscopy", *Nature*, 430, 329-333, 2004. (Cited on pages 4.)

[16] M. Loehndorf, J. Moreland, P. Kabos, and N. Rizzo "Microcantilever torque magnetometry of thin magnetic films", *Journal of Applied Physics*, 87, 5995, 2000. (Cited on pages 4.)

[17] D. Min, A. McCallum, S. Russek, J. Moreland "Micromechanical torque magnetometer with sub-monolayer sensitivity", *Journal of Magnetism and Magnetic Materials*, 286, 329-335, 2005. (Cited on pages 4.)

[18] B. Lassagne, D. Ugnati, and M. Respaud, "Ultrasensitive Magnetometers Based on Carbon-Nanotube Mechanical Resonators", *Physical Review Letters*, 107, 130801-805, 2011. (Cited on pages 4, 31, 32, 120, 121 et 150.)

[19] M. Ganzhorn and W. Wernsdorfer, "Dynamics and dissipation induced by single-electron tunneling in carbon nanotube NEMS", *Physical Review Letters*, 108, 175502, 2012. (Cited on pages 5, 35, 37, 38, 60, 105, 119, 121 et 128.)

[20] M. Ganzhorn S. Klyatskaya, M. Ruben, and W. Wernsdorfer "Strong Spin-Phonon Coupling between a Single-Molecule Magnet and a Carbon Nanotube Nanoelectromechanical System", *Nature Nanotechnology*, XX, XXX-XXX , 2013. (Cited on pages 5, 14, 38, 60 et 128.)

[21] M. Baibich et al., "Giant Magnetoresistance of (001)Fe/(001)Cr Magnetic Snperlattices", *Physical Review Letters*, 61, 2472, 1988. (Cited on pages 7 et 8.)

[22] J. Barnas, A. Fuss, R. E. Camley, P. Grunberg, and W. Zinn "Novel magnetoresistance effect in layered magnetic structures: Theory and experiment", *Physical Review B*, 42, 8110, 1988. (Cited on pages 7 et 8.)

[23] Wolf, S. A. et al. "Spintronics: a spin-based electronics vision for the future.", *Science*, 194, 1488-1495, 2001. (Cited on pages 7, 9, 10 et 11.)

[24] D. Awschalom and M.E. Flatte "Challenges for semiconductor spintronics", *Nature Physics*, 3, 153-159, 2007. (Cited on pages 7 et 10.)

[25] Z.H. Xiong, D. Wu, Z. Valy Vardeny and J. Shi, "Giant magnetoresistance in organic spin-valves", *Nature*, 427, 821-824, 2004. (Cited on pages 7 et 10.)

[26] M.A. Ratner "Special feature on molecular electronics", *Proc. Natl Acad. Sci.*, 102, 8800-8837, 2005. (Cited on pages 7.)

[27] J.M. Kikkawa and D. Awschalom "Resonant spin amplification in n-type GaAs", *Physical Review Letters*, 80, 4313-4316, 1998. (Cited on pages 10.)

[28] Y. Ohno, D.K. Young, B. Beschoten, F. Matsukura, H. Ohno and D Awschalom "Electrical spin injection in a ferromagnetic semiconductor heterostructure", *Nature*, 402, 790-792, 1999. (Cited on pages 10.)

[29] J.M. Kikkawa, J.A. Gupta, I. Malajovich, D.D. Awschalom "Spin coherence in semiconductors: storage, transport and reduced dimensionality", *Physica E*, 9, 194-201, 2001. (Cited on pages 10 et 11.)

[30] C. Adelmann, X. Lou, J. Strand, C. J. Palmstrøm, and P. A. Crowell "Spin injection and relaxation in ferromagnet-semiconductor heterostructures", *Physical Review B*, 71, 121301, 2005. (Cited on pages 10.)

[31] J.M. Tang, J. Levy and M.E. Flatte "All electrical control of single ion spin in semiconductors", *Physical Review Letters*, 97, 106803, 2006. (Cited on pages 10.)

[32] G. Szulczewski, S. Sanvito and J. M. D. Coey, "A spin of their own", *Nature Materials*, 8, 693-695, 2009. (Cited on pages 11.)

[33] S. Sanvito "Molecular Spintronics", *Chem. Soc. Rev.*, 40, 3336-3355, 2011. (Cited on pages 10.)

[34] N. Roch, S. Florens, V. Bouchiat, W. Wernsdorfer and F. Balestro "Quantum phase transition in a single molecule quantum dot", *Nature*, 453, 633-636, 2008. (Cited on pages 12.)

[35] George Christou, Dante Gatteschi, David N. Hendrickson, and Roberta Sessoli "Single Molecule Magnets", *MSR bulletin* 2000. (Cited on pages 12 et 13.)

[36] Gatteschi, D., Sessoli, R., Villain, J., "Molecular Nanomagnets", *Oxford University Press* 2006. (Cited on pages 12, 13 et 121.)

[37] S. Klyatskaya, J.R. Galan Mascaros,L. Bogani, F. Hennrich, M. Kappes, W. Wernsdorfer, and M. Ruben "Anchoring of rare-earth-based single-molecule magnets on

single-walled carbon nanotubes", *Journal of the American Chemical Society*, 131, 15143-51, 2009. (Cited on pages 13, 15, 98, 101, 122 et 123.)

[38] M. Lopes et al., "Surface-enhanced Raman signal for terbium single-molecule magnets grafted on graphene", *ACS Nano*, 4, 7531, 2010. (Cited on pages 13 et 123.)

[39] N. Ishikawa, M. Sugita, T. Ishikawa, S. Koshibara and Y. Kaizu "Mononuclear Lanthanide Complexes with a long magnetization relaxation time at high temperature: A new category of magnets at the single molecule level", *Journal of Physical Chemistry B* , 108, 11265-11271, 2004. (Cited on pages 13.)

[40] K. Wieghardt, K. Pohl, I. Jibril, and G. Huttner "Mononuclear Lanthanide Complexes with a long magnetization relaxation time at high temperature: A new category of magnets at the single molecule level", *Angewandte Chemie, International Edition English*, 23, 77, 1984. (Cited on pages 13.)

[41] A. Giusti et al., "Magnetic Bistability of Individual Single-Molecule Magnets Grafted on Single-Wall Carbon Nanotubes", *Angewandte Chemie, International Edition English*, 48, 1-5, 2009. (Cited on pages 13.)

[42] W. Wernsdorfer and R. Sessoli "Quantum phase interference and parity effects in magnetic molecular clusters", *Science*, 284, 133-135, 1999. (Cited on pages 14 et 122.)

[43] Takahashi, S., et al. "Coherent manipulation and Decoherence of S = 10 Single-Molecule Magnet", *Physical Review Letters*, 102, 087603, 2009. (Cited on pages 14 et 122.)

[44] A. Ardavan et al. "Will spin-relaxation times in molecular magnets permit quantum information processing?", *Physical Review Letters*, 98, 057201, 2007. (Cited on pages 14.)

[45] Y.-S. Fu, J. Schwobel, S.-W. Hla, A. Dilullo, G. Hoffmann, S. Klyatskaya, M. Ruben, R. Wiesendanger, "Reversible chiral switching of bis(phthalocyaninato) terbium(III) on a metal surface", *Nano Letters*, 12, 3931, 2012. (Cited on pages 14 et 25.)

[46] J. Schwöbel, Y. Fu, J. Brede, A. Dilullo, G. Hoffmann, S. Klyatskaya, M. Ruben and R. Wiesendanger "Real-space observation of spin-split molecular orbitals of adsorbed single-molecule magnets.", *Nature communications*, 3, 953, 2012. (Cited on pages 14, 25 et 26.)

[47] R. Vincent, S. Klyatskaya, M. Ruben, W. Wernsdorfer and F. Balestro, "Electronic readout of a single nuclear spin in a single molecule transistor", *Nature*, 488, 357-360 , 2012. (Cited on pages 14, 25, 26, 122 et 134.)

[48] M. Urdampilleta, J.P. Cleuziou, S. Klyatskaya, M. Ruben, and W. Wernsdorfer "Supramolecular spin valves", *Nature Materials*, 10, 502-506 , 2011. (Cited on pages 14, 28, 29, 30, 98, 101, 122, 123, 124, 125, 126, 133, 136, 137 et 157.)

[49] N. Ishikawa, M. Sugita, and W. Wernsdorfer, "Quantum tunneling of magnetization in lanthanide single-molecule magnets: bis(phthalocyaninato)terbium and bis(phthalocyaninato)dysprosium anions", *Angewandte Chemie (International ed. in English)*, 44, 2931-2935, 2005. (Cited on pages 16, 18, 19, 123, 125 et 134.)

[50] Abragam, A., Bleaney, B., "Electron Paramagnetic Resonance of transition ions", *Oxford University Press* 1970. (Cited on pages 16, 17, 23, 24, 25, 121, 125, 126 et 183.)

[51] N. Ishikawa, M. Sugita, T. Okubo, N. Tanaka, T. Iino, and Y. Kaizu, "Determination of Ligand-Field Parameters and f-Electronic Structures of Double-Decker Bis(phthalocyaninato)lanthanide Complexes.", *Inorganic Chemistry*, 42, 2440-2446, 2003. (Cited on pages 17 et 147.)

[52] K.W.H Stevens, "Matrix elements and operator equivalents connected with the magnetic properties of rare earth ions", *Proceeding of the Physical Society A*, 65, 209, 1952. (Cited on pages 17, 147 et 148.)

[53] H. Konami, M. Hatano and A. Tajiri, "An analysis of paramagnetic shifts in proton NMR spectra of non-radical lanthanide(III)-phthalocyanine sandwich complexes", *Chemical Physics Letters*, 160, 163-167, 1989. (Cited on pages 17, 147 et 148.)

[54] W. Wernsdorfer, "From micro- to nano-SQUIDs: applications to nanomagnetism", *Superconductor Science and Technology*, 22, 064013 , 2009. (Cited on pages 21 et 120.)

[55] C. Zener "Non-adiabatic crossing of energy levels", *Proceeding of the royal society of london serie A*, 137, 696-702 , 1932. (Cited on pages 22.)

[56] T. Komeda, H. Isshiki, J. Liu, Y. Zhang, N. Lorente, K. Katoh, B. K. Breedlove and M. Yamashita "Observation and electric current control of a local spin in a single-molecule magnet", *Nature communications*, 2, 217, 2011. (Cited on pages 25.)

[57] R. Maurand "Carbon nanotube SQUID's: From Josephson junctions to quantum dots, Pi-junctions, Kondo effect and detection of single molecule magnets", PhD thesis, University Joseph Fourier et Institut Neel-CNRS, 2011. (Cited on pages 27, 79 et 80.)

[58] J.-P. Cleuziou, W. Wernsdorfer, V. Bouchiat, Th. Ondarçuhu, M. Monthioux "Carbon nanotube superconducting interference device", *Nature Nanotechnology*, 1, 53-59 , 2006. (Cited on pages 27.)

[59] J.-C. Charlier, X. Blase, and S. Roche, "Electronic and transport properties of nanotubes", *Review of Modern Physics*, 79, 677, 2007. (Cited on pages 28.)

[60] J. Nygård, D. H. Cobden, and P. E. Lindelof, "Kondo physics in carbon nanotubes", *Nature (London)*, 408, 342-46, 2000. (Cited on pages 28.)

[61] G. A. Steele, A. K. Hüttel, B. Witkamp, M. Poot, H. B. Meerwaldt, L. P. Kouwenhoven, and H. S. J. van der Zant, "Strong Coupling Between Single-Electron Tunneling and Nanomechanical Motion", *Science*, 325, 1103-1106, 2009. (Cited on pages 36, 37, 44, 48, 50, 51, 52, 53, 54, 61, 75, 88, 105, 107, 109, 110, 115, 119 et 121.)

[62] M. Poot, S. Etaki, H. Yamaguchi, and H. S. J. van der Zant "Discrete-time quadrature feedback cooling of a radio-frequency mechanical resonator", *Applied Physics Letter*, 99, 013113, 2011. (Cited on pages 36.)

[63] M. D. LaHaye, O. Buu, B. Camarota, K. C. Schwab "Approaching the quantum limit of a nanomechanical resonator", *Science*, 304, 74, 2004. (Cited on pages 36.)

[64] B. Witkamp, M. Poot, H.S.J. van der Zant, "Bending-mode vibration of a suspended nanotube resonator", *Nano Letters*, 6, 2904, 2006. (Cited on pages 36.)

[65] E. Laird, F. Pei, W. Tang, G. A. Steele, and L. P. Kouwenhoven, "A High quality factor carbon nanotube mechanical resonator at 39 GHz", *Nano Letters*, 12, 193-197, 2011. (Cited on pages 37, 38, 42, 43, 61, 75, 121, 127 et 128.)

[66] J. O. Island, V. Tayari, A. C. McRae, and A. R. Champagne "Few-Hundred GHz Carbon Nanotube Nanoelectromechanical Systems (NEMS)", *Nano Letters*, 12, 4564-4569, 2012. (Cited on pages 37, 38, 127, 128, 153 et 155.)

[67] R. Leturcq, C. Stampfer, K. Inderbitzin, L. Durrer, C. Hierold, E. Mariani, M. Schultz, F. von Oppen, and K. Ensslin, "Franck-Condon blockade in suspended carbon nanotube quantum dots", *Nature Physics*, 5, 327-331, 2009. (Cited on pages 38, 54, 55, 58, 59, 60, 121, 127, 128, 131, 132 et 155.)

[68] S. Sapmaz, P. Jarillo-Herrero, Y.M. Blanter, C. Dekker, and H. S. J. van der Zant, "Tunneling in suspended carbon nanotubes assisted by longitudinal phonons", *Physical Review Letters*, 96, 026801, 2006. (Cited on pages 38, 54, 55, 58, 121, 127, 128, 130 et 155.)

[69] L. Landau, and E. Lifschitz "Course of Theoretical Physics: Theory of Elasticity", *Elsevier* 1986. (Cited on pages 39 et 58.)

[70] V. Sazonova "A tunable carbon nanotube resonator", PhD thesis, Cornell University, 2004. (Cited on pages 39, 40, 41, 42, 44, 46, 47, 53, 117 et 118.)

[71] S. Sapmaz, Y.M. Blanter, L. Gurevich, and H.S.J van der Zant, "Carbon nanotubes as nanoelectromechanical systems", *Physical Review B*, 67, 235414, 2003. (Cited on pages 40 et 41.)

[72] A. K. Hüttel, H. B. Meerwaldt, G. A. Steele, M. Poot, B. Witkamp, L. P. Kouwenhoven, H. S. J. van der Zant "Single electron tunnelling through high-Q single-wall carbon nanotube NEMS resonators", *Physica status solidi b*, 247, 2974, 2010. (Cited on pages 42 et 43.)

[73] M. Poot "Mechanical systems at the nanoscale", PhD thesis, Technische Universiteit Delft, 2009. (Cited on pages 44, 45 et 46.)

[74] B. Lassagne, Y. Tarakanov, J. Kinaret, D. Garcia-Sanchez, and A. Bachtold, "Coupling Mechanics to Charge Transport in Carbon Nanotube Mechanical Resonators", *Science*, 325, 1106-1111, 2009. (Cited on pages 44, 48, 49, 105, 107, 110, 115, 119 et 121.)

[75] A. K. Hüttel, G. A. Steele, B. Witkamp, M. Poot, L. P. Kouwenhoven, and H. S. J. van der Zant, "Carbon Nanotubes as Ultrahigh Quality Factor Mechanical Resonators", *Nano Letters*, 9, 2547-2552, 2009. (Cited on pages 45, 61, 105, 107, 109, 116, 119 et 121.)

[76] C. W. J. Beenakker "Theory of Coulomb-blockade oscillations in the conductance of a quantum dot", *Physical Review B*, 44, 1646-1656, 1991. (Cited on pages 49.)

[77] H.B. Meerwaldt, G. Labadze, B.H. Schneider, A. Taspinar, Ya.M. Blanter, H.S.J. van der Zant, and G.A. Steele "A nanomechanical resonator as a probe of the charge of a quantum dot", *Physical Review B*, 86, 115454, 2012. (Cited on pages 53.)

[78] E. Mariani, and F. von Oppen "Electron-vibron coupling in suspended carbon nanotube quantum dots", *Physical Review B*, 80, 155411, 2009. (Cited on pages 54, 55 et 56.)

[79] A. K. Huettel, B. Witkamp, M. Leijnse, M. R. Wegewijs, and H. S. J. van der Zant "Pumping of Vibrational Excitations in the Coulomb-Blockade Regime in a Suspended Carbon Nanotube", *Physical Review Letters*, 102, 225501, 2009. (Cited on pages 58, 121, 127, 130, 131 et 132.)

[80] N.R. Franklin, Q. Wang, T.W. Tombler, A. Javey, M. Shim, and H.J. Dai "Integration of suspended carbon nanotube arrays into electronic devices and electromechanical systems", *Applied Physics Letters*,81, 913, 2002. (Cited on pages 61 et 75.)

[81] J. Cao, Q. Wang, D. Wang, H. Dai "Suspended carbon nanotube quantum wires with two gates", *Small*,1, 138-141, 2005. (Cited on pages 61, 63, 68, 75 et 85.)

[82] L. Shon-Roy, A. Wiesnoski, and R. Zorich, "Advanced Semiconductor Fabrication Handbook", *Scottsdale, Ariz.: Integrated Circuit Engineering Corporation* 1998. (Cited on pages 62 et 63.)

[83] Rogue Valley Microdevices Website: www.roguevalleymicro.com/DryChlorinatedThermalOxidation.php (Cited on pages 62 et 63.)

[84] H. Kahn, N. Jing, M. Huh and A.H. Heuer "Growth stresses and viscosity of thermal oxides on silicon and polysilicon", *Journal of Materials Research*, 21, 209-214, 2006. (Cited on pages 62.)

[85] A. Stesmans "Relationship between stress and dangling bond generation at the (111)Si/SiO_2 interface", *Physical Review Letters*, 70, 1723-1726, 1993. (Cited on pages 62.)

[86] NOVA Electronic Materials Website: www.novawafers.com (Cited on pages 63.)

[87] Wikipedia Website, *Photolithography*: www.wikipedia.org/wiki/Photolithography (Cited on pages 65.)

[88] MicroChemicals Technical Handbook "Photolithography: Theory and Application of Photoresists, Etchants and Solvents", *MicroChemicals* 2012. (Cited on pages 65.)

[89] S. George "Atomic Layer Deposition: An Overview", *Chemical Review*, 110, 111-131, 2010. (Cited on pages 70 et 72.)

[90] Cambridge Nanotech Website, *Atomic Layer Deposition*: www.cambridgenanotech.com/ald, (Cited on pages 71 et 72.)

[91] H. Klauk (Ed.), "Organic Electronics: Materials, Manufacturing and Applications", *Wiley-VCH Verlag GmBH & Co. KGaA* 2006. (Cited on pages 72.)

[92] V. Ngoc-Nguyen "Synthesis and electronic transport of ultraclean single wall carbon nanotubes", PhD thesis, University Joseph Fourier et Institut Neel-CNRS, 2012. (Cited on pages 75, 76 et 77.)

[93] H. Koops, J. Kretz, M. Rudolph, M. Weber, G. Dahm and K.L. Lee "Characterization and Application of Materials grown by electron-beam-induced deposition", *Japanese Journal of Applied Physics*,33, 7099-7107, 1994. (Cited on pages 79.)

[94] M.F. Yu, O. Lourie, M.J. Dyer, K. Molony, T.F. Kelly, R.S. Ruoff "Strength and Breaking Mechanism of Multiwalled Carbon Nanotubes Under Tensile Load", *Science*,287, 637-640, 2000. (Cited on pages 79.)

[95] N. Roch "Single molecule transistors: From exotic Kondo effects to molecular spintronics", PhD thesis, University Joseph Fourier et Institut Neel-CNRS, 2009. (Cited on pages 79 et 80.)

[96] R. Picquerel "", PhD thesis, University Joseph Fourier et Institut Neel-CNRS, 2012. (Cited on pages 79.)

[97] C.M. Aguirre, P.L. Levesque, M. Paillet, F. Lapointe, B.C. St-Antoine, P. Desjardins, and R. Martel "The Role of the Oxygen/Water Redox Couple in Suppressing Electron Conduction in Field-Effect Transistors", *Advanced Materials*,21, 1-5, 2009. (Cited on pages 85.)

[98] M.J. O'Connell, P. Boul, L.M. Ericson, C3 Huffman, Y. Wang, E. Haroz, C. Kuper, J. Tour, K.D. Ausman, and R.E. Smalley "Reversible water-solubilization of single-walled carbon nanotubes by polymer wrapping", *Chemical Physics Letters*,342, 265-271, 2001. (Cited on pages 85.)

[99] A. Vijayaraghavan, S. Kar, C. Soldano, S. Talapatra, O. Nalamasu, and P.M. Ajayan "Charge-injection-induced dynamic screening and origin of hysteresis in field-modulated transport in single-wall carbon nanotubes", *Applied Physics Letters*,89, 162108, 2006. (Cited on pages 87.)

[100] W. Kim, A. Javey, O. Vermesh, Q. Wang, Y. Li, and H. Dai "Hysteresis Caused by Water Molecules in Carbon Nanotube Field-Effect Transistors", *Nano Letters*,3, 193-198, 2003. (Cited on pages 87.)

[101] H. Ingerslev Jørgensen, T. Novotny, K. Grove-Rasmussen, K. Flensberg, and P. E. Lindelof "Critical Current 0-π Transition in Designed Josephson Quantum Dot Junctions", *Nano Letters*, 7, 2441-2445, 2007. (Cited on pages 109.)

[102] J. Koenig, J. Schmid, H. Schoeller, and G. Schoen, "Resonant tunneling through ultrasmall quantum dots: Zero-bias anomalies, magnetic-field dependence, and boson-assisted transport", *Physical Review B*, 54, 16820, 1996. (Cited on pages 109.)

[103] V. Sazonova, Y. Yaish, H. Ustunel, D.Roundy, T.A. Arias and P.L. McEuen, "A tunable carbon nanotube electromechanical oscillator", *Nature (London)*, 431, 284-87, 2004. (Cited on pages 110, 115 et 119.)

[104] T. S. Jespersen , K. Grove-Rasmussen, J. Paaske, K. Muraki, T. Fujisawa, J. Nygård, and K. Flensberg, "Gate dependant spin orbit coupling in multielectron carbon nanotube quantum dots", *Nature Physics*, 7, 348-53, 2011. (Cited on pages 110.)

[105] G. A. Steele, G. Gotz, and L. P. Kouwenhoven, "Tunable few-electron double quantum dots and Klein tunnelling in ultraclean carbon nanotubes", *Nature Nanotechnology*, 4, 363-67, 2009. (Cited on pages 110.)

[106] S.B. Shim, J.S. Chun, S.W. Kang, S.W. Cho, and S.W. Cho "Micromechanical resonators fabricated from lattice-matched and etch-selective GaAs/InGaP/GaAs heterostructures", *Applied Physics Letters*, 91, 133505, 2007. (Cited on pages 116, 117 et 119.)

[107] G. Zolfagharkhani, A. Gaidarzhy, S.B. Shim, R.L. Badzey, and P. Mohanty "Quantum friction in nanomechanical oscillators at millikelvin temperatures", *Physical Review B*, 72, 224101, 2005. (Cited on pages 116, 117 et 119.)

[108] C. Seoanez, F. Guinea and A. H. Castro Neto "Dissipation due to two-level systems in nano-mechanical devices", *EPL*, 78, 60002, 2007. (Cited on pages 117 et 119.)

[109] J. Hone, M.C. Llaguno, M.J. Biercuk, A.T. Johnson, B. Batlogg, Z. Benes, J.E. Fischer "Thermal properties of carbon nanotubes and nanotube-based materials", *Applied Physics A*, 74, 339-343, 2002. (Cited on pages 117 et 118.)

[110] Y.-K. Kwon, S. Berber, and D. Tomanek "Thermal Contraction of Carbon Fullerenes and Nanotubes", *Physical Review Letters*, 92, 015901, 2004. (Cited on pages 117 et 118.)

[111] M. Bockrath, D. H. Cobden, J. Lu, A. G. Rinzler, R. E. Smalley, L. Balents and P.L. McEuen, "Luttinger-liquid behaviour in carbon nanotubes", *Nature (London)*, 397, 598-601, 1999. (Cited on pages 118.)

[112] C. Kane, L. Balents, and M. Fisher, "Coulomb Interactions and Mesoscopic Effects in Carbon Nanotubes", *Physical Review Letters*, 79, 5086-89, 1997. (Cited on pages 118.)

[113] R. Egger and A. Gogolin, "Effective Low-Energy Theory for Correlated Carbon Nanotubes", *Physical Review Letters*, 79, 5082-85, 1997. (Cited on pages 118.)

[114] A. A. Kovalev, L. X. Hayden, G. E. W. Bauer, and Y. Tserkovnyak "Macrospin Tunneling and Magnetopolaritons with Nanomechanical Interference", *Physical Review Letters*, 106, 147203 , 2011. (Cited on pages 120, 121, 122, 147, 148 et 149.)

[115] D. Garanin and E. Chudnovsky, "Quantum Entanglement of a Tunneling Spin with Mechanical Modes of a Torsional Resonator", *Physical Review X*, 1, 011005 , 2011. (Cited on pages 120, 121, 122 et 149.)

[116] Heitler, W., Teller, E., "Time Effects in the Magnetic Cooling Method", *Proc. R. Soc. Lond. A*,155, 629, 1936. (Cited on pages 121.)

[117] Van Vleck, J.H., "Paramagnetic Relaxation Times for Titanium and Chrome Alum", *Physics Review*,57, 426, 1940. (Cited on pages 121.)

[118] Villain, J., Hartman-Boutron, F,. Sessoli, R., Rettori, A., "Magnetic Relaxation in Big Magnetic Molecules", *Europhysics Letters*,27, 159, 1994. (Cited on pages 121.)

[119] Garanin, D.A., Chudnosvky, E.M., "Thermally activated resonant magnetization tunneling in molecular magnets: Mn12Ac and others", *Physical Review B*,56, 11102, 1997. (Cited on pages 121.)

[120] Leuenberger, M., Loss, D., "Spin relaxation in Mn12-acetate", *Europhysics Letters*,46, 629, 1999. (Cited on pages 121.)

[121] Sessoli, R., Gatteschi, D., Caneschi, A., Novak, N.A., "Magnetic Bistability of a metal-ion cluster", *Nature*,365, 141, 1993. (Cited on pages 121.)

[122] Palyi, A., Struck, P.R., Rudner M., Flensberg, K. and Burkard, G., "Spin-orbit-induced strong coupling of a single spin to a nanomechanical resonator", *Physical Review Letters*,108, 206811, 2012. (Cited on pages 121, 122, 127, 149, 150 et 158.)

[123] H.B. Peng, C.W. Chang, S. Aloni, T. Yuzvinsky, and A. Zettl, "Ultrahigh frequency nanotube resonator", *Physical Review Letters*, 97, 087203, 2006. (Cited on pages 121.)

[124] H.-Y. Chiu, P. Hung, H. W. C. Postma, and M. Bockrath "Ultrasensitive mass sensing with a nanotube electromechanical resonator", *Nano Letters*, 8, 3735-3738, 2008. (Cited on pages 121.)

[125] B. Lassagne, D. Garcia-Sanchez, A. Aguasca, and A. Bachtold, "Atomic-Scale Mass Sensing Using Carbon Nanotube Resonators", *Nano Letters*, 8, 4342-46, 2008. (Cited on pages 121.)

[126] H. Heersche et al. "Electron transport through single Mn12 molecular magnets", *Physical Review Letters*, 96, 206801 , 2006. (Cited on pages 122.)

[127] A.S. Zyazin, et al. "Electric field controlled magnetic anisotropy in a single molecule", *Nano Letters*, 10, 3307-3311 , 2010. (Cited on pages 122.)

[128] J.R. Friedman, M.P. Sarachik, J. Tejada, J., and R. Ziolo, "Macroscopic measurement of resonant magnetization tunnelling in high-spin molecules", *Physical Review Letters*, 76, 3830-3833 , 1996. (Cited on pages 122.)

[129] L. Thomas et al., "Macroscopic quantum tunnelling of magnetization in a single crystal of nanomagnets", *Nature*, 383, 145-147, 1996. (Cited on pages 122.)

[130] M. Urdampilleta "Molecular Spintronics: From a supramolecular spin valve to single spin detection", PhD thesis, University Joseph Fourier et Institut Neel-CNRS, 2012. (Cited on pages 126, 127, 133, 136 et 137.)

[131] M.S. Dresselhaus, G. Dresselhaus, R. Saito, A. Jorio "Raman spectroscopy of carbon nanotubes", *Physics Reports*, 409, 47-99, 2005. (Cited on pages 128.)

[132] E. Chudnovsky, D.A. Garanin and R. Schilling "Universal mechanism of spin relaxation in solids", *Physical Review B*, 72, 094426, 2005. (Cited on pages 147 et 148.)

[133] A. Cottet and T. Kontos "Spin Quantum Bit with Ferromagnetic Contacts for Circuit QED", *Physical Review Letters*, 105, 160502, 2010. (Cited on pages 149 et 158.)

[134] A. De Martino, R. Egger, and A. O. Gogolin "Phonon-phonon interactions and phonon damping in carbon nanotubes", *Physical Review B*, 79, 205408, 2009. (Cited on pages 152 et 154.)

Appendix A

Nanofabrication of alternate carbon nanotube NEMS designs

A.1 Carbon nanotube NEMS with multiple local gates

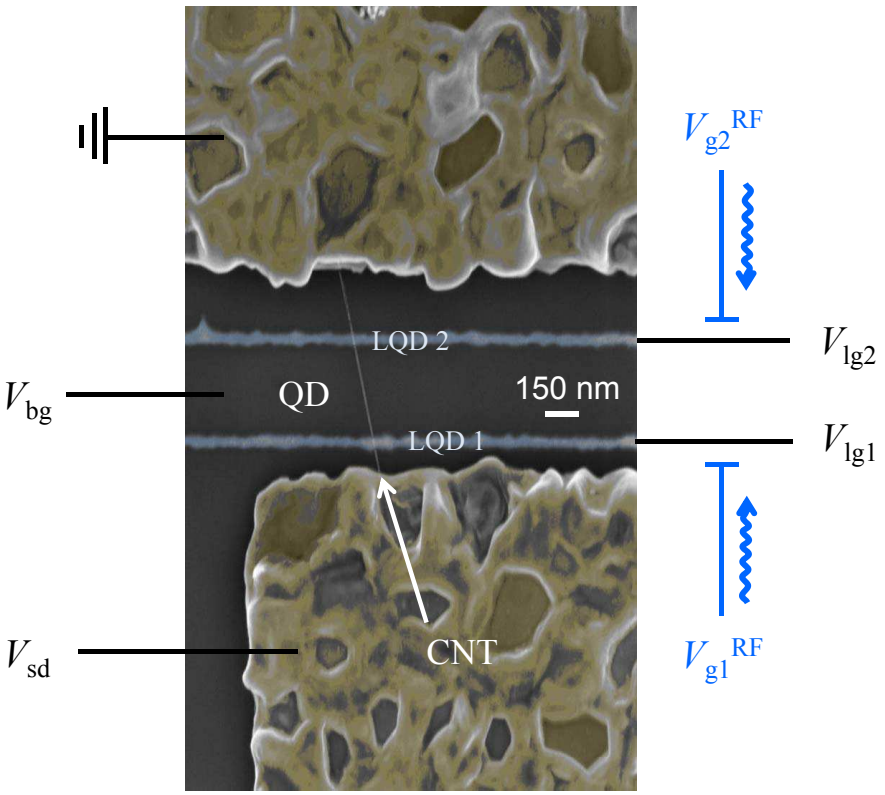

Figure A.1: False color SEM image of a carbon nanotube NEMS with two 50 nm wide metal gates, V_{lg1} and V_{lg2}, and Si++ backgate V_{bg}. One can create two or more localized quantum dots (LQD) using those gates and indivually adress them with DC or RF voltages. A single molecule magnet coupled to one of the LQD can thus be manipulated for example with a microwave.

Here we describe the implementation of a carbon nanotube NEMS junction with sev-

eral localgates. We will describe the nanofabrication process for a junction with two 100 nm wide local gates, which can be readily extended to 3 or 4 gates if necessary. These gates can for instance be used to create and individually adress several localized quantum dots on a carbon nanotube as well as manipulate single molecule magnets coupled to these localized dots, using for example a microwave.

Since the lateral dimension of the gates is below the resolution of optical lithography, we proceed all steps with electron beam lithography. The devices were designed and fabricated with the help of Thierry Crozes and Thierry Fournier at the Nanofab facility at Neel Institute. We used a LEO 1530 SEM controlled by a Raith ELPHY command module (and user interface). The devices are fabricated in three ebeam lithography steps and layers which we describe in the following.

First lithography step: Local metallic gates

Step	description	equipement	parameters, comments
0	cleaning	O_2 plasma, RIE	10 min at 50W, 20 cc O_2
1	PMMA 2 % resist	spin coater	2000 rpm, 2000rpm/s for 60s thickness 110 nm
2	PMMA 2 % softbake	hotplate	5 min at 180°C
3	e-beam exposure	SEM LEO 1530 ELPHY 6.0	$E = 20$ kV settling time 2.5 ms
	100 μm^2 writefield 1 mm^2 writefield	7.5 μm aperture 120 μm aperture	275 $\mu C/cm^2$ 350 $\mu C/cm^2$
4	development	MIBK/IPA 1:3	30s
5	developper neutralization	IPA	60s
6	removing residual resist	O_2 plasma, RIE	3s at 50W, 20 cc O_2
7	metal depostion	ebeam evaporator PLASSYS	15 nm Mo or W 15 nm Pt
8	metal lift off	acetone	5 min at 45°C until excess metal is removed

Table A.1: Fabrication process for carbon nanotube NEMS backbone junction with multiple backgate *via* e-beam lithography: first localgate layer

Following the process listed in table A.1, we first pattern a localgate array (Fig. A.2), reproduced and arranged in a 1"x1" matrix, on a 2" Si++ wafer covered by 300 nm of dry chlorinated SiO_2. After metallization of the first layer, 50 nm of Al_2O_3 are deposited by ALD which will serve as gate dielectric.

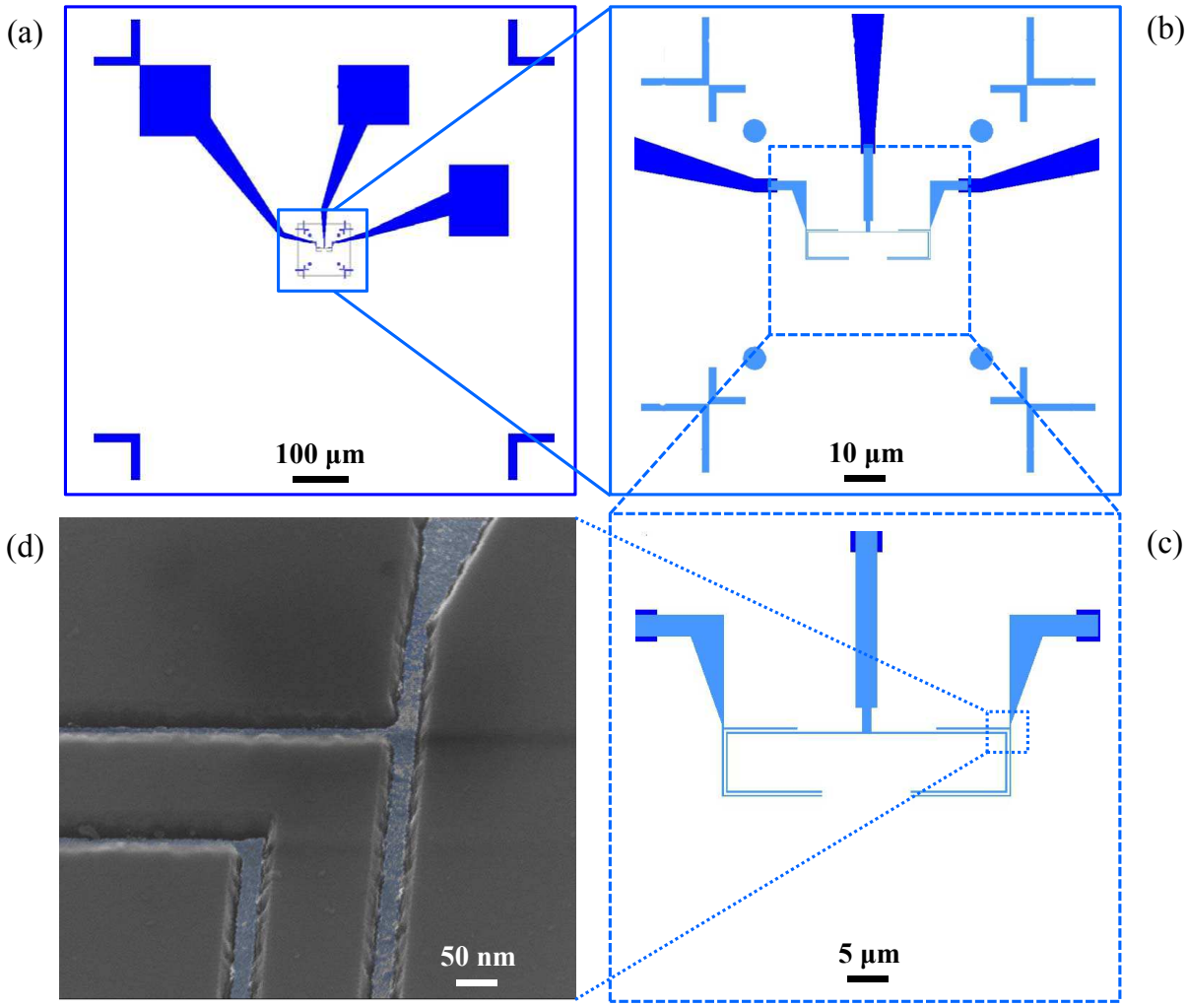

Figure A.2: Multiple gate carbon nanotube NEMS, first layer local gates (blue colors). (a) 1 mm writefield, displaying pads for electrical connection, alignement marks and the central writefield (blue box). (b) 100 μm writefield, showing the local gate pattern at the center (light blue dotted box) and marks (crosses and circles) for the alignement of the second layer. (c) 50 μm writefield, showing the local gate pattern. We have two 100 nm wide gates separated by 300 nm. (d) Falso color SEM image of a portion of the local gates after metallization of the first layer.

Second lithography step: High precision alignement and source-drain junctions

The key step of the process is the accurate alignement of the second lithography layer (Fig. A.3) with respect to the first one (Fig. A.2). The alignement procedure consists of

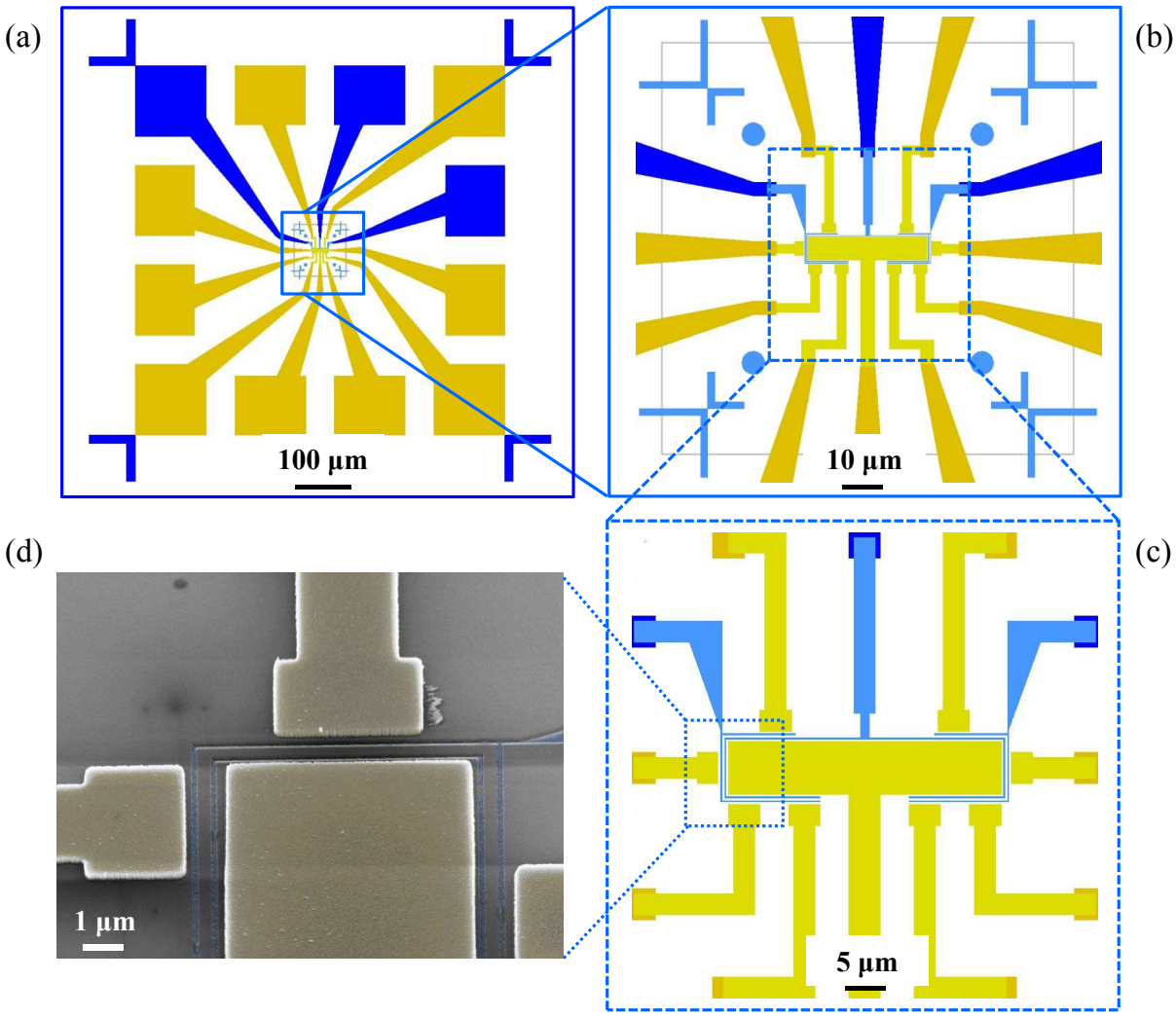

Figure A.3: Multiple gate carbon nanotube NEMS, second layer source-drain junctions (yellow colors). (a) 1 mm writefield, displaying pads for electrical connection, alignement marks and the central writefield (blue box). (b) 100 μm writefield, showing the central pattern (light blue dotted box) and the marks (crosses and circles) used for the alignement of the second layer. (c) 50 μm writefield, showing the 8 junctions aligned above the local gates. (d) Falso color SEM image of after the metallization of the second layer.

three steps.

First, we have to position the 1 mm^2 localgate array from the first layer (blue Fig. A.2a and A.4a) within the 1 mm^2 writefield of the electron beam. This can be achieved by moving the SEM microstage with the sample to the corresponding set of coordinates. This first alignement however has an inaccuracy on the order of 10 μm. In order to improve

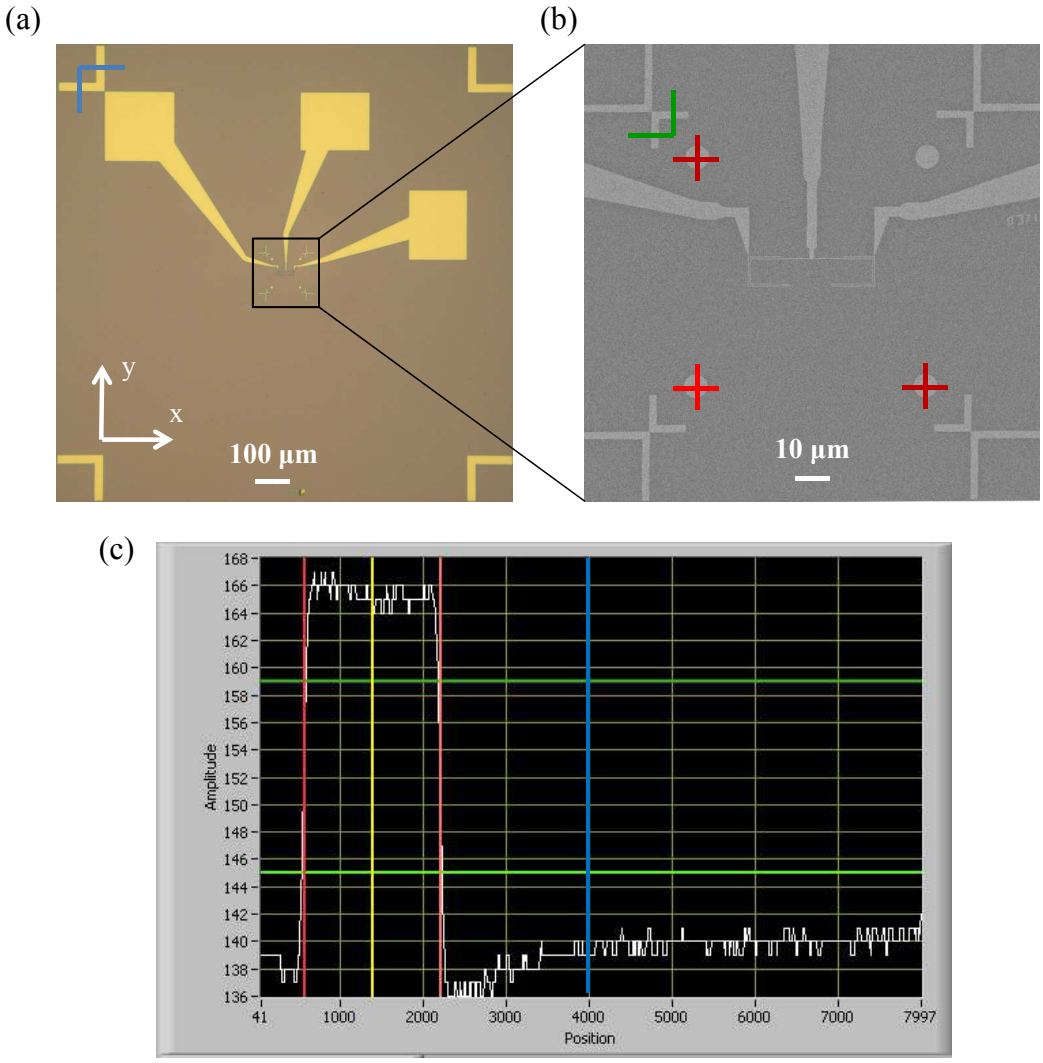

Figure A.4: Alignement procedure. (a) Photograph of the 1 mm^2 field of the metallized first layer, with the first set of linescans (blue). (b) SEM image of the 100 μm^2 central field of the metallized first layer, with the second and third set of linescans (green and red). (c) Backscattered electron intensity profile of a linescan along one of the blue lines in (a). The metallic mark yields a much higher intensity than the substrate. The center of the mark profile (yellow line) is strongly misaligned with respect to the center of the scan window (blue line). The algorithm calculates the difference and corrects the position the electron beam writefield accordingly.

the accuracy, we will use a numerical algorithm implemented by Edgar Bonet into the ELPHY command module, which calculates and corrects the misalignement between the electron beam writefield and the first layer by scanning different sets of alignement marks

in the first layer.

We now perform two electron beam linescans (along the x and y direction respectively) on a mark in the upper left corner of 1 mm^2 field of the first layer (blue linescans in Fig. A.4a), while recording the intensity of the backscattered electron from the sample with the ELPHY command module. The different yields of backscattered electrons of the metallic mark and the substrate results in an intensity profile of the linescan as depicted in Fig. A.4c. The algorithm then calculates the difference between the center of the mark (yellow line in Fig. A.4c) and the center of the scan window (blue line in Fig. A.4c) for the linescans in both x and y direction. The algorithm then adjusts the (x-y) position of the electron beam 1 mm^2 writefield to the position of the 1 mm^2 field of the first layer using the calculated corrections. The alignement error is reduced to 600 nm.

Step	description	equipement	parameters, comments
0	cleaning	O_2 plasma, RIE	10 min at 50W, 20 cc O_2
1	PMMA 4 % resist	spin coater	2000 rpm, 2000rpm/s for 30s thickness 380 nm
2	PMMA 4 % softbake	hotplate	2 min at 180°C
3	e-beam exposure	SEM LEO 1530 ELPHY 6.0	$E = 30$ kV settling time 2.5 ms
	100 μm^2 writefield 1 mm^2 writefield	20 μm aperture 120 μm aperture	325 μC/cm^2 400 μC/cm^2
4	development	MIBK/IPA 1:3	30s
5	developper neutralization	IPA	60s
6	removing residual resist	O_2 plasma, RIE	3s at 50W, 20 cc O_2
7	metal depostion	ebeam evaporator PLASSYS	20 nm Mo or W 160 nm Pt
8	metal lift off	acetone	5 min at 45°C until excess metal is removed

Table A.2: Fabrication process for carbon nanotube NEMS backbone junction with multiple backgate *via* e-beam lithography: second source-drain layer

In the last step, we have to align the 100 μm^2 electron beam writefield with respect to the 100 μm^2 central field of the first layer. Using the described algorithm, we now perform an alignement using the cross in the upper left corner of the 100 μm^2 central field of the first layer (green linescan Fig. A.4b) followed by an alignement using 3 of the 4 circles (red linescans Fig. A.4b). It should be noted that the 3 circle alignement is essential for a reproducibly accurate alignement. For instance, using only a 2 circle alignement often results in a distortion and misalignment of the writefield (Fig. A.5). This final step reduces the misalignment in both directions to 30 nm. Once the alignment

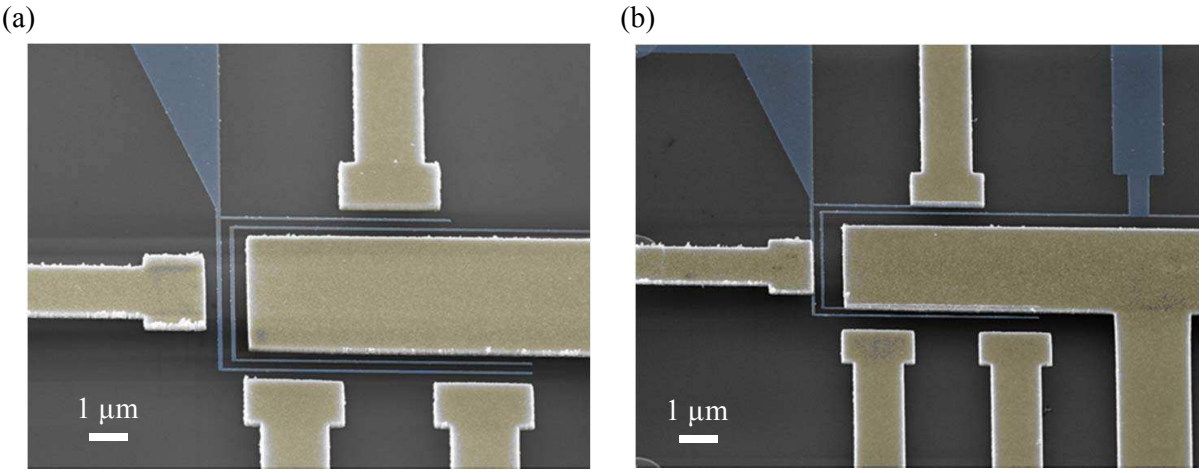

Figure A.5: Three circle (a) vs two circle alignment (b).

is completed, the second layer is patterned into the PMMA layer.

The SEM microstage is then moved to the position of the next array in 1"x1" matrix of localgates patterned during the first step, followed by the alignement and the exposure of the second layer pattern, etc.... In this way, one can align and pattern the second layer on all the localgate arrays of the 1"x1" matrix, with a reproducible alignement precision of 30 nm. The fabrication process of the second layer is summarized in Table A.2.

Third lithography step: Catalyst islands and CVD growth

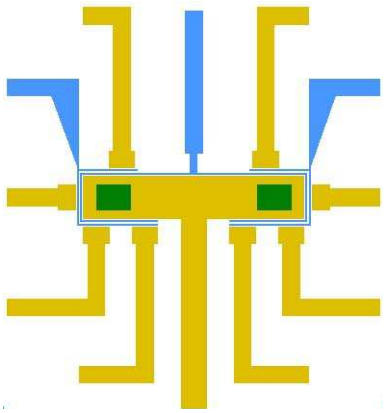

Figure A.6: Multiple gate carbon nanotube NEMS, third layer catalyst islands (green colors). 50 μm writefield, showing two 3x4 μm catalyst islands on the central drain electrode.

Step	description	equipement	parameters, comments
0	cleaning	O_2 plasma, RIE	10 min at 50W, 20 cc O_2
1	PMMA 4% resist	spin coater	2000 rpm, 2000rpm/s for 30s thickness 360 nm
2	PMMA 4% softbake	hotplate	2 min at 180°C
3	e-beam exposure	SEM LEO 1530 ELPHY 6.0	$E = 20$ kV settling time 2.5 ms
	100 μm^2 writefield	10 μm aperture	215 $\mu C/cm^2$
4	development	MIBK/IPA 1:3	30s
5	developper neutralization	IPA	60s
6	removing residual resist	O_2 plasma, RIE	3s at 50W, 20 cc O_2
7	catalyst deposition	spin coater	3000 rpm, 1000 rpm/s for 20s repeated 2 times (*low density*) repeated 4 times (*high density*)
8	post deposition bake	hotplate	60s at 120°C
9	Catalyst liftoff	acetone	45°C for an hour
10	Pre-CVD cleaning	O_2 plasma, RIE	20 min at 50W, 20 cc O_2
11	CVD growth	EasyTube 2000 CVD system	770°C-800°C, 1.2 L/min CH_4, 0.8 L/min H_2 12 min

Table A.3: Catalyst deposition and ultraclean CVD growth of carbon nanotube NEMS with multiple gates.

Using the same alignement and patterning sequence, one can define catalyst islands on the central drain electrode of each array (Fig. A.6) and grow carbon nanotube NEMS by CVD. The process is summarized in Table A.3.

A.2 Ultrashort and high frequency carbon nanotube NEMS

In order to achieve high resonance frequencies one has to significantly reduce the length of the carbon nanotube NEMS. Using electron beam lithography, we designed a carbon nanotube NEMS with suspended portion of about 50 to 100 nm (Fig. A.7).

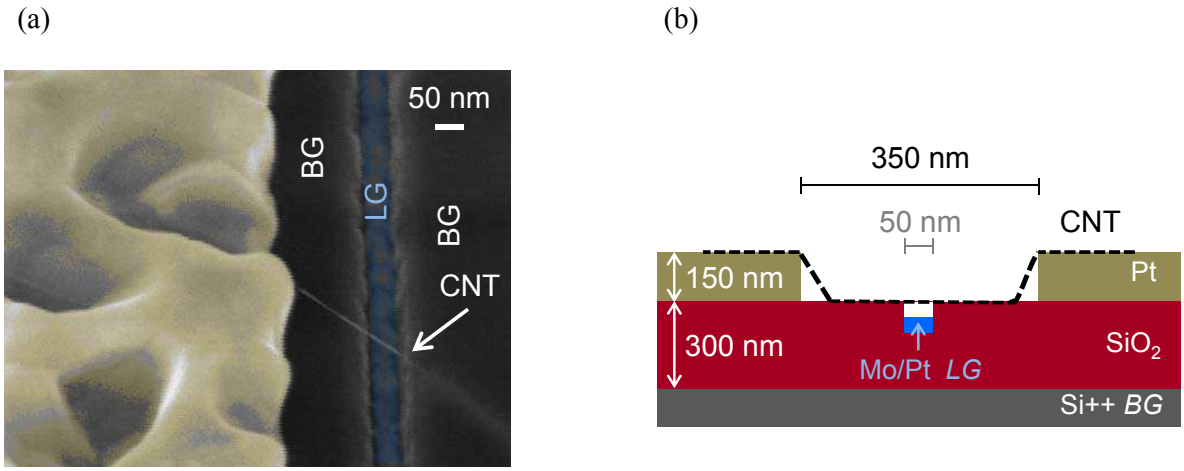

Figure A.7: Multiple gate carbon nanotube NEMS, third layer catalyst islands (green colors). 50 μm writefield, showing two 3x4 μm catalyst islands on the central drain electrode.

Following a similar lithography process than in Table. A.1, we first pattern a single 50 nm wide localgate into the PMMA resist. After development, we etch 70 nm of SiO_2 in a low power CHF_3 plasma (17 min at **20W and 18°C** in 15 cc CHF_3) using the patterned PMMA layer as a etching mask prior to the metal depostion. It should be noted, that the plasma chamber has to cleaned extensively for 10 min in an oxygen plasma before the main etching step in order to garanty a reproducible etching rate. Table A.4 summarizes the modified process.

After the lift-off, we then align the source-drain electrodes with a gap of 350 nm in a second lithography step, using the same recipes and procedures described in Appendix A.1. Finally we pattern catalyst islands into the resist prior to the CVD growth.

The carbon nanotube will subsequently grow along the SiO_2 and over the embedded localgate, to form a suspended portion of up to 100 nm.

Step	description	equipement	parameters, comments
0	cleaning	O_2 plasma, RIE	10 min at 50W, 20 cc O_2
1	PMMA 2 % resist	spin coater	2000 rpm, 2000rpm/s for 60s thickness 110 nm
2	PMMA 2 % softbake	hotplate	5 min at 180°C
3	e-beam exposure	SEM LEO 1530 ELPHY 6.0	$E = 20$ kV settling time 2.5 ms
	100 μm^2 writefield 1 mm^2 writefield	7.5 μm aperture 120 μm aperture	275 $\mu C/cm^2$ 350 $\mu C/cm^2$
4	development	MIBK/IPA 1:3	30s
5	developper neutralization	IPA	60s
6	removing residual resist	O_2 plasma, RIE	3s at 50W, 20 cc O_2
7	SiO_2 etching	CHF_3 plasma, RIE PMMA etch mask	17 min at **20W & 18°C** 15 cc CHF_3 etch rate SiO_2: 4 nm/min etch rate PMMA: 2 nm/min
8	metal depostion	ebeam evaporator PLASSYS	5 nm Mo or W 15 nm Pt
9	metal lift off	acetone	5 min at 45°C until excess metal is removed

Table A.4: Fabrication process for carbon nanotube NEMS backbone junction with embedded local backgate *via* e-beam lithography: first localgate layer

Appendix B

Stevens operators

k	q	O_k^q
2	0	$3J_z^2 - j\mathbb{I}$
	± 1	$c_\pm \{J_z, J_+ + J_-\}$
	± 2	$c_\pm \left(J_+^2 \pm J_-^2\right)$
4	0	$35J_z^4 - (30j - 25) J_z^2 + (3j^2 - 6j)\mathbb{I}$
	± 1	$c_\pm \left\{7J_z^2 - (3j + 1) J_z, J_+ \pm J_-\right\}_S$
	± 2	$c_\pm \left\{7J_z^2 - (j + 5)\mathbb{I}, J_+^2 \pm J_-^2\right\}_S$
	± 3	$c_\pm \left\{J_z, J_+^3 \pm J_-^3\right\}_S$
	± 4	$c_\pm \left(J_+^4 \pm J_-^4\right)$
6	0	$231J_z^6 - (315j - 735) J_z^4 - (105j^2 - 525j + 294) J_z^2 + (5j^3 - 40j^2 + 60j)\mathbb{I}$
	± 1	$c_\pm \left\{33J_z^5 - (30j - 155) J_z^3 - (5j^2 - 10j + 12) J_z, J_+ \pm J_-\right\}_S$
	± 2	$c_\pm \left\{33J_z^4 - (18j + 123) J_z^2 - (j^2 + 10j + 102)\mathbb{I}, J_+^2 \pm J_-^2\right\}_S$
	± 3	$c_\pm \left\{11J_z^3 - (3j + 59) J_z, J_+^3 \pm J_-^3\right\}_S$
	± 4	$c_\pm \left\{11J_z^2 - (j + 38)\mathbb{I}, J_+^4 \pm J_-^4\right\}_S$
	± 5	$c_\pm \left\{J_z, J_+^5 \pm J_-^5\right\}_S$
	± 6	$c_\pm \left(J_+^6 \pm J_-^6\right)$

Table B.1: Stevens Operators as tabulated in Abragam and Bleany [50] with $\{A, B\}_S = \frac{1}{2}(AB + BA)$, $j = J(J + 1)$, $\mathbb{I}$ the identity operator, $c_+ = \frac{1}{2}$ and $c_- = \frac{i}{2}$.

Appendix C

Publications

Dynamics and Dissipation Induced by Single-Electron Tunneling in Carbon Nanotube Nanoelectromechanical Systems

Marc Ganzhorn and Wolfgang Wernsdorfer

Institut Néel, CNRS & Université Joseph Fourier, BP 166, 25 Avenue des Martyrs, 38042 Grenoble Cedex 9, France

(Received 13 November 2011; revised manuscript received 28 January 2012; published 24 April 2012)

We demonstrate the effect of single-electron tunneling (SET) through a carbon nanotube quantum dot on its nanomechanical motion. We find that the frequency response and the dissipation of the nanoelectromechanical system to SET strongly depends on the electronic environment of the quantum dot, in particular, on the total dot capacitance and the tunnel coupling to the metal contacts. Our findings suggest that one could achieve quality factors of 10^6 or higher by choosing appropriate gate dielectrics and/or by improving the tunnel coupling to the leads.

DOI: 10.1103/PhysRevLett.108.175502 PACS numbers: 81.07.Oj, 81.07.De, 85.85.+j

Carbon nanotubes (CNT) have become an essential building block for nanoelectromechanical systems (NEMS). Their low mass and high Young's modulus allow for instance ultrasensitive mass [1–3] or force detection [4,5] (electric and magnetic) over a wide range of frequencies and its small diameter enables even single-molecule detection [5–7]. Moreover, CNT devices exhibit remarkable electronic transport properties, ranging from Kondo physics [8] to Coulomb blockade at high temperature [9]. It was recently demonstrated that a CNT NEMS' nanomechanical motion at very low temperature (i.e., in Coulomb blockade regime) is strongly affected by the electronic transport through the CNT quantum dot (QD), and vice versa: For instance, single-electron tunneling (SET) caused a frequency softening and increased dissipation when tuning the CNT dot's potential through a Coulomb peak [10–12].

Here we demonstrate that the response and dissipation of a CNT NEMS at very low temperature induced by zero bias SET through the CNT NEMS QD critically depends on the dot capacitance, the tunnel coupling to the metal leads, and temperature. We studied the frequency and dissipation response of nanomechanical bending modes to zero bias SET in suspended CNT devices with tunable tunnel couplings and different gate dielectrics, i.e., different dot capacitance. We observe that SET causes a frequency softening for small dot capacitance and/or tunnel coupling, whereas a frequency hardening or no frequency modulation is observed for large dot capacitance and/or tunnel coupling. We show that the dissipation of the CNT NEMS is mainly dominated by the capacitance, when electron tunneling through the dot is suppressed (i.e.. in the Coulomb valley), whereas it is limited by the mean tunneling rate Γ and the conductance, when electron tunneling through the dot is allowed (i.e., on a Coulomb peak). Finally we demonstrate that the tunnel current is the dominant dissipation mechanism in CNT NEMS at low temperature. Our findings are in fair agreement with a theoretical model provided previously [10,12].

Low capacitance CNT quantum dots ($C_{\mathrm{dot}} \approx 20$–$40$ aF) were obtained by using silicon dioxide as gate dielectric [Fig. 1(a)]. First, source-drain electrodes are patterned by optical deep ultraviolet (DUV) lithography and *e*-beam evaporation of Mo (20 nm) and Pt (160 nm) on 500 nm of thermal SiO_2. To ensure the suspension of the CNT, 150 nm of SiO_2 are dry etched in CHF_3 plasma. High capacitance CNT quantum dots ($C_{\mathrm{dot}} \approx 160$–$260$ aF) are obtained with high-κ gate dielectrics Al_2O_3 [Fig. 1(b)]. First, a 1 μm-wide metallic local gate is patterned by optical DUV lithography and *e*-beam evaporation of Mo (20 nm) on 300 nm of thermal SiO_2. A layer of 100 nm of Al_2O_3 is then deposited by atomic layer deposition. Using optical DUV lithography and *e*-beam evaporation of Mo (20 nm) and Pt (160 nm), source-drain electrodes are aligned above the local gate. Suspended CNT are finally grown by chemical vapor deposition at 800 °C from a CH_4 feedstock and Fe/Mo catalyst spots patterned on the

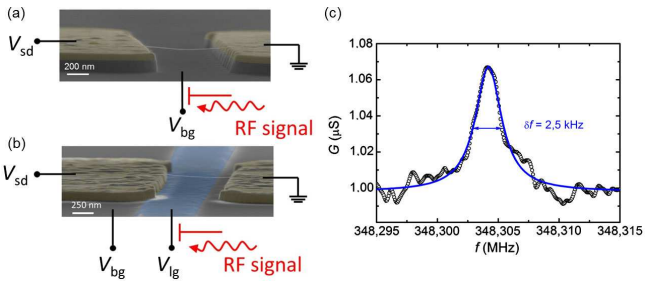

FIG. 1 (color online). False color SEM image of (a) a low capacitance device based on a SiO_2 covered Si backgate (grey) and (b) a high capacitance device based on an Al_2O_3 covered local metallic gate (blue). The rf actuation signal is injected into the local metallic gate and Si backgate, respectively, through a home-built bias-*T*. As the induced mechanical motion changes the charge flow through the CNT quantum dot and vice versa, we can detect the CNT resonance through a change in zero bias conductance. (c) Mechanical resonance of a typical CNT NEMS at low driving power $P_{\mathrm{rf}} = -100$ dBm. The resonance width $\delta f = 2.5$ kHz leads to a quality factor of $Q \approx 140\,000$.

source-drain electrodes next to the junction. The CNT device length is approximately 800 nm (± 50 nm) and the dot capacitances are deduced from the dot's charging energy at low temperature. The spread in capacitance values of nominally identically fabricated devices is due to variations in the nanotubes' length and slack (see [13]).

The measurements are carried out in a ^{3}He/^{4}He dilution refrigerator with a base temperature of 30 mK. The NEMS actuation and detection scheme used in our experiment is similar to the one used by Steele and co-workers [11,12]. The rf actuation signal is injected into the gate electrode via a home-built bias T. As the induced mechanical motion changes the charge flow through the CNT quantum dot and vice versa, we can detect the CNT resonance through a change in zero bias conductance. The actuation power is kept to a minimum ($P_{\mathrm{rf}} \approx -100$ dBm) in order to ensure a quasilinear regime of the oscillator and a high Q Lorentzian resonance shape [Fig. 1(c)]. All measurements were done under zero bias with a standard lock-in technique.

SET in a CNT NEMS QD can be considered an external perturbation to the CNT mechanical motion, and vice versa. This perturbation can be described as an electrodynamic force acting on the CNT. The contribution of this force, which is in phase with the mechanical motion, is responsible for a frequency modulation Δf, whereas a contribution of the force being out of phase with mechanical motion induces a modification of the dissipation and the quality factor Q. Δf and Q can be expressed as follows [10]:

$$\Delta f = -\frac{f_0}{2}\frac{C_g'^2}{k}\frac{V_g^2}{C_{\mathrm{dot}}}\left(\frac{2G}{C_{\mathrm{dot}}\Gamma} - 1\right), \tag{1}$$

$$\frac{1}{Q} = 2\pi f \frac{C_g'^2}{k} V_g^2 \left(\frac{2}{\Gamma C_{\mathrm{dot}}}\right)^2 G, \tag{2}$$

where Γ is the mean tunnel coupling of the dot to the leads, yielding $\Gamma = (\Gamma_d + \Gamma_s)/2$, and C_{dot} is the total dot capacitance. We can estimate the tunnel coupling Γ for each device from the line shape of the Coulomb blockade peaks (see [13]). Equations (1) and (2) are valid in the regime of the Coulomb blockade and if $\Gamma \gg f_0$.

First, we compare the frequency response Δf (scaled with fV_g^2) of devices with different dot capacitances C_{dot}. We studied the frequency response for comparable Coulomb peaks height, i.e., for comparable conductance $G(V_g) \approx 20\ \mu$S. The tunnel coupling are on the order of 10 GHz. As depicted in Fig. 2(a), we observe a strong frequency softening for small dot capacitances, whereas for high dot capacitances a frequency hardening or no modulation is observed. As shown in Fig. 2(b), the

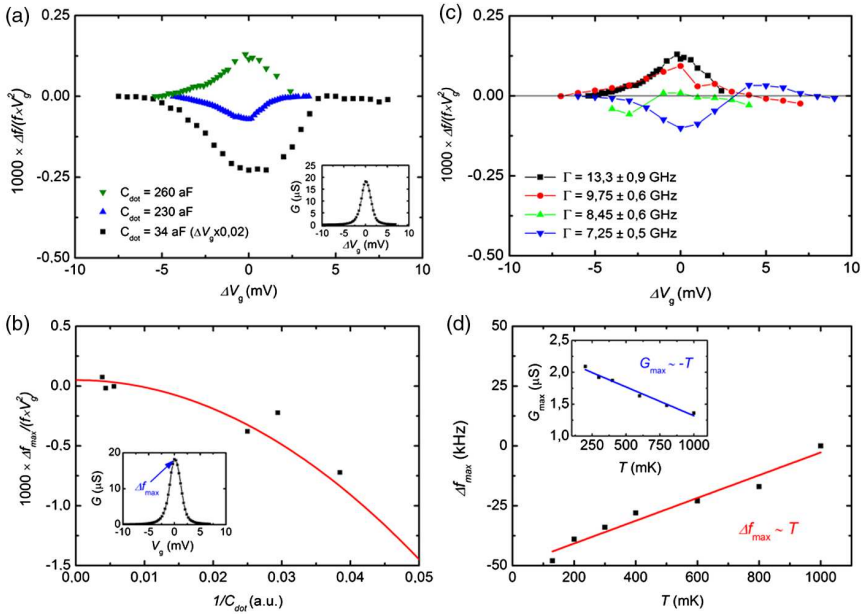

FIG. 2 (color online). Modulation of the resonance frequency due to SET: (a) Frequency shift Δf (scaled with fV_g^2) for different dot capacitance C_{dot}, with comparable tunneling rates Γ. Inset shows a typical Coulomb peak centered at $\Delta V_g = 0$. (b) Maximum scaled frequency shift at maximum tunnel current $G_{\mathrm{max}}(\Delta V_g = 0)$ vs the dot capacitance for all measured devices. The solid red line corresponds to the fit using Eq. (1) with $C_g'^2/k = 8 \times 10^{-22}$ F^2/N m and $\Gamma_d \approx 10$ GHz. The data are in fair agreement with the model. (c) Scaled frequency shift for different Coulomb peaks, i.e., tunneling rates Γ, with a fixed dot capacitance $C_{\mathrm{dot}} = 260$ aF (device 1). The tunneling rate Γ is estimated from the line shape of the respective Coulomb peaks (see [13]). (d) Maximum frequency shift Δf_{max} at maximum tunnel current $G_{\mathrm{max}}(\Delta V_g = 0)$ vs temperature for a device yielding $C_{\mathrm{dot}} = 160$ aF (device 2). The inset shows the evolution of G_{max} as a function of temperature.

experimental data are in fair agreement with the model. A fit with Eq. (1) yields fitting parameters $C_g'^2/k = 8 \times 10^{-22}$ F^2/N m and $\Gamma \approx 10$ GHz, which are in rather good agreement with previous experiments [10,12,14]. Figure 2(c) shows the (scaled) frequency modulation for different Coulomb peaks and tunneling rates Γ on a given device (device 1). It was shown previously that one can tune a CNT quantum dot from a Coulomb blockade regime to a regime of strong tunnel coupling by simply changing the CNT's gate potential [15,16]. Hence, we can change the tunnel coupling Γ by tuning the gate voltage of our CNT device and estimate the values of Γ from the Coulomb peak line shape (see [13]). The dot capacitance $C_{\mathrm{dot}} = 260$ aF remains unchanged by tuning the gate voltage. As Γ increases, the CNT becomes stiffer, resulting in a sign change of Δf and the transition from a frequency softening to frequency hardening, in qualitative agreement with Eq. (1) [Fig. 2(c)].

Figure 3(a) depicts the effect of SET on the dissipation of the CNT NEMS, i.e., the Q factor (scaled with fV_g^2), for devices with different dot capacitances. From Eq. (2), we expect an increase of the Q factor with increasing capacitance in the limit of suppressed SET through the dot. Indeed, in a region of suppressed SET ($|\Delta V_g| \gg 0$), the Q factor is larger for devices with higher dot capacitance [Fig. 3(a)]. The tunnel coupling $\Gamma \approx 10$ GHz and the conductance $G(V_g) \approx 18$ μS are comparable for both traces. Figure 3(b) shows the Q factor (scaled with fV_g^2) in the limit of suppressed SET ($|\Delta V_g| \gg 0$) as a function of the dot capacitance for all measured devices. The fit with Eq. (2) yields $C_g'^2/k = 1 \times 10^{-21}$ F^2/N m and $\Gamma \approx 10$ GHz, which is consistent with the fitting parameters of Fig. 2(b) and previous experiments [10,12,14]. Despite the good agreement between theory and experiment, we observe deviations from the model for some devices in Fig. 2(b) and 3(b) that we attribute to variations in $C_g'^2/k$ (see [13]). Moreover, we expect from Eq. (2) and previous experiments [10,12] an enhanced electromechanical dissipation in a given device if the conductance G (i.e., the tunnel current) and the tunnel resistance at the nanotube-electrode interface $R \sim 1/\Gamma_d$ are increased, in analogy to the current dissipation in a simple resistance. Indeed we observe increased dissipation (decreased Q factor) when tuning the gate voltage through a Coulomb peak [Figs. 3(a) and 3(c)]. In Fig. 3(c) (device 2), this effect becomes more pronounced as we move to gate voltage regions with a smaller tunneling rate Γ, i.e., larger tunnel resistance at the nanotube-electrode interface. The dot capacitance C_{dot} yields 160 aF for this device and the height of the Coulomb peak is comparable for all traces ($G \approx 7$ μS).

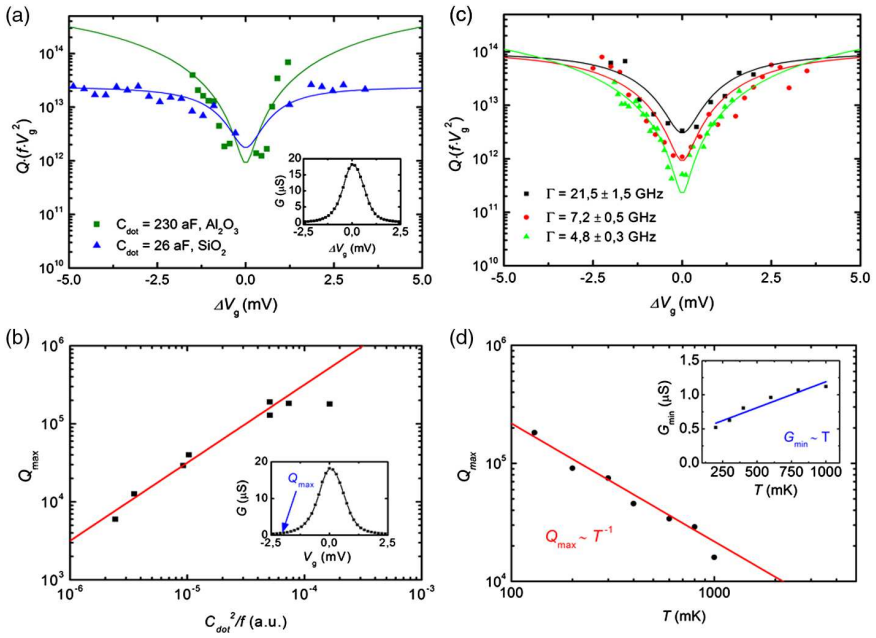

FIG. 3 (color online). Modulation of the Q factor (scaled with fV_g^2) due to SET: (a) For different dot capacitances, with comparable tunneling rates Γ. The solid lines are to guide the eye and the inset shows a representative Coulomb peak centered at $\Delta V_g = 0$. (b) Maximum quality factor Q_{max} at minimal tunnel current $G(|\Delta V_g| \gg 0)$ vs the dot's capacitance for all measured devices. The solid red line represents the fit with Eq. (2) with $C_g'^2/k = 1 \times 10^{-21}$ F^2/N m and $\Gamma \approx 10$ GHz. Our findings are in good agreement with the model. (c) Modulation of the Q factor (scaled with fV_g^2) for different tunneling rates Γ, with a fixed dot capacitance $C_{\mathrm{dot}} = 160$ aF (device 2). The solid lines are to guide the eye and the tunnel coupling Γ is estimated from the line shape of the respective Coulomb peaks (see [13]). (d) Maximum quality factor Q_{max} at minimal tunnel current $G(|\Delta V_g| \gg 0)$ vs temperature for a device yielding $C_{\mathrm{dot}} = 160$ aF (device 2). The inset shows the evolution of G_{min} as a function of temperature.

Therefore, the CNT capacitance is the limiting factor for the dissipation in regions of suppressed SET, whereas the mean tunnel coupling and the tunneling current itself define the dissipation in regions of strong SET. We conclude that the electron transport through the CNT is the main dissipation mechanism in our nanoelectromechanical system.

Finally, we study the temperature dependence of the frequency response and the dissipation. Figure 2(d) depicts the frequency shift $\Delta f_{\max}$ for $G_{\max} = G(\Delta V_g = 0)$ whereas Fig. 3(d) shows the quality factor $Q_{\max}$ for $G_{\min} = G(|\Delta V_g| \gg 0)$ as a function of temperature. A fit of the data yields $\Delta f_{\max} \sim T$ and $Q_{\max} \sim 1/T$. As temperature increases the Coulomb blockade peak broadens and becomes smaller (see[13], Fig. S3). As a result $G_{\max} = G(\Delta V_g = 0)$ decreases whereas $G_{\min} = G(|\Delta V_g| \gg 0)$ increases with temperature, as depicted in the insets of Figs. 2(d) and 3(d). From the data fit we obtain $G_{\max} \sim -T$ and $G_{\min} \sim T$. It was previously demonstrated that carbon nanotubes show Luttinger liquid behavior [17–19], where the conductance follows a characteristic power law dependence as a function of temperature $G(T) \sim T^{\alpha}$, α being related to the Luttinger parameter g by $\alpha = (g - 1 + g - 2)/2$ [17,18]. We find $\alpha \approx 1$ and a Luttinger parameter of $g = 0{,}1$, which is close to previous measurements [17] and theoretical predictions [18,19]. Comparing the temperature dependence of the conductance, the quality factor, and the frequency shift, we finally obtain $\Delta f_{\max} \sim -G_{\max}$ and $Q_{\max} \sim 1/G_{\min}$, which is in full agreement with Eqs. (1) and (2). We can conclude that the current is the dominant dissipation mechanism for carbon nanotube-based NEMS in a Coulomb blockade regime at cryogenic temperatures.

We have demonstrated that the response and the dissipation to single-electron tunneling of carbon nanotube NEMS at low temperature depends on the dot capacitance and the tunnel coupling to the leads, the tunnel current itself being the main dissipation mechanism in the system. By choosing high-κ dielectrics (HfO_2 or ZrO_2) and improving the tunnel contact to the metal leads, one could significantly enhance the quality factor Q to values exceeding 10^6. It was proposed in theoretical calculation that one can use such high -Q CNT NEMS as magnetic torque or force detectors for nanoparticles [5] or single-molecule magnets [20,21] grafted to the CNT NEMS. In principle, one can achieve a sensitivity of one μ_B at low temperature, whereas the best magnetometers, for instance the micro-SQUID, only have a sensitivity of 10^3 μ_B [22]. Finally, such molecular quantum spintronic device would allow single spin manipulation on a molecular level.

This work is partially supported by the ANR-PNANO project MolNanoSpin No. ANR-08-NANO-002 and ERC Advanced Grant MolNanoSpin No. 226558. M. G. acknowledges financial support from the RTRA Nanosciences Foundation. Samples were fabricated in the NANOFAB facility of the Neel Institute. We thank F. Balestro, E. Bonet, T. Crozes, J. P. Cleuziou, E. Eyraud, T. Fournier, R. Haettel, C. Hoarau, D. Lepoittevin, V. Nguyen, V. Reita, A. Reserbat-Plantey, C. Thirion, and M. Urdampilleta.

[1] B. Lassagne, D. Garcia-Sanchez, A. Aguasca, and A. Bachtold, Nano Lett. **8**, 3735 (2008).
[2] H.-Y. Chiu, P. Hung, H. W. C. Postma, and M. Bockrath, Nano Lett. **8**, 4342 (2008).
[3] K. Jensen, K. Kim, and A. Zettl, Nature Nanotech. **3**, 533 (2008).
[4] A. Eichler, J. Moser, J. Chaste, M. Zdrojek, I. Wilson-Rae, and A. Bachtold, Nature Nanotech. **6**, 339 (2011).
[5] B. Lassagne, D. Ugnati, and M. Respaud, Phys. Rev. Lett. **107**, 130801 (2011).
[6] L. Bogani and W. Wernsdorfer, Nature Mater. **7**, 179 (2008).
[7] M. Urdampilleta, S. Klyatskaya, J.-P. Cleuziou, M. Ruben, and W. Wernsdorfer, Nature Mater. **10**, 502 (2011).
[8] J. Nygård, D. H. Cobden, and P. E. Lindelof, Nature (London) **408**, 342 (2000).
[9] J.-C. Charlier, X. Blase, and S. Roche, Rev. Mod. Phys. **79**, 677 (2007).
[10] B. Lassagne, Y. Tarakanov, J. Kinaret, D. Garcia-Sanchez, and A. Bachtold, Science **325**, 1107 (2009).
[11] A. K. Hüttel G. A. Steele, B. Witkamp, M. Poot, L. P. Kouwenhoven, and H. S. J. van der Zant, Nano Lett. **9**, 2547 (2009).
[12] G. A. Steele A. K. Hüttel, B. Witkamp, M. Poot, H. B. Meerwaldt, L. P. Kouwenhoven, and H. S. J. van der Zant, Science **325**, 1103 (2009).
[13] See Supplemental Material at http://link.aps.org/supplemental/10.1103/PhysRevLett.108.175502 for the estimation method of the dot capacitance and tunnel coupling, a discussion about the model accuracy and the temperature evolution of the zero bias conductance.
[14] V. Sazonova, Y. Yaish, H. Üstünel, D. Roundy, T. A. Arias, and P. L. McEuen, Nature (London) **431**, 284 (2004).
[15] T. Jespersen K. Grove-Rasmussen, J. Paaske, K. Muraki, T. Fujisawa, J. Nygård, and K. Flensberg, Nature Phys. **7**, 348 (2011).
[16] G. A. Steele, G. Gotz, and L. P. Kouwenhoven, Nature Nanotech. **4**, 363 (2009).
[17] M. Bockrath, D. H. Cobden, J. Lu, A. G. Rinzler, R E. Smalley, L. Balents, and P. L. McEuen, Nature (London) **397**, 598 (1999).
[18] C. Kane, L. Balents, and M. P. A. Fisher, Phys. Rev. Lett. **79**, 5086 (1997).
[19] R. Egger and A. O. Gogolin, Phys. Rev. Lett. **79**, 5082 (1997).
[20] A. A. Kovalev, L. X. Hayden, G. E. W. Bauer, and Y. Tserkovnyak, Phys. Rev. Lett. **106**, 147203 (2011).
[21] D. Garanin and E. Chudnovsky, Phys. Rev. X **1**, 011005 (2011).
[22] W. Wernsdorfer, Supercond. Sci. Technol. **22**, 064013 (2009).

nature nanotechnology

LETTERS

PUBLISHED ONLINE: 3 FEBRUARY 2013 | DOI: 10.1038/NNANO.2012.258

Strong spin–phonon coupling between a single-molecule magnet and a carbon nanotube nanoelectromechanical system

Marc Ganzhorn[1], Svetlana Klyatskaya[2], Mario Ruben[2,3] and Wolfgang Wernsdorfer[1]*

Magnetic relaxation processes were first discussed for a crystal of paramagnetic transition ions[1]. It was suggested that mechanical vibrations of the crystal lattice (phonons) modulate the crystal electric field of the magnetic ion, thus inducing a 'direct' relaxation between two different spin states[1–3]. Direct relaxation has also been predicted for single-molecule magnets with a large spin and a high magnetic anisotropy[1,4–7] and was first demonstrated in a Mn_{12} acetate crystal[8]. The spin-lattice relaxation time for such a direct transition is limited by the phonon density of states at the spin resonance[1]. In a three-dimensional system, such as a single-molecule magnet crystal, the phonon energy spectrum is continuous, but in a one-dimensional system, like a suspended carbon nanotube, the spectrum is discrete and can be engineered to an extremely low density of states[9]. An individual single-molecule magnet, coupled to a suspended carbon nanotube, should therefore exhibit extremely long relaxation times[9] and the system's reduced size should result in a strong spin–phonon coupling[10,11]. Here, we provide the first experimental evidence for a strong spin–phonon coupling between a single molecule spin and a carbon nanotube resonator, ultimately enabling coherent spin manipulation and quantum entanglement[10,11].

Carbon nanotubes (CNT) have become an essential building block for nanoelectromechanical systems (NEMS). Their low mass and high Young's modulus give rise to high oscillation frequencies for transverse[12,13] and longitudinal modes[14–16], therefore enabling ground-state cooling with state-of-the-art cryogenics and a large zero point motion in the quantum regime[17]. Moreover, the strong coupling between nanomechanical motion and single-electron tunnelling in high-Q CNT NEMS allows electronic actuation and detection of the nanomechanical motion[18–21]. As such, CNT NEMS can be used for ultrasensitive mass sensing[22–24] or as magnetic torque detectors for single spin systems[25].

A single spin, strongly coupled with a CNT NEMS in the quantum regime, could serve as an elementary qubit in quantum information processing. It has been suggested recently that a strong coupling between a quantum CNT NEMS and a single electron spin would enable basic qubit control and the implementation of entangled states[9]. In this framework, coupling a single-molecule magnet (SMM) to the quantized nanomechanical motion of a CNT NEMS is a very attractive option[26]. Chemical engineering allows the synthesis of perfectly identical SMMs, as well as their integration into nanoscale devices such as electromigrated junctions[27–29] or CNT transistors[30]. A large magnetic moment and a strong, uniaxial magnetic anisotropy enable, for instance, quantum tunnelling of magnetization[31,32] or quantum phase interference[33], yielding coherence times on the order of microseconds in crystalline form[34]. Moreover, it was recently predicted that the spin–phonon coupling between an SMM and a quantum CNT NEMS is strong enough to allow coherent spin manipulation and quantum entanglement of a spin and a resonator[10,11]. In this Letter, we first present the SMM and CNT NEMS. We then establish a strong spin–phonon coupling between the two systems, that is, between an individual $TbPc_2$-SMM and the quantized high-Q longitudinal stretching mode (LSM) of the CNT resonator. The strong spin–phonon coupling presented here would enable the quantum control of magnetization at a single-phonon level[9,10] and the entanglement of a single spin with quantized mechanical motion[9,11].

We study the magnetization reversal of a pyrene-substituted bis(phthalocyaninato)terbium(III) SMM (hereafter $TbPc_2$, Fig. 1a) grafted to a CNT resonator[36]. The $TbPc_2$ is a rare earth SMM in which the magnetic moment is carried by a single Tb^{3+} ion sandwiched between two organic phthalocyanine (Pc) ligand planes[35]. The $TbPc_2$ has a $S = 1/2$ radical delocalized over the Pc ligand planes. As a result of π–π interaction, this radical can easily hybridize with the π electrons of any form of sp^2 carbon without affecting the magnetic properties of the Tb^{3+} ion[30,36,37]. The highly anisotropic $4f$ shell of the Tb^{3+} ion and its intrinsically strong spin–orbit coupling result in a magnetic ground state of $J = 6$ and a pronounced uniaxial magnetic anisotropy (Fig. 1a). The ground-state doublet $J_z = \pm 6$ is separated from the excited states by several hundreds of kelvin, which makes the $TbPc_2$ an Ising-like spin system at low temperatures ($T < 5$ K) and small magnetic fields ($B < 10$ T)[35]. A strong hyperfine interaction with the nuclear spin $I = 3/2$ of the Tb^{3+} ion splits the ground-state doublet $J_z = \pm 6$ into four states each (Fig. 1b). Finally, the ligand field generates a small transverse magnetic anisotropy resulting in avoided level crossings (black circles in Fig. 1b)[35].

At cryogenic temperatures, magnetization reversal can occur through two different processes. Around zero magnetic field, the avoided level crossings allow for quantum tunnelling of magnetization $|J_z,I_z\rangle \rightarrow |-J_z,I_z\rangle$ (refs 30,35). At high magnetic fields the magnetization reverses through a direct relaxation process involving non-coherent tunnelling events combined with the emission of a phonon[30] (Fig. 1b). Previous experiments on $TbPc_2$ single crystals[35] and on $TbPc_2$ coupled to a non-suspended CNT[30] have shown that the spin relaxation was mainly enabled by bulk phonons in the environment of an individual SMM (crystal or substrate). However, an individual $TbPc_2$-SMM grafted onto a suspended CNT is physically decoupled from the bulk phonons in the substrate or the transistor leads. As a consequence, the $TbPc_2$-SMM can only couple to one-dimensional phonons, associated with the

[1]Institut Néel, CNRS et Université Joseph Fourier, BP 166, F-38042 Grenoble Cedex 9, France, [2]Institute of Nanotechnology (INT), Karlsruhe Institute of Technology (KIT), 76344 Eggenstein-Leopoldshafen, Germany, [3]Institut de Physique et Chimie des Matériaux de Strasbourg (IPCMS), CNRS-Université de Strasbourg, 67034 Strasbourg, France. *e-mail: wolfgang.wernsdorfer@grenoble.cnrs.fr

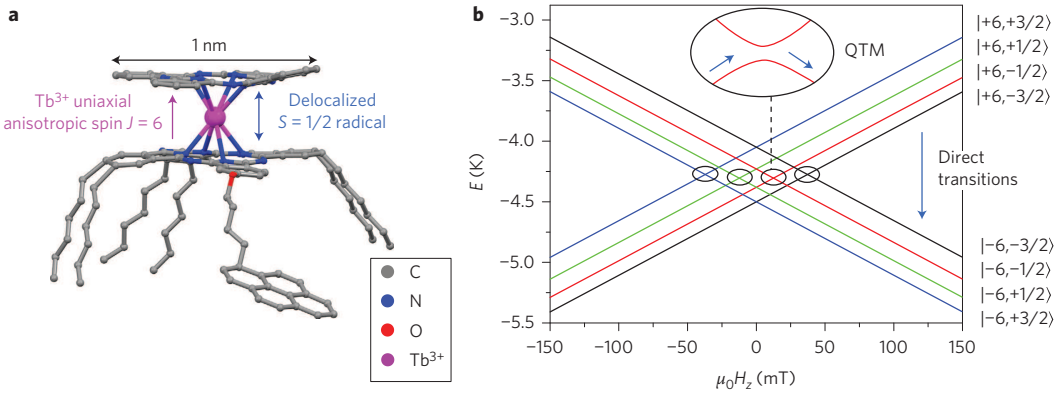

Figure 1 | Rare-earth SMM. a, Schematic representation of a pyren-substituted $TbPc_2$-SMM. A Tb^{3+} ion (pink) is sandwiched between two organic phthalocyanine (Pc) ligand planes. Owing to the highly anisotropic 4*f* shell of the Tb^{3+} ion and strong spin–orbit coupling, the $TbPc_2$ can be considered as an Ising-like spin system, with high magnetic anisotropy and a ground-state doublet $J_z = \pm 6$. The oxidation state of the Tb^{3+} ion generates a spin $S = 1/2$ radical delocalized over the phthalocyanine planes. **b**, Zeeman diagram presenting the energy E of the two ground states $J_z = \pm 6$ as a function of the magnetic field $\mu_0 H_z$. The strong hyperfine coupling with the nuclear spin $I = 3/2$ in the Tb^{3+} ion splits the ground-state doublet $J_z = \pm 6$ into four states. The corresponding Zeeman diagram reveals four avoided level crossings (black circles) around zero field, allowing for QTM $|J_z, I_z\rangle \rightarrow |-J_z, I_z\rangle$. Alternatively, magnetization reversal can occur through a direct relaxation process, involving the excitation of a phonon.

nanomechanical motion of the CNT. It was recently demonstrated that high-frequency and high-Q transverse[12] and longitudinal phonon[14–16] modes in a CNT at cryogenic temperatures should be quantized, thus yielding a discrete phonon energy spectrum.

Single-electron tunnelling (SET) onto the CNT quantum dot shifts the equilibrium position of the CNT along the axis of the CNT by an amount proportional to the electron–phonon coupling g (ref. 14). For an intermediate electron–phonon coupling $g \approx 1$, the electron therefore effectively tunnels into an excited vibrational state (Fig. 2b). If the tunnel rate Γ_{out} is larger than the relaxation rate γ into the vibrational ground state, the electron tunnels out of the dot, resulting in equidistant excited states in the region of SET, running parallel to the edge of the Coulomb diamond (black arrows, Fig. 2c)[14,15]. For large electron–phonon coupling $g \gg 1$, one also observes a current suppression at low bias, a phenomenon known as Franck–Condon blockade[16]. It was also demonstrated that one can pump excited vibrational states in a Coulomb-blockade regime by means of higher-order co-tunnelling processes[15].

For the device studied in this Letter, we observe a spectrum of equidistant excited states in the region of SET (black arrows, Fig. 2c), with an average energy separation of $\hbar\omega = 140\ \mu eV = 1.5$ K (Fig. 2d). According to $\hbar\omega = 110\ \mu eV/L\ [\mu m]$ (ref. 14) this corresponds to an oscillator length of $L = 800$ nm, which is consistent with the length of the CNT quantum dot, $L_D = 850$ nm (Fig. 2a). From the current intensity of these excited states we can estimate the electron–phonon coupling g (Fig. 2d) using the following equation[16]:

$$\Delta I \propto \frac{e^{-g} g^n}{n!} \qquad (1)$$

where n is the phonon quantum number. We obtain $g = 0.6 \pm 0.3$, which is comparable to the results of previous experiments[14]. Finally, we can estimate a lower boundary for the quality factor of this longitudinal phonon[15]. The quality factor is given by $Q = \omega/(2\pi\gamma)$, where γ is the relaxation rate into the ground state. For the vibrational states to be visible in a SET, we should have $\Gamma_{out} > \gamma$. The tunnel current at the edge of the Coulomb diamond $I \approx 50$ pA gives an approximation of the tunnelling rate $\Gamma_{out} \approx 310$ MHz. Hence, the quality factor yields $Q > \omega/(2\pi\Gamma_{out}) \approx 110$, corresponding to a phonon linewidth of the order of 15 mK. We now demonstrate that this high-Q longitudinal phonon mode can be activated by the magnetization reversal of a single $TbPc_2$, thus revealing strong spin–phonon coupling.

First, we tune our CNT quantum dot to a regime of Coulomb blockade ($V_{sd} = 0$, $V_{lg} = 16.5$ mV). In a regime of strong spin–phonon coupling, the magnetization reversal of an individual $TbPc_2$-SMM via direct transition can induce the excitation of this longitudinal stretching mode phonon on the CNT quantum dot (Fig. 3a). The linewidth of the high-Q phonon was estimated to be on the order of 15 mK and is therefore smaller than the energy level spacing $\delta E_z = 120$, 150 and 180 mK between the nuclear spin states of the Tb^{3+} ion[29,35]. Consequently, we should observe four different direct transitions matching the phonon energy $\hbar\omega = 1.5$ K, that is, four switching fields at 89, 113, 137 and 161 mT, corresponding to the different nuclear spin states of the Tb^{3+} ion (Fig. 3a). By sweeping the magnetic field component parallel to the $TbPc_2$ easy axis, we can induce magnetization reversal of the Tb^{3+} ion. As described by Urdampilleta *et al.*[30], reversal of the SMM causes an abrupt increase in the differential conductance through the CNT quantum dot, thus enabling an electronic readout and revealing the four switching fields of the Tb^{3+} ion (Fig. 3b). Note that the field sweep direction was previously aligned with the $TbPc_2$ easy axis (see Supplementary Information).

We performed magnetic field sweeps along the $TbPc_2$ easy axis at a rate of 50 mT s^{-1}, from negative to positive field values at different transverse magnetic fields $\mu_0 H_{trans}$, while monitoring the differential conductance in the CNT ($V_{sd} = 0$ and $V_{lg} = 16.5$ mV). The magnetization reversal of the Tb^{3+} ion in a sweep translates as a jump in the differential conductance of the CNT, as described above (see also Fig. 3b). The corresponding magnetic field, the switching field $\mu_0 H_{sw}$, is extracted and plotted as a function of the transverse magnetic field $\mu_0 H_{trans}$ (Fig. 4a). The measurement reveals four switching fields between 80 and 160 mT, which are independent of the transverse magnetic field component $\mu_0 H_{trans}$. By reversing the field sweep direction, the $TbPc_2$ magnetization is reversed symmetrically between −80 mT and −160 mT. To obtain a magnetization reversal statistic, we performed 200 sweeps back and forth at zero transverse magnetic field. The histogram of the extracted switching fields shows four dominant switching events at 88, 112, 137 and 160 mT with an average full-width at half-maximum (FWHM) of 2 mT (Fig. 4b). The model described in Fig. 3 predicts that in the case of a strong coupling between the $TbPc_2$ spin and the observed quantized longitudinal phonon mode in the CNT (energy $\hbar\omega = 1.5$ K and linewidth $\delta E_{ph} = 15$ mK),

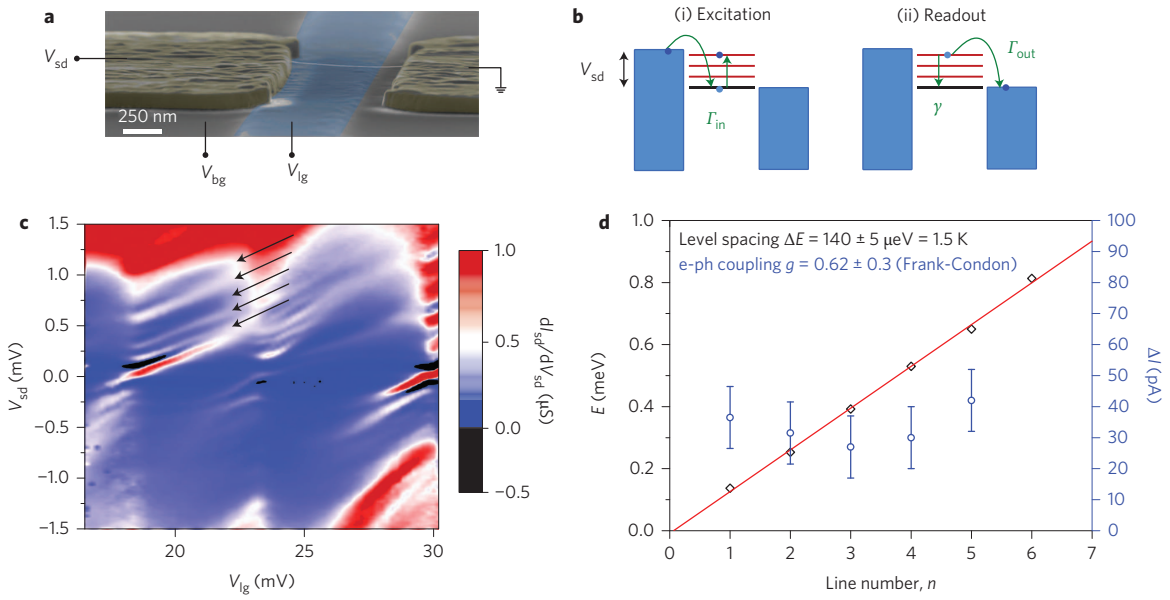

Figure 2 | Longitudinal stretching modes in CNT NEMS. a, False-colour SEM image of a CNT NEMS with local metallic (V_{lg}, blue) and Si++ (V_{bg}, grey) backgate. **b**, Actuation and detection of longitudinal stretching modes (LSM) of a CNT NEMS. (i) SET onto the suspended CNT shifts the equilibrium position of the CNT along its axis and proportional to the electron–phonon (e-ph) coupling g, leaving the electron in an excited vibrational state (red). (ii) If $\Gamma_{out} > \gamma$, the electron tunnels out of the dot, resulting in equidistant excited states running parallel to the edge of the Coulomb diamond (indicated by the black arrows in **c**. **c**, Stability diagram of the CNT showing the differential conductance as a function of gate and bias voltages at 20 mK and 1.4 T. The black arrows indicate the excited vibrational states attributed to an LSM, as described above. **d**, Energy of excited vibrational states (black diamonds) versus excitation line number n at $V_g = 18$ mV. A linear fit suggests an LSM frequency of $\hbar\omega = 140$ μeV, which is consistent with the CNT length of 850 nm (see text). From the maximum current intensity ΔI (blue circles) of the excited vibrational states we can estimate the LSM e-ph coupling factor as $g \approx 0.6 \pm 0.3$. Owing to measurement uncertainties in **c**, the relative error for ΔI is estimated to be 10%.

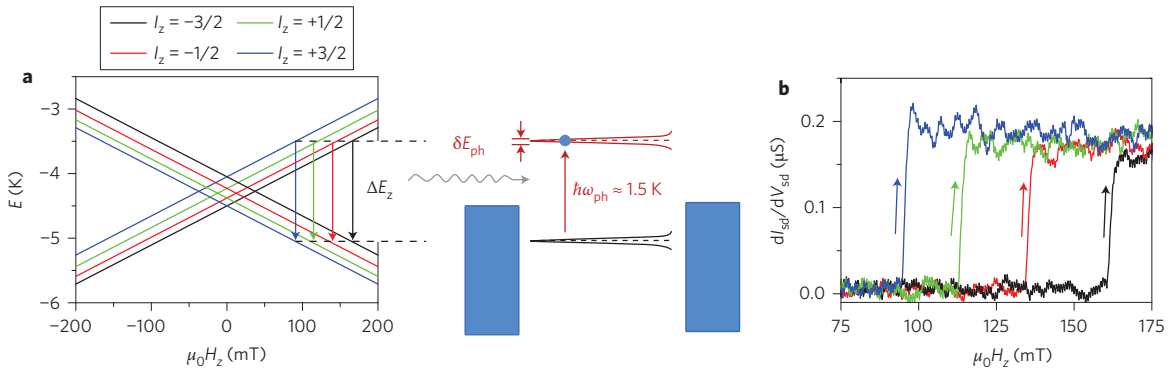

Figure 3 | Strong spin–phonon coupling of a $TbPc_2$-SMM and a CNT NEMS. a, The CNT quantum dot is tuned to a regime of Coulomb blockade ($V_{sd} = 0$, $V_{lg} = 16.5$ mV in Fig. 2c). The magnetization reversal of the $TbPc_2$ via direct transition results in excitation of the electron into a vibrational (LSM) state in the CNT resonator. In contrast to bulk phonons, the energy spectrum of an LSM phonon in one-dimensional CNTs is discretized and yields high quality factors around $Q \approx 1 \times 10^2$. The corresponding phonon linewidth $\delta E_{ph} \approx 15$ mK is smaller than the energy separation between the Tb^{3+} nuclear spin states $\Delta E_I > 120$ mK. Hence, we observe four different transitions, corresponding to the four nuclear spin states as depicted by the coloured arrows and a transition energy $\Delta E_z = \hbar\omega_{ph} = 1.5$ K. **b**, By sweeping the magnetic field component $\mu_0 H_z$ (parallel to the easy axis of the SMM), we induce magnetization reversal of the Tb^{3+} ion, resulting in an abrupt increase in the differential conductance through the dot. The switching field depends on the nuclear spin state occupied before magnetization reversal. The arrows depict the scan direction.

the magnetization reversal of the $TbPc_2$ will indeed occur from each of the four nuclear spin states of the Tb^{3+} ion at magnetic fields of 89, 113, 137 and 161 mT (Fig. 3). Also, the Zeeman energy corresponding to the FWHM of each switching event in Fig. 4b is ~30 mK, which is in close agreement with the phonon linewidth of $\delta E_{ph} = 15$ mK determined in the previous section. Moreover, all four switching events in the $TbPc_2$ have a transition energy of $\Delta E_z = 1.5$ K, which is in perfect agreement with the LSM phonon energy of $\hbar\omega = 1.5$ K. The experimental findings are thus in excellent agreement with the provided model. The strong interaction between the molecular $TbPc_2$ spin and the quantized LSM phonon is further supported by the magnitude of the spin–phonon coupling, which we will evaluate in the following.

Finally, we can estimate the spin–phonon coupling between the magnetization of the $TbPc_2$-SMM and the quantized longitudinal phonon. For this purpose, we consider a $TbPc_2$-SMM rigidly grafted to the suspended CNT. Owing to the conservation of total angular momentum, the magnetization reversal of the Tb^{3+} ion

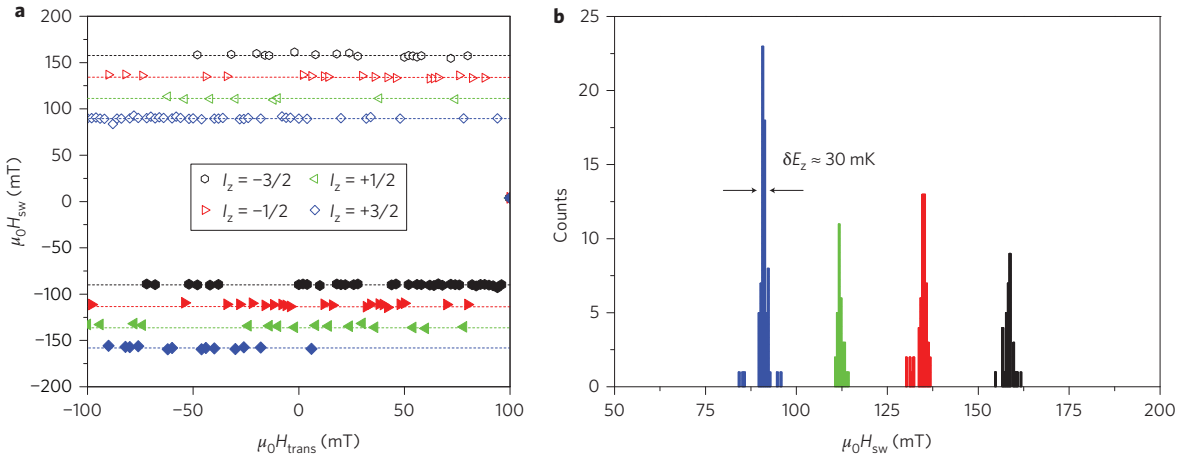

Figure 4 | Nuclear spin-dependent magnetization reversal of a single $TbPc_2$ coupled to a CNT NEMS. a, Switching field $\mu_0 H_{sw}$ versus transverse magnetic field component $\mu_0 H_{trans}$ for a sweep rate of 50 mT s^{-1}. We observe four distinct switching fields at positive values when sweeping the field from negative to positive values (open symbols) and at negative values when reversing the sweep direction (filled symbols). The switching does not depend on the transverse magnetic field component. We therefore attribute these events to the magnetization reversal of the Tb^{3+} ion via a nuclear spin-dependent direct transition enabled by strong spin–phonon coupling. No quantum tunnelling of magnetization was observed in our measurement. The dotted lines are to guide the eye. **b**, Histogram of the switching fields obtained for 200 field sweeps with a zero transverse magnetic field component for one sweep direction and a sweep rate of 50 mT s^{-1}. We observe four dominant switching events at 88, 112, 137 and 160 mT corresponding to the switching fields for the +3/2, +1/2, −1/2 and −3/2 nuclear spin states, respectively. The FWHM of the switching field yields $\delta B = 2$ mT and the corresponding Zeeman energy of $\delta E_z \approx 30$ mK is consistent with the phonon linewidth $\delta E_{ph} \approx 15$ mK.

causes a rotation of the molecule by an angle φ, in a plane perpendicular to its easy axis[10,11,38] (Supplementary Fig. S5). Because of the rigid grafting to the CNT, the lattice rotation of the SMM translates to a longitudinal stretching mode in the suspended CNT resonator beam[10,38]. The Hamiltonian of the hybrid SMM–resonator can be written as

$$H = H_{ph} + H_B + e^{-iJ_z\hat{\varphi}} H_{cf} e^{iJ_z\hat{\varphi}} \quad (2)$$

where $H_{ph} = \hbar\omega_l(a^\dagger a + 1/2)$ corresponds to the energy of the quantized phonon mode and $H_B = g\mu_B B_z J_z$ is the Zeeman energy of the $TbPc_2$ (Supplementary Section S3). The last term describes the modification of crystal electric field (cf) by the rotation of the $TbPc_2$, where H_{cf} is the unperturbed crystal field and φ is the angle of rotation of the crystal lattice. Equation (2) can be reduced to an effective Jaynes–Cummings Hamiltonian (Supplementary Section S3):

$$H = H_{ph} + H_{cf} + H_B + \hbar g_{s-ph}\left(a + a^\dagger\right) O_4^{-4} \quad (3)$$

where H_{ph} describes the free quantized longitudinal phonon mode, $H_{TbPc_2} = H_{cf} + H_B$ the $TbPc_2$-SMM in the absence of the phonon, a and $a^\dagger$ the creation and annihilation operators of the phonon mode and O_4^{4-} the Stevens spin operator of the $TbPc_2$-SMM. The spin–phonon coupling then yields (Supplementary Section S3)

$$g_{s-ph} = \frac{\beta A_4^4}{2}\sqrt{\frac{2\hbar}{I_z\omega}} \quad (4)$$

with the moment of inertia of the $TbPc_2$-SMM is $I_z = 10^{-42}$ kg m^2, the phonon frequency is $\omega_l = 34$ GHz and the crystal field parameter is $\beta A_4^4 = 1.8$ mK. We therefore estimate the spin–phonon coupling to be $g_{s-ph} = 1.5$ MHz. A spin–resonator coupling of this magnitude could result in a suppression of quantum tunnelling of magnetization (QTM) on the SMM by nanomechanical quantum interference effects[10], the creation of coherent magneto-mechanical oscillations[10] or the entanglement of a single spin with quantum mechanical oscillator[9,11]. We would like to point out that we did not observe QTM in our spin–resonator system. Although the absence of QTM could be related to nanomechanical quantum interference effects, as stated above, we do not have sufficient evidence to support such a claim. This would require further study, which is beyond the scope of this work.

In conclusion, we have demonstrated a strong spin–phonon coupling between a single molecular spin and the quantized, high-Q mechanical motion of a CNT resonator. It has been predicted that a coupling of this magnitude would induce strong nonlinearities in the mechanical motion of a carbon nanotube, which can for instance be used to enhance the sensitivity of CNT-based magnetometers[9,25]. A sensitivity of a few μ_B is to be expected[25]. Moreover, the strong spin–phonon coupling would enable the electric manipulation of a single molecular spin by microwave irradiation[9]. Reciprocally, a strong spin–phonon interaction would allow the spin-based detection of the mechanical motion of the nanotube[39] or the ground-state cooling of the resonator by manipulating the molecular spin via electron spin resonance[9]. Ultimately, our results open the path to the quantum entanglement of a single spin and a quantized mechanical motion.

Methods

Sample preparation. A 1-μm-wide metallic local gate was patterned by optical deep-ultraviolet (DUV) lithography and subsequent electron-beam evaporation of molybdenum (20 nm) on a degenerately p-doped silicon wafer with a 300-nm-thick layer of thermal SiO_2. A layer of 100 nm of Al_2O_3 was then deposited by atomic layer deposition. Using optical DUV lithography and electron-beam evaporation of molybdenum (20 nm) and platinum (160 nm), source–drain electrodes were aligned above the local gate. Suspended CNTs were finally grown by chemical vapour deposition (CVD) at 800 °C from a CH_4 feedstock and iron/molybdenum catalyst spots patterned on the source–drain electrodes next to the junction. The CNT device length ranged from 800 nm to 1 μm. The pyrene-substituted $TbPc_2$ was synthesized as reported in ref. 36. $TbPc_2$ powder was dissolved in a solution of dichloromethane and dropcast onto the sample. The droplet was subsequently dried in a critical point dryer to avoid destruction of the suspended CNTs through capillarity effects.

Low-temperature measurements. Conductance measurements were carried out in a He_3/He_4 dilution refrigerator with a base temperature of 20 mK. The refrigerator was equipped with two orthogonal magnetic fields coils, generating up

to 1.4 T and 0.5 T respectively for both coils, in the plane of the sample, with a maximum sweep rate of 250 mT s^{-1}. We could orient the field direction with respect to the easy axis of the $TbPc_2$-SMM by probing the magnetization reversal at different magnetic field angles (Supplementary Section S1). The field sweep rate and temperature dependences of the switching fields are presented in Supplementary Section S2. The transport measurements were made with an ADWIN real-time data acquisition system.

Received 7 September 2012; accepted 11 December 2012; published online 3 February 2013

References

1. Abragam, A. & Bleaney, B. *Electron Paramagnetic Resonance of Transition Ions* (Oxford Univ. Press, 1970).
2. Heitler, W. & Teller, E. Time effects in the magnetic cooling method. *Proc. R. Soc. Lond. A* **155,** 629–639 (1936).
3. Van Vleck, J. H. Paramagnetic relaxation times for titanium and chrome alum. *Phys. Rev.* **57,** 426–447 (1940).
4. Gatteschi, D., Sessoli, R. & Villain, J. *Molecular Nanomagnets* (Oxford Univ. Press, 2006).
5. Villain, J., Hartman-Boutron, F., Sessoli, R. & Rettori, A. Magnetic relaxation in big magnetic molecules. *Europhys. Lett.* **27,** 159–164 (1994).
6. Garanin, D. A. & Chudnosvky, E. M. Thermally activated resonant magnetization tunneling in molecular magnets: $Mn_{12}Ac$ and others. *Phys. Rev. B* **56,** 011102 (1997).
7. Leuenberger, M. & Loss, D. Spin relaxation in Mn_{12}-acetate. *Europhys. Lett.* **46,** 692–699 (1999).
8. Sessoli, R., Gatteschi, D., Caneschi, A. & Novak, N. A. Magnetic bistability of a metal-ion cluster. *Nature* **365,** 141–144 (1993).
9. Palyi, A., Struck, P. R., Rudner, M., Flensberg, K. & Burkard, G. Spin–orbit-induced strong coupling of a single spin to a nanomechanical resonator. *Phys. Rev. Lett.* **108,** 206811 (2012).
10. Kovalev, A., Hayden, L., Bauer, G. & Tscherkovniak, Y. Macrospin tunneling and magneto-polaritons with nanomechanical interference. *Phys. Rev. Lett.* **106,** 147203 (2011).
11. Garanin, D. A. & Chudnovsky, E. Quantum entanglement of a tunneling spin with mechanical modes of a torsional resonator. *Phys. Rev. X* **1,** 011005 (2011).
12. Laird, E., Pei, F., Tang, W., Steele, G. A. & Kouwenhoven L. P. A high quality factor carbon nanotube mechanical resonator at 39 GHz. *Nano Lett.* **12,** 193–197 (2011).
13. Peng, H. B., Chang, C. W., Aloni, S., Yuzvinsky, T. D. & Zettl, A. Ultrahigh frequency nanotube resonator. *Phys. Rev. Lett.* **97,** 087203 (2006).
14. Sapmaz, S., Jarillo-Herrero, P., Blanter, Y. M., Dekker, C. & van der Zant, H. S. J. Tunneling in suspended carbon nanotubes assisted by longitudinal phonons. *Phys. Rev. Lett.* **96,** 026801 (2006).
15. Huettel, A., Witkamp, B., Leijnse, M., Wegewijs, M. R. & van der Zant, H. S. J. Pumping of vibrational excitations in the Coulomb-blockade regime in a suspended carbon nanotube. *Phys. Rev. Lett.* **102,** 225501 (2009).
16. Leturcq, R. *et al.* Franck–Condon blockade in suspended carbon nanotube quantum dots. *Nature Phys.* **5,** 327–331 (2009).
17. Poot, M. & van der Zant, H. S. J. Mechanical systems in the quantum regime. *Phys. Rep.* **511,** 273–335 (2011).
18. Ganzhorn, M. & Wernsdorfer, W. Dynamics and dissipation induced by single electron tunneling in carbon nanotube nanoelectromechanical system. *Phys. Rev. Lett.* **108,** 175502 (2012).
19. Lassagne, B., Tarakanov, Y., Kinaret, J., Garcia-Sanchez, D. & Bachthold, A. Coupling mechanics to charge transport in carbon nanotube mechanical resonators. *Science* **325,** 1107–1110 (2009).
20. Steele, G. *et al.* Strong coupling between single electron tunneling and nanomechanical motion. *Science* **325,** 1103–1107 (2009).
21. Hüttel, A. K. Carbon nanotubes as ultrahigh quality factor mechanical resonators. *Nano Lett.* **9,** 2547–2552 (2009).
22. Lassagne, A., Garcia-Sanchez, D., Aguasca, A. & Bachtold, A. Ultrasensitive mass sensing with a nanotube electromechanical resonator. *Nano Lett.* **8,** 3735–3738 (2008).
23. Chiu, H., Hung, P., Postma, H. W. Ch. & Bockrath, M. Atomic scale mass sensing using carbon nanotube resonators. *Nano Lett.* **8,** 4342–4346 (2008).
24. Jensen, K., Kim, K. & Zettl, A. An atomic-resolution nanomechanical mass sensor. *Nature Nanotech.* **3,** 533–556 (2008).
25. Lassagne, B., Ugnati, D. & Respaud, M. Ultrasensitive magnetometers based on carbon nanotube mechanical resonators. *Phys. Rev. Lett.* **107,** 130801 (2011).
26. Bogani, L. & Wernsdorfer, W. Molecular spintronics using single-molecule magnets. *Nature Mater.* **7,** 179–186 (2008).
27. Heersche, H. *et al.* Electron transport through single Mn_{12} molecular magnets. *Phys. Rev. Lett.* **96,** 206801 (2006).
28. Zyazin, A. S. *et al.* Electric field controlled magnetic anisotropy in a single molecule. *Nano Lett.* **10,** 3307–3311 (2010).
29. Vincent, R., Klyatskaya, S., Ruben, M., Wernsdorfer, W. & Balestro, F. Electronic readout of a single nuclear spin in a single molecule transistor. *Nature* **488,** 357–360 (2012).
30. Urdampilleta, M., Cleuziou, J-P., Klyatskaya, S., Ruben, M. & Wernsdorfer, W. Supramolecular spin valves. *Nature Mater.* **10,** 502–506 (2011).
31. Friedman, J. R., Sarachik, M. P., Tejada, J. & Ziolo, R. Macroscopic measurement of resonant magnetization tunnelling in high-spin molecules. *Phys. Rev. Lett.* **76,** 3830–3833 (1996).
32. Thomas, L. *et al.* Macroscopic quantum tunnelling of magnetization in a single crystal of nanomagnets. *Nature* **383,** 145–147 (1996).
33. Wernsdorfer, W. & Sessoli, R. Quantum phase interference and parity effects in magnetic molecular clusters. *Science* **284,** 133–135 (1999).
34. Takahashi, S. *et al.* Coherent manipulation and decoherence of S=10 single-molecule magnet. *Phys. Rev. Lett.* **102,** 087603 (2009).
35. Ishikawa, N., Sugita, M. & Wernsdorfer, W. Quantum tunneling of magnetization in lanthanide single-molecule magnets: bis(phthalocyaninato)terbium and bis(phthalocyaninato)dysprosium anions. *Angew. Chem. Int. Ed.* **44,** 2931–2935 (2005).
36. Kyatskaya, S. *et al.* Anchoring of rare-earth-based single-molecule magnets on single-walled carbon nanotubes. *J. Am. Chem. Soc.* **131,** 15143–15151 (2009).
37. Lopes, M. *et al.* Surface-enhanced Raman signal for terbium single-molecule magnets grafted on graphene. *ACS Nano* **4,** 7531–7536 (2010).
38. Chudnovsky, E., Garanin, D. A. & Schilling, R. Universal mechanism of spin relaxation in solids. *Phys. Rev. B* **72,** 094426 (2005).
39. Ohm, C., Stampfer, C., Splettstoesser, J. & Wegewijs, M. R. Readout of carbon nanotube vibrations based on spin–phonon coupling. *Appl. Phys. Lett.* **100,** 143103 (2012).

Acknowledgements

The authors thank E. Eyraud, D. Lepoittevin, L. Cagnon, R. Haettel, C. Hoarau, V. Reita and P. Rodiere for technical contributions and discussions, T. Fournier, T. Crozes, B. Fernandez, S. Dufresnes and G. Julie for lithography development, and J.P. Cleuziou and N.V. Nguyen for CNT CVD growth development. The authors also thank E. Bonet, C. Thirion and R. Piquerel for help with software development and M. Urdampilleta, S. Thiele, R. Vincent and F. Balestro for fruitful discussions. Samples were fabricated in the Nanofab facility of the Néel Institute. This work is partially supported by the French National Research Agency National Programme in Nanosciences and Nanotechnologies (ANR-PNANO) project MolNanoSpin (no. ANR-08-NANO-002), European Research Council Advanced Grant MolNanoSpin (no. 226558), ICT-2007.8.0 Future Emerging Technologies Open, Quantum Information Processing Specific Targeted Research Project (no. 211284 MolSpinQIP), the German Research Foundation programme TRR 88 '3Met', Cible 2009, and the Nanosciences Foundation of Grenoble. M.G. thanks the Nanoscience Foundation for financial support.

Author contributions

M.G. and W.W. designed, conducted and analysed the experiments. S.K. and M.R. designed, synthesized and characterized the molecule. M.G. and W.W. co-wrote the paper.

Additional information

Supplementary information is available in the online version of the paper. Reprints and permission information is available online at http://www.nature.com/reprints. Correspondence and requests for materials should be addressed to W.W.

Competing financial interests

The authors declare no competing financial interests.